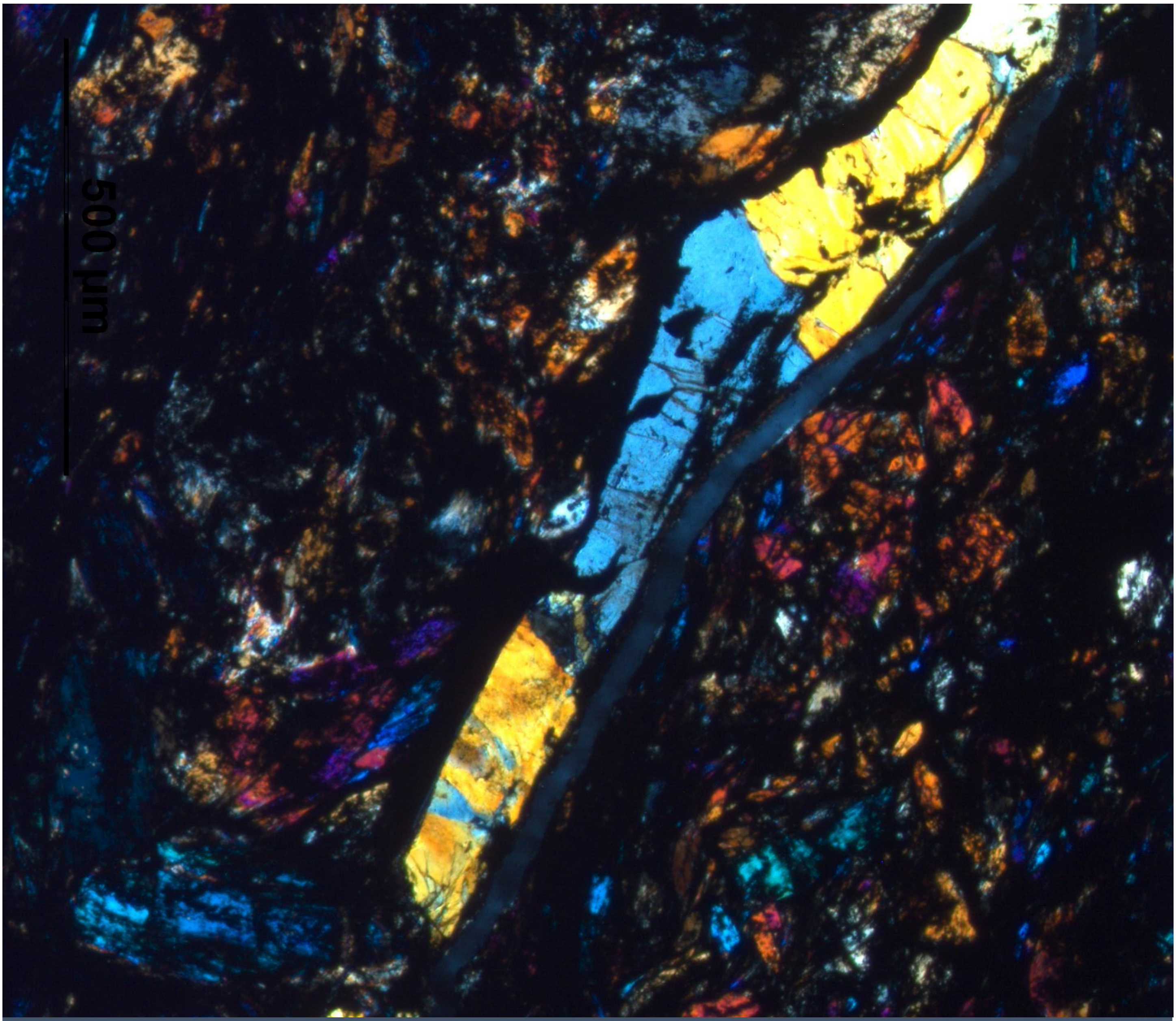

# Genesis and migration of abiotic hydrocarbons in subduction zones

Université de Paris

Antoine Boutier

2022

UNIVERSITA' DEGLI STUDI DI: Torino

DIPARTIMENTO DI: Scienze della Terra

DOTTORATO DI RICERCA IN: Scienze della Terra

CICLO: 34

TITOLO DELLA TESI: Genesis and migration of abiotic hydrocarbons in subduction zones

TESI PRESENTATA DA: Antoine Boutier

TUTORS:
Albeto Vitale Brovarone
Isabelle Martinez
COORDINATORE DEL DOTTORATO: Prof Francesco Dela Pierre

ANNI ACCADEMICI: 2018-2022

SETTORE SCIENTIFICO-DISCIPLINARE DI AFFERENZA:

# Abstract

Highly reducing fluids produced by aqueous alteration of ultramafic rocks, also called serpentinization, may react with a carbon source to produce hydrocarbons through a complete abiotic process. Examples of serpentinization in natural settings are numerous, particularly in relation to seafloor hydrothermalism. At greater depths, abiotic methane genesis may occur in subduction zone settings, where ultramafic minerals with reducing potential, significant fluid circulation, and various carbon sources are present. This production of $CH_4$ bears important implications on our understanding of deep carbon cycling, the redox state of the Earth, on the genesis of prebiotic organic compounds linked to the origin of life, on the quantification of natural carbon emission, and on unconventional sources of energy.

The main aim of the present Ph.D thesis is to improve our understanding of serpentinization in subduction zones associated with abiotic methane formation and the fate of the released methane at depth. To achieve these research goals, this Ph.D thesis presents the results of a natural case study featuring remarkable examples of carbon mobility and fluid-rock interactions in subduction zones. The selected natural case study is the Belvidere Mountain Complex (BMC, Vermont, USA), which provides insight on high-pressure serpentinization in the antigorite stability field (P=<10 kbar, T= <400 °C) and formation of methane-rich metamorphic fluids. The combination of field, (micro) structural, petrological, and geochemical data with thermodynamic modeling provide new insights on the interactions of metamorphic fluid with ultramafic bodies in subduction, and the related implication on deep carbon cycling. Additionally, a Python-based software coupling isotopic and thermodynamic numerical modeling, called Thermotopes-COH, has been developed during this Ph.D. The software allows to quickly model the isotopic composition of various carbon-bearing species,

to calculate the composition and component speciation of COH fluids, and to model the precipitation and dissolution of graphite/diamond through various geological processes. Such tools not only allow us to deepen our understanding of carbon in subduction zones, but also in multiple scientific targets where carbon is of prime importance.

The first chapter of this thesis is an introduction on the Ph.D topic. A general presentation of subduction, serpentinization and abiotic hydrocarbons is provided. Additionally, the main study zones of this Ph.D are presented.

The second and third chapters of this manuscript present the aim of this Ph.D project and the methodology, respectively.

The fourth chapter presents the characterization of the serpentinization patterns in the BMC, with a particular focus on the related genesis of abiotic hydrocarbons in subduction zones. This chapter is presented in the form of a scientific article that was published in Lithos (Boutier et al., 2021), and for which a brief summary is presented in the following. Serpentinization is the process of hydroxylation of olivine-rich ultramafic rocks to produce minerals such as serpentine, brucite and magnetite. This process is commonly accompanied by Fe oxidation and release of $H_2$, which can be involved in abiotic reaction pathways leading to the genesis of light hydrocarbons such as methane ($CH_4$). Examples of this phenomenon exist at the seafloor, for example at the serpentinite-hosted Lost City hydrothermal field, and on land in ophiolites at relatively shallow depths. However, the possibility for serpentinization to occur at greater depths, especially in subduction zones, raises new questions on the genesis of abiotic hydrocarbons at convergent margins and its impact on the deep carbon cycle. High-pressure ultramafic bodies exhumed in metamorphic belts can provide insights on the mechanisms of high-pressure serpentinization in subduction zones and on the chemistry of the resulting fluids. In the Belvidere Mountain complex (BMC, Vermont, USA), microstructures show overgrowth of both primary (Mg# 0.91) and metamorphic (Mg# 0.95) olivine by delicate antigorite crystals, pointing to at least one stage of serpentinization at high-temperature conditions and consistent with the high-pressure subduction evolution of the massif. Formation of ubiquitous magnetite and local Fe-Ni alloys testify to the partial oxidation of $Fe^{2+}$ into $Fe^{3+}$ and generation of reduced conditions. Fluid inclusion trails cross-cutting the primary olivine relicts suggest their formation during the antigorite serpentinization event. MicroRaman spectroscopy on the fluid inclusions reveals a $CH_4$-rich gaseous composition, as well as $N_2$, $NH_3$ and $H_2S$. Moreover, the precipitation of daughter minerals such as lizardite and brucite in the fluid inclusions indicate the initial presence of $H_2O$ in the fluid. High-pressure serpentinization driven by the infiltration of metasediment-derived aqueous fluids is proposed at the origin of $CH_4$ and other reduced fluid species preserved in the fluid inclusions. This suggests the Belvidere Mountain complex as an example of deep abiotic hydrocarbon genesis related to high-pressure serpentinization in an early Paleozoic subduction zone.

In the fifth chapter, the fate of metamorphic methane in subduction is explored by investigating fluid-rock interactions in slab ultramafic and mafic rocks and their implications as potential proxies for metasomatism and carbon recycling in the mantle wedge at convergent margins. Ultramafic and mafic rocks may record dramatic redox variations affecting the exchanges of deep carbon between solid and fluid phases. The Belvidere Mountain Complex includes remarkable examples of deep carbon recycling, which were investigated in order to reconstruct the origin and recycling of carbon, in particular metamorphic methane. This chapter presents new in-situ microRaman data on fluid inclusions and $\delta^{13}C$ of methane extracted from them, bulk $\delta^{13}C$, $\delta^{11}B$ and $^{87}Sr/^{86}Sr$ data, as well as numerical modeling to constrain the pathways of carbon recycling in the BMC. Methane-rich fluid inclusions can be observed in partially serpentinized peridotites (Boutier et al., 2021), in carbonate veins crosscutting the serpentinized rocks and from rodingites, and in amphibolite bodies. Graphite-rich rocks, up to 3.90 wt.% graphite, were collected from a ~6 m-thick metasomatized shear zone within the ultramafic rocks, and from the contact separating the serpentinized ultramafics and the amphibolite. The $\delta^{13}C$ composition of graphite clusters at -15 ‰ (±1.2 ‰ VPBD). Carbonates of the BMC rocks have $\delta^{13}C$ values ranging from -7.26 to -1.27 ‰. The $\delta^{13}C$ of methane extracted from fluid inclusions shows a wide range of values in BMC rocks from -45.2 ‰ to -12.6 ‰. Bulk $^{87}Sr/^{86}Sr$ ratio and $\delta^{11}B$ data suggest infiltration of metasediment-derived fluids, which is further suggested by the abundance of nitrogen and carbon in the fluid inclusions. The mixing between metasediment-derived fluid and serpentinization-related methane from the BMC is proposed as the mechanism leading to graphite precipitation. Further complexity is suggested by the presence of carbonate reduction in samples. The BMC rocks highlight the variability of carbon recycling in a dynamic fluid-rock system, with carbon sources and sinks adapting to evolving redox conditions.

The sixth chapter of this Thesis presents Thermotopes-COH, a python-based software allowing modeling of conventional carbon isotopic exchanges and more advanced thermodynamic and isotopic processes in the C-O-H system in the 300 - 900 °C and 1 - 50 kbar pressure-temperature range. The software allows user-friendly modeling and graphical visualization of five major functions: (1) Carbon isotope equilibrium between two phases, (2) Carbon isotope fractionation modeling, (3) C-O-H fluid speciation, (4) Multi-component

graphite/diamond precipitation, and (5) Graphite/diamond precipitation/dissolution. The software is available for Windows or MacOS. Data produced by the software can be saved as .txt file and .svg file. Along with a description of the software functions, this chapter also provides practical examples based on published geological data. The software manual is provided in the Annexes.

The seventh chapter presents a brief summary of the main Ph.D project results and present possible perspectives for future work.

Keywords: HP Serpentinization, Abiotic methane, C fluxes at subduction zones, Belvidere Mountain Complex, Metamorphic olivine, deep carbon cycle, thermodynamic modeling, isotopic modeling, fluid infiltration, graphite.

## Riassunto

L'alterazione delle rocce ultramafiche, anche nota come serpentinizzazione, può generare fluidi altamente riducenti, la cui interazione con una fonte di carbonio può portare alla formazione di idrocarburi attraverso processi puramente abiotici. Gli esempi di serpentinizzazione in ambienti naturali sono numerosi, in particolare legati ai processi idrotermali dei fondali oceanici. A maggiori profondità, la genesi di metano abiotico può verificarsi in contesti di subduzione dove si riscontri la presenza di minerali ultramafici con potenziale redox, di une significativa circolazione di fluidi, e di fonti di carbonio. La produzione di metano ($CH_4$) abiotico profondo può avere grande importanza per la comprensione del ciclo profondo del carbonio, dello stato di ossidoriduzione della Terra, della genesi di composti organici prebiotici legati all'origine della vita, per migliorare le stime sulle emissioni naturalis di carbonio, e per l'identificazioni di fonti di energia non convenzionali.

L'obiettivo principale di questo dottorato di ricerca è di migliorare la nostra comprensione del processo di serpentinizzazione legato alla formazione di metano abiotico nelle zone di subduzione e al divenire del metano rilasciato in profondità. Per raggiungere questo obiettivo di ricerca, questa tesi di dottorato presenta i risultati ottenuti dallo studio di un esempio naturale caratterizzato da un'eccezionale mobilità del carbonio associato a processi di interazione fluido-roccia in zona di subduzione. L'esempio scelto viene dal Belvidere Mountain Complex (BMC) (Vermont, USA), e fornisce l'opportunità di investigare il processo di serpentinizzazione in condizioni di alta pressione nel campo si stabilità dell'antigorite delle i inclusioni fluide ricche di metano ad esso associate. La combinazione di dati di terreno, microstrutturali, petrologici, geochimici e di modellazione termodinamica ha fornito nuove informazioni sull'interazione tra fluidi metamorfici e corpi ultramafici in subduzione e le loro implicazioni sul ciclo profondo del carbonio. Inoltre, durante questo dottorato è stato sviluppato un software basato su Python, chiamato Thermotopes-COH, che mette in relazione la modellazione numerica isotopica e termodinamica. Il software consente agli utenti di modellare rapidamente la composizione isotopica del carbonio, calcolare la composizione e la speciazione dei componenti di fluidi COH, e di calcolare la precipitazione e/o la dissoluzione del grafite/diamante attraverso vari processi geologici. Tale strumento non solo consente di approfondire la nostra comprensione del carbonio nelle zone di subduzione, potrebbe osservare applicazioni in altri campi di ricerca in cui il carbonio è di primaria importanza.

Il primo capitolo di questa tesi presenta un'introduzione al soggetto di studio. Vengono presentate informazioni sulla subduzione, sulla serpentinizzazione e sugli idrocarburi abiotici. Inoltre, viene introdotta l'area di studio principale di questo studio.

Il secondo e terzo capitolo presentano rispettivamente lo scopo di questo dottorato e la metodologia.

Il quarto capitolo presenta la caratterizzazione dei processi di serpentinizzazione al Monte Belvidere, con un focus particolare alla genesi di idrocarburi abiotici nelle zone di subduzione. Questo capitolo è presentato in forma di articolo in quanto già pubblicato sulla rivista Lithos (Boutier et al., 2021), e per il quale un breve riassunto è presentato di seguito.

La serpentinizzazione è il processo di idratazione di rocce ultramafiche ricche di olivina che porta alla produzione di minerali come serpentino, brucite e magnetite. Questo processo è comunemente accompagnato dall'ossidazione del Fe e dal conseguente rilascio di $H_2$, che può alla formazione di idrocarburi abiotici leggeri, come il metano tramite reazioni abiotiche. Esempi di questo fenomeno sono stati identificati sui fondali marini, come al sito idrotermale di Lost City, serpentinizzato , e sulla terraferma nei massicci ofiolitici a profondità relativamente basse. Tuttavia, la possibilità che la serpentinizzazione avvenga a profondità maggiori, specialmente nelle zone di subduzione, solleva nuovi interrogativi sulla genesi degli idrocarburi abiotici nei margini convergenti e sul suo impatto sul ciclo profondo del carbonio. I corpi ultramafici ad alta pressione esumati nelle catene metamorfiche possono fornire informazioni sui meccanismi di serpentinizzazione ad alta pressione nelle zone di subduzione e sulla chimica dei fluidi ad essi associati. Questo studio si concentra sul complesso ultramafico del Monte Belvidere, appartenente alla catena appalachiana del Vermont settentrionale, negli Stati Uniti. Le microstrutture dei campioni studiati mostrano la sostituzione dell’olivina primaria (Mg# 0,91) e metamorfica (Mg# 0,95) da parte di antigorite, che indica almeno uno stadio di serpentinizzazione in condizioni di alta temperatura coerente con l'evoluzione metamorfica di alta pressione del complesso ultramafico del Monte

Belvidere. L’onnipresente formazione di magnetite e locali leghe Fe-Ni testimoniano il processo di ossidazione parziale di $Fe^{2+}$ in $Fe^{3+}$ e la generazione di condizioni ridotte. La presenza di trails di inclusioni fluide che attraversano i relitti primari di olivina suggeriscono la loro formazione durante l'evento di serpentinizzazione in facies antigorite. Indagini in spettroscopia MicroRaman sulle inclusioni fluide hanno rivelato una composizione gassosa ricca di $CH_4$, oltre a $N_2$, $NH_3$ e $H_2S$. Inoltre, la precipitazione di minerali figli come lizardite e brucite nelle inclusioni fluide indica la presenza iniziale di $H_2O$ nel fluido. L’origine di questo metano e di altre specie fluide ridotte conservate nelle inclusioni fluide è interpretata come il risultato della serpentinizzazione ad alta pressione promossa dall'infiltrazione di fluidi acquosi derivati da metasedimenti. Ciò suggerisce come il complesso del Monte Belvidere possa rappresentare un esempio di genesi profonda di idrocarburi abiotici correlata alla serpentinizzazione ad alta pressione in una zona di subduzione di età Paleozoica.

Nel quinto capitolo di questa tesi vengono discusse le sorti del carbonio in subduzione considerando le interazioni fluido-roccia nei sistemi ultramafici e le loro implicazioni come potenziali proxy per il metasomatismo e il riciclaggio del carbonio nel cuneo del mantello ai margini convergenti. Le rocce ultramafiche possono registrare forti variazioni redox che influenzano gli scambi di carbonio profondo tra le fasi solide e fluide. Il Belvidere Mountain Complex (BMC) è un corpo ultramafico coinvolto nella subduzione Taconica nell’Ordoviciano, fino a condizioni metamorfiche pari a 510-520 °C e 0,9-1,3 GPa. Precedenti indagini indicano che il BMC ha subito una parziale serpentinizzazione e un riciclaggio del carbonio nella zona di subduzione (Boutier et al., 2021). Qui presentiamo dati MicroRaman sulle inclusioni fluide, i dati $\delta^{13}C$, $\delta^{11}B$ e $^{87}Sr/^{86}Sr$ e i risultati della modellazione numerica volti a limitare i percorsi di riciclaggio del carbonio nel BMC. La spettroscopia MicroRaman sulle inclusioni fluide rivela composizioni gassose ricche di $CH_4$, insieme a $N_2$, $NH_3$ e composti S-H. Queste inclusioni fluide ricche di metano possono essere osservate nelle peridotiti parzialmente serpentinizzate, nelle vene carbonatiche e nei corpi anfiboliti ci associati al corpo ultramafico. Il BMC ospita anche un esempio eccezionale di deposito di grafite , con concentrazioni fino al 3,9 % in peso,lungo una vena spessa circa 6 m all'interno del corpo ultramafico serpentinizzato e lungo i contatti litologici. Le composizioni $\delta^{13}C$ della grafite nei campioni ricchi in grafite studiati è si concentrano intorno a -15 ‰ (VPBD). I carbonati presenti nel sistema hanno valori di $\delta^{13}C$ compresi tra -7,26 e -1,27 ‰. Le indagini su $\delta^{13}C$ del metano nelle inclusioni fluide mostrano un'ampia gamma di valori nelle rocce ultramafiche da -45,2 ‰ a -12,6 ‰. Il rapporto $^{87}Sr/^{86}Sr$ e $\delta^{11}B$ suggeriscono un'infiltrazione di fluido dalle rocce metasedimentarie, che è ulteriormente suggerita dall'abbondanza di azoto e carbonio nelle inclusioni fluide. Questa grafite viene interpretata come il risultato del mescolamento dei fluidi ricchi in metano prodotti dalla serpentinizzazione del BMC con un fluido di affinità metasedimentaria. Ulteriore complessità è suggerita dalla presenza di grafite interpretabile come il risultato di riduzione di carbonato. Le rocce BMC evidenziano la diversità dei processi di riciclaggio del carbonio in un sistema dinamico di interazione roccia-fluido, con la mobilizzazione del carbonio e i reservoir di carbonio che si adattano alle condizioni redox in evoluzione.

Il sesto capitolo di questa tesi presenta Thermotopes-COH, un software basato su Python che consente la modellazione degli scambi isotopici del carbonio convenzionali e di processi termodinamici e isotopici più avanzati nel sistema COH e nell'intervallo di pressione-temperatura da 300 a 900 °C e da 1 a 50 kbar. Il software consente la modellazione intuitiva e la visualizzazione grafica di cinque funzioni principali: (1) equilibrio isotopico del carbonio tra due fasi, (2) modellazione del frazionamento isotopico del carbonio, (3) speciazione di fluidi COH, (4) precipitazione di grafite in sistemi multicomponente, e (5) mobilità del carbonio. Il software è disponibile per Windows o MacOS. I dati prodotti dal software possono essere estratti come file .txt e file .svg. Insieme a una descrizione delle funzioni del software, questo capitolo fornisce anche esempi pratici basati su dati geologici pubblicati. Un manuale d’uso è presentato negli Annessi.

Il settimo capitolo presenta una breve sintesi dei risultati raggiunti durante questo dottorato e possibili prospettive per lavori futuri.

Keywords: Serpentinizzazione HP, Metano abiotico, Flussi C nelle zone di subduzione, Belvidere Mountain Complex, Olivina metamorfica, ciclo profondo del carbonio, modellazione termodinamica, modellazione isotopica, infiltrazione di fluidi, grafite.

## Abstract

L'altération des roches ultramafiques génère des fluides hautement réducteurs riches en $H_2$, pouvant réagir avec une source de carbone pour produire des hydrocarbures par un processus complètement abiotique. Les preuves de ce processus dans les milieux naturels sont nombreuses, en particulier dans le cas de l'hydrothermalisme des fonds marins. À plus grande profondeur, la méthanogenèse abiotique peut se produire dans des contextes de subduction en fonction de la disponibilité des minéraux ultramafiques ayant un potentiel de réduction, une importante circulation de fluide et la présence d'une source de carbone. Cette production de $CH_4$ revêt une importance dans notre compréhension du cycle profond du carbone, de l'état d'oxydation de la Terre, de la genèse des composés organiques

prébiotiques liés à l'origine de la vie et de la quantification des émissions naturelles de gaz ($CO_2$, $CH_4$). De plus ce méthane doit être quantifié si l'on veut faire des bilans corrects des émissions naturelles de gaz à effet de serre. De plus, ce méthane pourrait également être considéré comme une source d'énergie non conventionnelle.

L'objectif principal de cette thèse est d'améliorer notre compréhension de la serpentinisation en zone de subduction associée à la formation de méthane abiotique et du devenir du méthane libéré en profondeur. Pour faire avancer cet objectif global de recherche, ce doctorat présente les résultats d'une étude de cas naturel présentant un exemple exceptionnel de la mobilité du carbone et d'interaction fluide-roche en zone de subduction dans le cas du Belvidere Mountain Complex (BMC) (Vermont, États-Unis). Cet exemple fournit un aperçu de la serpentinisation à haute pression dans le champ de stabilité de l'antigorite et met en évidence la présence d'inclusions fluides riches en méthane. La combinaison de données de terrain, (micro)structurelles, pétrologiques et géochimiques associée à de la modélisation thermodynamique fournit de nouvelles informations sur les interactions des fluides métamorphiques avec les corps ultramafiques en subduction, et sur le cycle profond du carbone. De plus, un logiciel Python de modélisation numérique couplant des données isotopiques et thermodynamiques, appelé Thermotopes-COH, a été développé au cours de cette thèse. Il permet de modéliser rapidement les compositions isotopiques du carbone de différentes espèces carbonées, de calculer la composition de fluide porteur de COH et de calculer la précipitation et la dissolution du carbone solide lors de divers processus géologiques. Un tel outil permet non seulement d'approfondir notre compréhension du carbone en zone de subduction mais permettra également d'étudier d'autres domaines où le carbone est d'une importance primordiale.

Le premier chapitre de cette thèse est une introduction au sujet de thèse. Une présentation générale de la subduction, de la serpentinisation et des hydrocarbures abiotiques est fournie. De plus, les principales zones d'étude de cette thèse sont présentées.

Les deuxième et troisième chapitres de ce manuscrit présentent respectivement l'objectif de ce projet de doctorat et la méthodologie.

Le quatrième chapitre présente les caractérisations de la serpentinisation du BMC. La serpentinisation est le processus d'hydroxylation des roches ultramafiques riches en olivine pour produire des minéraux tels que la serpentine, la brucite et la magnétite. Ce processus s’accompagne généralement d'une oxydation du fer associée à une libération de $H_2$ qui peut alors être impliquée dans des réactions abiotiques conduisant à la genèse d'hydrocarbures légers tels que le méthane ($CH_4$). Des exemples de ce phénomène existent dans les fonds marins, comme le champ hydrothermal de Lost City, mais aussi à la surface des continents dans les massifs ophiolitiques pour des profondeurs relativement faibles. Cependant, la possibilité que la serpentinisation se produise à de plus grandes profondeurs, en particulier dans les zones de subduction, soulève de nouvelles questions sur la genèse de ces hydrocarbures abiotiques dans les marges actives et son impact sur le cycle profond du carbone. Les corps ultramafiques de haute pression, exhumés dans les ceintures métamorphiques des massifs orogéniques, peuvent fournir des informations sur les mécanismes de serpentinisation à haute pression dans les zones de subduction et sur la chimie des fluides résultants. Cette étude porte sur le complexe ultramafique de Belvidere Mountain appartenant à la ceinture des Appalaches, au nord du Vermont (USA). Les microstructures montrent une surcroissance de cristaux d'antigorite au dépend d’olivine primaire (Mg # 0,91) et métamorphique (Mg # 0,95), indiquant au moins une étape de serpentinisation à haute température, cohérente avec l'évolution de la subduction à haute pression du Belvidere Mountain Complexe (BMC). La formation de magnétite et localement d'alliages Fe-Ni témoigne de l'oxydation partielle du $Fe^{2+}$ en $Fe^{3+}$ et de conditions réduites. Des traînées d'inclusions fluides recoupant les reliques primaires d'olivine suggèrent leur formation lors de l'événement de la serpentinisation en antigorite. La spectroscopie microRaman sur les inclusions fluides révèle une composition gazeuse riche en $CH_4$, ainsi qu'en $N_2$, $NH_3$ et $H_2S$. De plus, la présence de minéraux fils tels que la lizardite et la brucite dans les inclusions fluides atteste la présence initiale de $H_2O$ dans le fluide. Une serpentinisation à haute pression entraînée par l'infiltration de fluides aqueux dérivés de métasédiments est proposée pour l'origine du $CH_4$ et des autres espèces fluides réduites piégées dans les inclusions fluides. Cela suggère que le massif du BMC est un exemple de genèse abiotique profonde d'hydrocarbures liée à la serpentinisation à haute pression dans une zone de subduction du Paléozoïque précoce.

Le devenir du carbone dans la subduction est exploré dans le Chapitre 5 en considérant les interactions fluide-roche dans les roches ultramafiques en dalles et leurs implications en tant que proxys potentiels pour le métasomatisme et le recyclage du carbone dans le coin du manteau aux marges convergentes. Les roches ultramafiques peuvent connaître des variations redox spectaculaires affectant les mal dit aussi… phases porteuses de C et leurs équilibres notamment entre les phases solide et fluide. Le Belvidere Mountain Complex (BMC), qui a connu des conditions P, T allant jusqu'à 510-520 °C et 0,9-1,3 GPa, a subi une serpentinisation partielle et un recyclage du carbone dans la zone de subduction (Boutier et al., 2021). Nous présentons dans ce chapitre un ensemble de données microRaman sur les inclusions fluides, les analyses du $\delta^{13}C$ du CH4 présent dans ces IF, des données de $\delta^{13}C$, $\delta^{11}B$

et $^{87}Sr/^{86}Sr$ sur roche totale ainsi que les résultats de modélisation numérique visant à contraindre les voies de recyclage du carbone dans le BMC. La spectroscopie MicroRaman sur les inclusions fluides révèle des compositions gazeuses riches en CH4, ainsi que des composés N2, NH3 et S-H. Des inclusions fluides riches en méthane peuvent être observées dans les péridotites partiellement serpentinisées, dans les veines carbonatées et dans les corps amphiboliques associés au corps ultramafique. Le BMC abrite également un exemple exceptionnel de dépôt de graphite, pour lequel les concentrations atteignent jusqu'à 3,90 % en poids le long d'une veine d'environ 6 m d'épaisseur dans le corps ultramafique serpentinisé et le long des contacts lithologiques. La composition en $\delta^{13}C$ du graphite se regroupe autour de -15 ‰ (VPBD). Les carbonates présents dans le système ont des valeurs de $\delta^{13}C$ allant de -7,26 à -1,27 ‰. Enfin, les analyses du $\delta^{13}C$ du méthane présent dans les inclusions fluides montrent une large gamme de valeurs dans les roches ultramafiques allant de -45,2 ‰ à -12,6 ‰. Le rapport $^{87}Sr/^{86}Sr$ et $\delta^{11}B$ suggèrent une infiltration fluide à partir des roches métasédimentaires, ce qui est également suggéré par l'abondance d'azote et de carbone dans les inclusions fluides. La libération de méthane liée à la serpentinisation du massif BMC, se mélangeant à un fluide infiltrant d'affinité métasédimentaire est proposée comme un mécanisme conduisant à la précipitation du graphite. Une complexité supplémentaire est suggérée par la réduction direct de carbonate dans les échantillons. Les réactions observées dans les roches du BMC mettent en évidence la variabilité du recyclage du carbone dans un système fluide-roche dynamique, avec une mobilisation et un puits de carbone s'adaptant à l'évolution des conditions redox.

Le chapitre 6 est une présentation du logiciel Thermotopes-COH, logiciel Python permettant la modélisation des échanges isotopiques conventionnels entre différentes

phases carbonés ainsi que la modélisation des processus thermodynamiques et isotopiques plus avancés dans le système C-O-H dans la gamme de pression-température 300 - 900 °C et 1 - 50 kbar. Le logiciel permet une modélisation avec une prise en main facile et une visualisation graphique de cinq fonctions principales : (1) l'équilibre isotopique du carbone entre deux phases, (2) la modélisation du fractionnement isotopique du carbone, (3) la spéciation des fluides COH, (4) la précipitation du graphite à partir de plusieurs composants et (5) la mobilité du carbone. Le logiciel est disponible pour Windows ou MacOS. Les données produites par le logiciel peuvent être extraites sous forme de fichier .txt et de fichier .svg. Outre une description des fonctions du logiciel, ce chapitre présente également des exemples pratiques basés sur des données géologiques publiées.

Mots-clés : Serpentinisation HP, Méthane abiotique, Flux de C dans les zones de subduction, Complexe de Belvidere Mountain, Olivine métamorphique, cycle profond du carbone, modélisation thermodynamique, modélisation isotopique, infiltration fluide, graphite.

# Contents

# Part I - Introduction, aims, Thesis outline and methodology

# 1 Introduction

This Ph.D explores the possibility of ultramafic rocks in subduction to promote serpentinization and to produce abiotic hydrocarbons, especially methane, as well as the fate of the produced fluids in subduction zones. This research is based on two natural case studies, the Lanzo massif in the western Italian Alps, and the Belvidere Mountain Complex in Northern Vermont, which is part of the Appalachian belt. These localities are former asbestos mines that exhibit various pieces of evidence for deep carbon mobility through fluid-rock reactions involving C-bearing phases such as graphite, carbonates, and methane. The study samples provide new insights into the mechanisms of production and conversion of C-bearing species through abiotic processes linked to serpentinization in subduction zones, as well as the becoming of the resulting fluids. This chapter provides the background information and the state of the art about abiotic hydrocarbons, serpentinization, and their role in subduction zone element cycling.

## 1.1 Subduction and carbon cycling

Subduction zones are key geodynamic settings for carbon recycling on Earth. They control the influx of carbon from shallow reservoirs to the deep mantle, and the return of a part of this carbon to the surface. The depths at which carbon is mobilized during subduction may be strongly linked to the stability of hydrous phases in the subducted slab or in the overlying mantle wedge (Ague, 2017; Hacker, 2008; Scambelluri et al., 2019; Schmidt and Poli, 2014; Van Keken et al., 2011). The stability of hydrous and carbon-bearing phases during subduction metamorphism in turn is intimately linked to the structural, seismic, and thermal characteristics of subduction zones (Schmidt and Poli, 2014). Because serpentinites may strongly affect the water budget of subduction zone fluids, either during serpentinization or de-serpentinization, it is important to focus on the relationships between serpentinite formation/transformation and carbon budgets in subduction (Alt et al., 2013; Debret and Sverjensky, 2017; Menzel et al., 2018; Piccoli et al., 2019; Power et al., 2013; Vitale Brovarone et al., 2020).

### 1.1.1 Subduction zone

Subduction zones are sites where cooled oceanic crust and mantle lithosphere (also called slab) sink into the mantle at convergent plate margins. The slab pull of the descending plate is the main driving force regulating the plate motions and causes mid-ocean ridges to spread. Subduction zones are also Earth's largest systems for element cycling into the mantle (Stern, 2002). The subducted material consists of hydrated oceanic lithosphere and sediments, its transformation induces melting of the mantle on top of the slab (called mantle wedge), volcanic arc magmatism and the creation of new continental crust (Stern, 2002). They are also, by nature, regions of high geohazard related to earthquakes and volcanoes. As not all the subducted rocks are recycled in the upper few hundred kilometers of a subduction zone, slab materials may also sink to the core-mantle boundary, where this residue may be reheated for a billion years or so until it can be remobilized as a mantle plume (Hofmann, 1997). Subduction zones evolve over time, initiating with normal oceanic lithosphere, to the collision involving continental lithosphere or oceanic lithosphere with thickened crust. During collision, subducted material of both oceanic and continental origin may be exhumed, providing us indirect access to subduction zone metamorphism (O’Brien, 2001). In our solar system, only Earth appears to have subduction zones and plate tectonics. Mercury and Earth's moon are tectonically and magmatically dead, while Venus is dominated by thick lithosphere and mantle plumes, while geologic features of Mars suggest active plate tectonic in past time (Connerney et al., 1999; Phillips and Hansen, 1998; Rieder et al., 1997).

Subduction zones can differ in geometry and thermal structure depending on the age of the incoming plate, the convergence velocity, the dip angle and the relative proportions of sediments, oceanic crust and hydrated mantle in the subducting slab (Stern, 2002; Syracuse et al., 2010). Other relevant factors such as the evolution of the rheology of the slab-mantle interface and the amount of frictional heating along the subduction path are considered (Abers et al., 2006; Wada and Wang, 2009). All these parameters dictate the pressure-temperature (P-T) path of the subducting slab and will govern the slab lithologies and the intensity of devolatilization reactions (Syracuse et al., 2010; Van Keken et al., 2011). This results in usually three main types of subduction based on their thermal regime: warm, intermediate and cold subduction zones (Fig. 1.1).

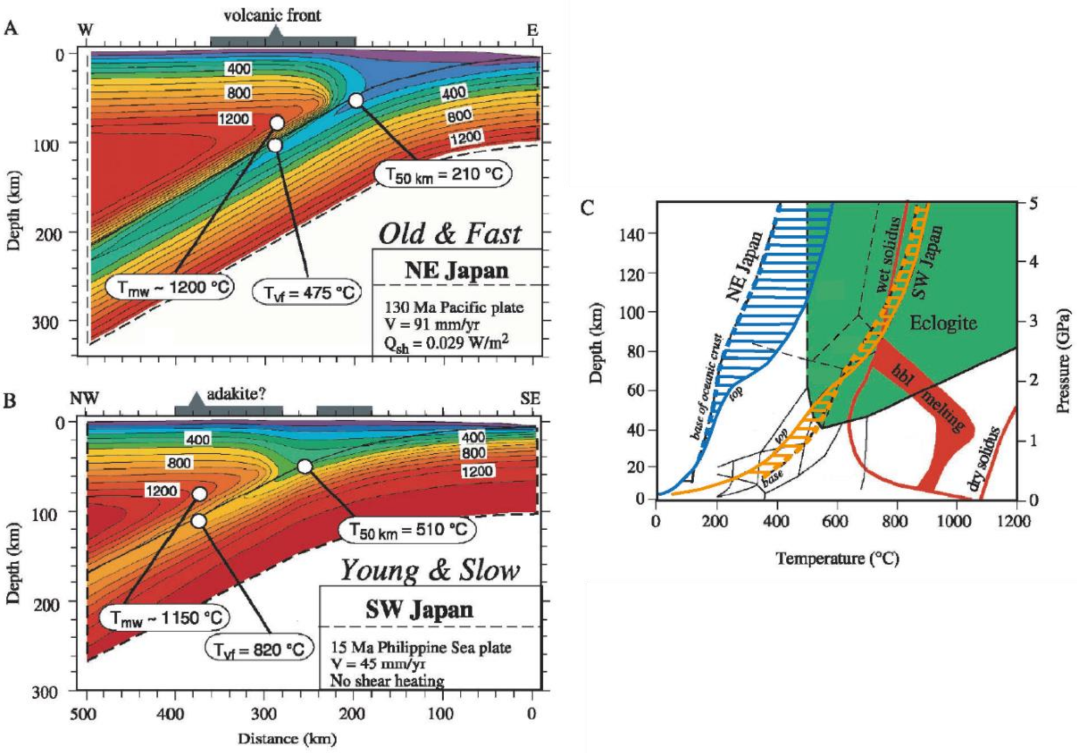

*Fig. 1.1: Thermal models of end-member (young and hot versus old and cold) subduction zones. A: NE Japan, example of a cold subduction zone. B: SW Japan arc, example of a hot subduction zone. C: P-T path adopted by hot subduction (orange) and cold subduction (blue). Modified from* Stern, 2002.

### 1.1.2 Dehydration reactions

Water in subduction plays a fundamental role for deformation, partial melting and seismicity in subduction zones (Hacker, 2008; Wassmann and Stoeckhert, 2013). Water is brought along in the subducting slab as pore fluids, structurally bound $H_2O$ or hydroxyl groups in hydrous minerals, and in fluid inclusions of minerals including nominally anhydrous minerals (Faccenda, 2014).

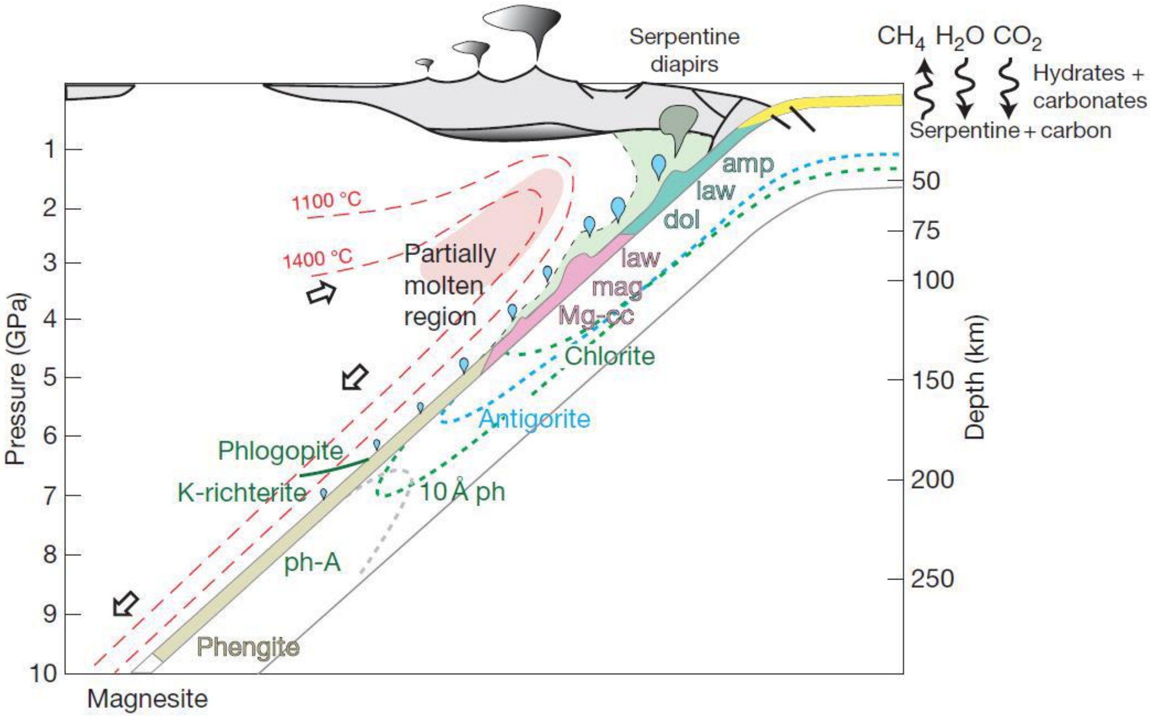

*Fig. 1.2: Schematic representation of devolatilization processes in subduction zones, showing the stability of major volatile phases in the subducting oceanic crust (yellow, blue and pink colors) and the slab mantle lithosphere (green and blue dashed lines), and serpentinization of the mantle wedge (green field). amp: amphibole; law: lawsonite; dol: dolomite; mag: magnesite; Mg-cc: magnesian calcite;10 Å ph: 10 Å-phase; ph-A: phase A (from* Schmidt and Poli, 2014*).*

This water is released from the slab through various processes acting at different depths (Fig. 1.2). The compaction of sediments along the shallow rocks of the upper ocean crust expels pore fluids from the slabs at shallow depth (Hyndman andPeacock, 2003). At greater depths, the bulk of the water released comes from the metamorphic breakdown reactions of hydrous minerals in sediments (e.g. clay minerals, biotite, phengite, chloritoid, zoisite), altered oceanic crust (e.g. chlorite, lawsonite, epidote, biotite, amphibole), and hydrated mantle (e.g. brucite, lizardite, antigorite, chlorite, talc, 10 Å-phase, humite-group minerals, phase A) (Faccenda, 2014; Schmidt and Poli, 2014). The importance of these minerals will depend on their water content and modal abundance in the crust. For example, lawsonite carries 11.3 wt.% water and is typically 7–15 vol.% of the altered oceanic crust, whereas the amphibole constitutes a larger fraction of the assemblage (20–60%) but contains only ~2 wt.% water. Because the water is stored within different mineral phases, it is progressively released as P-T conditions increase and different breakdown reactions occur. Part of this water, when stored in the most resilient minerals phase such as phengite and phase A, can be subducted deeply beyond the subarc depth (Hacker, 2008).

Thermodynamic models indicate that slabs release water continuously during subduction (Van Keken et al., 2011). However, the source of the released fluids changes with depth: firstly, sediments release water at shallow levels, followed by the altered oceanic crust, and finally the hydrated lithospheric mantle (Gorman et al., 2006; Hyndman and Peacock, 2003; Schmidt and Poli, 2014). Owing to the stability of antigorite and chlorite to high pressures and temperatures relative to other hydrous phases, serpentinized mantle rocks have the potential to transfer water to sub-arc and potentially post-arc regions. Depending on the thermal structure of the subducting slab, up to 40% of the water stored in serpentinized mantle may be transferred into the deeper mantle (Hacker, 2008; Rüpke et al., 2004; Ulmer and Trommsdorff, 1995). The fluids released from the slab rise along the slab-mantle interface, where they interact with the mantle wedge to form serpentinite and hybrid mélange rock rich in amphibole, talc, and chlorite (Bebout, 1991; Spandler et al., 2008). These mélange rocks, forearc mantle wedge serpentinites, and serpentinites from the hydrated lithosphere, may be dragged down with the slab and thereby deliver volatiles to depths of arc magma genesis (Hyndman and Peacock, 2003; Spandler and Pirard, 2013).

Serpentinites are considered the potentially most important water source below the magmatic arc (Padrón-Navarta et al., 2010b; Ulmer and Trommsdorff, 1995), which make serpentinite dehydration reactions of particular significance. Serpentine dehydration is a progressive process. The mineralogy of serpentinite evolves along the subduction initially composed of lizardite, chrysotile, and brucite, which usually contain about 13 wt% of $H_2O$. With increasing temperature (at 250-350 °C), lizardite and chrysotile are replaced by antigorite (Fig. 1.3)(Evans, 2004; Guillot et al., 2015; Schwartz et al., 2013).

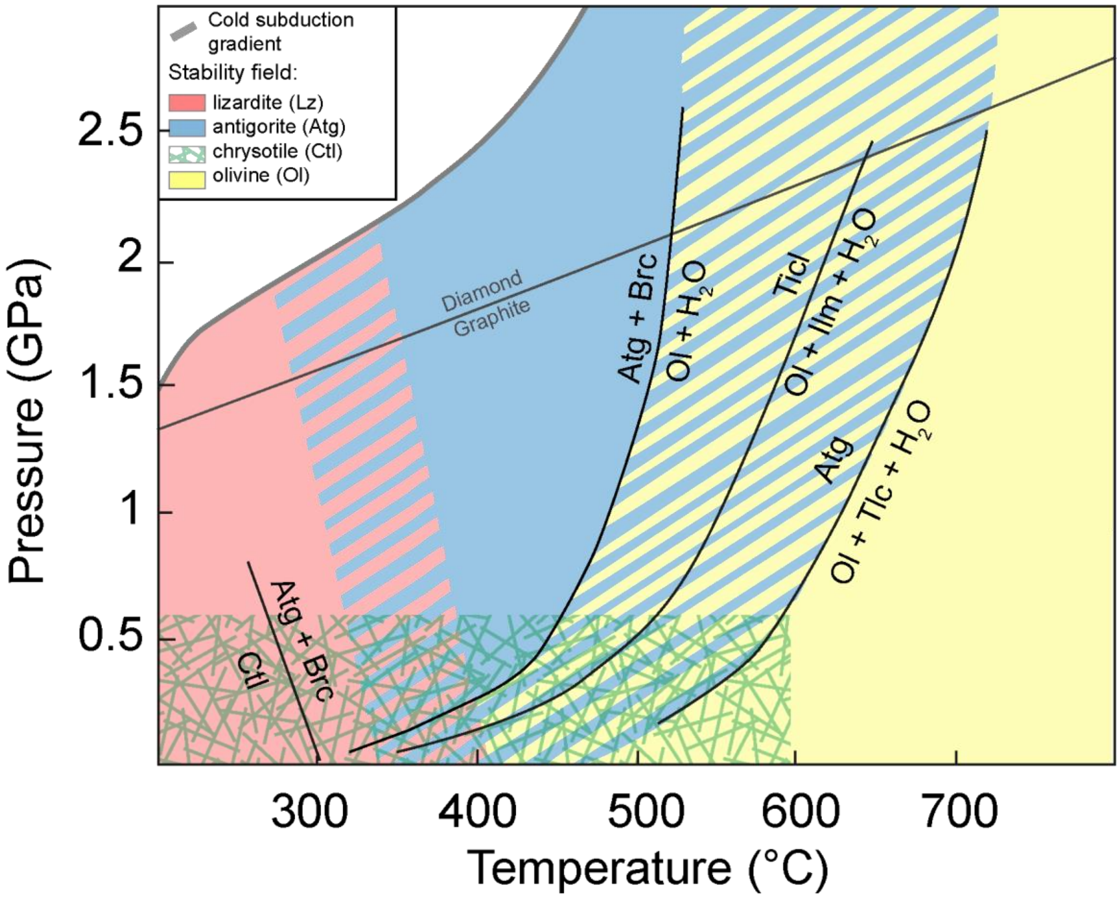

*Fig. 1.3: Simplified stability field of serpentine type minerals and olivine, modified from* Guillot et al., (2015) *(see references therein for details on the main reactions).*

This first metamorphic reaction releases up to 2 wt% of water with reaction such as:

$$17\, Lizardite/Chrysotile \;=\; Antigorite \;+\; 3\, Brucite\; (1.1)$$

$$16\, Lizardite/Chrysotile \;+\; 2\, SiO_{2,aq} \;=\; Atg \;+\; H_2O.\, (1.2)$$

These reactions are followed by the destabilization of brucite:

$$Antigorite \;+\; 20\, Brucite \;=\; 34\, Forsterite \;+\; 51\, H_2O\; (1.3)$$

Which average up to 2.2 wt% of $H_2O$ based on the initial amount of brucite in the serpentinite. Lastly the remaining antigorite in the rock releases between 6 and 11 wt% of water during its dehydration (Padrón-Navarta et al., 2013, and references therein). The temperature of antigorite dehydration varies according on the pressure an aluminum content of the rock from 500°C to 680 °C (Bromiley and Pawley, 2003; Padrón-Navarta et al., 2013, 2010a; Ulmer and Trommsdorff, 1995):

$$Antigorite \;=\; 18\, Forsterite \;+\; 4\, Talc \;+\; 27\, H_2O\; (1.4)$$

$$Antigorite \;=\; Olivine \;+\; Orthopyroxene \;+\; Chlorite \;+\; H_2O\; (1.5)$$

$$Antigorite \;=\; Orthopyroxene \;+\; Phase\ A \;+\; H_2O\; (1.6)$$

The phase assemblage produced by the low-pressure dehydration reaction (1.4) is common in contact-metamorphic serpentinites (e.g. Trommsdorff and Evans, 1972). The reaction (1.5) is the most relevant serpentinite dehydration reaction along warm and intermediate P-T paths in subduction zones, producing prograde chlorite-harzburgite (Bromiley and Pawley, 2003; Trommsdorff et al., 1998). The reaction (1.6) can occur in cold subduction zones where water can be retained in phase A after antigorite breakdown and delivered at subarc depth (Maurice et al., 2018; Rüpke et al., 2004).

As the serpentinization reaction commonly involve the oxidation of $Fe^{2+}$ in $Fe^{3+}$, the deserpentinization reaction may be accompanied by the inverse reaction with the reduction of $Fe^{3+}$ in magnetite to $Fe^{2+}$ incorporated in olivine and orthopyroxene and a coupled formation of hematite and oxidation of Fe-Ni sulphides to fluid-mobile sulphate (Alt et al., 2012; Debret et al., 2015; Merkulova et al., 2017). This accompanies the water transfer from deserpentinization by an oxidation from the slab to the overlying mantle wedge.

### 1.1.3 Deep carbon cycle, and carbon mobility

Earth's climate and habitability are highly dependent on the redistribution of carbon among geological reservoirs through time (Berner and Kothavala, 2001; Hayes and Waldbauer, 2006; Zahnle et al., 2007). The atmosphere and the biosphere represent only a small fraction of the total Earth's carbon, with most of it stored in the core, mantle, and crust (Dasgupta and Hirschmann, 2010; Hirschmann, 2018). The transfer of carbon from deep Earth to the atmosphere ("outgassing") and from surface reservoir into subduction ("ingassing") can varies through geological time, resulting in global climate changes (Berner, 1999; Dasgupta, 2013; Dasgupta and Hirschmann, 2010; Evans, 2011). This long term and global-scale carbon transfer has been termed "deep carbon cycle" and regulates processes both at the surface and in the mantle (Dasgupta, 2013; Orcutt et al., 2019). Moreover, carbon plays a key role in determining the oxygen fugacity condition of the atmosphere and mantle across geological time (Duncan and Dasgupta, 2017; Hayes and Waldbauer, 2006; Stagno, 2019).

Subduction zones are the only ingassing active fluxes storing the carbon back to the Earth mantle. However, the fate of the carbon brought along subductions is complex as a significant portion of this carbon can be released during burial. Estimates of the carbon budget at subduction zones need to take into account multiple processes and the associated fluxes (Fig. 1.4)(Kelemen and Manning, 2015).

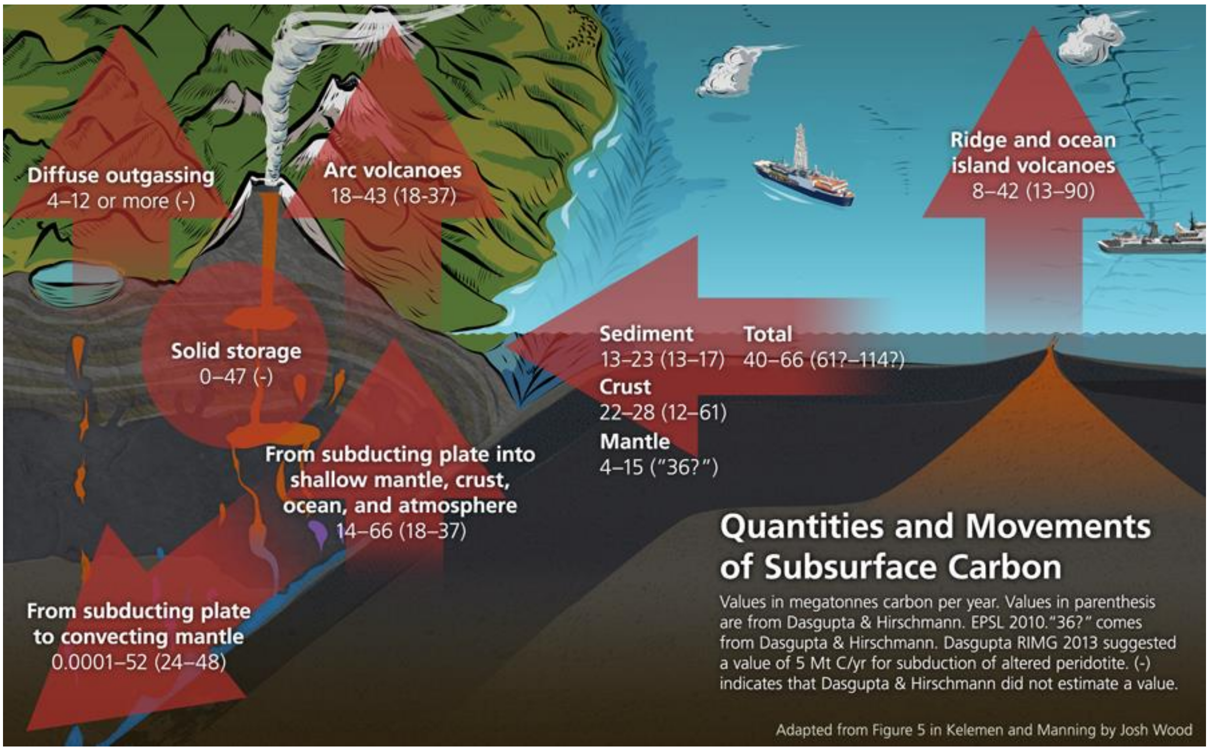

Quantities and Movements of Subsurface Carbon

Values in megatonnes carbon per year. Values in parenthesis are from Dasgupta & Hirschmann. EPSL 2010."36?" comes from Dasgupta & Hirschmann. Dasgupta RIMG 2013 suggested a value of 5 Mt C/yr for subduction of altered peridotite. (-) indicates that Dasgupta & Hirschmann did not estimate a value.

Adapted from Figure 5 in Kelemen and Manning by Josh Wood

*Fig. 1.4: Estimates of geological carbon fluxes. Data from Kelemen and Manning, (2015) and Dasgupta and Hirschmann, (2010) for comparison (©Deep Carbon Observatory).*

Carbon is stored in the oceanic lithosphere in marine sediments, altered crust and hydrated lithospheric mantle, which represent between 40 - 66 Mt C/year entering into subduction (Kelemen and Manning, 2015). As the carbon released at oceanic ridge and the associated volcanoes range at 8 - 42 Mt C/year, the formation and recycling of oceanic lithosphere amounts to a net sink of carbon from shallow reservoirs. Marine sediments (Plank and Langmuir, 1998) and altered oceanic crust (Alt and Teagle, 1999) make up ~80 - 90 % of the carbon budget of current subducting oceanic lithosphere (35 - 51 Mt C/year), while the hydrated lithospheric mantle represents a relatively minor sink of carbon (4 - 15 Mt C/year) (Alt et al., 2013; Kelemen and Manning, 2015). These fluxes are based on estimates with uncertainty of the carbon budget of oceanic mantle deriving from a relatively small number of samples and the large spatial heterogeneity of carbon content, which is often concentrated in localized carbonate-bearing veins and zones of intense alteration (e.g. Bach et al., 2011; Schroeder et al., 2015) that are poorly recovered by ocean drilling. Current estimations of the carbon budget of subduction zones are done according to $CO_2$- producing/consuming processes and may not capture the full range of carbon fluxes in subduction zones, as $CH_4$ dominated fluids investigated in this Ph.D. Better quantification and understanding of carbon fluxes in subduction zones is therefore fundamental for improving our estimates on the Earth carbon cycle.

The understanding and quantification of carbon cycling in subduction is challenging from mass balance considerations alone. The deep carbon cycling at subduction zones is still facing major imbalances. For example, although the carbon fluxes at volcanic arcs are comparable with the inputs of subduction (Burton et al., 2013; Hirschmann, 2018; Kelemen and Manning, 2015), a potentially large fraction of the carbon emissions at volcanic arcs derive from interaction of magma with crustal carbonate rocks (Carter and Dasgupta, 2016; Mason et al., 2017a). Also, it has been proposed that a part of the carbon degassed from subducting slabs does not reach the surface, making the mantle wedge or the deeper mantle potential carbon reservoirs (Kelemen and Manning, 2015).

Thermodynamic models have arisen to explore the release of carbon along subduction at different depths into sub-solidus aqueous fluids (Manning et al., 2013; Molina and Poli, 2000; Schneider and Eggler, 1986), super-critical liquids (Poli, 2015) or melts (Dasgupta et al., 2004; Dvir and Kessel, 2017; Tumiati et al., 2013; Woodland et al., 2018). More generally these models help determine the magnitude of carbon mobility and storage along the different stage of burial, and suggest that slab sediments, altered oceanic crust and the hydrated mantle retain large fractions of their carbon contents during subduction metamorphism (Gorman et al., 2006; Johnston et al., 2011; Kerrick and Connolly, 1998, 2001a, 2001b).

Carbon is stored in different phases such as carbonate minerals, organic compounds or graphite, and in fluid or multi-phase inclusions in silicate minerals. For most subduction P–T paths, thermodynamic models predict that the general sequence of stable carbonate phases with increasing metamorphic grade is Mg-calcite – aragonite/dolomite – aragonite/magnesite in meta-sediments (Kerrick and Connolly, 2001a), and Mg-calcite/aragonite – dolomite – magnesite in altered oceanic crust and carbonate-bearing, hydrated mantle (Fig. 1.2) (Kerrick and Connolly, 1998, 2001b).

Because the mantle wedge may potentially react with a large fraction of the fluid released from the subducted slab, metasomatized peridotites can store carbon bearing minerals, as carbonate, organic compounds, elemental carbon (graphite or diamond) or fluid inclusions (Förster et al., 2017; Malaspina and Tumiati, 2012; Sapienza et al., 2009). The fluids released by subduction may bear different redox conditions, and the metasomatic reaction resulting from the migration of such fluid can lead to change of the stability of carbon bearing minerals. The role of reduced carbonic fluids in subduction, however, is still poorly investigated. For instance, $H_2$-bearing fluid derived from serpentinization may lead to the precipitation of graphite from carbonates in subduction settings (Galvez et al., 2013; Vitale Brovarone et al., 2017). In this scope, mobilization of carbon through COH fluid is among the processes able to produce abiotic methane and other organic compounds. This can play a role in the mobility of carbon at depth and the general oxidation state of subductions zones (Arai et al., 2012; Galvez et al., 2013; Sverjensky et al., 2014a; Tao et al., 2018; Tumiati et al., 2017).

## 1.2 Serpentinization process

The process called serpentinization corresponds to the aqueous alteration of olivine-rich, ultramafic rocks to form serpentine-rich rocks. During this process, $Fe^{2+}$ contained in olivine and pyroxenes is oxidized to $Fe^{3+}$ and incorporated in Fe oxides such as magnetite and in serpentine minerals. The serpentine family consists mainly of three polysomes: lizardite, chrysotile, and antigorite, which can be described as hydrous magnesium-iron phyllosilicate minerals with a simplified structure of $(Mg,Fe)_3Si_2O_5(OH)_4$. The serpentine polysomes differ in their structures and chemical formulae (Moody, 1976). Temperature is the main factor controlling the stability of lizardite and antigorite, with lizardite being stable at lower temperature and antigorite at higher temperature conditions (Evans, 2004), even though the chemistry of the system may also affect their stability (Agrinier and Cannat, 1997; Andréani et al., 2007; Früh-Green et al., 1996; Padrón-Navarta et al., 2013, 2011, 2010a). Meanwhile, chrysotile generally forms at relatively low-pressure conditions, during late stages of serpentinization or in vein (Fig. 1.3)(Guillot et al., 2015).

### 1.2.1 Serpentinization reaction and settings

A typical serpentinization reaction goes as below (Frost and Beard, 2007):

$$3\,Mg_2SiO_4 + 2\,SiO_2 + H_2O = 2\,Mg_3Si_4O_5(HO)_4 \quad (1.7)$$

*Olivine +fluid = Serpentine*

The oxidation of iron in serpentine and magnetite is coupled with $H_2$ production through the generic reaction (Klein et al., 2019):

$$2\,FeO + H_2O = Fe_2O_3 + H_2 \quad (1.8)$$

Along with olivine, other Fe-bearing minerals can be affected by oxidation during serpentinization (Moody, 1976; Wicks and Whittaker, 1977). This is expected to happen if those minerals are far from equilibrium at the conditions of serpentinization, especially at low pressure and temperature conditions. The main mineral products of serpentinization are serpentine type minerals (lizardite, antigorite and chrysotile), brucite, magnetite, and iron-nickel alloys. In some occurrences, according to the initial chemistry of either the serpentinized rock or the infiltrating fluid, diopside and tremolite can be observed (Frost and Beard, 2007; Moody, 1976; Wicks and Whittaker, 1977).

Serpentinization may be associated with different microstructures. As serpentine minerals grow at the expense of other minerals, the perfection of pseudomorphism varies from excellent to indistinct and can display various characteristic features depending on which mineral is being replaced (Wicks and Whittaker, 1977).

In the case of olivine, the main textures observed are the mesh (Fig. 1.5A) and hourglass textures (Fig. 1.5B). Mesh structure is composed of a latticework of divided veins enclosing olivine cores, while hourglass texture results from serpentinization of olivine in a single stage, such that the fibrous mesh rims extend to the center of the grain. In the earliest stage of serpentinization, magnetite appears as very fine grains distributed throughout the serpentine. As serpentinization progresses, the magnetite forms bigger grain and concentrates in mesh centre or rims, to finally migrate out of the mesh or hourglass texture to form veinlets in the latest stage (Wicks and Whittaker, 1977).

In the case of pyroxene, the serpentine pseudomorph is called bastite (Fig. 1.5B). The terms can also be used for fully serpentinized amphibole as they are indistinguishable (Wicks and Whittaker, 1977). The serpentinization of pyroxenes begins at grain boundaries and fractures and follows along cleavages and partings to produce serpentine crystals oriented along the original cleavages. Bastite formation is not systematically associated with magnetite formation. When present, magnetite grains form with serpentine and outline the original cleavages.

On top of these mineral phases produced, and as a consequence of the oxidation, serpentinization can release reduced gas phases in the fluid such as $H_2$. The ability of serpentinization to release reduced gas can vary according to P-T condition and chemistry of the rock, as well as the degree of serpentinization (Klein et al., 2019, 2014).

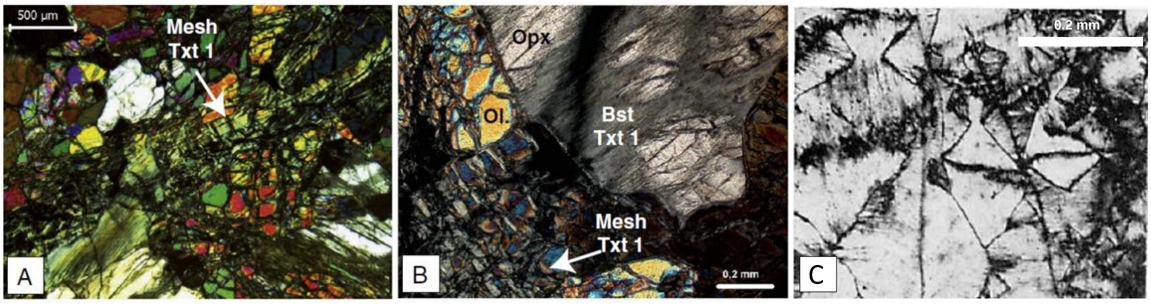

*Fig. 1.5: A: Partially serpentinized peridotite with mesh texture. B: Bastite texture in peridotite.* (Andreani et al., 2013). *C: Lizardite pure hourglass texture* (Wicks and Whittaker, 1977). *Ol: olivine, Opx: orthopyroxene, Bst: bastite.*

In the presence of carbon, $H_2$ can then react to produce $CH_4$ and even more complex organic compounds (Bach et al., 2004; Frost, 1985; Klein et al., 2014; McCollom and Bach, 2009; Ménez et al., 2018).

Serpentinization occurs in various settings. It mainly occurs where oceanic lithosphere is altered by seawater such as seafloor, particularly in magma-poor spreading ridges settings (Cannat et al., 2010; Rüpke and Hasenclever, 2017), along oceanic transform faults (Schlaphorst et al., 2016), or along deep bend faults at the outer rise prior to subduction (Faccenda, 2014; Ranero et al., 2003). Serpentinization has also been proven to occur in the upper cold (T<650 °C) mantle wedge in subduction zones from the infiltration of fluids sourced from the subducting slab (Blakely et al., 2005; Fryer et al., 1999; Hyndman and Peacock, 2003; Kamiya and Kobayashi, 2000).

### 1.2.2 Consequences of serpentinization

The process of serpentinization is key in Earth dynamics, playing a central role in global water cycling. It allows the recycling of water back inside the mantle along with several other elements associated with water-rock interaction (Guillot et al., 2015). Serpentinization decreases the density of peridotite and produces magnetite. During serpentinization, the rock density decreases from 3000 kg/m$^3$ to 2500 kg/m$^3$ for 0% to 95% of serpentinization, respectively (Christensen, 1966; Saad, 1969). This change in density and volume (about 44-52 % increase) of the ultramafic lithologies does not occur simultaneously in all lithologies and results in deformation of the surrounding rocks (Klein and Le Roux, 2020; Malvoisin et al., 2020). Because of the formation of magnetite, serpentinites usually have high magnetization (Blakely et al., 2005; Maffione et al., 2013; Oufi et al., 2002). Serpentinization also alters the chemical and microscopic elemental distribution of the rock, with the redistribution of major elements like Mg, Si and Al and mobility of Ca, Na, Fe and Mn at grain-size to regional scale (Iyer et al., 2008). Because of this, serpentinization of the oceanic lithospheric mantle may play an important role in constraining the global ocean chemical budget as well as ocean-floor mineral deposits (Ligi et al., 2015; Malvoisin, 2015; Pinto et al., 2017).

The low density of antigorite serpentinites (2.75 g/cm3) causes strong buoyancy, thus providing a mechanism for the exhumation of deeply subducted rocks (Hermann et al., 2000). Additionally, serpentine minerals weaken the physical strength of the plate interface in subduction zones, which leads to ductile behavior (Lundin and Doré, 2011). Moreover because of the incorporated water, it acts as a lubricant along plate boundaries. The presence of serpentinite in and near a subducting slab may favor subducted oceanic and continental rocks to be exhumed to the surface (Gorczyk et al., 2007; Guillot et al., 2009).

Fully serpentinized rocks can contain up to 13 wt.% and can incorporate a lot of fluid-mobile elements As, Sb, B, Li, Cs, Pb, U, Ba and Sr. This becomes of major significance when serpentinites are subducted and participate in geochemical cycling at depth (Fig. 1.6)(Deschamps et al., 2013, 2011, 2010). The release of water directly affects the overlying mantle rocks, lowering the melting temperature of mantle rock (Ranero et al., 2003). This leads to magma production migrating upward to form a volcanic arc. Additionally, the water released leads to the extensive serpentinization in the forearc mantle as indicated by a wide range of geophysical and geological data (Bostock et al., 2002; Hyndman and Peacock, 2003; Wada et al., 2008).

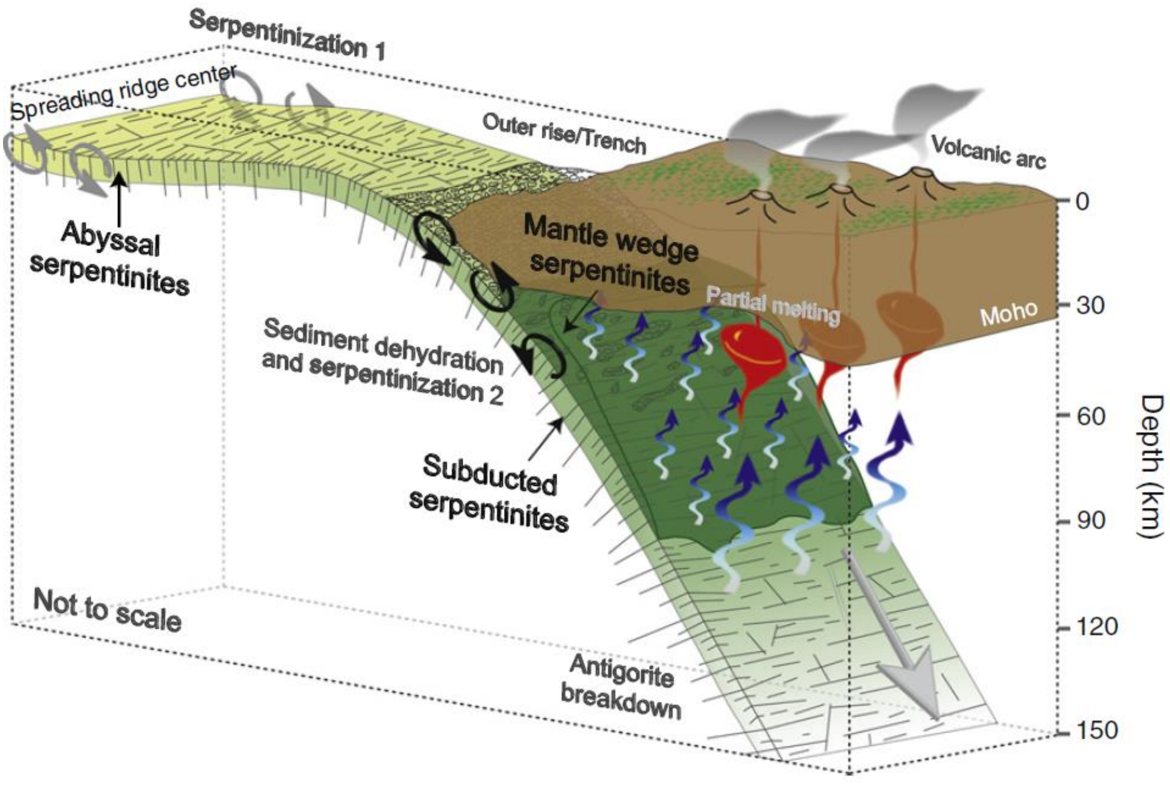

*Fig. 1.6: Schematic sketch illustrating the geological impact of serpentinites in subduction.* (Deschamps et al., 2013).

## 1.3 Abiotic hydrocarbons

Hydrocarbons are molecules entirely composed of carbon (C) and hydrogen (H) atoms. They form the basis of the oil and gas industry. On Earth, hydrocarbon formation is believed to be related mainly to biotic processes being either produced by life forms or their transformation during burial (Brooks and Smith, 1969, 1967; Welte and Tissot, 1984). Hydrocarbons are highly combustible compounds, releasing water, carbon dioxide ($CO_2$) and heat when ignited in presence of dioxygen ($O_2$). They represent on earth a widespread source of energy. Gaseous hydrocarbons are mainly alkanes, including methane ($CH_4$), ethane ($C_2H_6$), propane ($C_3H_8$), butane ($C_4H_{10}$). Hydrocarbons composed of 5 to 17 carbon molecules are found in a liquid state while heaviest hydrocarbons (18 to 40) can be found in a solid state. Because of the presence of carbon-hydrogen bonds, they are also described as organic compounds, as carbon can chain with other carbon atoms and form the basis of life as we know it on Earth (Luisi, 2016; Rasmussen et al., 2003; Szostak et al., 2001). In fact, hydrocarbons present on Earth atmosphere partly originate from either microbial processes or maturation /degradation of biological material (Ciais et al., 2014; Khalil et al., 2007; Khalil and Rasmussen, 1983; Rasmussen and Khalil, 1981). Carbon represents 0.3% mass fraction of the elements in the universe and is the fourth more abundant element (Croswell, 1996). Observation of this carbon on other planetary bodies of the Solar System indicates the presence of hydrocarbons despite the absence of life or life-associated processes for hydrocarbon synthesis (Ehrenfreund and Charnley, 2000; Kwok, 2009). Compared to the vast majority of hydrocarbons found at the Earth’s surface, at the Solar System scale, hydrocarbons are produced abiotically, i.e., formed by chemical reactions that do not directly involve life forms or their transformations.

As methane is the simplest and the most common of hydrocarbons on Earth, it will be the focus of this study.

### 1.3.1 Abiotic hydrocarbons on earth

Abiotic hydrocarbons on Earth are produced without the contribution of life process or organic matter degradation. As such, the maturation of biogenic organic matter and release of hydrocarbons with rising temperature (and pressure) is not considered abiotic (Etiope and Schoell, 2014; Sugisaki and Mimura, 1994; Truche et al., 2020). However, an abiotic process producing hydrocarbons from a carbon source related to life may still be considered of abiotic origin. On Earth, abiotic hydrocarbons can be found in a wide range of conditions, although their detection is challenging. A comprehensive review of abiotic hydrocarbons on Earth and the associated processes can be found in Etiope and Sherwood Lollar, 2013. Primordial hydrocarbons, almost exclusively represented by methane, correspond to the initial presence of hydrocarbons brought on Earth during its early accretion (Craig and Lupton, 1976; Etiope and Sherwood Lollar, 2013; Gold, 1979). To this day, Earth is still believed to degas some of its primordial volatile elements, especially helium which may be associated to carbon compound, delivering abiotic primordial methane to the Earth's shallowest envelopes (Gilat, 2012; Gonzalez et al., 2020; Hilton et al., 1997; Marty et al., 2013). However, the existence of fluxes of primordial methane remains controversial and have neither been observed nor quantified (Colman et al., 2017; Gold, 1979).

Nevertheless, several mechanisms and processes have been identified that can produce methane abiotically at crustal and upper mantle depths (Etiope and Sherwood Lollar, 2013; Sephton and Hazen, 2013; Truche et al., 2020). Magmatic abiotic hydrocarbons can originate from high-temperature reactions in the mantle such as hydrolysis of metal carbides (Beeskow et al., 2006; Petersilie et al., 1961). Additionally, as COH fluid are omnipresent in geological fluid, respeciation of CO and $CO_2$ to $CH_4$ can happen in a wide range of temperatures under circumstances promoting reduced conditions. Different reactions have been identified to produce abiotic hydrocarbons at laboratory conditions or observed in shallow geological environment (McCollom, 2013; Sephton and Hazen, 2013):

- The Fischer-Tropsch-Type (FTT) synthesis (Fischer and Tropsch, 1926) which was originally developed in the industry for dry gas mixtures, corresponds to a vast array of reactions implying the polymerization of oxidized carbon and dihydrogen to produce various "CHO" product, which can be broadly generalized as (Masters, 1979):

  $$CO\ +\ H2 \xrightarrow{catalyst} "CHO"\, product\ (1.9)$$

  This "CHO" product corresponds to a newly formed hydrocarbon accompanied by the release of water molecules. The reaction with carbon monoxide or carbon dioxide can be written as:

  $$nCO + (2n+1)H_2 \rightarrow C_nH_{2n+2} + nH_2O\ (1.10)$$

  $$nCO_2 + (3n+1)H_2 \rightarrow C_nH_{2n+2} + 2nH_2O\ (1.11)$$

  Fischer-Tropsch synthesis produces low molecular weight hydrocarbons, with exponentially decreasing concentration with the increasing carbon number. Even though numerous differences exist for geological systems, where water is often abundant, it has been debated as a potential process at the origin of hydrocarbons in hydrothermal vent settings (Foustoukos and Seyfried Jr, 2004; Horita and Berndt, 1999; McCollom and Seewald, 2006; Proskurowski et al., 2008). Catalysts such as transitional metals have been shown to enhance the reaction at laboratory conditions (Adams, 1992; Beinert et al., 1997).

- Serpentinization reactions can produce favorable conditions for methane formation through FTT reactions. Methane generation in serpentinization settings has been increasingly documented at oceanic ridges and ophiolites (Etiope et al., 2011; Holm and Charlou, 2001; Klein et al., 2019; McCollom and Seewald, 2007, 2006; McDermott et al., 2015; Vitale Brovarone et al., 2017), with the observation of more complex alkane through abiotic reaction (Ménez et al., 2018). As aqueous condition appears to not be favorable for FTT production of methane (McDermott et al., 2015), gaseous conditions found in minerals inclusions have been observed to bear light hydrocarbons. Suitable conditions are intimately linked to hydrogen production, imposing low oxygen fugacity conditions favorable for the conversion of carbon into methane, for example, through Fischer-Tropsch reactions.
- Thermal metamorphism of carbonates can lead to the release of hydrocarbons (Holloway, 1984). At a temperature between 300 and 400 °C, interaction with talc and water can lead to formation of dolomite and the release of methane as proposed in the unbalanced reaction:

$$\mathrm{Mg_3Si_4O_{10}(OH)_2 + CaCO_3 + C_{graphite} + H_2O \rightarrow CaMg(CO_3)_2 + SiO_2 + CH_4} \quad (1.12)$$

At temperature higher than 400°C, interaction with siderite and water can lead to reduction of the iron and the release of methane as proposed in the following reaction (Giardini and Salotti, 1969):

$$\mathrm{FeO + CaCO_3 + H_2O \rightarrow Fe_3O_4 + CH_4 + CaO} \quad (1.13)$$

Alternatively, in reduced environment, a reaction between dolomite and dihydrogen can results in the release of methane as follow in the unbalanced equation (Peng et al., 2021):

$$CaMg(CO_3)_2 + H_2 = CaCO_3 + Mg(OH)_2 + CH_4 + C_{graphite} + H_2O \ (1.14)$$

Carbon from carbonate can be mobilized along increasing PT conditions during subduction zones. Stored carbon can be released as methane in the fluid.

### 1.3.2 Abiotic hydrocarbons budget and environment impact

Abiotic hydrocarbon production on Earth is much smaller than biotic production, at least in its outermost envelopes. Moreover, abiotic and biotic hydrocarbons can often find themselves mixed in geological environments (Etiope and Sherwood Lollar, 2013; Young et al., 2017). Distinguishing abiotic and biotic hydrocarbons in such settings has been proven difficult with conventional techniques such as $\delta^{13}C$ and $\delta^{2}H$ isotope geochemistry. Methane doubly substituted isotopologues, or methane "clumped" isotopes, provide an emerging and potentially valuable technique to discuss the origin of formation of hydrocarbons, but only a few laboratories worldwide dispose of adequate facilities to date (Beaudry et al., 2021; Douglas et al., 2017; Etiope et al., 2011; Ono et al., 2021; Stolper et al., 2014b, 2015). Another limitation of the techniques is so far the large quantity of gas needed.

Because of its powerful infrared absorption, methane is among the most potent natural greenhouse gases, in a similar fashion to carbon dioxide ($CO_2$) and nitrous oxide ($N_2O$). Despite its presence being in a significantly lower amount than carbon dioxide in the atmosphere (0.0407% $CO_2$ vs 0.00018% $CH_4$), its global warming potential is significantly higher. The effect of a greenhouse gas on climate is quantified in terms of radiative forcing, corresponding to how much a gas changes the balance between incoming solar radiation and outgoing infrared radiation within the Earth's atmosphere (expressed in W.m$^{-2}$) (Forster et al., 2007). Foster and al. 2007 report atmospheric concentration of $CO_2$ of 379 ppm and associated radiative forcing of 1.66 W.m$^{-2}$ and for $CH_4$ concentration of 1774 ppb with a radiative forcing of 0.48 W.m$^{-2}$, indicating an effect of one mol of $CH_4$ about 61.8 time higher than one mol of $CO_2$ on a 250-year time span. Because of this, the release of $CH_4$ in the atmosphere is not to be underestimated on the climatic evolution of Earth, be it from biotic, abiotic, or anthropogenic sources. The methane concentration in Earth's atmosphere has been subject to variation through the geologic timescale and is believed to have played a primordial role in the Earth's primitive atmosphere. Especially before the appearance of complex life, concentration of $CH_4$ could have been much higher than present and is discussed as one of the factors for Precambrian relatively high temperature (above freezing) despite reduced solar activity at the time (Kasting, 2005). With the recent global warming, anthropogenic and biotic fluxes of methane have benefited from substantial effort and quantification (Reay et al., 2010) (Table 1.1). However, abiotic sources remain largely unconstrained and unquantified. It can be observed that most of the methane fluxes presented as geological methane in Table 1.1 correspond mainly to $CH_4$ hydrates (also called clathrates) which, as the authors argue, not only remains speculative but is not exhaustive of the overall geological sources of $CH_4$ on Earth. To depict a more accurate picture of geological hydrocarbons, the following sources should be considered: volcanic eruptions, fumaroles, mofettes, hydrothermal springs, and seepage in sedimentary basin. Additionally, methane (and heavier hydrocarbons) productions from serpentinization reactions in a wide range of subsurface hydrothermal conditions are neither fully understood nor quantified and require further studies. More recent estimations of the contribution of geological sources by taking into account seeps, mud volcanoes and geothermal/volcanic areas would amount to 40 to 60 Mt $CH_4$ yr$^{-1}$ making geological sources as a whole the second largest natural contributor after wetland to atmospheric $CH_4$ (Reay et al., 2010). Most geologic sources previously mentioned correspond to abiotic hydrocarbon forming processes, however the $CH_4$ seeping from sedimentary basin can originate from thermogenic transformation of biologic organic matter and thus is not classified among the abiotic processes. Reay et al., (2010) described three main sinks of atmospheric $CH_4$, two of them corresponding to the interactions of $CH_4$ with OH radicals in the troposphere (about 87%) and stratosphere (about 7%), and the last one corresponding to methanotrophs bacteria in soils (about 5%). One particularity of the interaction between OH radicals and $CH_4$ in the upper atmosphere is that it leads to the formation of ozone, and decreases its oxidizing potential, increasing $CH_4$ atmospheric lifetime.

Table 1.1: Global estimates of methane sources and sinks (Reay et al., 2010).

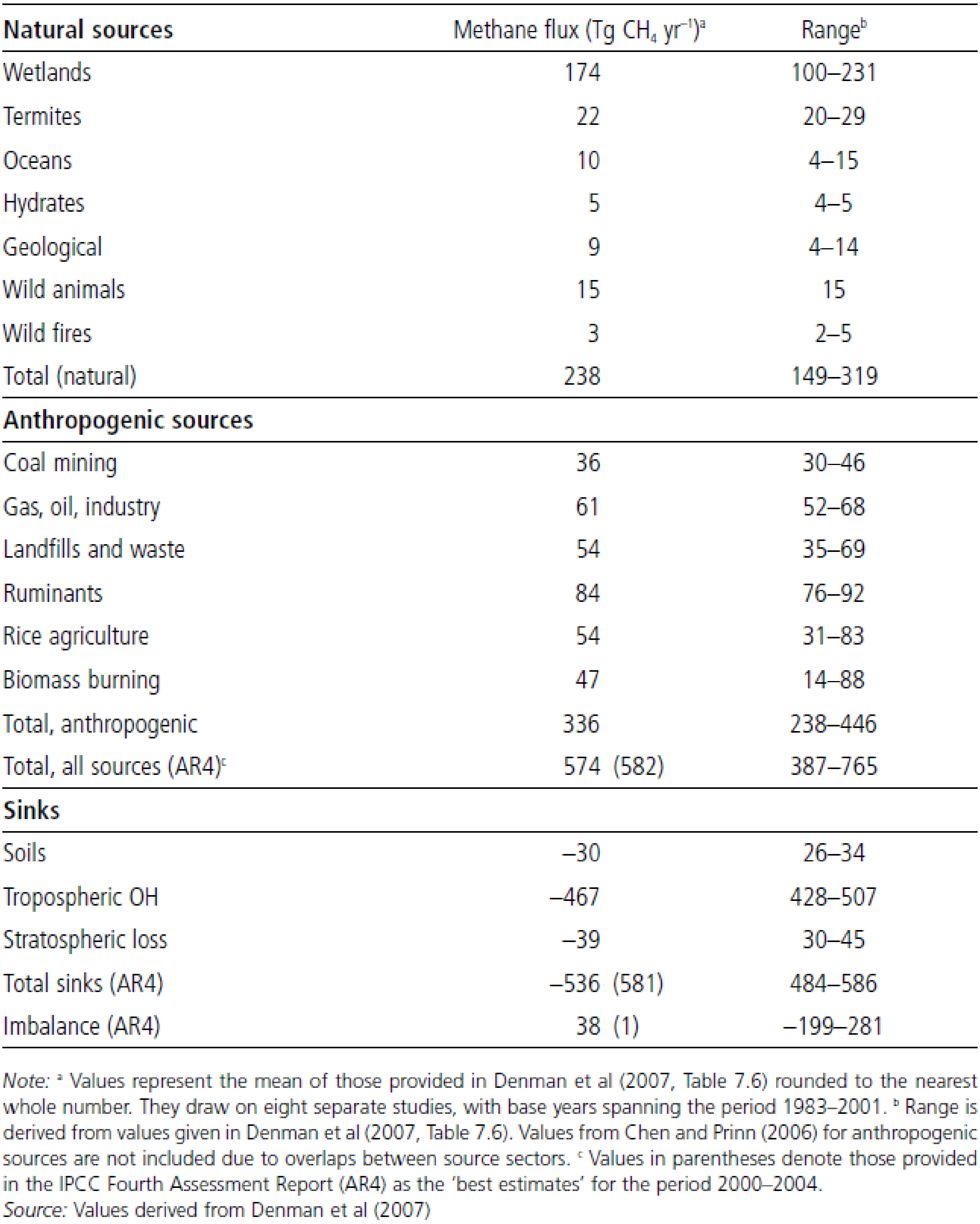

| **Natural sources** | Methane flux (Tg $CH_4$ $yr^{-1}$)[a] | Range[b] |
|---|---|---|
| Wetlands | 174 | 100–231 |
| Termites | 22 | 20–29 |
| Oceans | 10 | 4–15 |
| Hydrates | 5 | 4–5 |
| Geological | 9 | 4–14 |
| Wild animals | 15 | 15 |
| Wild fires | 3 | 2–5 |
| Total (natural) | 238 | 149–319 |
| **Anthropogenic sources** | | |
| Coal mining | 36 | 30–46 |
| Gas, oil, industry | 61 | 52–68 |
| Landfills and waste | 54 | 35–69 |
| Ruminants | 84 | 76–92 |
| Rice agriculture | 54 | 31–83 |
| Biomass burning | 47 | 14–88 |
| Total, anthropogenic | 336 | 238–446 |
| Total, all sources (AR4)[c] | 574 (582) | 387–765 |
| **Sinks** | | |
| Soils | –30 | 26–34 |
| Tropospheric OH | –467 | 428–507 |
| Stratospheric loss | –39 | 30–45 |
| Total sinks (AR4) | –536 (581) | 484–586 |
| Imbalance (AR4) | 38 (1) | –199–281 |

*Note:* [a] Values represent the mean of those provided in Denman et al (2007, Table 7.6) rounded to the nearest whole number. They draw on eight separate studies, with base years spanning the period 1983–2001. [b] Range is derived from values given in Denman et al (2007, Table 7.6). Values from Chen and Prinn (2006) for anthropogenic sources are not included due to overlaps between source sectors. [c] Values in parentheses denote those provided in the IPCC Fourth Assessment Report (AR4) as the 'best estimates' for the period 2000–2004.
*Source:* Values derived from Denman et al (2007)

### 1.3.3 Abiotic hydrocarbons and the origin of life

Life on Earth revolves mainly around one element, carbon. When considering the origin of life on Earth, it’s especially interesting to look at the transition of geologically occurring hydrocarbons to complex carbon chains present in living organisms. As $CH_4$ is the simplest hydrocarbon, it is a widely available potential source of carbon to form more complex carbon chains (Barry et al., 2019; Colman et al., 2017; Fullerton et al., 2019). For this reason, the formation or availability of abiotic hydrocarbons takes a place on the investigation of the age-old question on the origin of life (Holloway, 1984; Martin et al., 2008; Ménez et al., 2018; Nisbet and Sleep, 2001; Russell and Nitschke, 2017; Ueno et al., 2006). When considering suitable conditions for the emergence of life, three conditions must be met: liquid environments, the availability of organic matter, and a source of energy (Colman et al., 2017; Kompanichenko, 2017). In this context, abiotic hydrocarbons are considered as a suitable source of carbon to build primitive life forms. In some cases, such as hydrothermal vent and/or serpentinization, abiotic hydrocarbon formation is associated with the release of $H_2$ and this kind of system can also be accompanied by other volatile elements such as sulfur and nitrogen. Molecular hydrogen or sulfates are candidates as a possible energy source to be processed to fuel primitive metabolism, and along with nitrogen can be building blocks of organic compounds.

Hydrothermal vents located at mid-ocean ridge are good candidates for the study of the emergence of life on Earth, as they provide copious amount of $H_2$, $CO_2$, and other light elements, producing the concept of “organic soups'' (Alt et al., 2007; Martin et al., 2008). scientists stumbled upon a hydrothermal field called Lost City, located in the Atlantic Ocean at 750 to 900 m depth at more than 15km from the Mid-Atlantic Ridge, and hosting carbonate-rich chimneys called "white smoker" (Fig. 1.7)(Kelley et al., 2005). These hydrothermal chimneys emit alkaline high-pH hydrothermal fluid cooler (260–300 °C) than those emitted by black smokers (360 °C), from the underlying serpentinized mantle peridotites. These systems were found to support their own microbial communities related to the methane-cycling, such as Archaea and macrofaunal ecosystems.

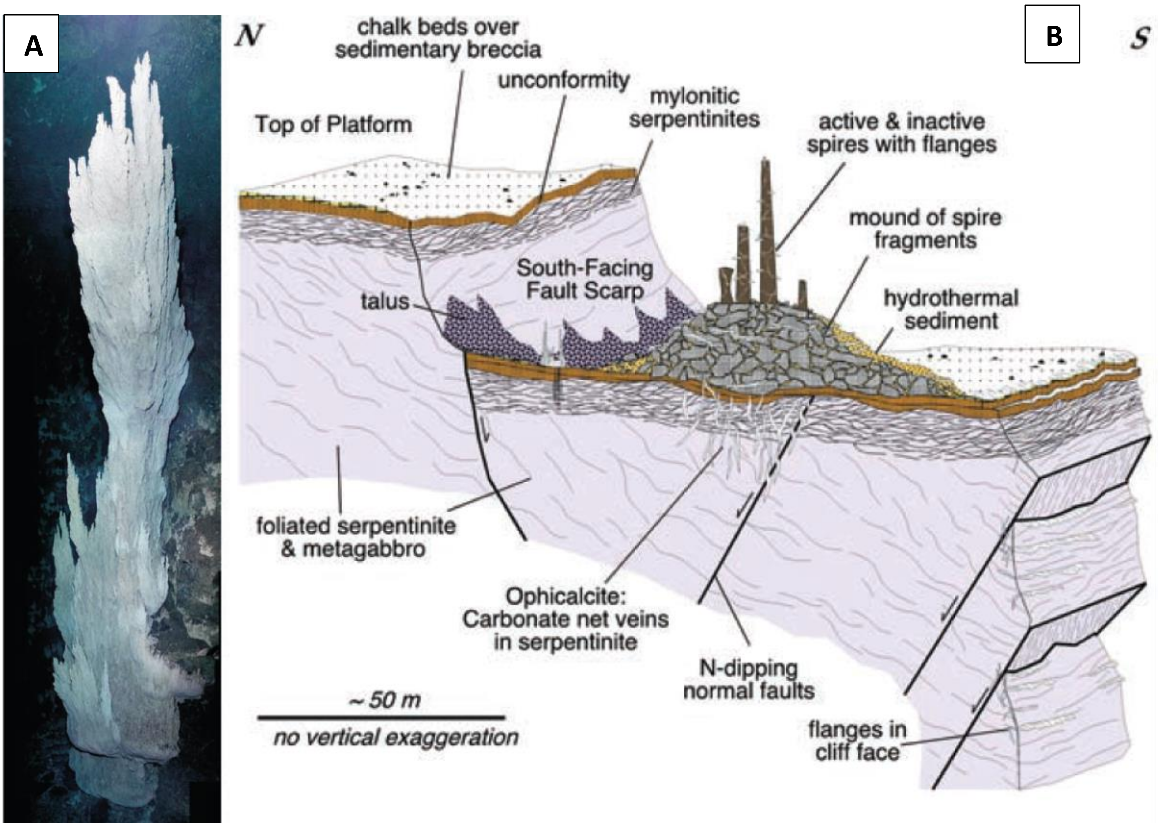

*Fig. 1.7: A: 10 m tall actively venting carbonate growing directly out of a serpentinite cliff. Lost City hydrothermal field, Atlantis Massif. B: Sketch showing geologic and tectonic relationships at Lost City. Hydrothermal structures are located on a faulted down-dropped block of variably altered and deformed crust composed predominantly of serpentinite. From Kelley et al., 2005.*

Because of its potential to produce favorable settings for $H_2$ and $CH_4$ abiotic production, the hydration of mantle rocks has been the subject of several studies over the past decades (Nisbet and Sleep, 2001; Schulte et al., 2006; Sleep et al., 2004; Sleep and Bird, 2007). At slow to ultraslow spreading ridges (<40 mm $y^{-1}$ (Carbotte and Scheirer, 2004)), mantle rocks can be unroofed and react with seawater to form serpentinite, $H_2$, and abiotic $CH_4$ (Kelley et al., 2005; Klein et al., 2013; Konn et al., 2009; McCollom and Seewald, 2001). Ménez et al., (2018) were able to detect from natural samples from the Lost City abiotic formation of amino acids through mineral reaction catalyzed metals. Several studies have focused on the emergence of microbial communities at hydrothermal conditions (Nakamura et al., 2009; Takai et al., 2006; Ueno et al., 2006). Potential links between abiotic hydrocarbons and the emergence of life also extend to the deep subsurface biosphere (Schrenk et al., 2013). The investigation on life habitability at depth supported by serpentinization processes has also been explored and hint at the possibility of deep microbial life in subseafloor conditions and at convergent margins (Curtis et al., 2013; Ohara et al., 2012; Plümper et al., 2017b; Reveillaud et al., 2016; Vitale Brovarone et al., 2017).

## 1.4 Geological settings of this study

### 1.4.1 Lanzo massif

The Lanzo Massif is a large (∼150 $km^2$) body of ultramafic rocks located in the internal part of the Western Italian Alps. It features occurrence of abiotic methanogenesis and carbon mobility (Giuntoli et al., 2020; Vitale Brovarone et al., 2020) and was one of the study zones of this Ph.D. Numerous field sessions and analysis on samples from this locality have been conducted, but due to inconclusive results, they are not presented in this manuscript.

### 1.4.2 Belvidere Mountain Complex

The Belvidere Mountain complex (BMC) area is part of a North-South trending belt of mafic/ultramafic rocks belonging to the Appalachian Mountain system and extending from

Newfoundland to Georgia (Gale, 2007; Hibbard et al., 2006)(Fig. 4.1). These ultramafic bodies mainly consist of variably serpentinized peridotites, and associated metabasic and metafelsic rocks tectonically embedded within Cambro-Ordovican metasedimentary and metavolcanics formations (Chidester et al., 1978; Gale, 1986, 1980; Laird et al., 1984; Van Baalen et al., 2009). The BMC, as well as other mafic/ultramafic complexes such as the Tillotson Peak and the Pennington complexes, are interpreted to represent remnants of an ocean-continent transition zone associated with the extension of the Laurentian margin (Chew and van Staal, 2014). These terranes were successively involved in the closure of the Iapetus Ocean during the Ordovican Taconic orogeny (Doolan et al., 1982; Honsberger et al., 2017; Karabinos et al., 1998; Laird et al., 1984; Stanley et al., 1984). The BMC forms a 6.5 km long body that structurally overlies the metasedimentary Ottauquechee and Stowe Formations to the East and is overlain by the Hazen Notch formation to the West. The Stowe Formation is late Cambrian, composed of gray-green quartz -chlorite-sericite +/- magnetite schists. The Ottauquechee Formation is middle Cambrian consisting of carbonaceous pyritiferous phyllite. The Hazen Notch Formation is dated from Neoproterozoic to Cambrian, graphitic and non-graphitic quartz-albite-sclerite-chlorite schist, along medium-grained, massive, quartz-albite-muscovite gneiss. The internal architecture of the BMC comprises, from top to bottom, variably serpentinized dunite and harzburgite, coarse-grained and fine-grained amphibolite, greenstone, muscovite schist, and albite gneiss (Gale, 1986, 1980; Van Baalen et al., 2009). Lenticular bodies composed of talc-carbonate rocks and steatite, often including cores of relatively unserpentinized peridotite, are observed within the BMC, and range in size from a few meters to several tens of meters (Chidester et al., 1978). The BMC rocks underwent Taconic blueschist-facies peak metamorphic conditions constrained at 0.9-1.3 GPa and 510-520 °C in metabasic rocks (Honsberger, 2015; Laird et al., 1993). Slightly higher P, blueschist-to-eclogite-facies metamorphic conditions are recorded by the Tilliston Peak mafic rocks located just north of the BMC (Laird et al., 1993, 1984). This tectonometamorphic event has been dated at 505-473 Ma by $^{40/39}$Ar amphibole and mica geochronology (Castonguay et al., 2012; Laird et al., 1993).

## 2 Aims and thesis outline

### 2.1 Aims

The main goal of this Ph.D. thesis is to improve our understanding of the formation of hydrocarbons from abiotic processes in subduction zones, and in particular the role of occurring from the subduction serpentinization in controlling the mobility or storage of deep carbon under reducing conditions. Subduction zones are the main drivers of element recycling on Earth, acting as an interface between shallow envelopes and deep Earth reservoirs. In the context of subduction, the mantle overlying the subducting plate, the so-called mantle wedge, acts as the receptor of aqueous fluids resulting from the dehydration of the subducted slab. Assessing the potential of peridotite in subduction to release $H_2$ and hydrocarbon by fluid interaction in the presence of carbon is the main aim of this study to fill gaps in the current state of knowledge on deep fluxes, sinks and sources of carbon in subduction. To advance in this overall research goal, the Ph.D. thesis is aiming to:

i. Understand peridotite hydration along subduction zones with the study of ultramafic bodies in subduction.
ii. Constrain the mobility and storage of carbon species in the presence of serpentinization and graphite associated to ultramafic context.

iii. Develop numerical tools to calculate the composition and model the behavior of carbon-bearing fluid in subduction through various interactions and systems.

To address the first aim (i), I have carried out a detailed field, petrographic, petrologic, fluid inclusions and isotopic study of partially preserved ultramafic complex displaying variably serpentinized dunites from the Belvidere Mountain Complex (BMC), Vermont, USA. This study provides new insight on HP (high-pressure) serpentinization showing incipient serpentine growth in the antigorite stability field associated with methane-rich fluid inclusion. Thermodynamic modeling Deep Earth Water (DEW) model was used to confirm the possibility of $H_2$ and $CH_4$ formation.

To approach the second aim (ii), the graphite deposit associated to fluid channelization and serpentinization was investigated on the BMC, Vermont, located near the evidence of HP serpentinization and abiotic methane formation. I studied field microstructural, fluid inclusion, geochemical and isotopic data to investigate the mechanism of graphite deposit as well as the formation and migration of carbon compounds.

Finally, to understand carbon bearing fluid in subduction, I developed a software using python able to calculate carbon isotope equilibrium and fractionation, to calculate the molar composition Carbon-Oxygen-Hydrogen (COH) fluid and to model interaction leading to the precipitation or mobilization of solid carbon. By exploring variable P-T conditions corresponding to various settings, the user can model different processes such as mixing of fluid or changes in pressure or temperature and explore the effect on the molar and isotopic composition of the fluid. In order to be used by a wide range of users, this software does not require installation and is available on Windows OS and MacOS.

## 2.2 Structure of the thesis

The thesis comprises four main parts. **Part I** contains an introduction to the background and state-of-knowledge of the subject (**Chapter 1**), the aims and overview of the structure of the thesis (**Chapter 2**), and a description of the applied methodology (**Chapter 3**). For clarity and consistency, part of the introduction and methodology that are specific to the research addressed in the result section are provided in their respective chapter in **Part II**.

**Part II** shows the main findings and results of this Ph.D. thesis. **Chapter 4** addresses the first aim of the thesis, presenting field, microstructural, thermodynamic, and fluid inclusions data to investigate the patterns and timing of serpentinization of the Belvidere ultramafic complex, Vermont, with particular focus on the HP fluid-rock interactions recorded by these rocks. The results of this study have been published in the JCR journal *Lithos*. **Chapter 5** is dedicated to an interesting example of carbon mobility in the upper subduction from the Belvidere Mountain Complex (BMC), Vermont, which exhibits intense graphite deposit and methane rich inclusions. This work integrates field, microstructural, fluid inclusion, geochemical and isotopic data to investigate the mechanism of graphite deposit as well as the formation and migration of carbon. These results are the subject of the draft of the manuscript soon to be ready for submission. **Chapter 6** is a draft of a manuscript that addresses the third aim of this thesis and consists of the description of the Thermotopes-COH software different features and method with an example from a case study.

**Part III** presents the main conclusions of the three studies and open questions for the future investigations (**Chapter 7**), followed by a list of the references cited throughout the thesis (**Part IV**).

In addition to the publications cited above, the results of this thesis have been presented at the EGU conference (Austria, 2020) and the Goldschmidt (France, 2021).

# 3 Methodology

## 3.1 Rock sampling

Mafic and ultramafic rocks from the Belvidere Mountain Complex (Vermont, USA) were sampled during a field campaign in August 2018. The site is a former asbestos mining facility which provides remarkably fresh outcrop exposures. Several rock types were sampled, from variably serpentinized ultramafic rocks, to amphibolite-facies mafic rocks and various metasomatic rocks showing evidence of carbon mobility (see Table 1 of the Appendix to Ch. 5). Two targets were considered: relatively fresh peridotite rocks showing incipient serpentinization, and graphite-rich rocks.

### 3.1.1 Bulk rock and trace analysis

Whole-rock analyses of samples were performed at the Service d'Analyse des Roches et Minéraux (SARM, Centre de Recherches Pétrographiques et Géochimiques, Nancy, France) by alkali fusion of rock samples (LiBO2), followed by concentration measurements using an ICP-OES Icap 6500 (Thermoscientific) for major elements, and an ICP-MS X7 (Thermoscientific) for minor elements (protocol by Carignan et al., 2001).__ http://helium.crpg.cnrs-nancy.fr/SARM/pages/roches.html for details on uncertainty and detection limits.

### 3.1.2 Stable isotope C of carbonates and graphite

Portions of samples were cut to remove from weathered surfaces and organic contamination, and then crushed and pulverized with Plattner and an agate mortar. Considering the very high amount of graphite, the potential effect of organic contaminants by groundwater circulation was considered to be negligible. Analyses of total organic carbon (TOC) were performed on aliquots of about 1 g dried, decarbonated samples (HCl, 6 mol/L, attacked at ambient temperature for one night) using a Flash EA1112 elemental analyzer coupled to a Thermo Finnigan DELTA plus XP isotope ratio mass spectrometer via a ConFlo IV interface at IPGP, Paris. Aliquots of the companion, non-decarbonated sample were also analyzed for Total Carbon (TC=TIC+TOC). Graphitic C concentrations in samples presented here correspond to the measured TOC values. Each sample was analyzed in triplicate. Error bars on these concentrations correspond to the standard deviation on the triplicates (see 5.6.3).

The $\delta^{13}C$ and the $\delta^{18}O$ of carbonate were obtained at the Institute of Geosciences and Earth Resources, Pisa, on a GasBench II with a continuous-flow IRMS setup, after the method of Breitenbach and Bernasconi, (2011). Isotope ratios are reported in permil (‰) using the conventional δ-notation and with respect to the V-SMOW for oxygen and Vienna Pee Dee Belemnite (V-PDB) for carbon. Standard deviation was 0.05‰ for both $\delta^{13}C$ and $\delta^{18}O$.

### 3.1.3 Stable isotope C and H of methane from inclusions

The $\delta^{13}C$ and $\delta^{2}H$ of $CH_4$ was obtained at IFP energies nouvelles by extracting the gas after crushing inclusion-rich samples in a sealed modified planetary crusher. Once the sample was placed, the bowl was flushed with a flux of $N_2$ for around 60 seconds, then sealed and crushed at 700 rpm for 240 seconds. The gas was then extracted from the bowl by connecting exetainer sample vials under vacuum. Three different vials were collected for each sample. The first vial of each sample was then injected in triplicate in a Picarro G2210-i Isotope Analyzer, featuring internal calibration, to obtain the $\delta^{13}C$ of $CH_4$ and the C1/C2 ratio. The two other vials were respectively used to analyze the $\delta^{2}H$ and verify the $\delta^{13}C$ of $CH_4$ with a GC-MS. Analyses by GC-MS were calibrated using two gas internal standards.

### 3.1.4 Strontium and bore isotope analysis

Sample preparation of Sr analysis was done in a similar fashion to that of carbon analysis. Sr isotope analyses were performed using a Finnigan MAT 262 multi-collector mass-spectrometer (at IGG-CNR, Pisa) running in dynamic mode, after ion-exchange purification through Sr-spec resin. Measured $^{87}Sr/^{86}Sr$ ratios have been normalized to $^{86}Sr/^{88}Sr = 0.1194$. Values are corrected for $^{87}Sr/^{86}Sr$ of NBS 987 =0.710248. Interference of $^{87}Rb$ on $^{87}Sr$, and $^{86}Kr$ on $^{86}Sr$ were corrected according to average natural $^{85}Rb/^{87}Rb$ and $^{83}Kr/^{86}Kr$ ratios, respectively. Blanks were measured and corrected. Sample/Blank ratios vary typically from 5 $10^3$ and 5 $10^4$.

The $\delta^{11}B$ was collected at the IGG-CNR Pisa, Italy; ~0.2 g of sample powder was fused with $K_2CO_3$ in platinum crucibles with a 4:1 flux to sample ratio. Boron was then extracted from the fusion cakes by repeated crushing and centrifuging of the cakes in high pH B-free water. It was further purified by passing the solution through anion and cation exchange columns. Anion columns were packed with Amberlite IRA-743 boron-specific anion exchange resin, while cation-exchange columns were packed with AG 50W-X8 resin. The procedure used an anion column step, followed by a cation column step and then a final (repeat) anion column step to produce the final purified boron solution, as described by Tonarini et al., (1997). The B isotope compositions were measured on a Thermo Scientific$^{TM}$ Neptune series multi-collector (MC)-ICP-MS in Pisa, specially tuned for $^{11}B/^{10}B$ analysis (following Foster, 2008). Samples were diluted to contain ~20 ppb B and were then bracketed with NBS 951 boric acid standard solution of the same concentration, to correct for machine induced mass fractionation.

## 3.2 Micro-analytical methods

### 3.2.1 Raman spectroscopy

MicroRaman spectroscopy of minerals and fluid inclusions was done at the Department of Earth Sciences, University of Turin, with a LabRAM HR (VIS) (HORIBA Jobin Yvon) equipped with a 532.11 nm, solid-state Nd laser, a Super Notch Plus filter with spectral resolution of 1 $cm^{-1}$, and a grating of 600 grooves/mm. The laser of emission power was set at 80 mW and focused to 5 µm with a 100x objective with a laser power on the sample < 5 mW. Calibration was performed using the 520.6 $cm^{-1}$ band of a silicon standard for the 100-2000 $cm^{-1}$ range, and the 2331 $cm^{-1}$ band of atmospheric $N_2$ for the 2000-4000 $cm^{-1}$ range. Four accumulations of 30–60 s were collected for each spectrum. Raman spectra of fluid inclusions were performed on double-polished thick sections unless otherwise specified.

### 3.2.2 Scanning Electron microscopy (SEM, EDS)

Quantitative energy-dispersive X-ray spectroscopy (EDS) analyses and backscattered electron (BSE) imaging were carried out using the JSM-IT300LV Scanning Electron Microscope Oxford Inca Energy Dispersive Spectrometer at the Department of Earth Sciences of Turin University. Data was processed with the INCA software from Oxford Instruments. Quantitative analysis employed 15kV accelerating voltage and 20 s to 40 s counting time. Natural and synthetic mineral and oxide standards were employed. EDS calibration was made using Cobalt standard.

### 3.2.3 Electron microprobe analysis

Quantitative wavelength-dispersive spectrometer (WDS) analyses were carried out using a JEOL 8200 Super Probe at the Department of Earth Sciences “Ardito Desio” of Milan University. The microprobe was using a 15kV accelerating voltage under 5 nA, with 30s counting time under maximum emission peak. Sixteen oxide composition were measured, using synthetic and natural standards: grossular (Si, Al and Ca), omphacite (Na), K-feldspar

(K), fayalite (Fe), forsterite (Mg), rhodonites (Mn), niccolite (Ni), ilmenite (Ti), galena (Pb and S), pure Cr, pure Zn and pure Cu.

## 3.3 Thermodynamics modeling (phase, aqueous speciation and isotope)

### 3.3.1 Deep earth water model

Thermodynamic modeling was performed using the Deep Earth Water (DEW) Model (Huang and Sverjensky, 2019; Sverjensky et al., 2014a) and the EQ3/EQ6 software (Wolery and Jarek, 2003) with a modified Berman database (Berman, 1988). The speciation-solubility code EQ3 was used to calculate the composition of a fluid in equilibrium with a given mineral assemblage at fixed $fO_2$, P and T, and in the K-Na-Ca-Mg-Fe-Al-Si-O-H-C-N-S-Cl system. The reaction path modeling code EQ6 was used to model the irreversible reaction between 1kg of fluid as derived from EQ3, and a given number of moles of minerals constituting a rock reservoir and determining an initial fluid/rock (F/R) ratio for each calculation. The chosen EQ6 mineral assemblage corresponds to a dunite with mineral modal proportions comparable with the most preserved study samples and consisting of 92% olivine (forsterite 90%, fayalite 10%), 5.4% orthopyroxene (enstatite 90%, ferrosilite 10%), 2.5% clinopyroxene (diopside 90%, hedenbergite 10%) and 0.1% spinel.

### 3.3.2 Isotope modeling (Thermotopes-COH)

A thermodynamic model called Thermotopes-COH was developed in the frame of this Ph.D allowing modeling of conventional carbon isotopic exchanges and more advanced thermodynamic and isotopic processes in the C-O-H system and in the 300 - 900 °C and 1 - 50 kbar pressure-temperature range. Details of the principle of the software is available in **Chapter 6**, and full details of the Python code of the software is available in the appendix.

# Part II - Results

## 4 High-pressure serpentinization and abiotic methanogenesis in metaperidotite from the Appalachian subduction, northern Vermont

Antoine Boutier[1,2]*, Alberto Vitale Brovarone[3,4]*, Isabelle Martinez[2], Olivier Sissmann[5], Sara Mana[6]

[1]*Dipartimento di Scienze della Terra, Università degli Studi di Torino, Via Valperga Caluso 35, Torino, Italy*

[2]*Université de Paris, Institut de physique du globe de Paris, CNRS, F-75005 Paris, France*

[3]*Dipartimento di Scienze Biologiche, Geologiche e Ambientali, Alma Mater Studiorum Università di Bologna. Piazza di Porta San Donato 1, Bologna, Italy*

[4]*Institut de Minéralogie, de Physique des Matériaux et de Cosmochimie (IMPMC), Sorbonne Université, Muséum National d'Histoire Naturelle, UMR CNRS 7590, IRD UR206, 75005 Paris, France*

[5]*IFP Energies Nouvelles, 92500 Rueil-Malmaison, France*

[6]*Department of Geological Sciences, Salem State University, Salem, MA 01970, USA*

*Corresponding author: antoine.boutier@unito.it, alberto.vitaleb@unibo.it

### Abstract

Serpentinization is the process of hydroxylation of olivine-rich ultramafic rocks to produce minerals such as serpentine, brucite and magnetite. This process is commonly accompanied by Fe oxidation and release of $H_2$, which can be involved in abiotic reaction pathways leading to the genesis of abiotic light hydrocarbons such as methane ($CH_4$). Examples of this phenomenon exist at the seafloor, such as at the serpentinite-hosted Lost City hydrothermal field, and on land in ophiolites at relatively shallow depths. However, the possibility for serpentinization to occur at greater depths, especially in subduction zones, raises new questions on the genesis of abiotic hydrocarbons at convergent margin and its impact on the deep carbon cycle. High-pressure ultramafic bodies exhumed in metamorphic belts can provide insights on the mechanisms of high-pressure serpentinization in subduction zones and on the chemistry of the resulting fluids. This study focuses on the ultramafic Belvidere Mountain complex belonging to the Appalachian belt of northern Vermont, USA. Microstructures show overgrowth of both primary (Mg# 0.91) and metamorphic (Mg# 0.95) olivine by delicate antigorite crystals, pointing to at least one stage of serpentinization at high-temperature conditions and consistent with the high-pressure subduction evolution of the Belvidere Mountain complex. Formation of ubiquitous magnetite and local Fe-Ni alloys testifies to the partial oxidation of $Fe^{2+}$ into $Fe^{3+}$ and generation of reduced conditions. Fluid inclusion trails cross-cutting the primary olivine relicts suggest their formation during the antigorite serpentinization event. MicroRaman spectroscopy on the fluid inclusions reveals a $CH_4$-rich gaseous composition, as well as $N_2$, $NH_3$ and $H_2S$. Moreover, the precipitation of daughter minerals such as lizardite and brucite in the fluid inclusions indicate the initial presence of $H_2O$ in the fluid. High-pressure serpentinization driven by the infiltration of metasediment-derived aqueous fluids is proposed at the origin of $CH_4$ and other reduced fluid species preserved in the fluid inclusions. This suggests the Belvidere Mountain complex as an example of deep abiotic hydrocarbon genesis related to high-pressure serpentinization in an early Paleozoic subduction zone.

**Keywords:** HP Serpentinization, Abiotic methane, C fluxes at subduction zones, Belvidere Mountain Complex, Metamorphic olivine.

## 4.1 Introduction

Alteration of ultramafic rocks by aqueous fluids, or serpentinization, produces serpentine-rich rocks and may be accompanied by redox reactions leading to the formation of $H_2$ and abiotic light hydrocarbons (Mével, 2003; Moody, 1976; Seyfried Jr et al., 2007). Oxidation of $Fe^{2+}$ in mantle minerals and formation of $Fe^{3+}$ minerals such as magnetite produces $H_2$, which may then promote the conversions of dissolved carbon-bearing species into abiotic $CH_4$ (Andreani et al., 2013; Berndt et al., 1996). Serpentinization is well documented at mid-ocean ridges and on land (Andréani et al., 2007; Cannat et al., 2010; Etiope et al., 2011; Klein et al., 2014; Schrenk et al., 2013), where $H_2$ and $CH_4$ produced through serpentinization can support biological communities and could be linked to the emergence of early life on Earth (Kelley et al., 2005; Ménez et al., 2018; Sleep and Bird, 2007). Serpentinization processes may also happen at much greater depths and affect subducted mantle sections and the overlying mantle wedge at convergent margins (Guillot et al., 2015, 2000; Vitale Brovarone et al., 2017; Wada et al., 2008), owing to the availability of aqueous fluids (Bebout and Penniston-Dorland, 2016; Deschamps et al., 2013). However, the patterns of serpentinization reactions at high-temperature (HT) and high-pressure (HP) conditions, here defined with respect to the serpentine stability field, and the associated fluid-rock redox budgets are still largely unconstrained. The possibility that HT-HP serpentinization may not involve Fe oxidation and genesis of $H_2$ at 400-600°C has been proposed (Evans, 2010). However, natural case studies of slab and mantle wedge-derived serpentinized peridotites suggest that magnetite, $H_2$ and abiotic $CH_4$ can be produced at these conditions (Vitale Brovarone et al., 2020). Ultramafic bodies in metamorphic belts can provide insights on the mechanisms of HP-HT serpentinization and the resulting fluids (Evans et al., 2017), and therefore make good case studies for the investigation of the mechanisms of serpentinization in subduction zones.

The Belvidere ultramafic complex, Vermont, USA, is a fragment of the former Iapetus ocean that was involved in the Taconic orogeny and recorded subduction-related HP metamorphism during Cambrian-Ordovician (Chew and van Staal, 2014; Gale, 1980; Honsberger et al., 2017). This complex includes variably serpentinized peridotites containing antigorite, the HT serpentine minerals stable at subduction zone HP conditions (e.g., Evans, 2004; Schwartz et al., 2013), therefore making a potential example of HT-HP serpentinization. In this work, we integrate field, microstructural, thermodynamic, and fluid inclusions data to investigate the patterns and timing of serpentinization of the Belvidere ultramafic complex, with particular focus on the HP fluid-rock interactions recorded by these rocks.

## 4.2 Geologic setting

The Belvidere Mountain complex (BMC) area is part of a North-South trending belt of mafic/ultramafic rocks belonging to the Appalachian Mountain system and extending form Newfoundland to Georgia (Gale, 2007; Hibbard et al., 2006)(Fig. 4.1). These ultramafic bodies mainly consist of variably serpentinized peridotites, and associated metabasic and metafelsic rocks tectonically embedded within Cambrio-Ordovician metasedimentary and metavolcanics formations (Chidester et al., 1978; Gale, 1986, 1980; Labotka and Albee, 1979; Laird et al., 1984; Van Baalen et al., 2009). The BMC, as well as other mafic/ultramafic complexes such as the Tillotson Peak and the Pennington complexes, may represent remnants of an ocean-continent transition zone associated with the extension of the Laurentian margin (Chew and van Staal, 2014). These terranes were successively involved in the closure of the Iapetus Ocean during the Ordovican Taconic orogeny (Doolan et al., 1982; Honsberger et al., 2017; Karabinos et al., 1998; Laird et al., 1984; Stanley et al., 1984). The BMC forms a 6.5 km long body that structurally overlies the metasedimentary Ottauquechee and Stowe Formations to the East and is overlain by the Hazen Notch formation to the West. The Stowe Formation is late Cambrian, composed of gray-green quartz -chlorite-sericite +/- magnetite schists. The Ottauquechee Formation consists of middle Cambrian carbonaceous pyritiferous phyllites. The Neoproterozoic to Cambrian Hazen Notch Formation includes graphitic and non-graphitic quartz-albite-sclerite-chlorite schist, along with medium-grained, massive, quartz-albite-muscovite gneiss. The internal architecture of the BMC comprises, from top to bottom, variably serpentinized dunite and harzburgite, coarse-grained and fine-grained amphibolite, greenstone, muscovite schist, and albite gneiss (Gale, 1986, 1980; Van Baalen et al., 2009). Lenticular bodies composed of talc-carbonate rocks and steatite, often including cores of relatively unserpentinized peridotite, are observed within the BMC, and range in size from a few meters to several tens of meters (Chidester et al., 1978). The BMC rocks underwent Taconic blueschist-facies peak metamorphic conditions constrained at 0.9-1.3 GPa and 510-520 °C in metabasic rocks (Honsberger, 2015; Laird et al., 1993). Higher P metamorphic conditions, up to coesite ultra high-pressure (UHP) conditions, are recorded by the Tillotson Peak mafic rocks located just north of the BMC (Gonzalez et al., 2020; Laird et al., 1993, 1984). In the BMC, the HP tectonometamorphic event has been dated at 505-473 Ma by $^{40/39}$Ar amphibole and mica geochronology (Castonguay et al., 2012; Laird et al., 1993).

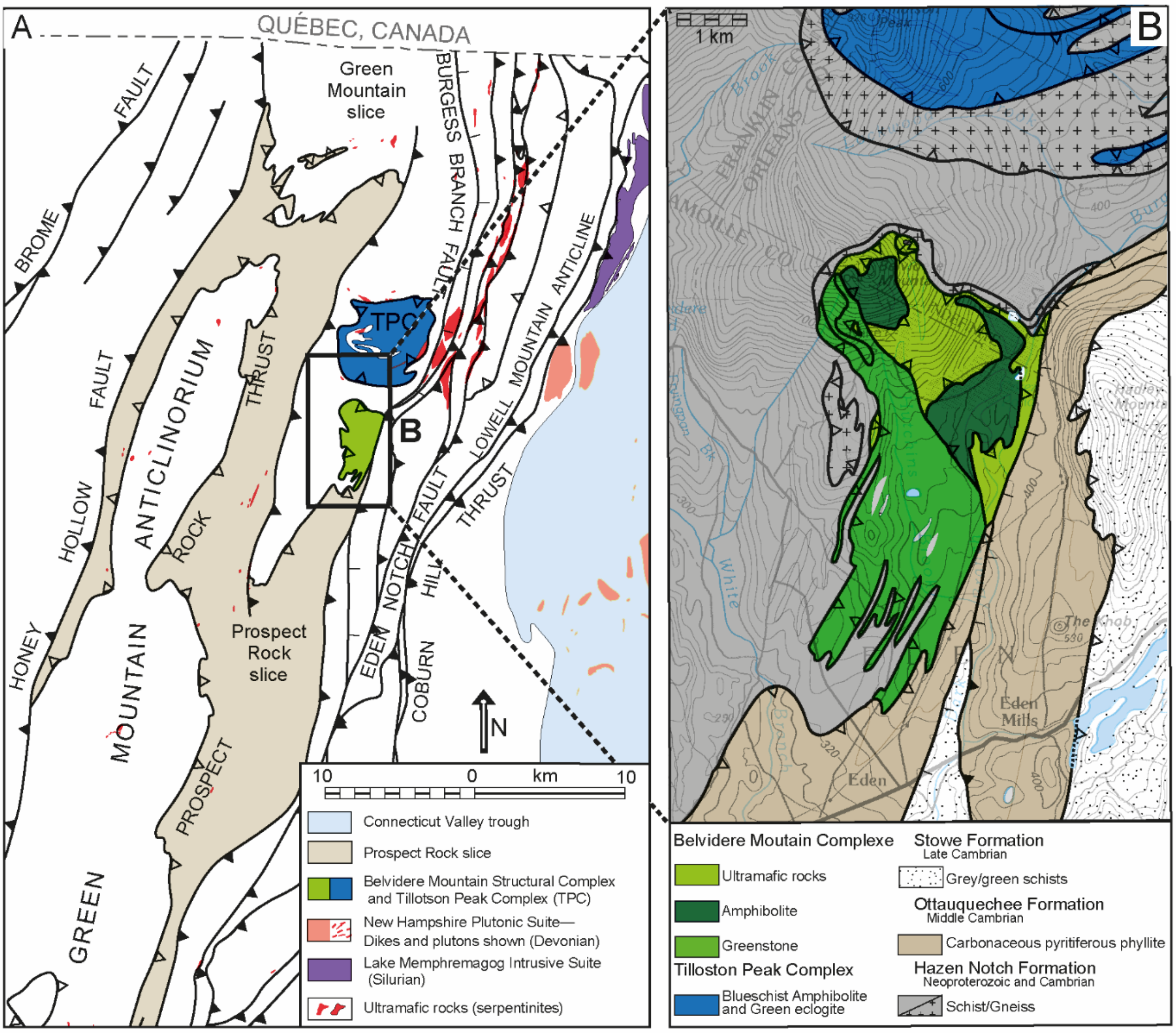

***Fig. 4.1***: *A: Simplified geological map of Vermont, modified from Hibbard et al., (2006). B: Simplified bedrock geologic map of the Belvidere Mountain Complex and the surrounding formations. Modified after Hibbard et al., (2006). Units description from Hibbard et al., (2006) and Gale, (2007).*

## 4.3 Methods

Quantitative energy-dispersive X-ray spectroscopy (EDS) analyses and backscattered electron (BSE) imaging were carried out using the JSM-IT300LV Scanning Electron Microscope Oxford Inca Energy Dispersive Spectrometer at the Department of Earth Sciences of Turin University. Data was processed with the INCA software from Oxford Instruments. Quantitative analysis employed 15kV accelerating voltage and a beam current of 50 nA and 20 s to 40 s counting total time. Natural and synthetic mineral and oxide standards were employed. EDS calibration was made using Cobalt standard.

Quantitative wavelength-dispersive spectrometer (WDS) analyses were carried out using a JEOL 8200 Super Probe at the Department of Earth Sciences "Ardito Desio" of Milan University. The microprobe was using a 15kV accelerating voltage under 5 nA, with 30s counting time under maximum emission peak. Sixteen oxide composition were measured, using synthetic and natural standards: grossular (Si, Al and Ca), omphacite (Na), K-feldspar (K), fayalite (Fe), forsterite (Mg), rhodonites (Mn), niccolite (Ni), ilmenite (Ti), galena (Pb and S), pure Cr, pure Zn and pure Cu.

MicroRaman spectroscopy of minerals and fluid inclusions was done at the Department of Earth Sciences, University of Turin, with a LabRAM HR (VIS) (HORIBA Jobin Yvon) equipped with a 532.11 nm, solid-state Nd laser, a Super Notch Plus filter with spectral resolution of 1 $cm^{-1}$, and a grating of 600 grooves/mm. The laser of emission power was set at 80 mW and focused to 5 µm with a 100x objective with a laser power on the sample < 5 mW. Calibration was performed using the 520.6 $cm^{-1}$ band of a silicon standard for the 100-2000 $cm^{-1}$ range, and the 2331 $cm^{-1}$ band of atmospheric $N_2$ for the 2000-4000 $cm^{-1}$ range. Four accumulations of 30–60 s were collected for each spectrum. Raman spectra of fluid inclusions were performed on double-polished thick sections unless otherwise specified.

Isotopic composition measurements of methane were performed on a MAT 253 (Thermo Fisher) mass spectrometer, coupled with gas chromatography (GCC-IRMS) device as CO2 gas, at a specific retention time, on masses 44 (for $\delta^{12}C$), 45 (for $\delta^{13}C$) and 46 (for $\delta^{18}O$), after the methane is completely oxidized into $CO_2$ through combustion at 1000°C. This is because it is not possible to directly measure methane isotopologues ($^{12}CH4$, $^{13}CH4$, $^{12}CH_3D$) on a "classical" magnetic sector IRMS, due to interferences on masses 16, 17 and 18 in the source (such as $CH_5^+$, $H_2O$ …). The value of the $CO_2$ internal reference gas was determined using multiple IAEA carbonate standards (IAEA-603, 610, 611, 612) on an EA-IRMS device. On the GCC-IRMS, the efficiency of $CH_4$ oxidation into $CO_2$ is checked before each analytical session by injecting, as a sample, two different commercial external methane isotopic standards (such as Air Liquide Thermo 1.2 and Air Liquide Bio 1.0 gases). If the analytical value of the commercial standards is within 0.1‰ of their independently determined value, then the combustion process is deemed valid and without fractionation. The samples collected from fluid inclusions can then be analyzed. The gas phase was extracted and measured after crushing 20 to 30 gr of rock sample under vacuum.

Thermodynamic modeling was performed using the Deep Earth Water (DEW) Model (Huang and Sverjensky, 2019; Sverjensky et al., 2014a) and the EQ3/EQ6 software (Wolery and Jarek, 2003) with a modified Berman database (Berman, 1988). The speciation-solubility code EQ3 was used to calculate the composition of a fluid in equilibrium with a given mineral assemblage at fixed $fO_2$, P and T, and in the K-Na-Ca-Mg-Fe-Al-Si-O-H-C-N-S-Cl system. The reaction path modeling code EQ6 was used to model the irreversible reaction between 1kg of fluid as derived from EQ3, and a given number of moles of minerals constituting a rock reservoir and determining an initial fluid/rock (F/R) ratio for each calculation. The chosen EQ6 mineral assemblage corresponds to a dunite with mineral modal proportions comparable with the most preserved study samples and consisting of 92% olivine (forsterite 90%, fayalite 10%), 5.4% orthopyroxene (enstatite 90%, ferrosilite 10%), 2.5% clinopyroxene (diopside

90%, hedenbergite 10%) and 0.1% spinel. Additional details regarding the modeling strategy are presented in Section 4.4.5.

## 4.4 Sample description and mineral chemistry

In this section, we present the petrography, microstructures and mineral chemistry of samples collected in the BMC (Fig. 4.2). The selected samples range from weakly serpentinized dunite (V18-2a and V18-2b) to partially serpentinized dunite including layers of boudinaged meta-pyroxenite (V18-3a and V18-3b), to fully serpentinized peridotite (V18-B3). One sample of rodingites consisting of carbonates, garnet, epidote and chlorite is also presented.

### 4.4.1 Microstructural characterization

Sample V18-2a (least serpentinized dunite) consists of olivine (~80 vol.%), antigorite (~10 vol.%), Cr-spinel (>5 vol.%), magnetite (<5 vol.%), chlorite (<1 vol.%), sulphides (<1 vol.%), and alloys (<1 vol.%) determined from visual estimate in thin section. Primary olivine forms crystals ranging in size from 0.25 to 1 mm (Fig. 4.3A) partially replaced by antigorite, as identified by MicroRaman spectroscopy (Fig. 4.4), along fractures (Fig. 4.3A-C). Antigorite is present as elongated crystals, up to 200 µm in length, which statically overgrew the olivine (Fig. 4.3C). Magnetite is present in three microstructural domains: as large, millimeter scale crystals rimming chromite relicts, as grains of ~50 µm, and as millimeter scale crystals in antigorite veins. Chlorite is found, together with magnetite, around Cr-spinel relicts (Fig. 4.3B).

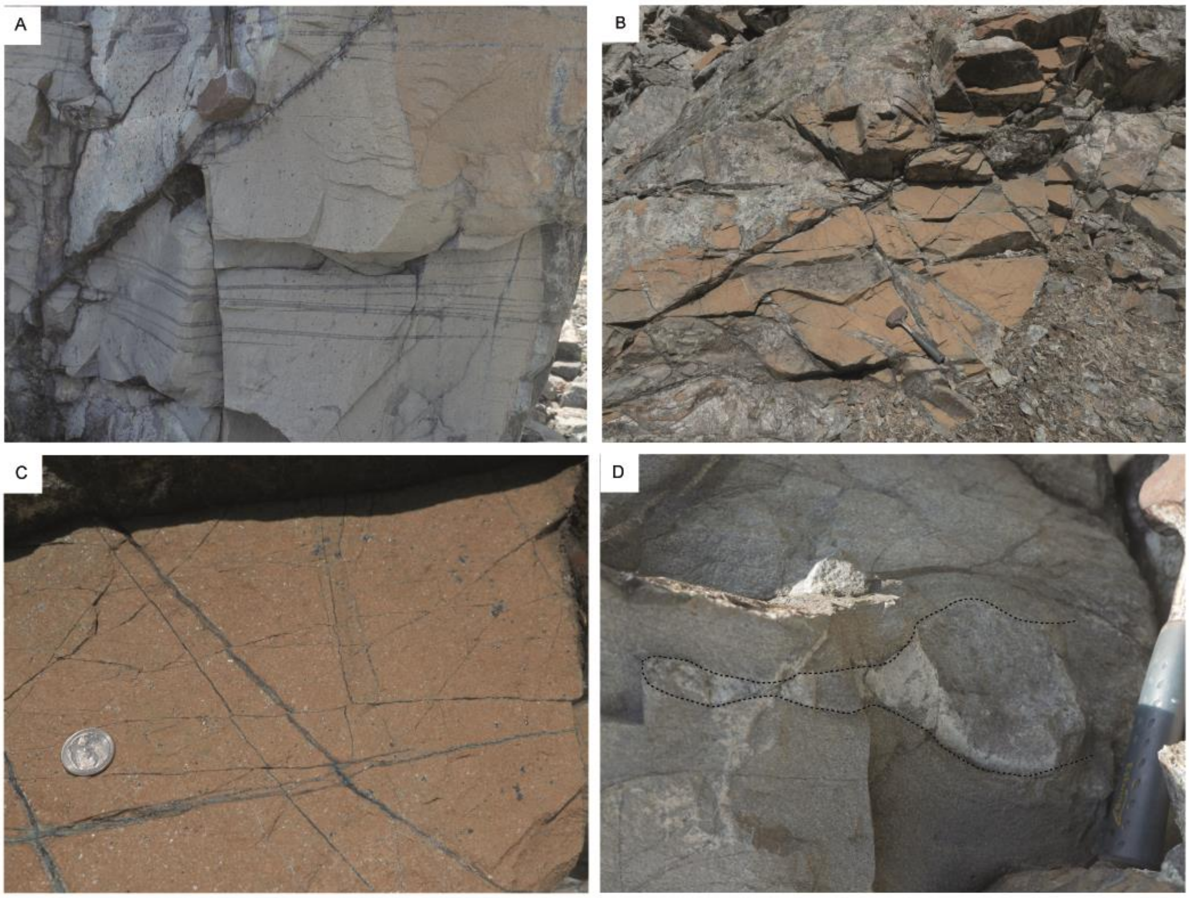

***Fig. 4.2****: A-B: Photographs of the Belvidere serpentinized peridotite in outcrop. C: Weakly serpentinized dunite (samples V18-2a and V18-2b). D: Serpentinized dunite, with boudinaged meta-gabbro (samples V18-3a and V18-3b).*

Sample V18-2b (serpentinized dunite) consists of antigorite (∼40 vol.%), olivine (∼40 vol.%, including primary and metamorphic olivine), magnetite (>5 vol.%), chlorite (>5 vol.%), brucite (<5 vol.%), and alloys (<1 vol.%). The structure is similar to V18-2a, but in this case the extent of serpentinization is higher. SEM backscattered-electron imaging reveals the presence of a second generation of olivine, hereafter metamorphic olivine (see Section 4.4.2 for discussion) growing in two different sites: epitaxially on the primary olivine and replacing former orthopyroxene (Fig. 4.5A-B). Striped zoning is observed in primary olivine (Fig. 4.5A), as described in Plümper et al., 2012a, alternating thin forsterite-richer and forsterite-poorer

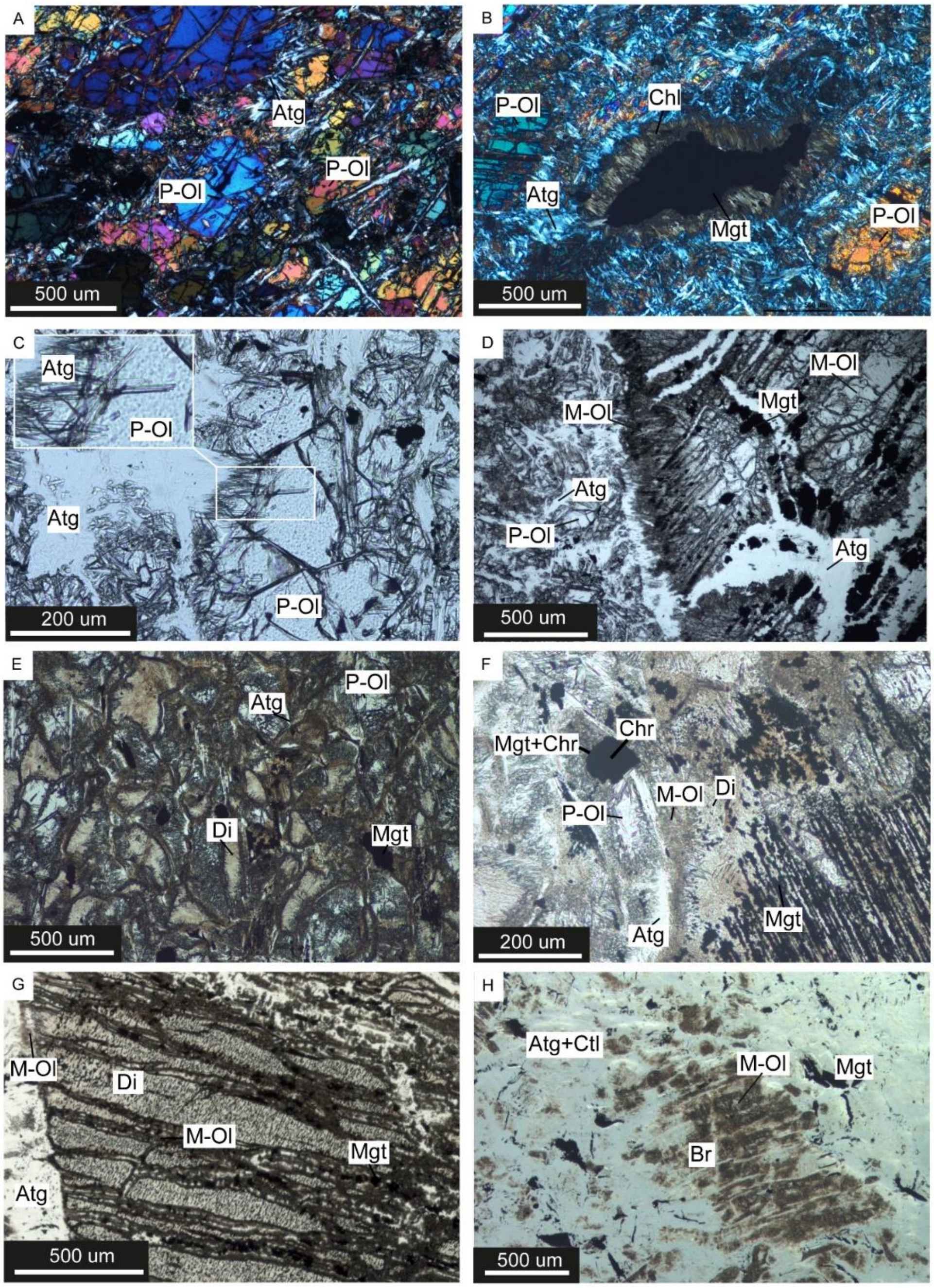

***Fig. 4.3****: A: Photomicrograph of a partially serpentinized dunite. B: Partial replacement of primary chromian spinel by magnetite and chlorite. C: Partial replacement of olivine by antigorite. D: Inferred primary orthopyroxene being pseudomorphically replaced by metamorphic olivine. See also Figure 4.5B. E: Photomicrograph of a pyroxenite layer included in the Belvidere peridotite. The photomicrograph shows radial diopside aggregate pseudomorphic on primary clinopyroxene. Partially serpentinized olivine is also visible. F: Magnetite-rich diopside pseudomorphosis on primary clinopyroxene. Note the growth of metamorphic olivine at the rim of the clinopyroxene site. See Figure 4.5A for SEM-based backscattered electron image. G: Metamorphic diopside replacing primary clinopyroxene. In this case, note the growth of metamorphic olivine along fractures cutting the pseudomorphosis. See Figure 4.5F for SEM-based backscattered electron image. H: Relict of metamorphic olivine pseudomorphic on primary clinopyroxene. The metamorphic olivine is then partially replaced by serpentine + brucite + magnetite. A-D: Sample V18-2b, E-G: Sample V18-3a; H: sample V18-B3. P-Ol: primary olivine, M-Ol: metamorphic olivine, Atg: antigorite, Chl: chlorite, Mgt: magnetite, Di: diopside, Chr: chromite, Br: brucite, Ctl: chrysotile.*

olivine composition. The initial presence of orthopyroxene in the rock is inferred based on the presence of clinopyroxene exsolutions preserved in metamorphic olivine-rich pseudomorphs (Fig. 4.3D and 4.5B). Antigorite is present as elongated (0.5 mm in length) crystals and as fine-grained aggregates in the matrix. The elongated antigorite crystals are chemically zoned, with bright core and dark rim in backscattered electron imaging (Fig. 4.5A). Raman spectra of both generations exhibit the characteristic 1043 cm$^{-1}$ band of antigorite, whereas the main OH stretching is at 3664 cm$^{-1}$ in the bright core and at 3673 cm$^{-1}$ in the dark rim (Fig. 4.4C), both consistent with antigorite Raman features. The higher Raman shift of the dark rim may be linked to variation of pressure condition (Auzende et al., 2004). The dark antigorite generation appears the same, forming the fine-grained aggregates. Only the dark generation was observed in contact with primary and metamorphic olivine (Fig. 4.5A). Magnetite is more abundant relative to sample V18-2a. Brucite was identified by SEM EPMA, and Raman (Fig. 4.4B) in veins, sometimes associated with metamorphic olivine (Fig. 4.5C). Alloys and sulphides are present in association with antigorite and are locally associated with magnetite (Fig. 4.5D).

Samples V18-3a and 3b are from a boudinaged layer of clinopyroxenite included in an intensely serpentinized dunite (Fig. 4.3E-G). The mineral assemblage and microstructures of the serpentinized dunite part of the sample is similar to sample V18-2b, yet more intensely serpentinized. The primary clinopyroxene is fully replaced by diopside aggregates in both the clinopyroxenite layer and the host dunite. The primary clinopyroxene sites in this sample are slightly different from the serpentinized dunite, with less abundant magnetite and characteristic fan-shaped diopside aggregates in the former compared to the latter. Metamorphic olivine is present at the rim of primary clinopyroxene and along its cleavages, together with antigorite (Fig. 4.5E-F). In the latter case, metamorphic olivine is localized along thin arrays encircled by antigorite (Fig. 4.5F). Antigorite shows the same chemical zoning as observed in the dunite, with brighter cores and darker rims in backscatter electron imaging (Fig. 4.5G). Backscattered electron imaging reveals that the dark antigorite shows similar overgrowth microstructural relationships with both primary and metamorphic olivine (Fig. 4.5E). The microstructures reflect either equilibrium between antigorite and the two olivine generations, or overgrowth of both olivine generations by the antigorite. Considering that the amount of primary olivine strongly decreases in favor of antigorite in several samples, which suggests serpentinization of the primary olivine, it is suggested that the dark antigorite generation formed after the growth of metamorphic olivine. It is possible, even though the microstructures could not confirm it, that the first antigorite generation grew prior to or together with the metamorphic olivine. Magnetite is present in four different structural sites: as arrays of ~50 µm size crystals scattered in the rock, as trails of ~50 µm crystals in primary olivine and clinopyroxene pseudomorphoses, as aggregates rimming the primary Cr-spinel, and as millimeter scale aggregates along discordant veins. The Cr-spinel sites are characterized by three different layers: a rather preserved core, a mantle of ferritchromite, and a rim of magnetite (Fig. 4.5E; see Section 4.4.2).

Sample V18-B3 is a fully serpentinized peridotite. The matrix is composed of a mixture of antigorite and chrysotile (identified by MicroRaman) with magnetite. Brucite is observed replacing pyroxene sites and is associated with magnetite and/or metamorphic olivine (Fig. 4.3H and 4.5H). Based on the microstructural observations on sample V18-2b, these pseudomorphoses are interpreted as former orthopyroxene crystals replaced by metamorphic olivine and successively hydrated to form serpentine + brucite ± magnetite.

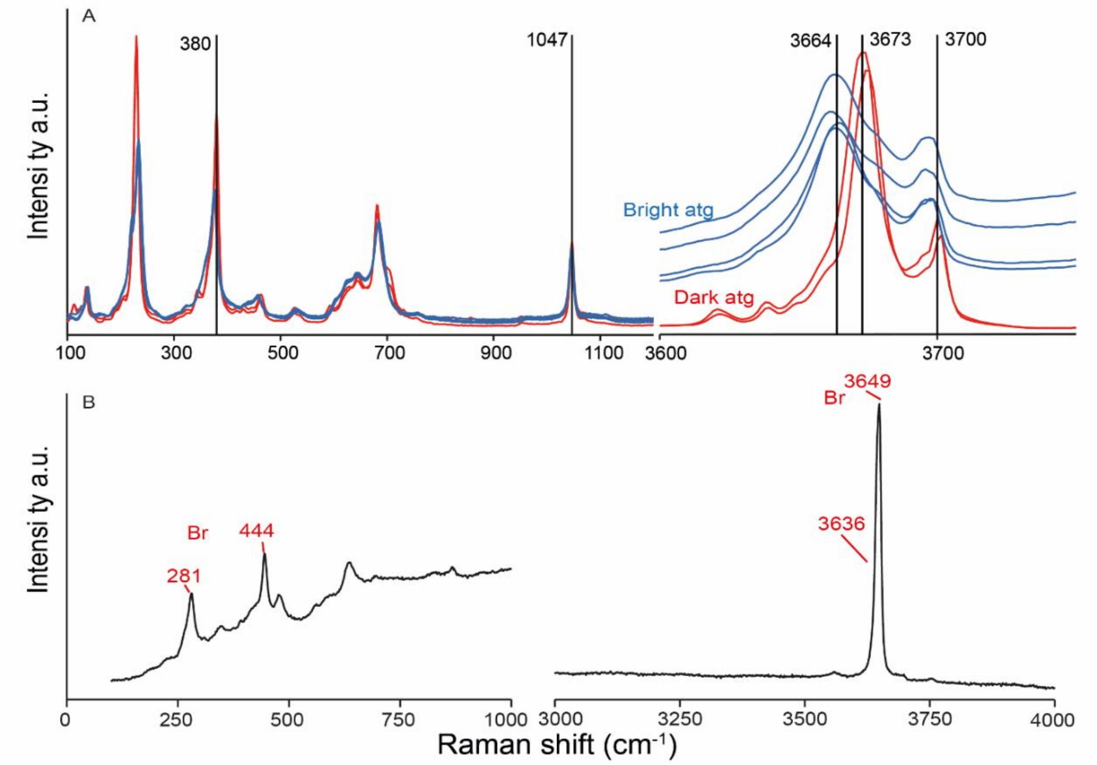

***Fig. 4.4**: Raman spectra of solid phases. A: Antigorite core (Atg1) and rim (Atg2) (see Fig. 4.5A). B: Brucite.*

### 4.4.2 Mineral chemistry

Primary olivine has Mg# of 0.91-0.92 [Mg# = Mg/(Fe+Mg)], whereas metamorphic olivine is enriched in Mg (Mg# of 0.95) (Table 4.1, Fig. 4.6). The Mn# [Mn# = Mn/(Mn+Fe+Ni)] of metamorphic olivine (0.0040 ±0.0006) is much higher than primary olivine (0.0015 ±0.0005). Metamorphic olivine analyses in sample V18-B3 show slightly lower Mg# and higher Mn# content relative to metamorphic olivine from other samples. Metamorphic olivine rimming the primary orthopyroxene sites in sample V18-3a has higher CaO content (0.25 wt.%) compared to the metamorphic olivine overgrowing primary olivine in V18-2b (0.02 wt.%). The NiO content of primary olivine (0.38 to 0.49 wt.%) and metamorphic olivine (0.39 to 0.46 wt.%) are similar.

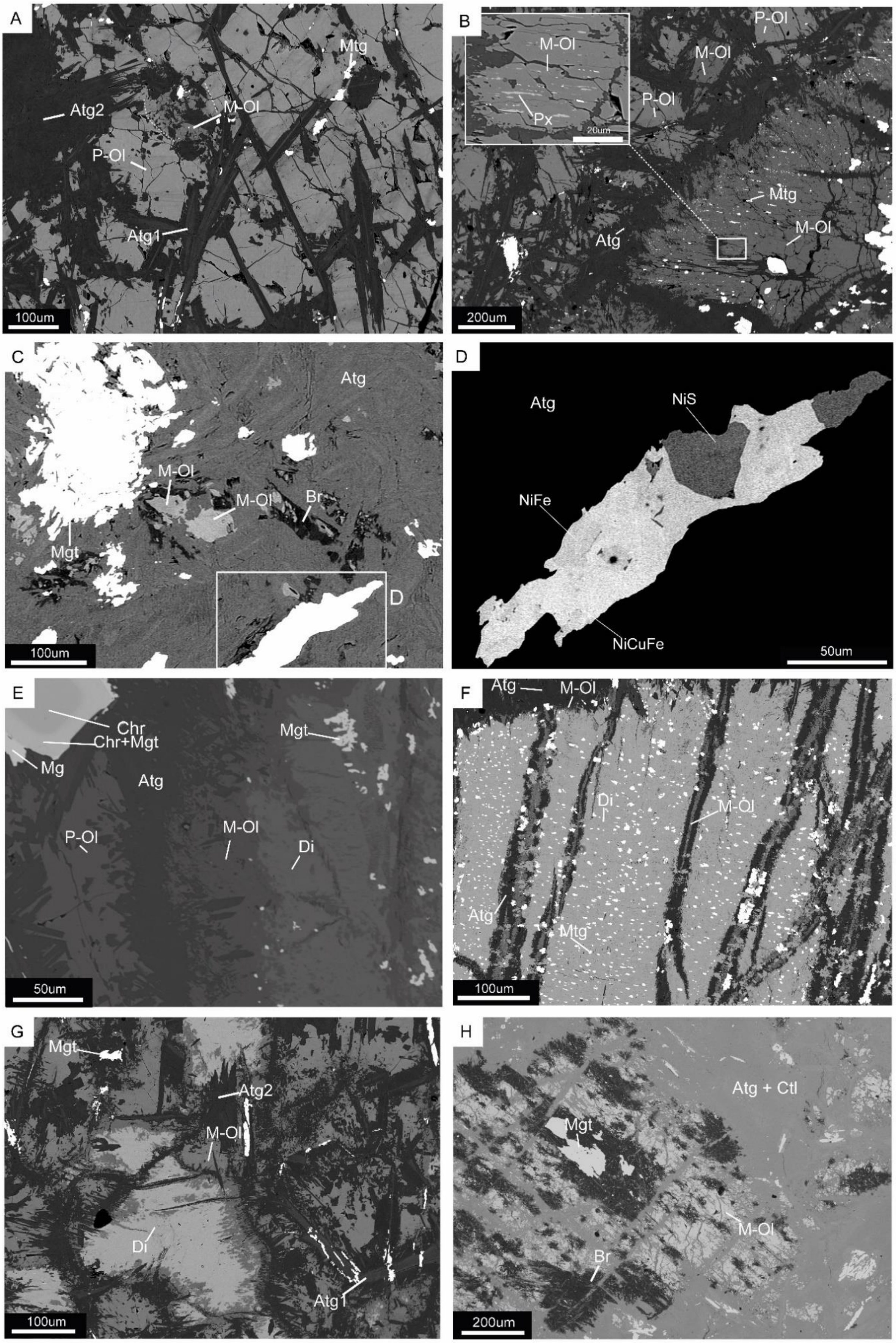
A
Mtg
Atg2
M-Ol
P-Ol
Atg1
100um
B
P-Ol
M-Ol
M-Ol
Px
20um
P-Ol
Mtg
Atg
M-Ol
200um
C
Atg
M-Ol
M-Ol
Br
Mgt
D
100um
D
Atg
NiS
NiFe
NiCuFe
50um
E
Chr
Chr+Mgt
Mg
Mgt
Atg
P-Ol
M-Ol
Di
50um
F
Atg
M-Ol
Di
M-Ol
Atg
Mtg
100um
G
Mgt
Atg2
M-Ol
Di
Atg1
100um
H
Atg + Ctl
Mgt
M-Ol
Br
200um

***Fig. 4.5****: SEM-BSE images of samples V18-2b, V18-3a and V18-B3. A: Microstructural patterns of serpentinization. Two generations of serpentine can be observed based on the BSE contract, a bright core (Atg1) and a dark rim (Atg2). Note also the striped zonation of primary olivine and the formation of metamorphic olivine. B: Replacement of an inferred primary orthopyroxene crystal by metamorphic olivine. The close-up shows the preservation of clinopyroxene relicts interpreted as exsolutions inside the former orthopyroxene. C: Formation of brucite at the expense of metamorphic olivine. D: Composite aggregate of Fe-Ni and Fe-Cu-Ni alloys and Ni sulphide. E: Growth of metamorphic olivine around a diopside-rich primary clinophyroxene pseudomorphosis. A primary chromina spinel partially converted into magnetite can also be observed. F: Metamorphic diopside replacing primary clinopyroxene. Note the presence of antigorite + metamorphic olivine ± magnetite along the fractures. In this case, metamorphic olivine occupies the centre of the fractures and is not in contact with diopside, whereas the metamorphic olivine rimming the primary clinopyroxene site is in contact with it. G: Metamorphic olivine growing at the expense of metamorphic diopside (former primary clinopyroxene). The microstructure suggests the former presence of serpentine needles replacing the clinopyroxene and successively replaced by metamorphic olivine. Both Atg1 and Atg2 antigorite generations are present. H: Relict of metamorphic olivine formed at the expense of a primary orthopyroxene site in V18-3b. The metamorphic olivine is partially converted into brucite + serpentine. P-Ol: primary olivine M-Ol: metamorphic olivine Px: pyroxene Di: diopside Mtg: magnetite Chr: chromite Atg: antigorite Br: brucite Ctl: chrysotile NiFeS: nickel and iron sulphite. The presence of antigorite was confirmed by Raman spectroscopy.*

The incorporation of Mn in olivine appears to be characteristic of metamorphic olivine from several localities worldwide regardless of the olivine formation conditions (dehydration vs. hydration) (Fig. 4.6) (e.g., Frost and Beard, 2007; Majumdar et al., 2016; Nozaka, 2018, 2003). The Mg# of metamorphic olivine relative to primary olivine may depend upon several parameters such as the stability of different Fe-bearing minerals, the Fe partitioning among them, and P-T and redox conditions. An increase in Mg# (and MnO) in metamorphic olivine relative to primary olivine has been observed in inferred mantle wedge peridotites recording HP serpentinization (Dandar et al., 2019; Guillot et al., 2000). Our data, together with previous work, indicate that iron was not preferentially partitioned into olivine during HT serpentinization (Evans, 2010) but other Fe-bearing minerals, such as serpentine and magnetite, could form. Plümper et al., 2012a report striped Mg# zoning similar to the BMC samples in hydrated supra-subduction mantle rocks as the result of chemical interaction during antigorite serpentinization at high temperature conditions. Metamorphic olivine formed through prograde antigorite + brucite dehydration shows either lower or higher Mg# compared to mantle olivine (Arai et al., 2012; Debret et al., 2013; Iyer et al., 2008; Kempf and Hermann, 2018; Nozaka, 2018; Plümper et al., 2012b; Scambelluri et al., 1995; Shen et al., 2015)(Fig. 4.6).

In samples V18-2b and V18-3a, the core of individual, elongated antigorite crystals exhibits higher FeO (1.6 to 2.6 wt.% [Mg# 0.94-0.96]), $Al_2O_3$ (1.45-1.77 wt.%) [Mg# =Mg/(Mg+ΣFe)], and $Cr_2O_3$ (0.25-0.61 wt.%) than the rim (1.2-1.35 wt.% [Mg# 0.97], 0.47-0.52 wt.%, 0.10-0.13 wt.%, respectively) (Table 4.1). In both samples, unzoned matrix antigorite has a composition equivalent to the rim of the elongated antigorite crystals. The Mn# [Mn# = Mn/(Mn+Fe+Ni)] of antigorite is 0.0006 (±0.0004).

**Table 4.1:** MicroProbe analysis. Absence of SD value when n>1 indicates SD<0.01. *EDS analyses normalized at 100.

| **Minerals** | **Primary Olivine** | | **Metamorphic Olivine** | | | **Pyroxene** | **Serpentine (Bright core)** | | **Serpentine (Matrix)** | | **Chlorite** | |
|---|---|---|---|---|---|---|---|---|---|---|---|---|
| **Sample** | **V18-2b** | **V18-3a** | **V18-2b** | **V18-3a** | **V18-B3*** | **V18-3a** | **V18-2b** | **V18-3a** | **V18-2b** | **V18-3a** | **V18-2b** | **V18-3a** |
| **(n)** | 14 | 11 | 28 | 15 | 25 | 20 | 6 | 2 | 9 | 4 | 11 | 1 |
| **$SiO_2$** | 40.91 (0.25) | 40.83 (0.46) | 41.31 (0.49) | 41.95 (0.63) | 42.00 (0.12) | 54.96 (0.98) | 42.87 (1.21) | 43.41 (0.1) | 44.15 (0.17) | 43.1 (1.35) | 32.61 (1.34) | 32.03 |
| **$TiO_2$** | 0.01 (0.01) | 0.02 (0.02) | 0.02 (0.01) | 0.02 (0.02) | | 0.03 (0.02) | 0.01 (0.01) | 0.02 (0.01) | 0.02 (0.01) | 0 (0) | 0.02 (0.02) | 0.00 |
| **$Al_2O_3$** | 0.01 (0.01) | 0.01 (0.01) | 0.01 (0.02) | 0.04 (0.09) | | 0.15 (0.11) | 1.77 (1.22) | 1.45 (0.78) | 0.52 (0.21) | 0.47 (0.26) | 14.34 (2.39) | 11.78 |
| **$Cr_2O_3$** | 0.01 (0.02) | 0.01 (0.02) | 0.06 (0.18) | 0.04 (0.03) | | 0.17 (0.11) | 0.61 (0.85) | 0.25 (0.19) | 0.13 (0.09) | 0.1 (0.1) | 1.07 (0.56) | 4.07 |
| **FeO (tot)** | 8.97 (0.34) | 7.93 (0.22) | 4.83 (0.30) | 5.05 (0.57) | 4.71 (0.19) | 0.76 (0.16) | 2.60 (0.26) | 1.58 (0.27) | 1.35 (0.22) | 1.2 (0.29) | 3.31 (0.46) | 2.79 |
| **MnO** | 0.15 (0.04) | 0.12 (0.06) | 0.45 (0.08) | 0.37 (0.06) | 1.02 (0.18) | 0.05 (0.03) | 0.04 (0.02) | 0.05 (0.05) | 0.04 (0.02) | 0.02 (0.02) | 0.06 (0.10) | 0.07 |
| **NiO** | 0.38 (0.03) | 0.49 (0.06) | 0.43 (0.07) | 0.39 (0.06) | 0.46 (0.08) | 0.03 (0.03) | 0.16 (0.02) | 0.18 (0.06) | 0.15 (0.04) | 0.19 (0.02) | 0.22 (0.05) | 0.24 |
| **ZnO** | 0.04 (0.04) | 0.03 (0.04) | 0.03 (0.04) | 0.03 (0.04) | | 0.01 (0.02) | | | | | 0.02 (0.04) | 0.00 |
| **MgO** | 50.23 (0.22) | 50.91 (0.22) | 52.8 (0.64) | 51.8 (1.57) | 51.80 (0.28) | 18.75 (1.15) | 37.97 (1.30) | 39.81 (0.59) | 39.6 (0.77) | 40.07 (0.61) | 34.34 (1.11) | 35.08 |
| **CaO** | 0.02 (0.01) | 0.01 (0.02) | 0.02 (0.02) | 0.25 (0.37) | | 24.87 (1.43) | 0.02 (0.02) | 0.05 (0.04) | 0.02 (0.02) | 0.02 (0.01) | 0.02 (0.01) | 0.05 |
| **$Na_2O$** | 0.09 (0.22) | 0.01 (0.01) | 0.02 (0.02) | 0.01 (0.01) | | 0.04 (0.02) | | | | | 0.02 (0.03) | 0.03 |
| **$K_2O$** | 0.01 (0.02) | 0.01 (0.01) | 0.01 (0.01) | 0.01 (0.01) | | 0.01 (0.01) | | | | | 0.02 (0.02) | 0.02 |
| **Total** | 100.82 (0.36) | 100.37 (0.70) | 100.06 (1.10) | 99.96 (1.63) | 100 | 99.83 (1.12) | 86.2 (0.63) | 86.93 (0.4) | 86.07 (0.82) | 85.25 (1.66) | 86.14 (0.65) | 86.17 |
| **Cations** | | | | | | | | | | | | |
| **$O^a$** | 4.0 | 4.0 | 4.0 | 4.0 | 4.0 | 6.0 | 6.8 | 6.8 | 6.8 | 6.8 | 28.0 | 28.0 |
| **Si** | 0.990 | 0.988 | 0.991 | 1.012 | 1.013 | 1.989 | 1.984 | 2.010 | 2.044 | 1.995 | 6.232 | 6.165 |
| **Ti** | 0.000 | 0.000 | 0.000 | 0.000 | | 0.001 | 0.000 | 0.001 | 0.001 | 0.000 | 0.004 | 0.000 |
| **Al** | 0.000 | 0.000 | 0.000 | 0.001 | | 0.006 | 0.091 | 0.079 | 0.028 | 0.026 | 3.229 | 2.672 |
| **Cr** | 0.000 | 0.000 | 0.001 | 0.001 | | 0.005 | 0.026 | 0.009 | 0.005 | 0.004 | 0.162 | 0.619 |
| **$Fe^{2+}$ (tot)** | 0.181 | 0.161 | 0.097 | 0.102 | 0.095 | 0.023 | 0.104 | 0.061 | 0.052 | 0.046 | 0.529 | 0.404 |
| **Mn** | 0.003 | 0.003 | 0.009 | 0.008 | 0.021 | 0.002 | 0.001 | 0.002 | 0.002 | 0.001 | 0.010 | 0.012 |
| **Ni** | 0.007 | 0.010 | 0.008 | 0.008 | 0.009 | 0.001 | 0.006 | 0.007 | 0.006 | 0.007 | 0.034 | 0.037 |
| **Zn** | 0.001 | 0.001 | 0.000 | 0.001 | | 0.000 | | | | | 0.003 | 0.000 |
| **Mg** | 1.812 | 1.837 | 1.891 | 1.861 | 1.862 | 1.012 | 2.486 | 2.747 | 2.733 | 2.765 | 9.782 | 10.06 |
| **Ca** | 0.000 | 0.000 | 0.001 | 0.006 | | 0.964 | 0.001 | 0.002 | 0.001 | 0.001 | 0.003 | 0.011 |
| **Na** | 0.004 | 0.000 | 0.001 | 0.000 | | 0.003 | | | | | 0.007 | 0.012 |
| **K** | 0.000 | 0.000 | 0.000 | 0.000 | | 0.000 | | | | | 0.005 | 0.005 |
| **Mg#** | 0.91 | 0.92 | 0.95 | 0.95 | 0.95 | 0.98 | 0.94 | 0.96 | 0.97 | 0.97 | 0.95 | 0.96 |

Mg# = Mg/(Mg+ΣFe)

The preserved spinel core in sample V18-3a has Cr# [Cr/(Cr+Al)] of 0.79 ±0.001 (Table 4.2). The mantle overgrowing the primary spinel has a ferritchromite mantle of Cr-magnetite with a Cr# of 0.91 and higher MnO relative to the core. The magnetite rims with no $Al_2O_3$, but high $Cr_2O_3$ (1.87 ±1.16 wt.%). The composition of the disseminated and vein magnetite differs from magnetite found in the spinel sites, with very little $Cr_2O_3$ (Table 4.2).

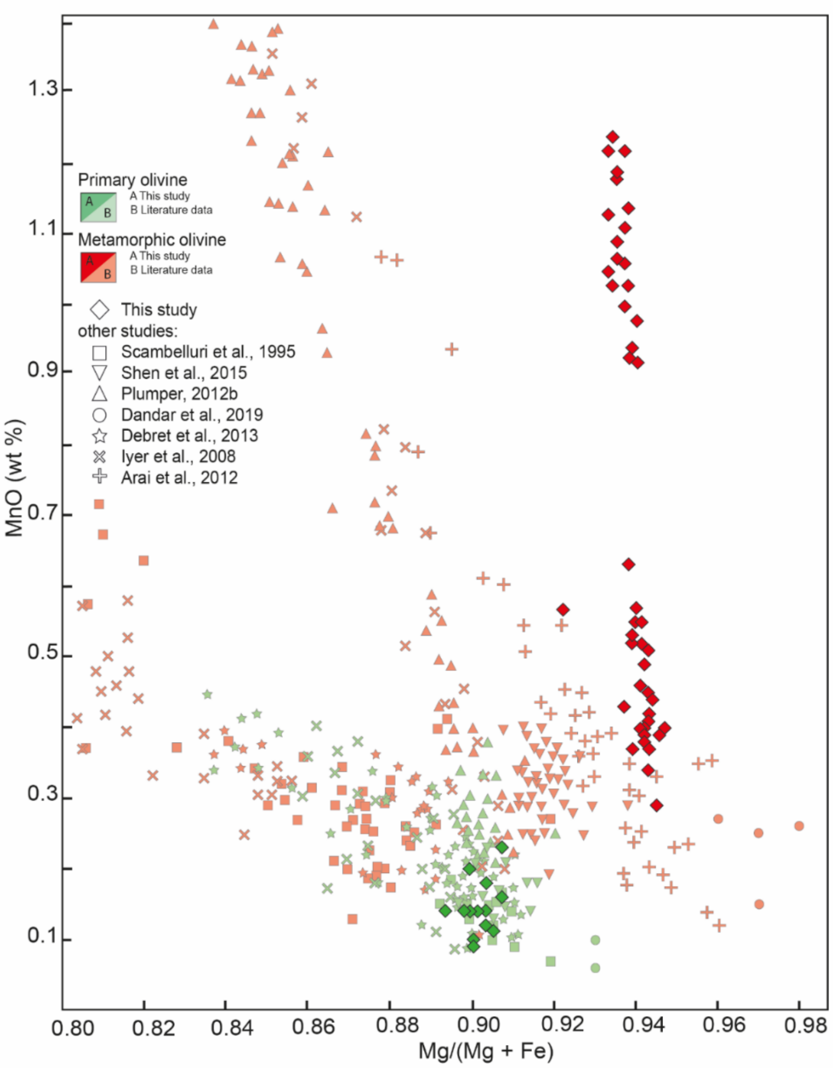

***Fig. 4.6****: Mg# versus MnO (wt%) diagram showing the compositional variation of primary and metamorphic olivine. The Mn-richest cluster of metamorphic olivine belongs to sample V18-B3 (fully serpentinized peridotite). Background data from Arai et al., (2012); Dandar et al., (2019); Debret et al., (2013); Iyer et al., (2008); Nozaka, (2018); Plümper et al., (2012b); Scambelluri et al., (1995); Shen et al., (2015).*

**Table 4.2:** MicroProbe analysis. Absence of SD value when n>1 indicates SD<0.01

| **Minerals** | **Spinel (nucleus)** | **Spinel (intermediate)** | **Magnetite (rim)** | **Magnetite (mesh and veins)** | | **Brucite** |
|---|---|---|---|---|---|---|
| **Sample** | **V18-3a** | **V18-3a** | **V18-3a** | **V18-3a** | **V18-2b** | **V18-2b** |
| **(n)** | 7 | 7 | 7 | 1 | 4 | 10 |
| **$SiO_2$** | 0.02 (0.02) | 0.03 (0.01) | 0.06 (0.07) | 0.07 | 0.05 (0.03) | 0.78 (2.20) |
| **$TiO_2$** | 0.09 (0.02) | 0.23 (0.05) | 0.03 (0.02) | 0.04 | 0.01 (0.01) | 0.01 |
| **$Al_2O_3$** | 12.63 (0.94) | 3.87 (1.34) | 0.00 | 0.03 | 0.01 (0.01) | 0.01 (0.01) |
| **$Cr_2O_3$** | 47.51 (0.57) | 41.6 (1.29) | 1.87 (1.16) | 0.01 | 0.02 (0.02) | 0.04 (0.05) |
| **FeO (tot)** | 34.12 (1.1) | 48.32 (2.02) | 91.45 (0.75) | 92.44 | 92.57 (0.28) | 2.91 (0.18) |
| **MnO** | 0.34 (0.04) | 0.95 (0.36) | 0.16 (0.03) | 0.12 | 0.19 (0.05) | 0.22 (0.04) |
| **NiO** | 0.09 (0.02) | 0.27 (0.05) | 1.05 (0.1) | 1.11 | 0.82 (0.09) | 0.38 (0.09) |
| **ZnO** | 0.49 (0.08) | 0.3 (0.1) | 0.04 (0.06) | 0.10 | 0.04 (0.08) | 0.01 (0.02) |
| **MgO** | 5.99 (0.32) | 3.37 (0.22) | 0.71 (0.09) | 0.62 | 0.82 (0.19) | 75.88 (3.93) |
| **CaO** | 0.01 (0.01) | 0.00 | 0 (0.01) | 0.00 | 0.00 | 0.02 (0.03) |
| **$Na_2O$** | 0.03 (0.04) | 0.02 (0.02) | 0.03 (0.03) | 0.03 | 0.02 (0.04) | 0.02 (0.02) |
| **$K_2O$** | 0.00 | 0.01 (0.01) | 0 (0.01) | 0.01 | 0.00 | 0.01 (0.01) |
| **Total** | 101.4 (0.56) | 99.03 (0.6) | 95.46 (0.5) | 94.63 | 94.56 (0.45) | 80.33 (2.70) |
| **Cations** | | | | | | |
| **O*** | 4.0 | 4.0 | 4.0 | 4.0 | 4.0 | 2 |
| **Si** | 0.00 | 0.00 | 0.00 | 0.00 | 0.00 | 0.01 |
| **Ti** | 0.00 | 0.01 | 0.00 | 0.00 | 0.00 | 0.00 |
| **Al** | 0.49 | 0.16 | 0.00 | 0.00 | 0.00 | 0.00 |
| **Cr** | 1.24 | 1.17 | 0.06 | 0.00 | 0.00 | 0.00 |
| **$Fe^{3+}$** | 0.26 | 0.66 | 1.94 | 1.99 | 2.00 | 0.00 |
| **$Fe^{2+}$** | 0.68 | 0.78 | 0.92 | 0.92 | 0.92 | 0.02 |
| **Mn** | 0.01 | 0.03 | 0.01 | 0.00 | 0.01 | 0.00 |
| **Ni** | 0.00 | 0.01 | 0.03 | 0.03 | 0.02 | 0.00 |
| **Zn** | 0.01 | 0.01 | 0.00 | 0.00 | 0.00 | 0.00 |
| **Mg** | 0.29 | 0.18 | 0.04 | 0.03 | 0.05 | 0.97 |
| **Ca** | 0.00 | 0.00 | 0.00 | 0.00 | 0.00 | 0.00 |
| **Na** | 0.00 | 0.00 | 0.00 | 0.00 | 0.00 | 0.00 |
| **K** | 0.00 | 0.00 | 0.00 | 0.00 | 0.00 | 0.00 |
| **Cr#** | 0.79(0.01) | 0.92(0.2) | 1.00 | | | |

Cr# = Cr/(Al+Cr)

*As per normalization

Diopside in sample V18-3a has a Mg number [Mg# =Mg/(Mg+Fe)] of 0.98. Chlorite in V18-2b and V18-3a has an Mg# [Mg# =Mg/(Mg+ΣFe)] of 0.95, and $Cr_2O_3$ up to 4.07 wt.% (Table 4.1).

Brucite has up to 3 wt.% FeO (as total Fe), Mg# [Mg# =Mg/(Mg+Fe)] of 0.97 (Table 4.2). Alloys and sulfides are Ni rich, with various amounts of S, Fe and trace amounts of Pb, Cu, et Co (Table 4.3). Alloys mainly consist of Cu-bearing FeNi alloy (taenite) (Table 4.3). Sulphides include Ni, Cu, and Fe sulphides. Only heazlewoodite (NiS) was analysed whereas for other sulphides proper analyses could not be obtained owing to the small grain sizes.

**Table 4.3:** MicroProbe analysis of alloys

| **Sample** | **V18-2b** | | | | | | **V18-3a** | | |
|---|---|---|---|---|---|---|---|---|---|
| **Alloy** | **NiFeCu** | **NiS** | **NiS** | **NiS** | **NiFeCu** | **NiFeCu** | **NiS** | **NiS** | **NiS** |
| **S** | | 24.06 | 24.25 | 24.12 | | | 24.59 | 24.52 | 24.50 |
| **Fe** | 12.21 | 0.90 | 0.51 | 1.35 | 13.35 | 20.07 | 0.84 | | 0.95 |
| **Pb** | | | | 0.13 | | | 0.18 | | |
| **Ni** | 86.23 | 72.68 | 72.71 | 73.55 | 86.05 | 80.03 | 72.97 | 72.85 | 73.30 |
| **Cu** | 1.94 | | | | 1.75 | 1.49 | | | |
| **Total** | 100.45 | 97.9 | 97.59 | 99.18 | 101.28 | 101.71 | 98.70 | 97.72 | 99.04 |

### 4.4.3 Fluid inclusion analysis

Primary olivine in all samples is rich in fluid inclusions forming secondary trails (Fig. 4.7). The fluid inclusion trails are confined within individual crystals and show two alternative structural relationships relative to the antigorite veins, being either cut by them (Fig. 4.7A) or propagating from them (Fig. 4.7B-C). These patterns suggest a secondary fluid inclusions entrapment during the antigorite serpentinization event, which appears to be the dominant hydration event in the rock.

Fluid inclusions of 0.5 to 5 µm in size were analyzed and exhibit rounded to elongated shapes (Fig. 4.7D-E). Optical microscope observations at room conditions suggest that the fluid inclusions are either single-phase and gaseous, or bi-phase with solid and gas. MicroRaman spectra of fluid inclusions are presented in Fig. 4.8. The spectra show the presence of marked $CH_4$ bands (2912 $cm^{-1}$), as well as $N_2$ (2327 $cm^{-1}$), $NH_3$ (3324 $cm^{-1}$), S-H/$H_2S$ (2575 $cm^{-1}$). Free $H_2O$ in the fluid inclusions was not detected by MicroRaman. However, the presence of tiny amounts of free $H_2O$ in the fluid inclusions —undetectable by MicroRaman at room conditions— cannot be excluded (Berkesi et al., 2009; Lamadrid et al., 2017).

The molar fraction of gas in the gas mixture was estimated using the Raman scattering cross-section and the instrumental efficiency of each species. Using equation presented in Frezzotti et al., 2012, we obtain the following molar proportion: $CH_4$ = 92±6%, $N_2$ = 6±5%, $H_2S$ = 1±1% and $NH_3$ = 1±2% for the mean composition of twenty inclusions in olivine from all samples (supplementary material 4.1). Composition within the same inclusion trail shows molar fractionation variation smaller than 1% but different trails within the same crystal can exhibit up to 10% of the molar fraction of $CH_4$ and could reflect fluid heterogeneity. Alternatively, this effect can be the result of different crystal orientation during data acquisition (Caumon et al., 2019). No clear pattern was observed linked to the relationship between inclusion trails and antigorite veinlets.

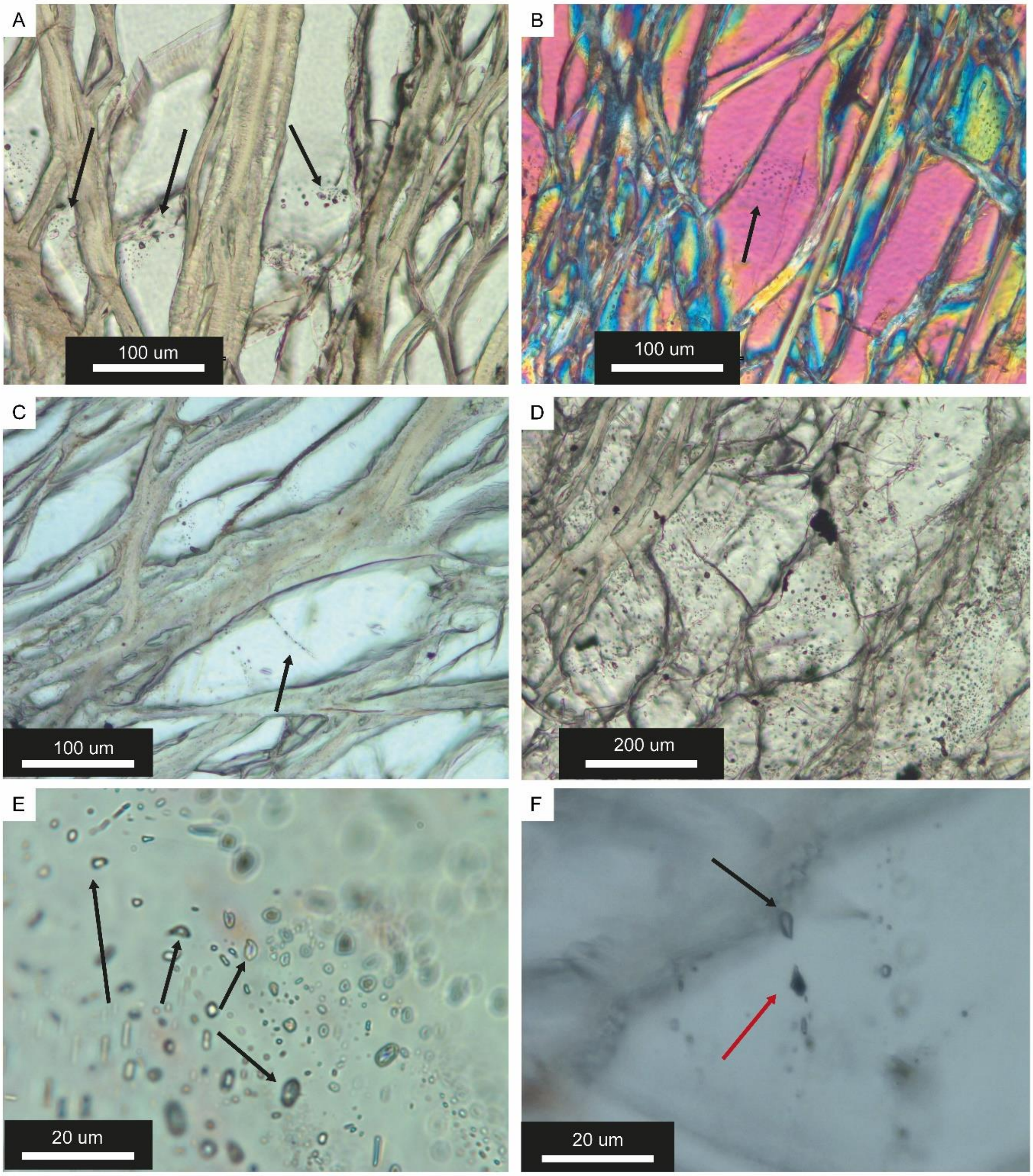

***Fig. 4.7**: Photomicrographs of methane-rich fluid inclusion trails in olivine from sample V18-2a. Black arrows indicate fluid inclusion trails. A: Inclusion trail being cut by lizardite* veinlets. B: Inclusion trail limited by lizardite* veins. C: Secondary trail of fluid inclusions propagating from a lizardite* veinlet. D: Photomicrograph showing a fluid-inclusion-rich olivine aggregate. E: Close up of the methane-rich fluid inclusions. F: Close up of a graphite bearing fluid inclusion (red arrow), as confirmed by Raman spectroscopy in (Fig. 4.8B). *antigorite in the original text*

Solid phases were identified in large (2-5 µm) fluid inclusions. MicroRaman analysis revealed the presence of lizardite and brucite but no magnetite was detected. Some inclusions contain graphite as a solid phase in the inclusion in addition (Fig. 4.7F and Fig. 4.8B). The only sporadic presence of graphite in the fluid inclusions, and in particular in inclusions resulting from necking processes, suggest that this mineral precipitated as a result of local respeciation of the fluid inclusions, such as post entrapment host-inclusion reaction with the inclusion wall and resulting respeciation of the fluid inclusion composition (Cesare, 1995). This feature is also suggested by the presence of hydrous phases in the inclusions, which indicates interaction of the inclusion fluid with the host olivine. However, the presence of step-daughter minerals in the inclusion is not systematic, suggesting that the initial fluid was already rich in $CH_4$ (-$N_2$-$NH_3$-$H_2S$) at the time of trapping, and that the reduced fluid species did not form only inside the fluid inclusions.

### 4.4.4 Rodingites

Rodingites have been identified inside the BMC and consist of garnet, diopside, epidote, carbonate ± graphite. While not being the focus of this study, the carbonate in the rodingites has abundant fluid inclusions. Fluid inclusions exhibit negative crystal shape and are single-phase gaseous at room conditions. The composition of the carbonate-hosted fluid inclusions, as revealed by Raman spectroscopy, is essentially $CH_4$ and $N_2$. The analyses of the collected Raman spectra in carbonates (see section 5.4.3) yield molar fractions of $N_2 = 67\pm4\%$, $CH_4 = 33\pm4\%$ on four different inclusions.

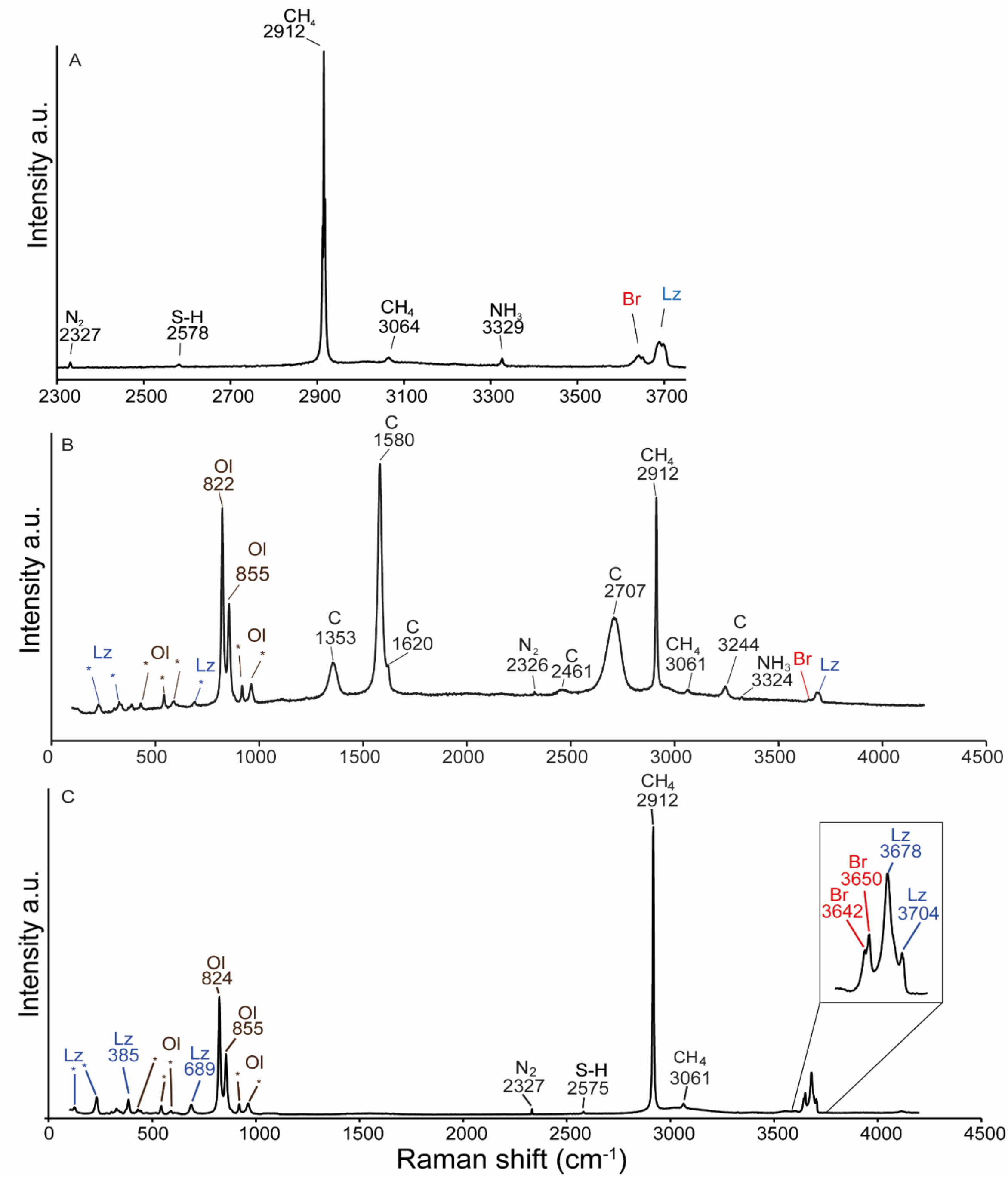

***Fig. 4.8**: Raman spectra of fluid inclusions and step-daughter solid phases. A: Inclusion showing a marked $CH_4$ band and minor peaks of $N_2$ $NH_3$ and S-H bond. Lizardite and brucite O-H bands are also observed. B: Graphite in fluid inclusions (see Fig. 4.6D). C: Methane-rich fluid inclusion with a close up of O-H bonds of lizardite and brucite.*

### 4.4.5 Thermodynamic modeling

Thermodynamic calculations were performed in order to constrain the mineralogical, fluid and redox evolution of the HP serpentinization. The calculations were done at temperatures consistent with the peak metamorphic conditions estimated for the BMC, i.e., 400 °C to 500 °C and 1 GPa (Honsberger, 2015; Laird et al., 1993), and for different F/R ratios (from 0.5 to 100). The selected partially serpentinized samples are embedded in strongly serpentinized rocks and, in turn, are included in metasedimentary rocks. For this reason, either ultramafic or metasedimentary were considered to calculate the EQ3 fluid compositions and as possible fluid sources responsible for the metamorphic serpentinization of the BMC rocks. The interaction of EQ3 fluids equilibrated with metasedimentary sources or Si-rich ultramafic sources (e.g. steatite) with the EQ6 dunitic assemblage (cf. Section 4.2), however, resulted in mineral assemblages inconsistent with the natural samples (Supplementary material 4.2). For this reason, in the following are presented in detail only the results obtained for EQ3 fluid compositions equilibrated with an ultramafic assemblage consisting of antigorite + magnetite + brucite + chlorite + olivine. The $fO_2$ of the infiltrating fluid was set at the quartz-fayalite-magnetite (QFM) buffer. Figure 4.10 shows the mineralogical evolution as a function of reaction progress at 450 °C and 1GPa for a F/R ratio of 1. The model reaction proceeds with progressive transformation of, from the first to the last reacting mineral, mantle spinel, clinopyroxene, orthopyroxene, and olivine. Magnetite starts to form during the early stages of the reaction along with chlorite in response to spinel consumption. Reaction of mantle pyroxenes marks the precipitation of metamorphic clinopyroxene (diopside 93%, hedenbergite 3.35% and clino-enstatite 3.65%), metamorphic olivine, antigorite, and additional magnetite. The late formation of antigorite marks the partial consumption of metamorphic olivine and a decrease in its Mg#, from Mg# 0.90 to Mg# 0.83. These patterns reflect the microstructural features observed in the natural samples. For example, spinel appears intensely replaced by chlorite in rather unserpentinized portions of the rock (Fig. 4.9A). Similarly, mantle olivine adjacent to fully replaced mantle pyroxenes is commonly little affected by the serpentinization. Both mantle and metamorphic olivine in the natural samples appear texturally replaced by antigorite, as also suggested by the modeling while approaching reaction completion. With the chosen bulk composition and used thermodynamic data set, the formation of antigorite is limited to $T < 470$ °C. The obtained antigorite stability field may be dependent on the absence of iron in the antigorite thermodynamic model considered in the database. The evolution of dissolved elements in the fluid (Fig. 4.9B) indicates that the total Mg content decreases during the reaction, while Si and Ca increase. The $fO_2$ decreases progressively during the reaction progress, with a steep decrease during the formation of antigorite down to $\Delta$Log QFM = -1.2 (Fig. 4.9D). Methane, initially about 1 order of magnitude less concentrated than $CO_2$ in the reacting fluid, becomes a dominant species at reaction completion (about 1 order of magnitude more concentrated than $CO_2$). Nevertheless, variations of parameters such as F/R ratio, mineralogy, or temperature, were found to affect the proportion of $CH_4$ and $CO_2$. As an example, increasing the modal proportion of either orthopyroxene or clinopyroxene in the initial rock or decreasing the F/R ratio appears to favor a higher proportion of $CH_4$ in the fluid in respect to $CO_2$. The model predicts high relative concentration of $H_2$ in the fluids, however $H_2$ was not detected in natural samples by micro-Raman spectroscopy. This may be due to leakage of $H_2$ from the inclusions or internal respeciation. Sulphur and nitrogen speciation were also assessed, with $HS^-$ and $H_2S$ and $NH_3$ being the dominant Sulphur species relative to $HSO_4^-$ and $N_2$ and $NH_4^+$, respectively (Fig. 4.9C).

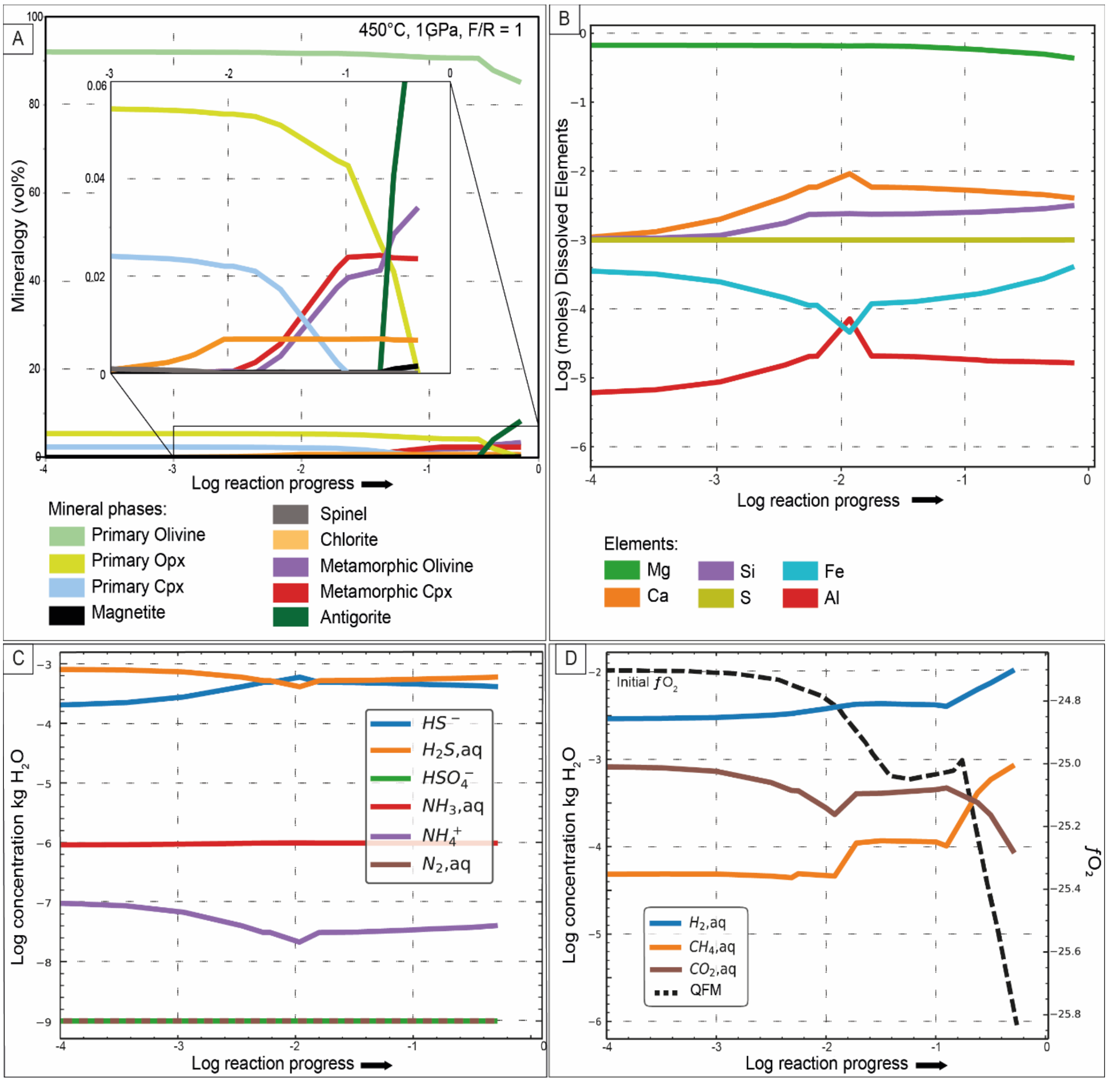

***Fig. 4.9****: Thermodynamic modeling of HP serpentinization of dunite and related mineralogical and fluid evolution. A: Mineralogical evolution during serpentinization at 450 °C and 1 GPa. B: Evolution of total dissolved elements in the fluid as a function of the reaction progress presented in A. C: Evolution of the nitrogen and sulphur fluid speciation as a function of the reaction progress presented in A. D: Evolution of the $fO_2$ and $H_2$, $CH_4$, and $CO_2$ concentrations in the fluid as a function of the reaction progress presented in A.*

## 4.5 Discussion

### 4.5.1 Patterns and timing of serpentinization

The timing of serpentinization of slab-derived, exhumed HP serpentinized rocks can span (sub)seafloor or trench conditions prior to subduction, prograde hydration during subduction, or retrograde hydration during exhumation. The BMC complex has been interpreted as a fragment of subducted Iapetus lithosphere, and therefore may have recorded different stages of serpentinization. Although the possibility of at least some (sub)seafloor serpentinization prior to the Taconic subduction cannot be excluded, our data cannot provide any proof of such a pre-subduction event and, instead, suggest a main hydration event at HP-HT conditions in the subduction zone.

Besides late chrysotile veinlets, antigorite is the only serpentine mineral identified in the BMC rocks. Although formation of antigorite may occur in a wide range of P-T conditions also as a function of chemical parameters such as the silica activity (Rouméjon et al., 2019), serpentinites dominated by antigorite are generally referred to the HT temperature part of the serpentine stability field, generally above ∼300-400 °C (e.g., Evans, 2004; Schwartz et al., 2013). In most subduction zone settings, these conditions also correspond to relatively HP conditions above 1 GPa. However, the presence of antigorite does not necessarily imply the serpentinization event to have happened at HP-HT conditions because it could also have formed as a result of the prograde transformation of lizardite or chrysotile following the reaction:

17 Lizardite/Chrysotile = Antigorite + 3 Brucite (4.1)

Nevertheless, several lines of evidence indicate that the BMC rocks recorded a stage of HP-HT serpentinization. As a first general consideration, the presence of fresh mantle assemblages throughout the complex (Chidester et al., 1978; Labotka and Albee, 1979, this study) represents a suitable condition to promote HP-HT serpentinization in the subduction zone, if aqueous fluids are available. Such a process has already been proposed in other HP ultramafic massifs preserving fresh mantle assemblages (e.g., Dandar et al., 2019; Früh-Green et al., 2004; Nozaka, 2018; Scambelluri and Tonarini, 2012; Vitale Brovarone et al., 2020, 2017). The BMC rocks provide evidence for such a HP hydration event. Figure 4.10

summarizes the proposed fluid-rock evolution of the BMC rocks as inferred from the studied samples. The first indication of serpentinization (stage I in Fig. 4.10) is suggested by the growth of elongated metamorphic olivine on the primary clinopyroxene sites (Fig. 4.5G), which suggests the former presence of serpentine blades overgrowing the primary clinopyroxene. The selective growth of serpentine at the expense of clinopyroxene rather than primary olivine places this hypothetical event at HT conditions (Klein et al., 2013) and possibly in the antigorite stability field (Fig. 4.11). Metamorphic olivine is most commonly interpreted to form in response to serpentine dehydration during prograde metamorphism (Plümper et al., 2017a; Scambelluri et al., 1991). Figure 4.11 provides a compilation of generic antigorite dehydration reactions leading to the formation of metamorphic olivine. Although these reactions may be shifted to higher or lower temperatures depending on compositional features (e.g., Padrón-Navarta et al., 2013), the peak metamorphic conditions proposed for the BMC (0.9-1.3 GPa and 520 °C) are consistent with the first olivine-forming reaction involving antigorite + brucite as reactants. Moreover, several studies have shown that olivine can form at T conditions lower than the reactions shown in Figure 4.11 as a result of local bulk compositional features (Plümper et al., 2017a). Alternatively, metamorphic olivine after orthopyroxene may also have formed in response to hydration rather than dehydration reactions, as already proposed for serpentinized mantle wedge rocks (Dandar et al., 2019) following the reaction:

Orthopyroxene + 0.46 Water + 0.35 $Mg^{2+}$=

0.59 M-olivine +0.06 Antigorite + 0.29 Silica + 0.7 $H^+$ (4.2)

The thermodynamic modeling results support this reaction, as suggested by the decrease of total dissolved Mg and the increase of Si in the fluid during the early growth of metamorphic olivine (Fig. 4.9A and 4.10B). In either case (hydration or dehydration), the amount of serpentinization predating the formation of metamorphic olivine must have been very low and, if any, related to a HT event.

The second, more robustly constrained stage of transformation (stage II in Fig. 4.10) is characterized by the formation of metamorphic olivine after primary orthopyroxene, and as rim around primary clinopyroxene (now recrystallized into diopside). This reaction was observed in rocks containing rather undisturbed primary olivine, which again point to HT serpentinization conditions (Klein et al., 2013). The partial preservation of clinopyroxene exsolution lamellae inside metamorphic olivine pseudomorphic on orthopyroxene may suggest nearly isovolumetric replacement during this event (Plümper et al., 2012b; Viti et al., 2005). The thermodynamic modeling results suggest that, at 450 °C and 1 GPa, a transient antigorite generation may have formed together with metamorphic olivine early in the fluid-rock interaction, along with spinel breakdown. The Al-Cr-rich antigorite cores (Atg1) observed in the studied samples may testify to this transient antigorite formation. Measured distribution coefficients between antigorite and olivine also suggest different stages of antigorite formation (Supplementary materials 4.3). The third stage (stage III in Fig. 4.10) is characterized by the growth of a matrix antigorite (Atg2) at the expense of both primary and metamorphic olivine. This event may mark either retrograde hydration along the exhumation path of the BMC, or the progression of the fluid-rock interaction. As indicated by the thermodynamic modeling results, a second antigorite generation is expected to form at 450 °C and 1 GPa after the precipitation of metamorphic olivine (Fig. 4.9A).

The fourth stage of serpentinization (IV in Fig. 4.10) is characterized by the complete serpentinization of primary olivine and partial to full serpentinization of metamorphic olivine.

The partial preservation of metamorphic olivine after orthopyroxene in samples free of any primary olivine relict indicates that the largest event of serpentinization of the BMC rocks took place after the formation of metamorphic olivine. The presence of both antigorite and chrysotile + brucite at the expense of metamorphic olivine after orthopyroxene suggests that this event protracted during the cooling of the BMC metamorphic path to temperatures lower than 400 °C (Fig. 4.11).

In summary, based on the collected petrographic and thermodynamic data, the dominant serpentinization event observed in the BMC complex is interpreted to have taken place in the Taconic subduction zone.

### 4.5.2 Timing of fluid inclusion formation and origin of $CH_4$

#### 4.5.2.1 Timing of fluid inclusion entrapment

Fluid inclusions in the BMC ultramafic and related metasomatic rocks contain reduced fluid species such as $CH_4$, $NH_3$, and $H_2S$. The timing of fluid inclusion formation, as well as the origin of their reduced speciation, is discussed in this section.

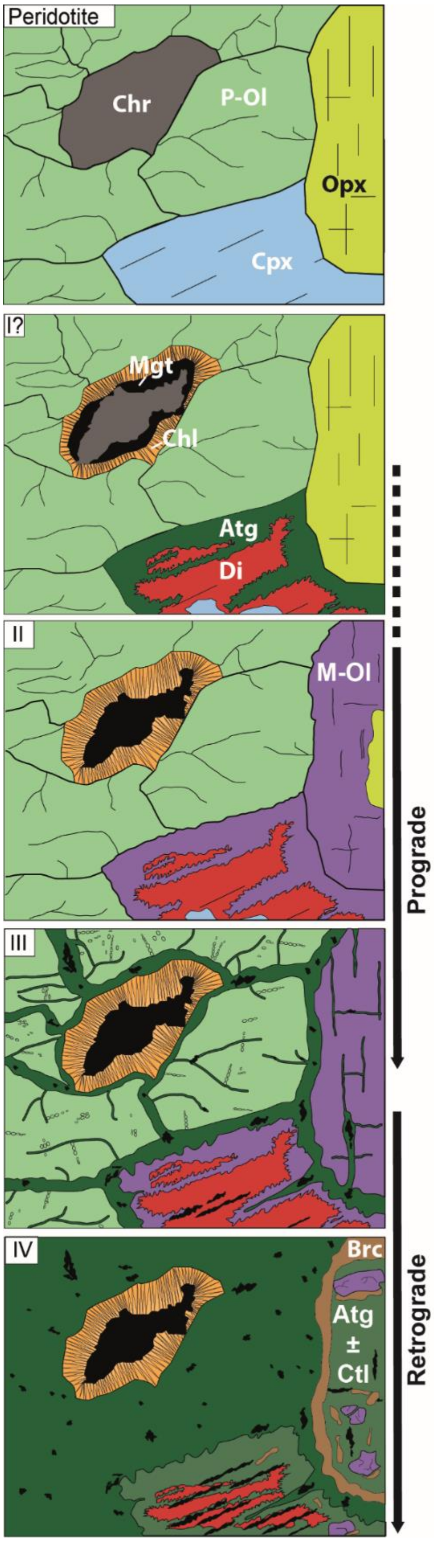

***Fig. 4.10**: Reconstruction of the mineralogical evolution of the BMC partially serpentinized peridotite. An early step of serpentinization is proposed based on the needle-like growth of metamorphic olivine on primary clinopyroxene, suggesting the presence of serpentine prior to the formation of metamorphic olivine. The successive growth of antigorite at the expense of both primary and metamorphic olivine constrains the main serpentinization event to metamorphic conditions. Finally, a late serpentinization event is proposed based on the growth of brucite + antigorite + chrysotile on relict metamorphic. Chr : chromite, P-Ol : primary olivine, M-Ol : metamorphic olivine, Opx : primary orthopyroxene, Cpx : primary clinopyroxene, Chl : chlorite, Mgt : magnetite, Atg : antigorite, Di : diopside, Brc : brucite, Ctl : chrysotile.*

Reduced fluids have been found to form in ultramafic systems in a wide range of geologic conditions spanning mid-ocean ridges, obducted ophiolitic massifs, orogenic peridotite bodies, in subduction, and in the upper mantle (Andréani et al., 2007; Etiope et al., 2011; Schrenk et al., 2013; Vitale Brovarone et al., 2020). In the BMC rocks, the fluid inclusions may have formed in three different stages of the evolution of the massif and corresponding to three different geodynamic settings: (i) in the mantle prior to the formation of the Iapetus Ocean, (ii) during the (sub)seafloor evolution prior to subduction, and (iii) in the subduction zone.

A primary mantle origin can be ruled out because the observed fluid inclusions occur as secondary trails propagating from the antigorite veinlets crossing olivine crystal. A (sub)seafloor origin would match the identification of $CH_4$-rich fluid inclusions in oceanic peridotite (Cannat et al., 2010; Holm and Charlou, 2001). However, in this case, the fluid inclusions would have been preserved during prograde metamorphism to at least 520 °C and 1 GPa, which is unlikely (Touret, 2001). Moreover, the BMC fluid inclusions are rich in N species ($NH_3$, $N_2$), which seems to be an uncommon feature in fluid inclusions from oceanic peridotites (Grozeva et al., 2020; Klein et al., 2019). Instead, N-rich, $NH_3$-bearing fluid inclusions have been recently documented in $CH_4$-rich fluid inclusions in HP serpentinized peridotites from the Alpine belt and proposed to represent a distinctive feature of subduction zone serpentinizing fluids relative to mantle or (sub)seafloor fluids, especially in the presence of metasediment-derived fluids (Vitale Brovarone et al., 2020). Considering the microstructural and petrologic features discussed in Section 5.1, and the abundance of N species, a metamorphic origin in the Taconic subduction is proposed for the studied fluid inclusions.

The formation of lizardite and brucite as step-daughter minerals inside the fluid inclusions can be interpreted (1) as a prograde, pre-antigorite inclusion-host interactions, (2) as a retrograde reequilibration of antigorite during cooling of the BMC below ~400 °C with excess brucite (Reaction 4.1), or (3) as a retrograde host-inclusion interaction below ~400 °C (Fig. 4.11). Excluding lizardite (meta)stability due to local equilibrium/kinetic features or faster antigorite-lizardite conversion in the inclusions relative to the host rock, we interpret the formation of step-daughter lizardite and brucite as a retrograde host-inclusion interaction. Similar interpretations have been proposed for analogous inclusions from Alpine belt (Vitale Brovarone et al., 2020).

#### 4.5.2.2 Origin of the reducing potential and fluid sources

Another important question is the origin of the identified reduced fluids species. In particular, several studies over the last decades have investigated the biotic or abiotic origin of geological

$CH_4$ and associated reduced fluid species (Etiope et al., 2011; Etiope and Sherwood Lollar, 2013; McCollom, 2016; Ménez et al., 2018). Ultramafic systems are generally favorable environments for the genesis of abiotic $CH_4$ (Section 4.5.2.1), but other interpretations are also possible.

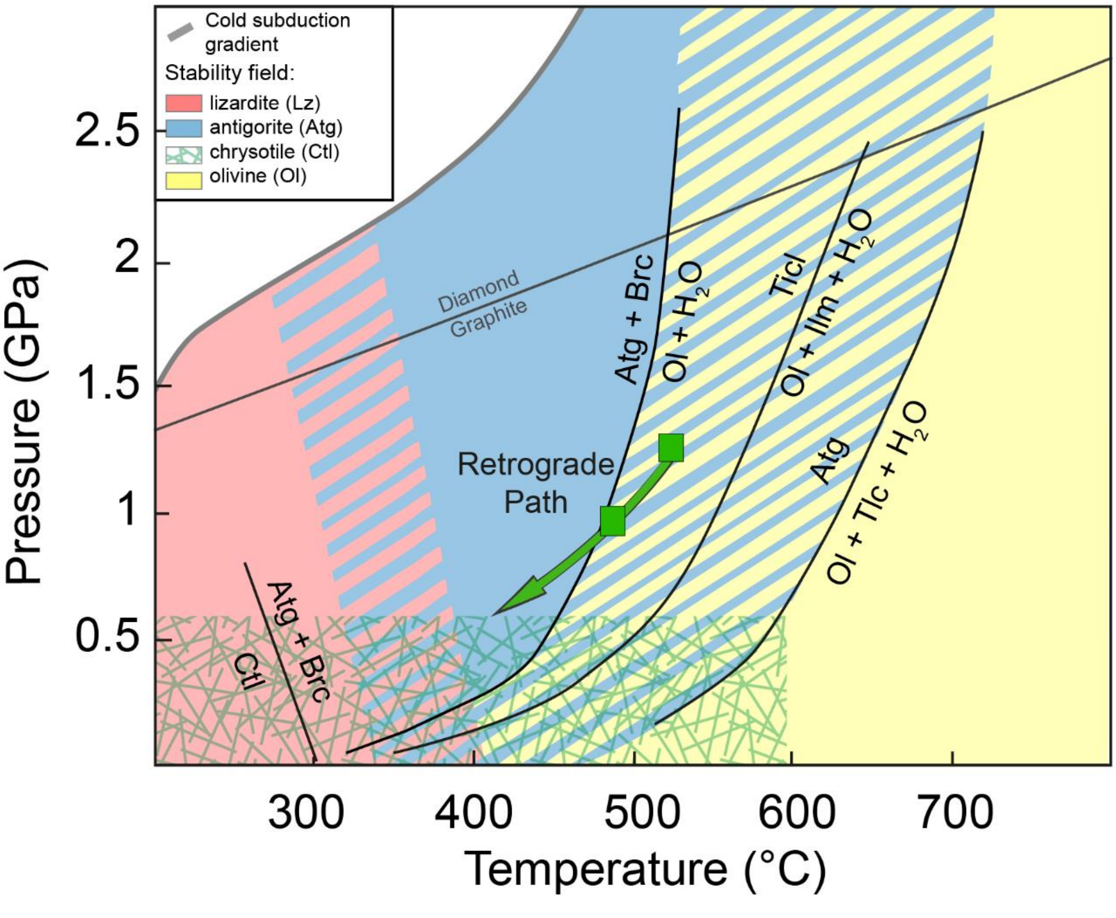

***Fig. 4.11***: *Simplified stability field of serpentine type minerals and olivine, modified from Guillot et al., (2015) (see references therein for details on the main reactions). The retrograde P-T path of BMC from Honsberger, (2015) is also shown for reference. Atg : antigorite, Brc : brucite; Ctl : chrysotile; Ilm : ilmenite; Ol : olivine; Tlc : talc; Ticl : titanian clinohumite. Diamond graphite transition from Day, (2012).*

For example, the abundance of metasedimentary rocks in the study area may have promoted the formation of thermogenic gases during their prograde evolution. This hypothesis would be also consistent with the production of $NH_3$ through degassing of organic matter in metasedimentary rocks (Bebout and Fogel, 1992; Li et al., 2009). Biotic processes, including thermogenic gas formation, typically show very light $\delta^{13}C_{CH4}$ signatures (Etiope and Sherwood Lollar, 2013), whereas abiotic processes generally result in much heavier $\delta^{13}C_{CH4}$ (~-50 to 0‰) (Etiope and Sherwood Lollar, 2013). In order to test this hypothesis, we performed reconnaissance $\delta^{13}C$ analysis of $CH_4$ in the fluid inclusions (see section 5). The analyses yielded $\delta^{13}C$ in the range of -14‰ (±2‰) for inclusions in olivine, and -13‰ (±1‰) for carbonate-hosted methane-rich inclusions from the rodingites. Even though these results must be considered as preliminary test data, they seem to exclude the possibility of a pure thermogenic source.

Following the hypothesis of an abiotic origin, two possible mechanisms for the formation of $CH_4$ can be considered with either external or internal sources, respectively. External sources correspond to the infiltration of $CH_4$ and other reduced species formed abiotically in other geological reservoirs. A deep mantle origin for the reduced fluids detected in the BMC fluid inclusions appears unlikely if the syn-inclusion, water-rich nature of the serpentinizing fluid is considered. The metasedimentary formations adjacent to the BMC contain carbonate, graphitic carbon, sulphides, and phyllosilicates as potential sources of the C-N-S-H fluid identified in the fluid inclusions. Previous studies along the Appalachian belt have reported evidence of carbon mobilization from these metasedimentary formations or their along-strike equivalents. For example, Zhang et al., 2018 documented metamorphic loss of isotopically light carbon from the Wepawaug schists, Connecticut. The possibility for these carbonate-bearing formations to generate strongly reduced fluids abiotically is not obvious —for reference, water-maximum conditions in graphite-saturated fluids contain roughly equal proportions of $CH_4$ and $CO_2$ (Connolly, 1995; Holloway, 1984) —. Nevertheless, evidence for the circulation of $CH_4$-rich fluids in equivalent formations in East Central Vermont and New Hampshire has been reported (Evans et al., 2002; Rumble and Hoering, 1986). Nevertheless, most petrological studies focusing on New England metasediment-derived fluids point to more oxidized, $CO_2$-dominated aqueous fluids (Ferry, 2007; Penniston-Dorland and Ferry, 2006). Alternative external sources of reduced fluids would require unidentified processes, including mixing of different carbon reservoirs, or water-rock interactions equivalent to those that took place in the BMC.

A reducing potential internal to the BMC, and in particular the hydroxylation of fresh mantle peridotites during the Taconic subduction, appears the most likely interpretation for the genesis of the identified reduced fluid species. The presence of Fe-Ni alloys in the BMC partially serpentinized peridotites indicates that the rock recorded reducing conditions, as already observed in several oceanic and ophiolitic, and some subduction zone serpentinites (Evans et al., 2017; Frost, 1985; Klein and Bach, 2009; Vitale Brovarone et al., 2020). Alternatively, reducing fluids may also be produced by serpentinite dehydration (Evans and Frost, 2021; Piccoli et al., 2019). However, the small amount of metamorphic olivine observed in the BMC rocks seems to contradict this hypothesis. High-pressure syn-serpentinization reducing conditions are also suggested by the thermodynamic modeling results presented in this study, which indicates $fO_2$ values as low as –3.2 ΔQFM at 400 °C and 1 GPa to -1.2 ΔQFM at 450 °C and 1 GPa, and the formation of significant amounts of $H_2$ in the fluid (Fig. 4.9D)(see also Labotka and Albee, 1979). The interaction of this $H_2$ with dissolved carbon, nitrogen, and Sulphur species present in the serpentinizing fluid, could have favored the formation of $CH_4$ $H_2S$, and $NH_3$ from more oxidized species. For $NH_3$, the modeling also indicates that this species is already the dominant N species in the infiltrating fluid buffered at QFM. This feature suggests that the $N_2$ detected in the fluid is most likely formed through post-entrapment respeciation of $NH_3$, unless the serpentinizing fluid was more oxidized than QFM. The absence of detectable $H_2O$ in the fluid inclusions is interpreted to result from host-inclusion interaction and formation of step-daughter lizardite and brucite, or by the preferential entrapment of immiscible reduced gases relative to aqueous fluids (Huang et al., 2017; Vitale Brovarone et al., 2017). The absence of residual $H_2$ in the fluid inclusions may be explained by the much faster diffusion of $H_2$ relative to other fluid species through the host olivine, or by selective leakage.

The most plausible sources of serpentinizing fluid were the metasedimentary formations surrounding the BMC complex. These rock types host substantial amounts of subducted carbon, sulphur, and nitrogen (Bebout and Fogel, 1992; Evans et al., 2014; Kelemen and Manning, 2015; Plank and Manning, 2019). An ultramafic source internal to the BMC would not be consistent with the general retention of N during prograde metamorphism and dehydration of serpentinites (Halama et al., 2014). The hypothesis of a metasediment-derived serpentinizing fluid was also suggested by previous oxygen and hydrogen isotopic data on antigorite from the BMC complex (Wenner and Taylor, 1974, 1971). Moreover, the authors proposed antigorite-magnetite equilibration T in the range of 220-460 °C, which is consistent with the prograde P-T of the BMC (Fig. 4.11). This supports the interpretation of a subduction-related serpentinization related to the infiltration of metasedimentary-derived fluids in a rather dry ultramafic body.

## 4.6 Acknowledgments

The authors wish to thank Mark Van Baalen for logistic support and fruitful discussion, and Leslie white for fundamental support during the field work. J.C.M De Hoog is thanked for a very constructive review on an earlier version of this article. AVB acknowledges a MIUR Rita Levi Montalcini grant and a Richard Lounsbery Foundation grant. Simona Ferrando is thanked for her helpful discussions and insights on fluid inclusions. IFP Energies Nouvelles and their helpful personnel are thanked for its help in the acquisition of test isotopic data of methane. Andrea Risplendente is thanked for assistance with the microprobe analyses.

## *4.7* Appendices

### 4.7.1 Fluid inclusions composition

The compositions of the fluid inclusions were estimated for samples V18-2a and V18-4 using the instrumental efficiency and the intensity of observed species following the method by Frezzotti et al., 2012. The results are presented in Supplementary Table 1. Sample V18-2a, corresponding to the least serpentinized dunite, has $CH_4$ dominated (around 90%) olivine-hosted fluid inclusions, and notable presence of $N_2$. Trace amounts of $H_2S$ and $NH_3$ are also present. Sample V18-4, a carbonate bearing rodingites, has carbonate-hosted fluid inclusions rich in $N_2$ and $CH_4$ ($N_2$-$CH_4$ ratio = 2:1).

*Supplementary Table 1: Calculated molar fractions of $CH_4$, $N_2$, $H_2S$ and $NH_3$.*

| **Sample** | **V18-2a** | **V18-4** |
|---|---|---|
| **Composition (%)** | | |
| **$N_2$** | 6 (5) | 67 (4) |
| **$H_2S$** | 1 (1) | |
| **$CH_4$** | 92 (6) | 33 (4) |
| **$NH_3$** | 1 (2) | |
| **Number of inclusions** | 20 | 4 |

### 4.7.2 Thermodynamic modeling

Besides an external fluid equilibrated with a serpentine (presented in section 4.4 of the main text), Si-richer fluid sources were also considered for the EQ3/EQ6 modeling of the hydration of the BMC. Because the BMC is embedded in metasedimentary rocks, two other assemblages were considered. Firstly, a steatite, corresponding to Si-enriched ultramafic rocks, and secondly a metasedimentary assemblage. In the first case, the infiltrating fluid was equilibrated with a steatite composition of antigorite, clinochlore, talc and magnetite. The interaction with a dunite produces olivine, chlorite, Ca-clinopyroxene, antigorite, tremolite and magnetite (Supplementary Fig. 1A). In the second case, the infiltrating fluid was equilibrated with a metasedimentary assemblage consisting of muscovite, chlorite, calcite and quartz. The interaction with a dunite produces quartz, chlorite, talc, tremolite, calcite, antigorite and magnetite (Supplementary Fig. 1B). The mineral assemblages shown in Figure A and B do not match the natural samples. For these reasons a fluid source equilibrated with steatite or metasedimentary rocks is not privileged.

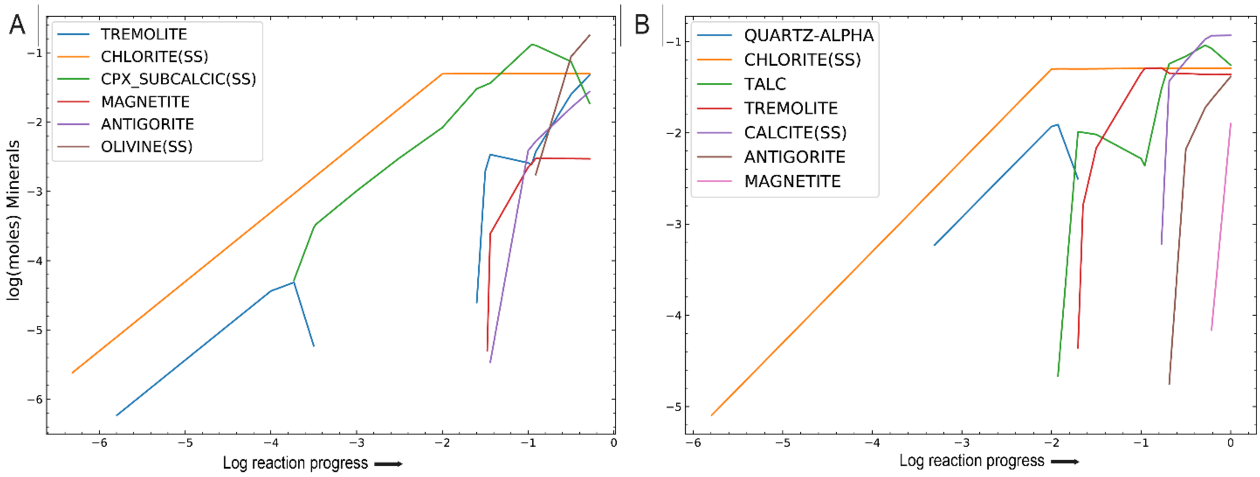

Supplementary Figure 1: Moles of newformed minerals as a function of reaction progress for infiltrating steatite (A) or metasedimentary (B) fluid compositions interacting with a dunite at 450°C and $f\mathrm{O}_2$ at QFM as a result of EQ3/EQ6 modeling.

### 4.7.3 Partition coefficient:

The application of empirical distribution coefficient $K_D$ for antigorite and olivine by Evans, (2008) and Trommsdorff and Evans, 1974 support the hypothesis of transient antigorite generation forming together with metamorphic olivine early in the fluid-rock interaction, along with spinel breakdown. The empirical Mg distribution coefficient $K_D$ [antigorite/olivine, $K_D = (\sum Fe/Mg_{Srp})/(Fe/Mg_{Ol})$] proposed by Evans, 2008 is 0.45-0.35 upon consideration of ferric iron in the antigorite. The Atg1/metamorphic olivine apparent $K_D$ is 0.49-0.25, which agrees with the value proposed by Evans, 2008 for equilibrium, compared with other antigorite/olivine pairs (Atg1/primary olivine = 0.14-0.25; matrix antigorite (Atg2)/primary olivine = 0.11; Atg2/metamorphic olivine = 0.17-0.25). The Mn distribution between antigorite and olivine gives similar results. The empirical Mn distribution coefficients for antigorite/olivine equilibria is 0.18 (Trommsdorff and Evans, 1974). The Atg1/metamorphic olivine pair has an apparent $K_D$ of 0.14-0.18, thus consistent with the predicted equilibrium. The modeling predicts the second antigorite and metamorphic olivine to be stable together. However, the apparent $K_D$ for matrix antigorite and metamorphic olivine suggest disequilibrium (equilibrium Mg $K_D$ = 0.45, measured = 0.17-0.25; equilibrium Mn $K_D$ = 0.18, measured = 0.09-0.14). This feature suggests that stage III marks the beginning of retrograde hydration.

*Table 2: Calculated partition coefficient between antigorite and olivine for Mg and Mn*

| | **$K_D$ Mg** | | **$K_D$ Mn** | |
|---|---|---|---|---|
| **Calculated $K_D$** | **V18-2** | **V18-3b** | **V18-2** | **V18-3b** |
| **Atg1 / P-Ol** | 0.25 | 0.14 | 0.42 | 0.54 |
| **Atg2 / P-Ol** | 0.11 | 0.11 | 0.42 | 0.27 |
| **Atg1 / M-Ol** | 0.49 | 0.23 | 0.14 | 0.18 |
| **Atg2 / M-Ol** | 0.21 | 0.17 | 0.14 | 0.09 |
| **$K_D$ Atg/Ol from bibliography** | | | | |
| | 0.45-0.35 | | 0.18 | |

*$K_D$ Atg/Ol Mg from Evans et al., (2008) and Mn from Trommsdorff and Evans, (1974).*

# 5 Redox-dependent recycling of carbon in subduction zones: a petrological and isotope study from the Belvidere Mountain complex ultramafic body

Antoine Boutier[1,2]*, Alberto Vitale Brovarone[3,4], Isabelle Martinez[2], Olivier Sissmann[5], Samuele Agostini[6], Isabelle Daniel[7], Sara Mana[8]

[1]*Dipartimento di Scienze della Terra, Università degli Studi di Torino, Via Valperga Caluso 35, Torino, Italy*

[2]*Institut de Physique du Globe de Paris, Sorbonne Paris Cité, Université Paris Diderot, UMR 7154 CNRS, 1 rue Jussieu, F-75005 Paris, France*

[3]*Dipartimento di Scienze biologiche, geologiche e ambientali, Via Zamboni, 67, Bologna, Italy*

[4]*Institut de Minéralogie, de Physique des Matériaux et de Cosmochimie (IMPMC), Sorbonne Université, Muséum National d'Histoire Naturelle, UMR CNRS 7590, IRD UR206, 75005 Paris, France*

[5]*IFP Energies Nouvelles, Rueil-Malmaison Cedex, France*

[6]*Istituto di Geoscienze e Georisorse, Pisa, Italy*

[7]*Université Lyon, Université Lyon 1, Ens de Lyon, CNRS, UMR 5276, Laboratoire de Géologie de Lyon, Villeurbanne, France*

[8]*Department of Geological Sciences, Salem State University, Salem, MA 01970, USA*

## Abstract

The fate of carbon in subduction is explored by considering fluid-rock interactions in slab-derived ultramafic rocks as potential proxies for metasomatism and carbon recycling in the mantle wedge at convergent margins. Ultramafic rocks may record intense redox variations affecting the exchanges between solid and fluid carbon-bearing phases. The Belvidere Mountain Complex (BMC) is an ultramafic body that underwent Ordovician Taconic subduction metamorphism up to 510-520 °C and 0.9-1.3 GPa. Previous investigations indicate that the BMC experienced partial serpentinization and carbon recycling in the subduction zone. Here bulk $\delta^{13}C$, $\delta^{11}B$, and $Sr^{87}/Sr^{86}$ data, in-situ µRaman spectroscopy and bulk and $\delta^{13}C_{CH4}$ and $\delta^{2}H_{CH4}$ on fluid inclusions, and numerical modeling results aimed at constraining the pathways of carbon recycling in the BMC. MicroRaman spectroscopy on the fluid inclusions reveals $CH_4$-rich gaseous compositions, along with $N_2$, $NH_{3,}$ and S-H compounds. Methane-rich fluid inclusions can be observed in partially serpentinized peridotites, in carbonate veins, and in amphibolite bodies associated with the ultramafic body. The BMC also hosts a remarkable example of graphite deposit, with up to 3.90 wt% graphite, along a ~6 m-thick zone within the serpentinized ultramafic body and along lithologic contacts. The $\delta^{13}C$ composition of the graphite clusters at -15 ‰ (VPBD). Carbonates present in the studied ultramafic and mafic rocks have $\delta^{13}C$ values ranging from -7.26 to -1.27 ‰. Investigations on $\delta^{13}C$ and $\delta^{2}H$ of methane in fluid inclusions show a wide range of values in ultramafic rocks from -45.2 ‰ to -12.6 ‰ for carbon and -226‰ to -140‰ for hydrogen. Bulk $^{87}Sr/^{86}Sr$ ratios and $\delta^{11}B$ suggest infiltration of metasediment-derived fluids, which is further suggested by the abundance of nitrogen and carbon in the fluid inclusions. The mixing between

metasediment-derived and serpentinization-related methane is proposed as the mechanism leading to graphite precipitation. Further complexity is suggested by carbonate reduction evidenced in the samples. The BMC rocks highlight the variability of carbon recycling during subduction in a dynamic fluid-rock system, with carbon mobilization and sink adapting to evolving redox conditions.

## 5.1 Introduction

Subduction is a major actor in the cycling of carbon between surface and deep reservoirs. As material is brought down along the subducted slab, fluid release and interaction with the overlying mantle wedge creates complex pathways for element mobility as well as fluid intake and outtake (Dasgupta, 2013; Dasgupta and Hirschmann, 2010; Manning, 2014). Metamorphic reactions along the subduction path can regulate element mobility as well as fluid speciation (e.g, Evans, 2012; Hayes and Waldbauer, 2006). Carbon in subduction can be present under different valence states, from -4 to +4, in various forms, such as carbonate, organic matter, and several fluid species such as $CO_2$, $CH_4$, as well as many others. Carbon mobilization is subduction is known to produce different carbonic fluids: $CO_2$-rich fluids resulting from decarbonation reactions (Gorman et al., 2006; Kerrick and Connolly, 1998, 2001a, 2001b; Stewart et al., 2019), carbonate dissolution (Ague and Nicolescu, 2014; Facq et al., 2014; Frezzotti et al., 2011), $CH_4$-rich fluids from serpentinization of preserved peridotite in the slab and of the overlying mantle wedge (Boutier et al., 2021; Peng et al., 2021; Vitale Brovarone et al., 2020, 2017) or from organic matter-rich metasedimentary rocks (Clift, 2017; Poli, 2015; Sverjensky et al., 2014b) and mantle derived $CO_2$/$CH_4$ fluids (Dasgupta, 2013 and references therein; Green et al., 1987). Understanding carbon speciation and migration is key to understanding deep carbon cycling on earth and on other celestial bodies where subduction is or was once active. The formation and migration of $CH_4$ and associated reduced fluid species –most notably $H_2$– is of particular interest in the study of how life emerged on Earth –and potentially elsewhere– and how deep it could extend in the subsurface biosphere (Plümper et al., 2017b; Schrenk et al., 2013). The fate of metamorphic methane in subduction is strongly dependent upon multiple fluid-rock interactions that may take place in slab and mantle wedge forming rocks, including redox related respeciation precipitation of carbon, as carbonate, elemental carbon (graphite or diamond), or preserved in fluid inclusions (Förster et al., 2017; Malaspina and Tumiati, 2012; Sapienza et al., 2009). The fluids released by subduction may have different redox states, and the metasomatic reactions resulting from the migration of such fluids can modify the stability of carbon-bearing minerals. For instance, reducing fluids derived from serpentinization may lead to the reduction of carbonate minerals, the formation of abiotic methane, and/or the precipitation of graphite (Galvez et al., 2013; Vitale Brovarone et al., 2017). However, field examples recording interaction of carbon-rich fluids remain insufficient to understand the fate of carbon at depth. Here we present results from the Belvidere Mountain complex (BMC). The BMC consists of an ultramafic/mafic body that was interpreted as a fragment of the Iapetus ocean that was involved in the Taconic orogeny and recorded HP metamorphism during Cambrian-Ordovician (Chew and van Staal, 2014; Gale, 1980; Honsberger et al., 2017). This locality also hosts a remarkable example of fluid-mediated graphite deposition and methane-rich inclusions, making it relevant to carbon mobility in the upper subduction. This work integrates field, microstructural, fluid inclusions, major and trace element and isotopic geochemical data to investigate the mechanisms of deep carbon migration and transformation in a subduction setting.

## 5.2 Geological settings

### 5.2.1 Regional settings

The Belvidere Mountain Complex (BMC) is a body of mafic/ultramafic rocks located in Northern Vermont and belonging to the Appalachian Mountain system. The complex has been interpreted as a remnant of an ocean-continent transition zone associated with the extension of the Laurentian margin that underwent peak blueschist-facies metamorphism during the Ordovician Taconic subduction (Chew and van Staal, 2014; Gale, 1980). It exhibits variably serpentinized peridotites, mainly dunite and hazburgite, associated with metabasic and metafelsic rocks. The BMC is tectonically embedded within Cambrio-Odovician metasedimentary and metavolcanics formations (Fig. 5.1). Taconic, peak blueschist-facies metamorphic conditions of the BMC are constrained at 0.9-1.3 GPa and 510-520 °C in metabasic rocks (Honsberger et al., 2017; Laird et al., 1993). The rocks preserve features of interactions with fluids both during seafloor hydrothermalism and in the subduction zone, leading to present pervasive serpentinization (10-100% vol% serpentine). This tectonometamorphic event was dated at 505-473 Ma by $^{40/39}$Ar amphibole and mica geochronology (Castonguay et al., 2012; Laird et al., 1993).

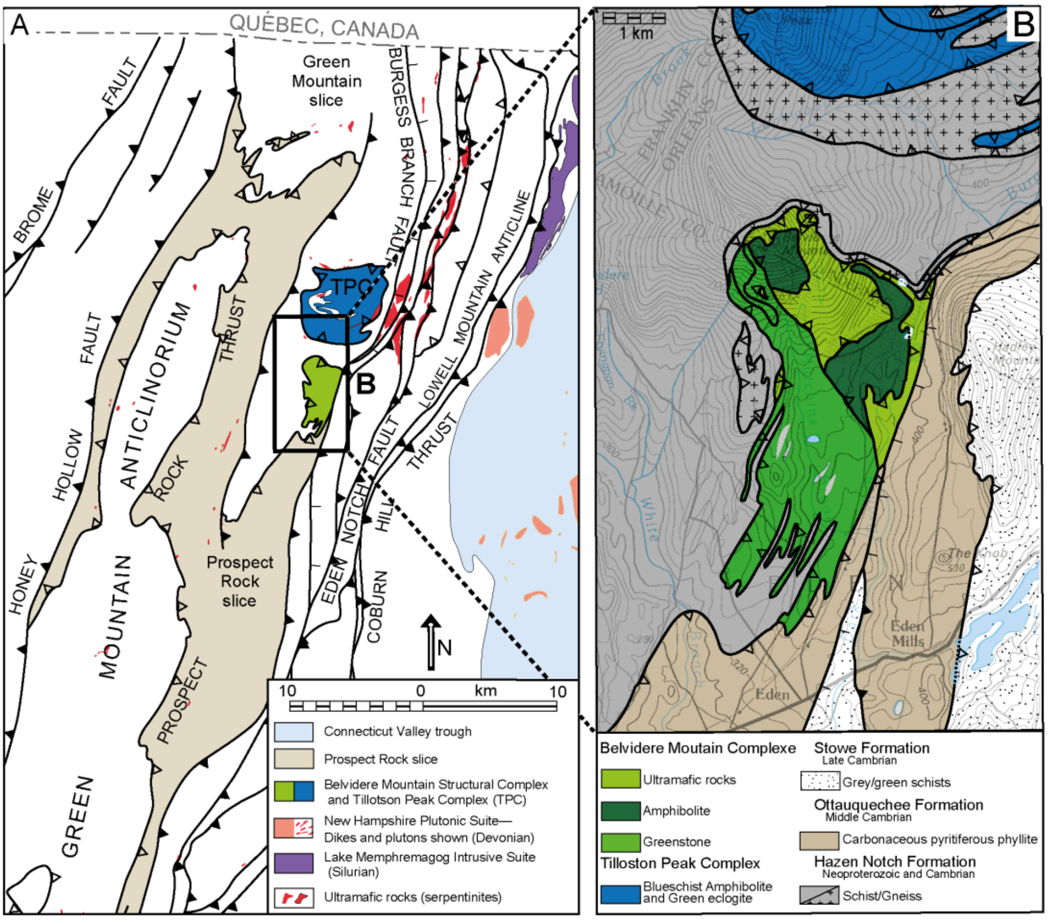

***Fig. 5.1:*** *A: Simplified geological map of Vermont, modified from Hibbard et al., (2006). B: Simplified bedrock geologic map of the Belvidere Mountain Complex and the surrounding formations. Modified after Hibbard et al., (2006). Units description from Hibbard et al., (2006) and Gale, (2007).*

## 5.3 Methods

MicroRaman spectroscopy of minerals and fluid inclusions was performed at the Department of Earth Sciences, University of Turin, with a LabRAM HR (VIS) (HORIBA Jobin Yvon) equipped with a 532.11 nm, solid-state Nd laser, a Super Notch Plus filter with spectral resolution of 1 cm$^{-1}$, and a grating of 600 grooves/mm. The laser of emission power was set at 80 mW and focused to 5 µm with a 100x objective with a laser power on the sample < 5 mW. Calibration was performed using the 520.6 cm$^{-1}$ band of a silicon standard for the 100-2000 cm$^{-1}$ range, and the 2331 cm$^{-1}$ band of atmospheric $N_2$ for the 2000-4000 cm$^{-1}$ range. Four accumulations of 30–60 s were collected for each spectrum. Raman spectra of fluid inclusions were performed on double-polished thick sections.

Scanning electron microscopy (SEM) imaging and energy-dispersive X-ray spectroscopy (EDS) compositional analyses were carried out using a Zeiss EVO15 equipped with an LaB6 source, a high-definition backscattered electron detector (HDBSE), and an Oxford Instruments UltimMax 100 detector at the DeepCarbonLab, Department of Biological, Geological, and Environmental Sciences, University of Bologna, Italy. Additional analyses were performed with a tungsten (W) SEM-JEOL JSM-IT300LV Scanning Electron Microscope combined with an energy dispersive spectrometry (EDS) Energy 200 system and an SDD X-Act3 detector (Oxford Inca Energy) at the Department of Earth Sciences of Turin University. Data were processed with the AztecLive and INCA softwares from Oxford Instruments. Semi-quantitative analysis employed 15kV accelerating voltage and a beam current of 50 nA and 20 s to 40 s counting total time. Natural and synthetic mineral and oxide standards were employed. EDS calibration was made using Cobalt standard.

Quantitative wavelength-dispersive spectrometer (WDS) analyses were carried out using a JEOL 8200 Super Probe at the Department of Earth Sciences “Ardito Desio” of Milan University. The microprobe was using a 15kV accelerating voltage under 5 nA, with 30s counting time under the maximum emission peak. Sixteen oxide composition were measured, using synthetic and natural standards: grossular (Si, Al and Ca), omphacite (Na), K-feldspar (K), fayalite (Fe), forsterite (Mg), rhodonites (Mn), niccolite (Ni), ilmenite (Ti), galena (Pb and S), pure Cr, pure Zn and pure Cu.

Portions of samples were cut to remove weathered and surface organic contaminations, and then crushed and pulverized with Plattner and agate mortars. Considering the very high amount of graphite, the potential effect of organic contaminations by groundwater circulation was considered negligible. Analyses of total organic carbon (TOC) were performed on aliquots of about 1 g of dried, decarbonated samples (HCl, 6 mol/L, attacked at ambient temperature for one night) using a Flash EA1112 elemental analyzer coupled to a Thermo Finnigan DELTA plus XP isotope ratio mass spectrometer via a ConFlo IV interface at IPGP, Paris. Aliquots of the companion, non-decarbonated sample were also analyzed for Total Carbon (TC=Total Inorganic Carbon (TIC)+TOC). Graphitic C concentrations in samples presented herein correspond to the TOC.

The $\delta^{13}C$ and the $\delta^{18}O$ of carbonate were obtained at the Institute of Geosciences and Earth Resources, Pisa, on a GasBench II with a continuous-flow IRMS setup, after the method of Breitenbach and Bernasconi, (2011). Isotope ratios are reported in permil (‰) using the conventional δ-notation and with respect to the V-SMOW for oxygen and Vienna Pee Dee Belemnite (V-PDB) for carbon. Standard deviation was 0.05‰ for both $\delta^{13}C$ and $\delta^{18}O$.

The $\delta^{13}C$ and $\delta^{2}H$ of $CH_4$ was obtained at IFP energies nouvelles by extracting the gas by crushing inclusion-rich samples in a sealed modified planetary mill. The samples were placed in a ZrO jar and sealed by an inlet/outlet-equipped cover. The jar was flushed with $N_2$ for around 60 seconds, then sealed and crushed at 700 rpm for 240 seconds. The gas was then extracted from the jar by connecting vacuum exetainer sample vials. Three different vials were collected for each sample. The $\delta^{13}C$ of each sample was measured by two independent techniques: the first vial of each sample was injected in triplicate in a Picarro G2210-i Isotope Analyzer, to obtain the $\delta^{13}C$ of $CH_4$ and the C1/C2 ratio. The two other vials were used to analyze the $\delta^2H$ and the $\delta^{13}C$ of $CH_4$ with a GC-MS, respectively. Analyses by GC-MS were calibrated using two internal gas standards.

Bulk $\delta^{11}B$ was analyzed at IGG-CNR, Pisa, Italy; for each sample ～0.2 g of sample powder was treated by alkaline fusion in platinum crucibles with a 4:1 flux to sample ratio. Boron was then extracted from the fusion cakes by repeated crushing and centrifuging of the cakes in high pH B-free water. It was further purified by passing the solution through anion and cation exchange columns. Anion columns were packed with Amberlite IRA-743 boron-specific anion exchange resin, while cation-exchange columns were packed with AG 50W-X8 resin. The procedure used an anion column step, followed by a cation column step and then a final (repeat) anion column step to produce the final purified boron solution, as described by Tonarini et al., (1997). The B isotope compositions were measured on a Thermo Scientific$^{TM}$ Neptune series multi-collector (MC)-ICP-MS in Pisa, specially tuned for $^{11}B/^{10}B$ analysis, following Foster, (2008). Samples were diluted to contain ～20 ppb B and were then bracketed with NBS 951 boric acid standard solution of the same concentration, to correct for instrument-induced mass fractionation.

Sample preparation of Sr analysis was done in a similar fashion to that of carbon analysis. Sr isotope analyses were performed using a Finnigan MAT 262 multi-collector mass-spectrometer (at IGG-CNR, Pisa) running in dynamic mode, after ion-exchange purification through Sr-spec resin. Measured $^{87}Sr/^{86}Sr$ ratios have been normalized to $^{86}Sr/^{88}Sr = 0.1194$. Values are corrected for $^{87}Sr/^{86}Sr$ of NBS 987 =0.710248. Interference of $^{87}Rb$ on $^{87}Sr$, and $^{86}Kr$ on $^{86}Sr$ were corrected according to average natural $^{85}Rb/^{87}Rb$ and $^{83}Kr/^{86}Kr$ ratios, respectively. Blanks were measured and corrected. Sample/Blank ratios vary typically from 5 $10^3$ and 5 $10^4$.

Whole-rock analyses of samples from the were performed at the Service d'Analyse des Roches et Minéraux (SARM, Centre de Recherches Pétrographiques et Géochimiques, Nancy, France) by alkali fusion of rock samples (LiBO2), followed by concentration measurements using an ICP-OES Icap 6500 (Thermoscientific) for major elements, and an ICP-MS X7 (Thermoscientific) for minor elements (protocol by Carignan et al., 2001). http://helium.crpg.cnrs-nancy.fr/SARM/pages/roches.html for details on uncertainty and detection limits.

Numerical modeling of isotopic fractionation was done with Rayleigh and batch equations and fractionation factors from Bottinga, (1969) using Python. Thermodynamic modeling of COH fluid and associated carbon solid was done using equations from Huizenga, (2005) to track the carbon activity of carbon and dissolve or precipitate accordingly using a python code. Both models were coupled to investigate and model the interaction of various COH fluids (see Part II chapter 6).

## 5.4 Results

### 5.4.1 Field relationships

Figure 5.2 and Table 5.1 show the location and main features of the selected samples. Besides samples of variably serpentinized peridotites, rodingites, and surrounding metasedimentary rocks, the core of the sample presented in this study were collected from two main outcrops, Graphite zone A and B hereafter, showing evidence of graphite precipitation. Graphite zone A consists of a vertical,~ 6 m thick graphite-rich shear zone cutting through the ultramafic body (Fig. 5.2A). Graphite zone A is separated by the enclosing serpentinized peridotite by a rather sharp boundary. However, the host serpentinite next to the graphite zone selvages appear variably carbonated. The carbonation is present as veins, mainly on the right side of the graphite zone, and micro-scale pervasive carbonation is visible on both sides of the graphite zone. The second outcrop, referred to as Graphite zone B, is located along the contact within the BMC serpentinized peridotites and amphibolites (Fig. 5.2B). The outcrop forms a vertical wall making the boundary of the adjacent amphibolite.

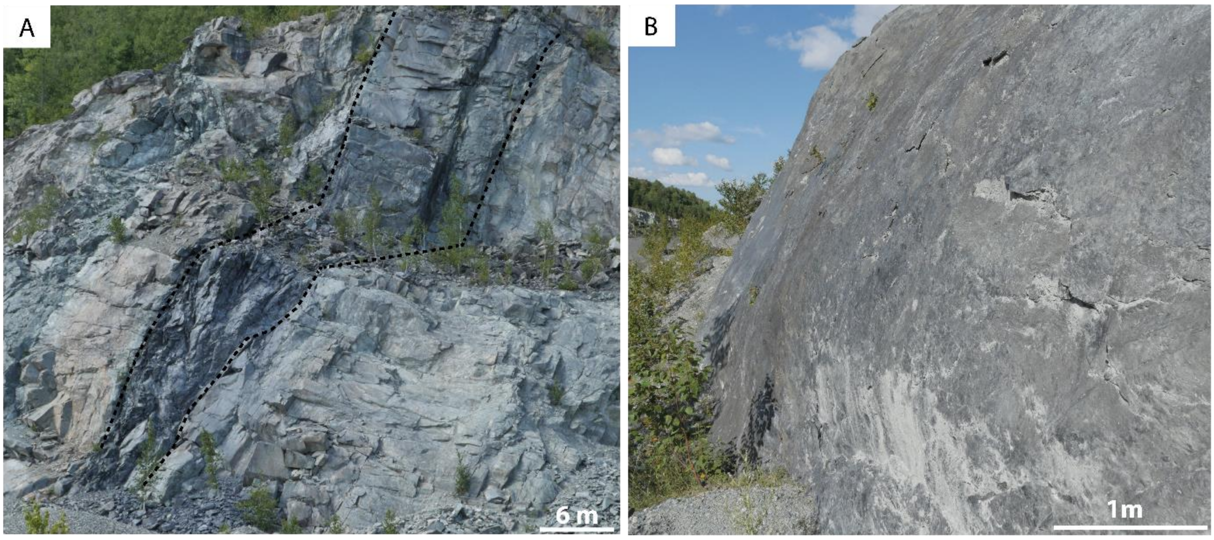

***Fig. 5.2:*** *A: Outcrop picture of the pluri-meter graphite veins cutting through the ultramafic bodies. B: Outcrop of the northern edge of the amphibolite. The surface exhibits graphite which progressively disappears toward the center of the amphibolite.*

Samples V18-1a,c,e correspond to metasedimentary rock of the Ottauquechee Formation, from an outcrop located 20 km south of the BMC. Sample V18-1a consists of fine-grained muscovite, quartz, chlorite, abundant organic matter, and other opaque minerals. Sample V18-1c is quartz-richer, and contains muscovite, chlorite, minor organic matter, coarse-grained isolated and locally disseminated carbonate, coarse-grained sulfides, and detrital zircons. Samples V18-2a,b, V18-3a,b and V18-11 consist of slightly serpentinized peridotites. Samples V18-5(a-i), V18-7a,c, and V18-Y(1,b) are from Graphite zone A. Samples V18-6a,d, V18-8, V18-9, and V18-10 are variably carbonated serpentinites from the selvage of Graphite zone A. Samples V18-12 to V18-15 are from Graphite zone B. Sample V18-4 is a graphite-carbonate-bearing rodingite.

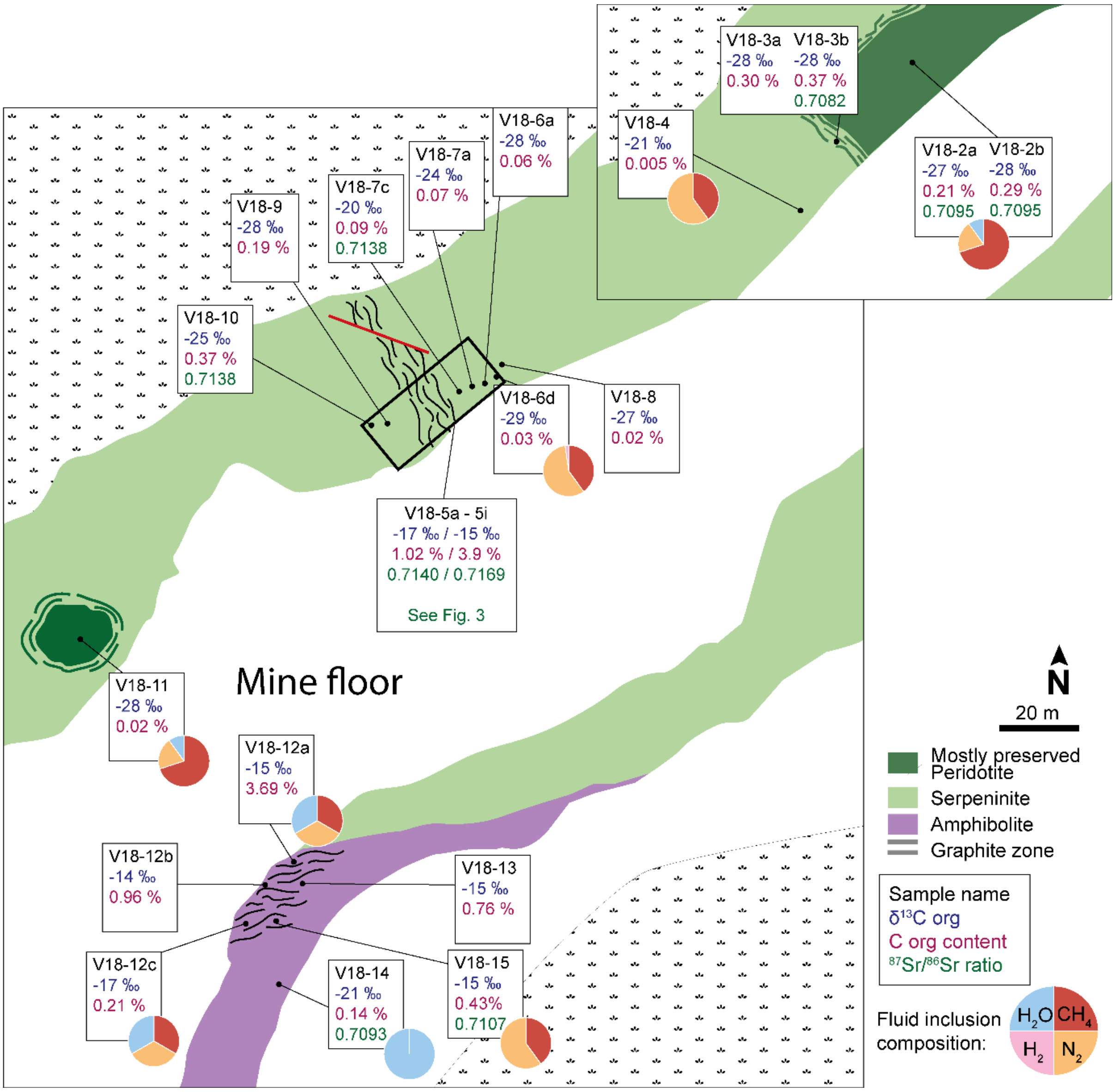

***Fig. 5.3**: Map showing the geology, sample location,* δ$^{13}$C (‰ VPDB), of organic carbon content (wt.%), and $^{87}$Sr/$^{86}$Sr ratio results. Pie charts indicate the relative composition of different phases in fluid inclusion as determined from Micro-Raman spectra following the method by Frezzotti et al., (2012). The initial presence of water in olivine-hosted fluid inclusions is deduced from the presence of hydrated step daughter minerals. See Fig. 5.4 for details on Graphite zone A.

**Table 5.1:** Studied BMC samples and related carbon, strontium and boron data.

| Samples | | $C_{org}$ (wt%) | $\delta^{13}C_{org}$ VPDP | $\delta^{13}C_{inorg}$ VPDP | $\delta^{18}O_{carbonate}$ VSMOW | $\delta^{13}C_{CH4}$ VPDP $_{picarro}$ | $\delta^{13}C_{CH4}$ VPDP $_{IRMS}$ | $\delta^{2}H_{CH4}$ VSMOW | $\delta^{2}H_{H2}$ VSMOW | C1/C2 | $^{87}Sr/^{86}Sr$ | $\delta^{11}B$ |
|---|---|---|---|---|---|---|---|---|---|---|---|---|
| V18-1a | metasedimentary rocks | 0.58 | -25.3 | | | -46.28 | -46.34 | -226 | -812 | 13 | 0.7578 | -8.48 |
| V18-1c | | 0.17 | -25.0 | | | | | | | | | |
| V18-1e | | 1.99 | -25.0 | | | | | | | | | |
| V18-2a | mostly preserved peridotite | 0.02 | -27.4 | | | -12.66 | -12.93 | -171 | | 1992 | 0.7095 | -1.57 |
| V18-2b | | 0.03 | -28.3 | | | | | | | | 0.7095 | -0.83 |
| V18-3a | | 0.03 | -28.1 | | | | | | | | 0.7082 | -1.41 |
| V18-3b | | 0.03 | -28.5 | | | | | | | | | |
| V18-4 | rodingites | 0.01 | -21.7 | | | -15.48 | -17.88 | -177 | | 6154 | | |
| V18-Y1 | graphite zone A | | | | | | | | | | | |
| V18-Yb | | | | | | | | | | | | |
| V18-5a | | 1.39 | -15.5 | | | | | | | | | |
| V18-5b | | 1.65 | -15.2 | | | | | | | | 0.7140 | |
| V18-5c | | 1.51 | -15.6 | | | | | | | | 0.7167 | -3.45 |
| V18-5d | | 1.08 | -14.6 | | | | | | | | | |

|  |  |  |  |  |  |  |  |  |  |  |  |  |
|---|---|---|---|---|---|---|---|---|---|---|---|---|
| V18-5e |  | 1.03 | -17.0 |  |  |  |  |  |  |  |  |  |
| V18-5f |  | 3.91 | -15.3 |  |  |  |  |  |  |  |  |  |
| V18-5g |  | 2.76 | -15.6 |  |  |  |  |  |  |  | 0.7177 |  |
| V18-5h |  | 1.45 | -16.5 |  |  |  |  |  |  |  | 0.7140 |  |
| V18-5i |  | 1.02 | -17.7 | -1.43 | 16.64 |  |  |  |  |  |  |  |
| V18-6a | serpentinite with variable amount of carbonate | 0.06 | -28.6 | -6.49 | 8.91 |  |  |  |  |  |  |  |
| V18-6d |  | 0.03 | -29.5 |  |  | -31.25 | -29.00 |  |  | 635 |  |  |
| V18-7a |  | 0.07 | -24.7 |  |  |  |  |  |  |  |  |  |
| V18-7c |  | 0.09 | -20.2 | -1.27 | 15.15 |  |  |  |  |  | 0.7138 | -2.38 |
| V18-8 |  | 0.02 | -27.7 | -4.50 | 10.83 |  |  |  |  |  |  |  |
| V18-9 |  | 0.02 | -27.9 | -4.13 | 11.81 |  |  |  |  |  |  |  |
| V18-10 |  | 0.37 | -25.1 |  |  |  |  |  |  |  | 0.7138 | -4.56 |
| V18-11 | mostly preserved peridotite | 0.02 | -27.7 |  |  | -45.23 | -42.48 | -226 |  | 668 |  |  |
| V18-12a | graphite zone B | 3.69 | -15.5 |  |  | -22.36 | -22.46 | -161 |  |  |  |  |
| V18-12b |  | 0.96 | -13.6 |  |  |  |  |  |  |  |  |  |
| V18-12c |  | 0.22 | -16.9 |  |  | -18.59 | -20.66 | -140 | -680 |  |  |  |
| V18-13 | amphibolite | 0.77 | -14.8 |  |  |  |  |  |  |  |  |  |
| V18-14 |  | 0.14 | -20.5 | -7.26 | 11.41 | -36.95 | -33.45 | -168 |  |  | 0.7093 | -3.49 |
| V18-15 | amphibolite with carbonate | 0.43 | -15.4 |  |  | -20.19 | -20.18 | -168 |  |  | 0.7107 |  |

### 5.4.2 Petrographic features

Although the petrologic features of the BMC serpentinized peridotites and related mafic rocks have been treated in the literature (Boutier et al., 2021; Labotka and Albee, 1979; Laird et al., 2001), the associated graphite mineralization remain poorly investigated (Carlsen et al., 2015; Chidester et al., 1978; Kerper et al., 2008; Van Baalen et al., 2009). In this section, the main features of Graphite zones A and B are presented. Details on samples V18-2a,b, V18-3 and V18-4 (rodingites) can be found in Boutier et al. (2021). The samples series V18-5 corresponds to a transect across graphite zone A (Fig. 5.4). The outcrop comprises two main lithologies, namely tremolite-chlorite-graphite-rich rocks located at the center of the zone (samples V18-5c,d), and antigorite-graphite-rich rocks located at the selvages (samples V18-5a,b,e,f,g,h,i). Carbonate is present at the edge of the graphite zone as discordant veins (sample V18-5a), or in the matrix of both antigorite-graphite rocks (V18-5i). Samples V18-7a,c are graphite-carbonate as rich as sample V18-5i. Samples V18-6(a,d), V18-8, V18-9, and V18-10 have disseminated carbonate-veins and do not contain graphite. Samples V18-Y1 and V18-Yb are two loose blocks collected at the base of the graphite zone showing complementary features, possibly reflecting the early stages of fluid/rock interaction.

V18-5c and V18-5d correspond to samples at the center of graphite zone A. They consist of tremolite (up to 200µm long), antigorite, chlorite, and graphite, and show complex deformation features (Fig. 5.5A). Graphite is present in the matrix forming coronas around tremolite crystals. Microstructural relationships indicate that at least some of the antigorite present in these samples formed at the expense of former tremolite (Fig. 5.5A).

Sample V18-5a is composed of antigorite and graphite with discordant carbonate veins (Fig. 5.5B). However, the former presence of tremolite is clearly indicated by the pseudomorphic growth of antigorite aggregates on euhedral amphibole crystals (Fig. 5.5B). By comparison with samples V18-5c,d, the microstructures suggest that the graphite rims surrounding these pseudomorphoses forms prior to the replacement of tremolite by antigorite. The graphite deposit outlines the deformation experienced along the graphite zone A. Similar pseudomorphic structure and deformation can be observed in other antigorite samples from V18-5e-i.

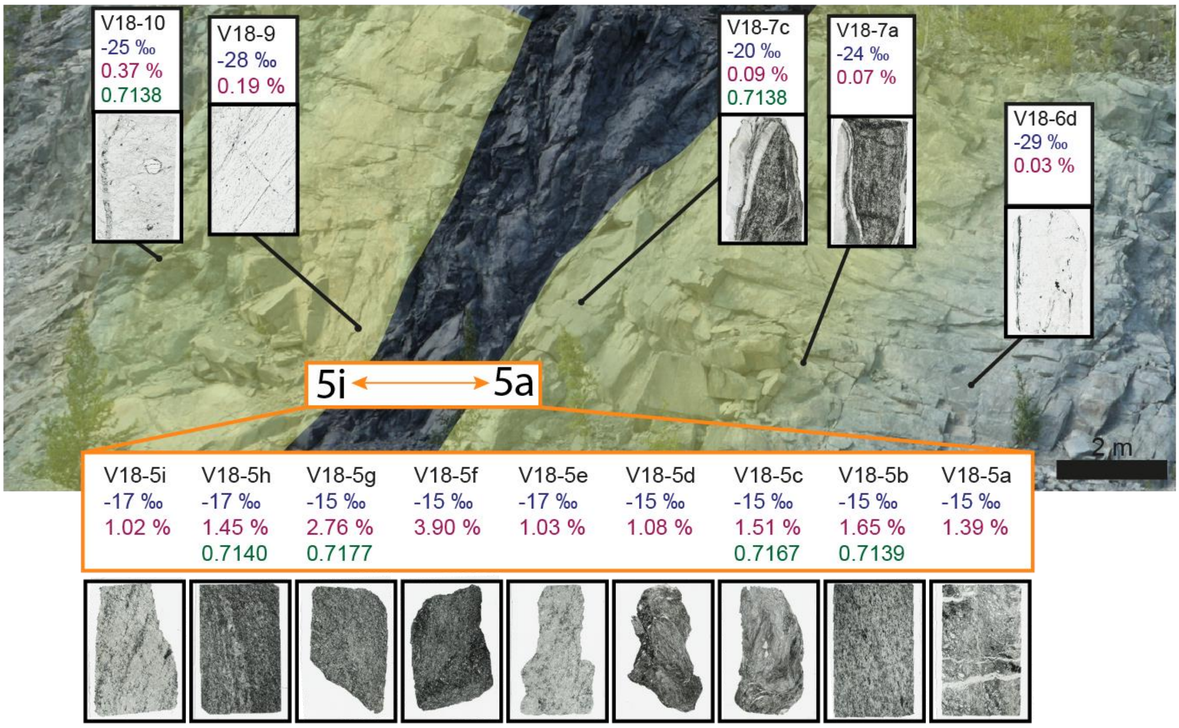

***Fig. 5.4:*** *Field view details of Graphite zone A. The location of the studied samples and associated values of* $\delta^{13}C$ *‰ (VPDB), wt.% of organic carbon and* $^{87}Sr/^{86}Sr$ *ratios are also shown. The black-colored area represents the location of the graphite-rich shear zone. The shaded yellow-colored area indicates the carbonate-enriched selvages next to the graphite zone. Thin section scans are also shown in order to highlight the distribution of graphite (dark samples) with respect to the enclosing graphite-free ultramafic rocks.*

Sample V18-7c corresponds to a metasomatized serpentinite to the right of Graphite zone A, and consists of antigorite, dolomite, calcite, brucite, and graphite. SEM-based BSE imaging suggests at least local conversion of dolomite into calcite, brucite, and graphite (Fig. 5.5C). This microstructure, however, was not observed in any of the other studied samples.

V18-Y1 has a breccia-like structure and consists of clasts of antigorite in a matrix of fine-grained foliated tremolite. Post-kinematic diopside porphyroblast partially overgrew the foliated tremolite matrix and, to minor extent, the serpentine clasts (Fig. 5.5D). This sample does not contain graphite.

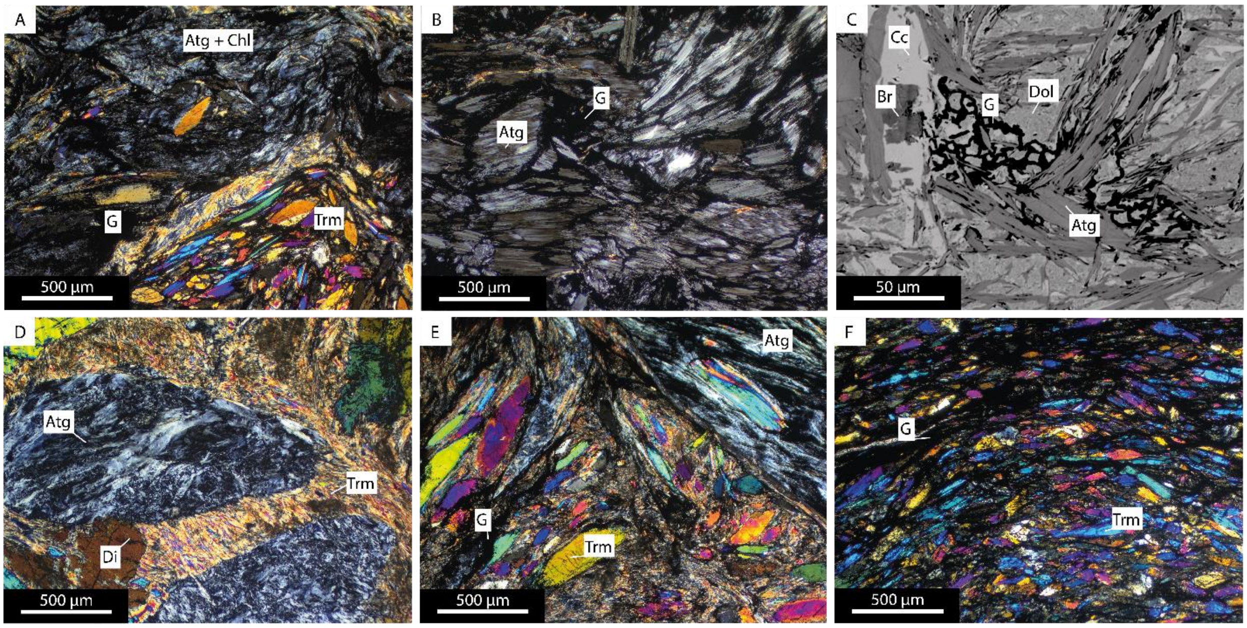

***Fig. 5.5:*** *A: Samples V18-5c from graphite veins A. The fine grain tremolite is replaced by larger tremolite crystals. Clasts of serpentine have been largely replaced by tremolite. Graphite appears inside antigorite clast and at the rim of tremolite crystals. B: Sample at the edge of graphite zone A (V18-5a). Tremolite crystals have been replaced by antigorite, with graphite rims outlining the pseudomorphic texture. C: SEM imaging of V18-7c. Carbonate reduction is present with the transformation of dolomite and* $H_2$ *in calcite + brucite + graphite. This reaction is accompanied by the release of* $CH_4$ *and water. D: Clasts of antigorite in a matrix of fine grained tremolite associated with graphite zone A (V18-Y1). Porphyroblasts of diopside can be observed growing from tremolite. E: A clast of antigorite in a matrix of tremolite with graphite deposit associated with graphite zone A (V18-Yb). Tremolite forms larger crystals inside the fine grain matrix and grows inside antigorite clasts. F: Tremolite crystals with rims of graphite from graphite zone B (V18). Atg: antigorite, Trm: tremolite, Di: diopside, G: graphite, Chl: chlorite, Cc: calcite, Dol, dolomite, Br: brucite*.

V18-Yb shares mineralogic features of V18-Yb with clasts of antigorite or tremolite aggregates in a matrix of fine-grained tremolite (Fig. 5.5E). Also, in this case, microstructures suggest that at least a part of the antigorite present in the rock formed after the former tremolite. Graphite is abundant in the rock. It is disseminated in the fine-grained tremolite matrix, and forms aggregates around larger tremolite crystals or antigorite aggregates in the clasts.

Six samples were collected from the Graphite zone B (samples V18-12a,b,c, V18-13a,b, V18-14 and V18-15). Samples V18-12a and V18-12c have structures and mineral assemblages similar to samples V18-5c and v18-5d of graphite zone A, with tremolite crystals up to ～200 µm long in a matrix of chlorite and antigorite. Graphite is abundant in the matrix and forms coronas around the tremolite crystals (Fig. 5.5F). Some sample display brecciation of plagioclase along precipitation of carbonate and graphite.

Samples V18-12c, V18-13a, V18-13b, V18-14, and V18-15 are composed of hornblende, plagioclase, titanite, and carbonate, consistent with the BMC amphibolite (Labotka and Albee, 1979), but show evidence of fluid infiltration as indicate by the presence of graphite and carbonate formed along grain boundaries or micro-cracks. Particularly V18-15 bears large amounts of carbonate featuring methane-rich fluid inclusions.

### 5.4.3 Fluid inclusions analysis

Boutier et al., (2021) described the presence of secondary fluid inclusions containing $CH_4$, $N_2$, $NH_3$ and S-H/$H_2S$ in olivine from sample V18-2a in the BMC ultramafic rocks. These reduced fluids were interpreted to have formed through the process of high-pressure serpentinization. Here we provide additional MicroRaman data on fluid inclusions from several other samples from the BMC, and more precisely in olivine from a different weakly serpentinized peridotite (V18-11), in vein calcite (V18-4 and V18-6d), in titanite, plagioclase, and carbonate from amphibolites (V18-12c and V18-14), and in quartz from nearby metasedimentary formations (V18-1b).

The fluid inclusion speciation as derived from MicroRaman spectra analysis is presented in Figure 5.3. MicroRaman spectra (Supplementary Materials 5.1) show the presence of marked $CH_4$ bands (2912 $cm^{-1}$), as well as $N_2$ (2327 $cm^{-1}$), $NH_3$ (3324 $cm^{-1}$), and S-H/$H_2S$ (2575 $cm^{-1}$). This water-free fluid inclusion composition was found in olivine from partially serpentinized peridotites and in calcite from the Graphite zone A. The proportion of $CH_4$ is dominant in olivine-hosted inclusions and decreases in carbonate-hosted inclusions. Olivine-hosted fluid inclusions contain step-daughter hydrous solid phases such as lizardite and brucite, indicating that the initial fluid trapped in the olivine was aqueous. In Graphite zone B, calcite-hosted inclusions show similar compositions, whereas plagioclase and titanite-hosted inclusions are water-dominated with less abundant $CH_4$ and $N_2$.

In Boutier et al. (2021) we stated that antigorite and chrysotile were the only serpentine polysomes present in the BMC rocks. However, complementary observations in sample V18-2a reveal the presence of veins of lizardite. In particular, Figure 7a shows the presence of brownish lizardite veins that were, instead, interpreted as antigorite. The presence of lizardite-vein in only a few samples is not associated with compositional changes in fluid inclusions, Supplementary material 5.6.1 shows olivine-hosted inclusions composition for V18-11 similar to the composition for V18-2a presented in Boutier et al. (2021). Therefore, we conclude that this feature does not substantially affect our interpretations on the metamorphic origin of the $CH_4$-bearing fluid inclusions and their most plausible formation at antigorite-facies conditions as proposed in Boutier el al. (2021). The chronological relationships between antigorite and lizardite in sample V18-2a are not obvious, which possibly suggest conditions close to the antigorite-lizardite transition (380-400 °C, Schwartz et al., 2013).

### 5.4.4 Bulk rocks trace and major elements compositions

Major elements of the BMC ultramafic rocks show that the least serpentinized samples of the BMC (V18-2a,b) share MgO vs $Al_2O_3$ compositions with both abyssal and orogenic/ophiolitic peridotites (Fumagalli and Klemme, 2015). Tremolite-rich samples located at the center of the graphite zone A display a decrease of SiO and MgO content, and an increase of $Al_2O_3$ and CaO content in respect to the surrounding ultramafic rocks. Samples most affected by graphite zone B (V18-12b) display a decrease of $Al_2O_3$, $Fe_2O_3$ and an increase of SiO and MgO in respect to the less or unaffected mafic rocks (V18-12c, V18-14, V18-15). The major elements composition of the samples less affected by the graphite zone B are in range of the mafic rocks composition presented in Spandler et al. (2003).

Chondrite-normalized rare-earth element (REE) spider diagrams of the studied samples along major elements are presented in Supplementary material 2. Sample V18-1a has a positive REE slope, i.e., LaN > LuN, consistent with terrigenous sedimentary rocks (Ague, 2017; Spandler et al., 2003). Samples of BMC variably serpentinized peridotites (V18-2a,b, V18-3a, V18-5b,c,d,g,h,i, V18-7a, V18-8, V18-10) have very low REE concentrations and patterns consistent with serpentinized ultramafic rocks (Deschamps et al., 2013). Samples from Graphite zone A (V18-5a-i) and highly rich in graphite (V18-7c) have REE patterns similar to the variably serpentinized peridotites. Samples from amphibolite and from Graphite zone B show patterns typical of gabbro, with the Eu positive anomaly attributed to preferential incorporation in plagioclase (Philpotts and Schnetzler, 1968). REE spectra indicate the protolith of graphite zone A and B corresponding respectively to depleted mantle and differentiated mantle.

### 5.4.5 Carbon content and isotopy

Organic carbon (OC) content is presented in table 5.1. The complete details including standard deviation is available in Supplementary material 5.6.3. Slightly serpentinized peridotite and serpentinized rocks have OC content of 0.001-0.02 wt. %. These values correspond to the range of OC contents in ultramafic rocks from Northern Apennines and ODP samples (>0.1% to 0.7%) (Schwarzenbach et al., 2013). The OC content of Graphite zone A rocks ranges between 1.02 and 3.90 wt. %, showing a peak of OC in samples close to the center of the shear zone (samples V18-5g and V18-5f). This peak of OC content is not correlated with the observed mineralogical variations within this graphite zone (see section 1.4.1).

The OC content of Graphite zone B ranges from 0.2 to 3.69 wt.% (Table 5.1). These values are higher relative to the OC content (>0.1 wt%) of mid-ocean ridge crustal rocks and their metamorphic equivalents (Schwarzenbach et al., 2013; Shilobreeva et al., 2011).

The OC contents of samples V18-1a,c,e from the Ottauquechee formation range from 0.17 wt% to 1.99 wt.% and are consistent with the range of OC contents of black schists (Peltola, 1968; Zhang et al., 2018).

Isotopic analyses of $\delta^{13}C_{org}$ were conducted to investigate the processes of graphite deposition and its carbon sources. $\delta^{13}C_{org}$ data are presented in Table 5.1 and figure 5.6. Samples from the Ottauquechee formation (V18-1a-e) exhibit an average $\delta^{13}C_{org}$ value of -25.1 ‰ (±0.2‰; n=3). These values are consistent with the $\delta^{13}C_{org}$ signature of chlorite-biotite zone metapelitic rocks unaffected by fluid-rock interactions from the Appalachian belt (Cook-Kollars et al., 2014; Zhang et al., 2018). The average $\delta^{13}C_{org}$ of least serpentinized peridotites is -27.9 ‰ (±0.4 ‰; n=5), which is consistent with the signature of serpentinized peridotites of oceanic affinity (Schwarzenbach et al., 2013). However, it corresponds to a relatively low amount of carbon (< 0.03 wt%) and could be attributed to recent or biological contamination, as $\delta^{13}C$ of C3 photosynthesis range around -28 %. The $\delta^{13}C_{org}$ values of samples from Graphite zone A and Graphite zone B are comparable and correspond to -15.9 ‰ (±1‰; n=9) and -15.2 ‰ (±1.2 ‰; n=3), respectively. These values are clearly different from the $\delta^{13}C_{org}$ signature of regular ultramafic rocks of the BMC. The value of graphite-free serpentinite located close to Graphite zone A ranges from -29.5 to -20.2 ‰ (Table 5.1). A graphite-bearing amphibolite next to Graphite zone B has a $\delta^{13}C_{org}$ value of -20.5 ‰ (Table 5.1).

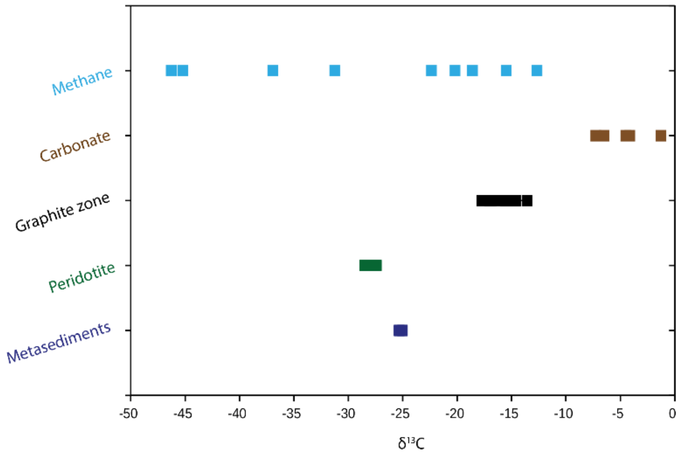

***Fig. 5.6:*** *A: Isotopic compositions of the main carbon bearing objects in the BMC. Error bars do not appear when comprised within the symbol.*

The $\delta^{13}C_{org}$ values of serpentinites around the graphite zone A show disparity which could correspond to the influence of the graphite zone A. The $\delta^{13}C_{org}$ of the samples are not correlated to the direct proximity to the graphite zone A, as the samples directly located near it, such as V18-6a ($\delta^{13}C$= -28.6 ‰), do not exhibit $\delta^{13}C_{org}$ value close to the graphite zone A ($\delta^{13}C$=-15.9). However, the OC content indicates a correlation with the graphite zones (Fig 5.7A), showing that samples with increasing OC content have values closer to that of the graphite zone A and B. Both sample from the graphite veins in the ultramafic body and the amphibolite contact show $\delta^{13}C$ signature centered around -15 ‰ and is homogeneous, indicating a common source for graphite zone A and B. However, the variation of the $\delta^{13}C$

inside the graphite veins appears to not be correlated to the OC content of the samples (Fig 5.7A), as samples with similar OC content ranges from -17.7 ‰ to -13.6 ‰.

Carbonates (inorganic carbon) present as veins, associated with serpentine, or in rodingites exhibit a $\delta^{13}C_{inorg}$ signature ranging from -6.49 to -1.27 ‰ (Table 5.1 and Fig. 5.6). The carbonate in altered amphibolite V18-14 has a value of -7.62 ‰. These values are lower relative to the average signature of carbonate in metamorphic carbonated ultramafic rocks (Collins et al., 2015), with the exception of rocks with low carbonate/silicate ratios and affected by $CO_2$-producing metamorphic decarbonation reactions or fluid-deposited carbonates derived from infiltration of fluids sourced from OC-bearing metasedimentary rocks (Bebout, 1991; Bebout and Barton, 1993; Scambelluri et al., 2016). Additional interpretations are discussed in Section 1.5.2. The oxygen isotopic composition $\delta^{18}O$ of carbonate relative to the SMOW ranges from 8.91 to 16.64 ‰ (Fig. 5.8). These values are consistent with $\delta^{18}O$ of carbonate in ultramafic rocks metamorphosed to blueschist-facies conditions (Collins et al., 2015). However, the carbonate $\delta^{18}O$ values indicate non-equilibrium with the associated BMC antigorite serpentinites. For instance, carbonates values close to 9 ‰ are in equilibrium with serpentine (at 6.4 ‰) for temperatures around 300-400 °C, however highest value (i.e. 16.64 ‰) would indicate equilibrium T <100 °C (Saccocia et al., 2009; Wenner and Taylor, 1971; Zheng, 1999, 1993) which are inconsistent with the antigorite-facies metamorphic evolution of the BMC (Guillot et al., 2015). From Figure 5.8, it can be observed that the variability of $\delta^{13}C$ and $\delta^{18}O$ of carbonate correlates with the distance from the graphite zone. This correlation will be discussed in Section 1.5.2.

Raman spectroscopy of carbonaceous material (RSCM) present in metasedimentary sample V18-1a was conducted to estimate maximum temperature of graphite crystallization according to (Lünsdorf et al., 2014, 2014). Spectra collected (n=14) indicate a temperature of 435 +/- 14 °C.

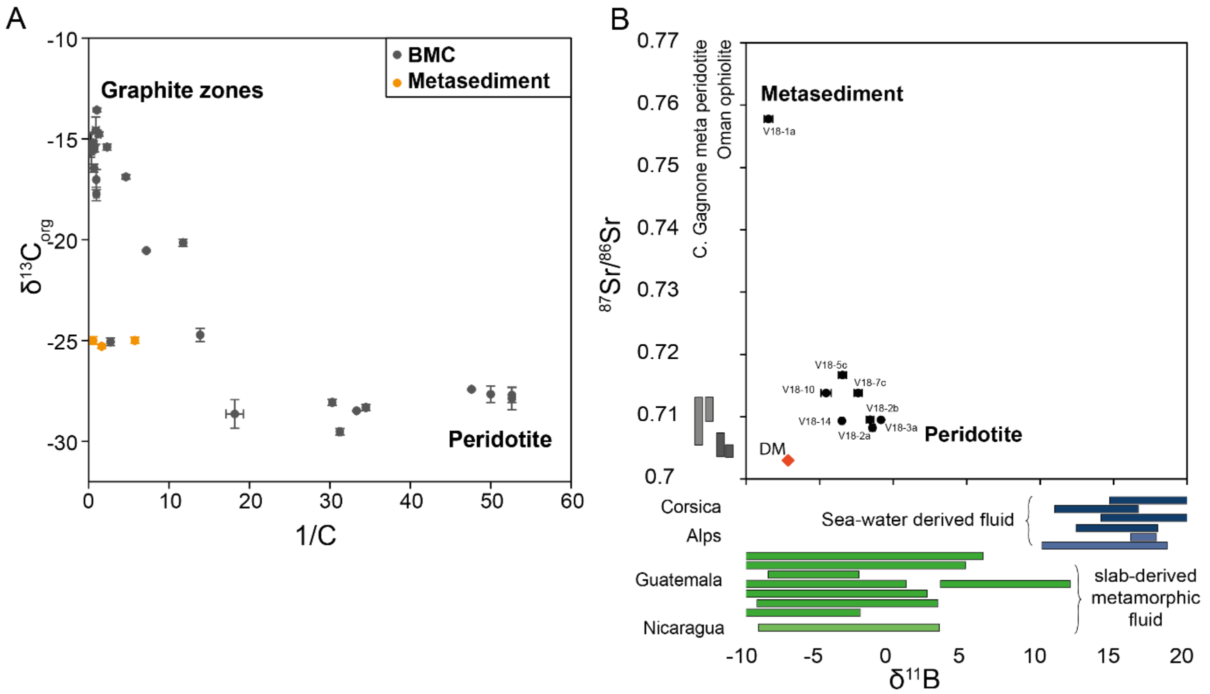

***Fig. 5.7:*** *A: Inverse of organic carbon concentration versus $\delta^{13}C_{org}$ composition of BMC samples. B: $\delta^{11}B$ value versus $^{87}Sr/^{86}Sr$ ratio with data. Boron data from* Martin et al., (2020) *and strontium data from* Cannaò et al., (2016)*(Cima di Gagnone) and* Yamaoka et al., (2012)*(Oman ophiolite). DM: depleted Mantle.*

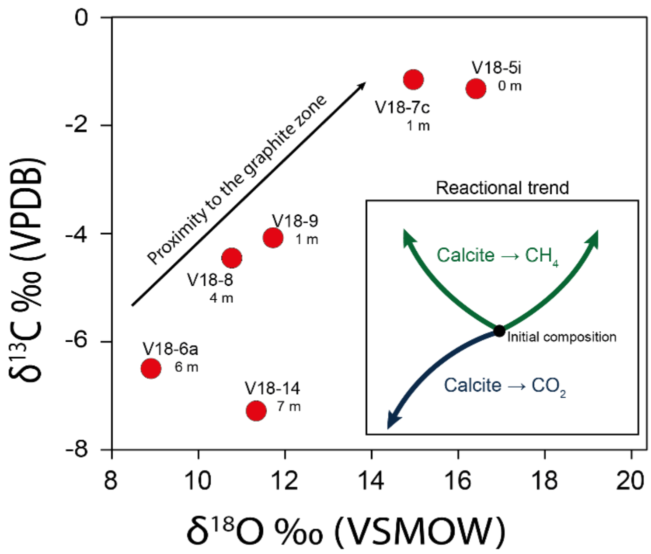

***Fig. 5.8:*** *Carbonate $\delta^{13}C$ and $\delta^{18}O$ Isotopic compositions from the BMC. Indicative proximities to the graphite zones indicated below samples' name. Reactional trend associated with formation of $CO_2$ from prograde decarbonation (blue), and carbonate reduction (green) from Piccoli et al., (2018) and Debret et al., (2015).*

The $\delta^{13}C$ and $\delta^{2}H$ of $CH_4$ extracted from fluid inclusions from the studied BMC and associated metasedimentary formations are available in Table 5.1. Fluid inclusions from metasedimentary sample V18-1 display a $\delta^{13}C$ of -46.3 ‰ and $\delta^{2}H$ of -226 ‰ for $CH_4$ and a $\delta^{2}H$ of -812 ‰ for $H_2$. Partially serpentinized peridotite (olivine-hosted) fluid inclusions from sample V18-2a show values of $\delta^{13}C_{CH4}$ of -12.6 ‰ and $\delta^{2}H_{CH4}$ of -171 ‰ while V18-11 show values of $\delta^{13}C_{CH4}$ of -45.2 ‰ and $\delta^{2}H_{CH4}$ of -226 ‰. Carbonate-hosted fluid inclusions from V18-4, V18-6d and V18-15 show values ranging from $\delta^{13}C_{CH4}$ of -15.5 ‰ and $\delta^{2}H_{CH4}$ of -168 ‰ to $\delta^{13}C_{CH4}$ of -31.3 ‰ and $\delta^{2}H_{CH4}$ of -177 ‰. Graphite-bearing titanite and plagioclase-hosted inclusions from samples V18-12a,c and V18-14 shows values ranging from $\delta^{13}C_{CH4}$ of -12.6 ‰ and $\delta^{2}H_{CH4}$ of -171 ‰ to $\delta^{13}C_{CH4}$ of -12.6 ‰ and $\delta^{2}H_{CH4}$ of -171 ‰. $H_2$ was present in measurable amounts only in sample V18-12c and has a value $\delta^{2}H_{H2}$ of -680 ‰ (Fig. 5.9B).

C1/C2 ratios are presented in Table 5.1 and show a low value of 13.23 for V18-1 typical of thermogenic sources (Martini et al., 2008), whereas samples from the BMC show a wider range of values. Olivine-hosted inclusion in sample V18-2a has a C1/C2 ratio of 1992, while V18-11 has a value of 668. Carbonate-hosted fluid inclusions in V18-4 has a C1/C2 ratio of 6154 and of 635 in V18-6d. The amount of $C_2H_6$ is below the detection threshold in some samples leading to the absence of C1/C2 ratio.

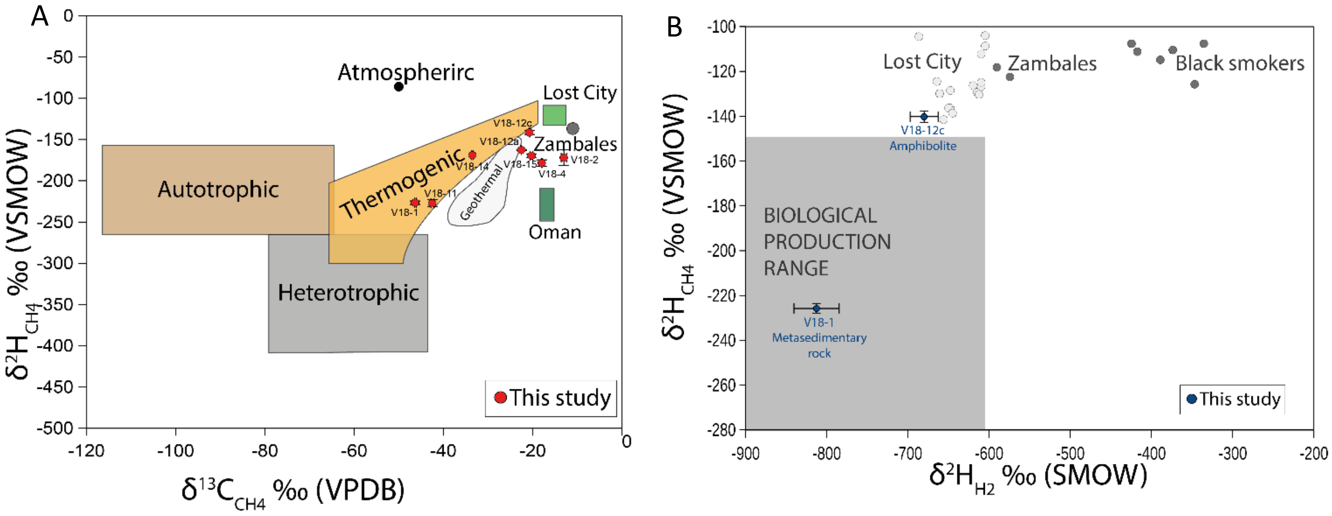

***Fig. 5.9:*** *A: Ranges of $\delta^{13}C$ and $\delta^2H$ measured in methane-rich fluid inclusions. A variety of sources are displayed as references from* Bradley and Summons, (2010). *'Autotrophic' refers to methane produced by $H_2/CO_2$ methanogenesis, while 'heterotrophic' refers to methane produced by fermentation of acetate or consumption of methylated organic compounds. 'Thermogenic' refers to cracking of biologically derived oils, while 'geothermal' refers to cracking of high-molecular-weight organic compounds. B: $\delta^2H$ values of $CH_4$ and $H_2$ from fluid inclusions. Methane and hydrogen produced by activity of methanogens are expected to fall within the grey box and additional reference data from* Bradley and Summons, (2010).

### 5.4.6 Sr and B results

Strontium isotopic analyses were conducted on different BMC rock types and are presented in Table 5.1 and Fig. 5.7B. The $^{87}Sr/^{86}Sr$ of the sample V18-1a from the Ottauquechee formation is 0.7578. The values of the BMC least serpentinized peridotites (V18-2a,b and V18-3a) range from 0.7082 to 0.7095 and $^{87}Sr/^{86}Sr$ of least altered amphibolite (V18-14) is 0.7093. Serpentinite and samples from the graphite zones have similar $^{87}Sr/^{86}Sr$ values between 0.7107 and 0.7177. Overall, the $^{87}Sr/^{86}Sr$ ratios of BMC samples is higher than Basaltic Achondrite Best Initial (BABI), and are not compatible with Mid-Ocean Ridge Basalt (MORB) signature and depleted mantle (DM) signature.

In a similar way, Boron isotopes $\delta^{11}B$ were investigated to assess fluid sources in the BMC. $\delta^{11}B$ values are negative (Table 5.1, Fig. 5.7B). The $\delta^{11}B$ of the Ottauquechee formation (V18-1a) is -8.5 ‰. The $\delta^{11}B$ of the BMC least serpentinized peridotites (V18-2a,b and V18-3a) ranges ranging from -1.6 to -0.8 ‰ and $\delta^{11}B$ of the least altered amphibolite (18-14) is -3.49 ‰. Serpentinite samples (V18-7c and V18-10) and from Graphite zone A (V18-5c) have $\delta^{11}B$ values ranging from -4.6 to -2.4 ‰.

## 5.5 Discussion

### 5.5.1 Origin of the Belvidere graphite

The BMC graphite distribution and isotopic signatures suggest a fluid-deposited origin. The graphite concentrations in the BMC up to 3.91 wt% are very high compared to the average organic carbon content of subducted ultramafic and mafic rocks, usually clustering at 0.1 wt % (Alt and Teagle, 1999; Collins et al., 2015; Schwarzenbach et al., 2013; Shilobreeva et al., 2011). The graphite $\delta^{13}C$ (-15.9 ‰, ± 1‰) in Zone A and (-15.3 ‰, ± 1.2‰) in zone B differs from the total organic carbon signature of subducted mafic and ultramafic rocks from -26.6 ‰ to -28 ‰ (Alt and Teagle, 1999; Collins et al., 2015; Schwarzenbach et al., 2013; Shilobreeva et al., 2011), and from mantle carbon at -10 ‰ to -4 ‰ (Deines, 1992; Javoy et al., 1986).

The graphite host rocks also confirm the hypothesis of fluid circulation and intense metasomatism. In particular, in Graphite zone A, structural and geochemical features indicate that the rock was transiently enriched in Ca, Si and Al, as indicated by the presence of tremolite and chlorite, as observed in sample V18-Y1 with the formation of tremolite matrix sealing serpentine clasts (Fig 5.5D). This stage is followed by graphite precipitation, as observed in samples V18-Yb and V18-5c, with the growth of tremolite crystal, the partial preservation of antigorite clasts and the precipitation of graphite coronae around tremolite crystals (Fig. 5.5(A,E)). Finally, the tremolite was statically replaced by antigorite, indicating a loss of Ca and enrichment in Mg, as observed in sample V18-5a (Fig. 5.5B). The collected samples suggest that this stage was more intense at the edges of zone A. Carbonate precipitation at zone A selvages may have occurred during the initial stages of fluid infiltration, or earlier. Microstructural features indicate that the initial stage of fluid infiltration was accompanied by fluid overpressure and brecciation, followed by intense syn-tremolite shear deformation, and finally static replacement of tremolite by antigorite.

In Graphite zone B, graphite precipitated at the interface between ultramafic and mafic rocks. Also, in this case, petrography and microstructural analysis indicate that fluid overpressure was locally achieved in the mafic rocks adjacent to the ultramafic rocks, as indicated by brecciation of plagioclase and precipitation of carbonate and graphite.

### 5.5.2 Source of carbon for methane formation

In this section, we discuss the possible source of carbon responsible for the graphite and methane formation in the BMC.

The graphite isotopic composition alone does not allow identifying a clear carbon source. In particular, the graphite signature of -17/-15 ‰ may be compatible with either organic or inorganic sources, internal or external to the BMC. For example, graphite in metasedimentary rocks from Appalachian metasedimentary rocks shows $\delta^{13}C$ ranging from about -27 to -2 ‰ (Evans et al., 2002; Zhang et al., 2018). Fluid-deposited graphite from New Hampshire, which is interpreted to derive from mixing of metasediment-derived fluids, shows $\delta^{13}C$ values ranging from -29 to -9 ‰ (Rumble et al., 1986). The methane isotopic signature of $\delta^{13}C$ and $\delta^{2}H$ from BMC rocks indicate, at least in some samples, the contribution of organic matter (Fig. 5.9A). Samples V18-11, with an isotopic composition of -45.2 ‰ for $\delta^{13}C_{CH4}$ and -226 ‰ for $\delta^{2}H_{CH4}$ has value similar to the methane from metasedimentary sample V18-1 (-46.3 ‰ for $\delta^{13}C_{CH4}$ and -226 ‰ for $\delta^{2}H_{CH4}$). In other samples of partially serpentinized peridotite petrographically equivalent to V18-11, sample V18-2, the methane signature is strongly different ($\delta^{13}C_{CH4}$ -12.9 ‰; $\delta^{2}H_{CH4}$ -171 ‰), which may be consistent with processes involving various sources, including organic and inorganic (i.e., carbonate) sources, internal or external to the BMC.

The combination of $^{87}Sr/^{86}Sr$ and $\delta^{11}B$ data show a mixing trend between two poles (Fig. 5.7B), with a metasedimentary pole defined by V18-1 with low $\delta^{11}B$ value (-8.48 ‰) and high $^{87}Sr/^{86}Sr$ value (0.7578) and a serpentinized peridotite pole defined by V18-2b and V18-3a ($\delta^{11}B$=-0.83 ‰ and -1.41 ‰, $^{87}Sr/^{86}Sr$= 0.7095 and 0.7082). The $^{87}Sr/^{86}Sr$ values of the BMC ultramafic and mafic rocks are higher relative to their protolith rocks which suggest contamination by sedimentary or crustal reservoirs (Cannaò et al., 2016; Yamaoka et al., 2012). The $\delta^{11}B$ values of the BMC rocks are negative, which is consistent with serpentinization and metasomatism driven by the infiltration of metamorphic fluids (Martin et al., 2020).

The presence of high nitrogen concentrations in the BMC fluid inclusions suggests a metasedimentary source (Boutier et al., 2021 and references therein). Additionally, the presence of abundant sulfur in the BMC fluid inclusions is also consistent with a metapelitic fluid source (Bebout and Fogel, 1992; Evans et al., 2014; Kelemen and Manning, 2015; Plank and Manning, 2019).

According to the above considerations, the study site recorded the infiltration of metasediment-derived fluids from the surrounding formations. At least a part of the carbon in the system was sourced from these external metasedimentary reservoirs. For example, fluid inclusion extracted from the metapelitic sample V18-1a contains abundant $CH_4$. However, the collected data also outline an internal production of $CH_4$. For example, SEM-based imaging suggests carbonates of the BMC as a potential source of carbon for methane production through reduction processes (Sections 5.4.2). The carbonate $\delta^{13}C$ and $\delta^{18}O$ data in the BMC ultramafic rocks may be interpreted as a reactional trend (Fig. 5.8). Graphite-free carbonated serpentinites (V18-6a and V18-14) show low carbonate $\delta^{13}C$ and $\delta^{18}O$ values while carbonate from graphite-bearing ultramafic rocks (V18-7c and V18-5i) shows higher $\delta^{13}C$ and $\delta^{18}O$ values. Carbonate-graphite isotopic equilibrium would lead to unrealistic temperatures or gradients, from 150°C to 550°C from the graphite-free selvages to the center of Graphite zone A (Bottinga et al). Instead, carbonate methanation is predicted to produce such a trend (Fig. 5.10; Galvez et al., 2013; Vitale Brovarone et al., 2017). Alternatively, reactions of silicate along increasing metamorphic conditions is known to induce a decrease in $\delta^{13}C$ (Cook-Kollars et al., 2014; Piccoli et al., 2016) and could explain the reactional trend. However, the observed isotopic shift seems to correlate with the formation of graphite rather than with an increase in carbonate-silicate reactions. Based on the above considerations, the lower $\delta^{13}C$ carbonates are interpreted as the earliest ones in the studied BMC rocks. These values are low compared to marine carbonate and carbonate in ophicarbonates (Collins et al., 2015). Such low values may have been achieved as a result of prograde decarbonation reactions, and successively shifted towards higher values through carbonate reduction, or as a result of precipitation from carbonic fluids derived from OC-bearing sedimentary rocks.

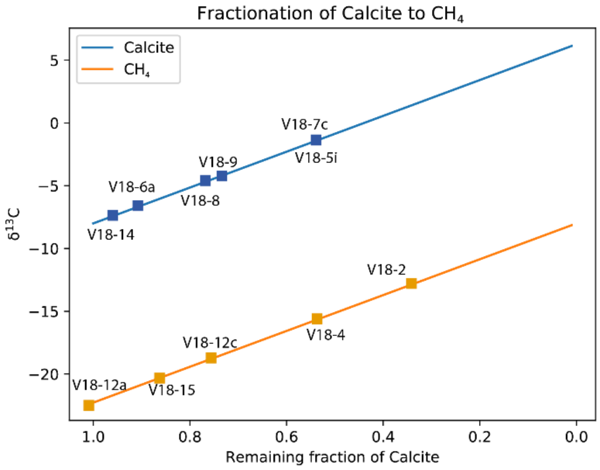

***Fig. 5.10:*** *Modeling of equilibrium fractionation for methanation of calcite at 450 °C. A calcite with an initial* δ$^{13}$C isotopic composition of -8 ‰ *is considered, using fractionation factor from* Bottinga, (1969).

### 5.5.3 Fluid evolution and mechanism of graphite formation

In this section, we propose a reconstructed evolution for the fluids infiltrating the BMC and the related formation of methane and graphite.

In a COH system, the graphite stability field expands with increasing pressure, and diminishes with increasing temperature (Cesare, 1995). Moreover, graphite stability is dependent on the fluid component speciation, which is in turn dependent on the fluid oxygen fugacity ($fO_2$). The redox state of a ternary COH system has been discussed as a function of the parameter $X_O$ ($X_O=\frac{n_O}{n_O+n_H}$) (Connolly, 1995; Connolly and Cesare, 1993). The maximum of graphite stability in a COH fluid is observed when the fluid speciation is dominantly $H_2O$, the so called "water maximum" ($X_O$=1/3). At fixed P and T, fluid infiltration can lead to graphite precipitation if $X_O$ changes during the fluid-rock interaction. In a similar fashion, fluid desiccation will lead to a change in the ratio of $H_2O$, $CO_2$ and $CH_4$ in the fluid and to the precipitation of graphite (Duke and Rumble, 1986). Fluid interactions have the potential to deposit graphite in amounts varying as a function of the intensity of the $fO_2$ variations. Fluid desiccation leads to graphite precipitation proportional to the intensity of the dehydration.

Based on the collected data, the earlier metamorphic fluid infiltration event can be described as an $H_2O$-rich fluid equilibrated with a carbon-bearing metasedimentary source. Sample V18-1 suggests that this fluid may have had a low $\delta^{13}C$ signature (Table 5.1). This initial composition may be preserved in the fluid inclusions of samples, V18-11 and V18-14, as indicated by the $\delta^{13}C$ and $\delta^{2}H$ values of $CH_4$. A slightly reduced ($X_O \gtrsim ⅓$) graphite-saturated COH fluid near water maximum can be dominated by $CH_4$ in respect to $CO_2$. For instance, a fluid at QFM -0.5 at 450°C and 11 kbar would consist of 98% (molar) of $H_2O$ with a $\frac{CO_2}{CH_4+CO_2}=0.32$ ($X_O$=0.33). Such fluid would have plenty of water available for hydration reactions. Based on the fluid inclusion composition presented in Supplementary material 1, this fluid infiltration may have also been responsible for the metamorphic serpentinization of the BMC (Boutier et al., 2021).

Low $fO_2$ conditions produced by serpentinization are suitable environments to promote the reduction of carbon species either in the fluid or as carbonates. The BMC presents evidence of carbonate reduction illustrated by SEM imaging (V18-7c) (Fig. 5.5C), suggesting reduction of dolomite into calcite and brucite along with the release of $CH_4$ and $H_2O$ (Peng et al., 2021).

Because a fluid at water maximum corresponds to the minimum of carbon solubility, lowering the $fO_2$ of the fluid will increase the fraction of carbon species and can quickly impose the global isotopic composition from the newly formed methane. Figure 5.9A shows the mixing trend of the sedimentary source at $\delta^{13}C$ =-45 ‰ $\delta^{2}H$ =-240 ‰ and the methane produced through carbonate reduction ranging from $\delta^{13}C$ = -23 ‰ to -12 ‰ and $\delta^{2}H$ = -140 ‰. Figure 5.10 shows that methanation of carbonate from the BMC is consistent with the isotopic value of the methane ranging outside the thermogenic domain. However, such a trend could have been enhanced to lower values by the mixing with the negative ($\delta^{13}C$= -45 ‰) metasedimentary source.

We propose that the process of graphitization is more likely to be the result of the precipitation of a carbon-saturated fluid encountering redox changes at a shear zone and at lithologic contact. The transformation of methane at $\delta^{13}C$ = -23 ‰ produced from carbonate methanation would lead to a graphite at $\delta^{13}C$ = -15 ‰ to -16.5 ‰ at 400-450°C (temperature constrained by the presence of antigorite throughout the graphite precipitation process and RSCM on metasedimentary rocks from the Ottauquechee formation). Moreover, the mixing of an external metasedimentary fluid with a $\delta^{13}C$ of methane at -45 ‰ (sample V18-1) and a methane-rich fluid around $\delta^{13}C$ = -23 ‰ (samples V18-2 and V18-4) formed inside the BMC, would lead to the precipitation of graphite at $\delta^{13}C$ =-14 ‰ to -18 ‰ at 450°C and 11 kbar (pressure constrained by Honsberger, 2015; Laird et al., 1993 for the BMC). Following this mechanism, the amount of graphite precipitated is estimated to be 1 mol for 200 mol of fluid and corresponds to 4% of the carbon in the initial fluid (Fig. 5.11) (source Thermotopes-COH see Part. 6).

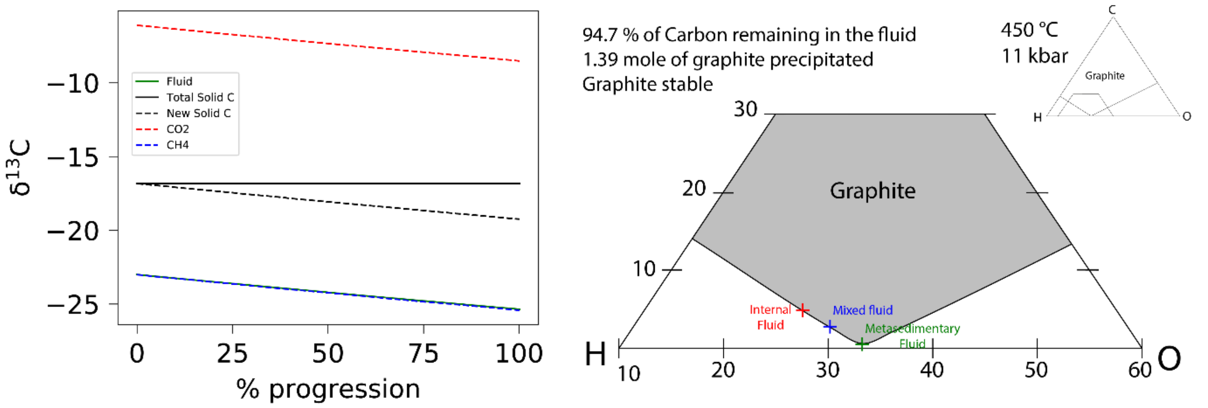

***Fig. 5.11:*** *Modeling of the mixing of a slightly reduced fluid with an isotopic composition of* $\delta^{13}C$=-45 ‰ and a reduced fluid with an isotopic composition of $\delta^{13}C$=-23 ‰ at 450°C and 11 kbar. The graphite precipitating from this interaction will average at $\delta^{13}C$ = -17 ‰. The model does a titration of one fluid in another and tracks the carbon activity of the system according to equation form Huizenga (2004). “Total Solid C” tracks the global isotopic composition of

the graphite in the system while “New Solid C” corresponds to the compositions of the neoformed graphite.

This model shows that the observed carbon isotope values of graphite, carbonate, and methane can be explained through the infiltration of a single low $\delta^{13}C$ fluid. An alternative interpretation may consider infiltration of metasediment-derived fluids with $\delta^{13}C$ varying as a function of the carbonate-OC ratio of the source rocks. The model suggested relies on an OC-dominated source. Instead, carbonate-dominated, OC-bearing metasedimentary sources may explain the signature of the earlies carbonate generations found at the selvages of Graphite zone A, as observed for fluid-deposited carbonates found in metasomatized ultramafic rocks in New Caledonia (Spandler et al., 2008).

The silicates show potential evidence of fluid infiltration, evolution, and mixing. Samples from Graphite zone A show an initial Ca enrichment consistent with sediment-derived fluids, followed by a Ca depletion and Mg enrichment, which may be consistent with a reinjection of evolved, serpentinization-related fluids inside a preferential fluid pathway such as graphite zones A and B. The petrological features observed at the edge of the graphite zone A are consistent with the escape of an internal Mg-rich fluid leading to the retromorphose of tremolite crystals in antigorite (V18-5a)(Fig. 5.5B).

In summary, the precipitation of graphite in the BMC can be summarized as follows, and is illustrated in an idealized sketch in Figure 5.12:

1- The BMC was infiltrated by metasediment-derived fluids, resulting in metasomatism (e.g, Ca enrichment; negative $\delta^{11}B$; high $^{87}Sr/^{86}Sr$) along major fluid channels (e.g. Graphite zones A and B).

2- This fluid progressively equilibrated with the BMC ultramafic rocks during pervasive serpentinization of the BMC in the antigorite stability field.

3- The metamorphic serpentinization of the BMC led to decreasing $fO_2$ conditions and internal methane formation through carbonate reduction or respeciation of more oxidized fluids.

4- The $CH_4$-enriched fluids resulting from the BMC pervasive serpentinization were reinjected along fluid channels, causing additional metasomatism (Mg enrichment and Ca depletion) and favoring fluid mixing and leading to graphite precipitation.

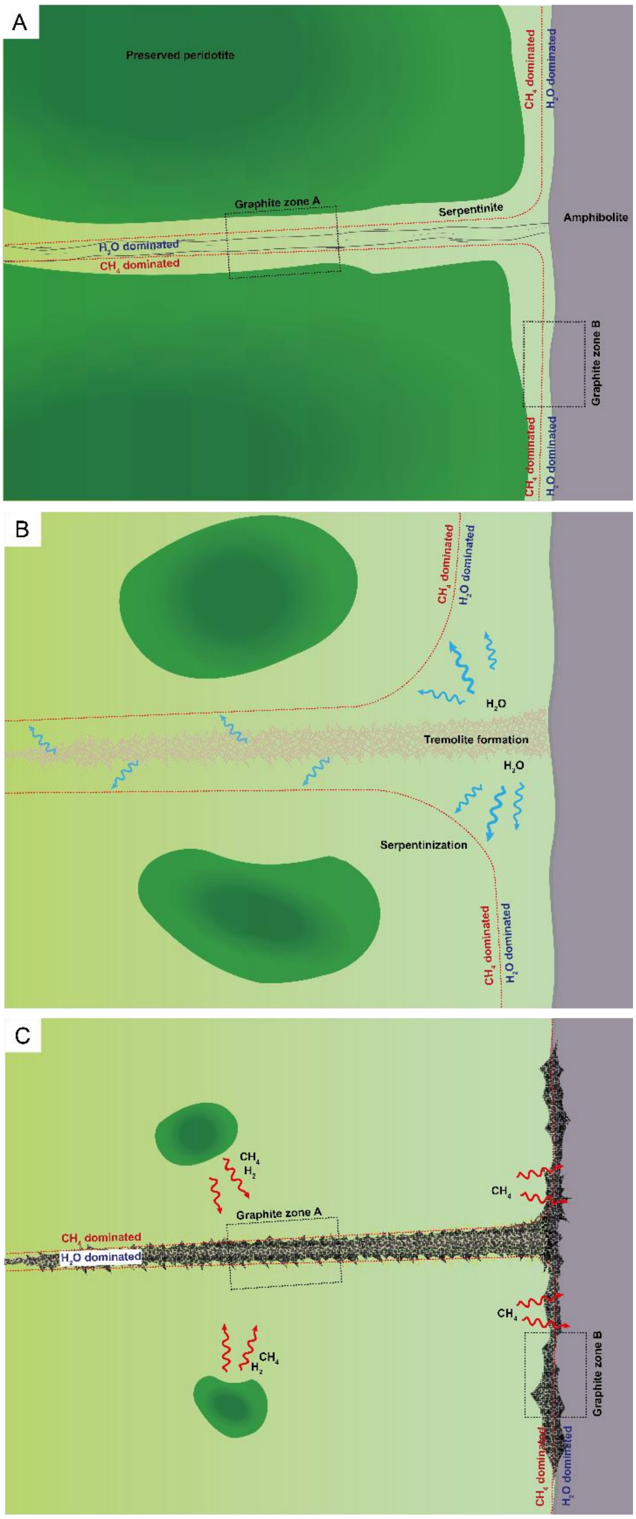

***Fig. 5.12:*** *Proposed model of BMC hydration in subduction zone associated with graphite deposition linked to $CH_4$ migration. A: Initial sage of the BMC in subduction, graphite zone A corresponds to a shear zone and graphite zone B to the lithologic contact with the amphibolite. B: Infiltration of a fluid from metasedimentary rocks. This fluid was $H_2O$ dominated, rich in Ca, Si, C, and N, and produced tremolite metasomatism along the main fluid channels. C: $CH_4$ released from serpentinization escape along main fluid channel and precipitate graphite when encountering redox barrier. D: As the $CH_4$ production and escape progress, the $CH_4$ becomes dominant across the study zone and the redox front progresses in the amphibolite.*

### 5.5.4 Consideration on the origin of metamorphic methane in the BMC

The BMC methane is an example of an increasing number of reports of methane in subduction zone metamorphic rocks. Abiotic methanogenesis in ultramafic rocks has been shown at natural conditions spanning seafloor hydrothermalism, magmatism, and on-land surficial serpentinization (Etiope and Sherwood Lollar, 2013). This is an important process in deep subsurface biosphere research and geoastrobiology, as it is considered as a source of prebiotic organic compounds and their possible role on the origin of life on Earth and potentially elsewhere (Colman et al., 2017; Holm et al., 2015; Schulte et al., 2006).

The initial infiltrating fluid of the proposed evolution may have contained $CH_4$. If this fluid equilibrates at water maximum, graphite-saturated conditions, a roughly comparable concentration of $CH_4$ and $CO_2$ is expected. Sample V18-1 from the Ottauquechee metasedimentary formation contains $CH_4$ in fluid inclusions. This $CH_4$ can be interpreted as methane formed as a result of graphite-saturated COH thermodynamics, as conventionally proposed for metapelitic rocks, which would be by definition abiotic. However, the analyzed $\delta^{13}C$ and $\delta^{2}H$ data of $CH_4$ form this sample indicate a thermogenic origin, which is classically considered biotic. Thermogenic production of $CH_4$ is generally believed to be limited to about 300 °C (Mangenot et al., 2018; Stolper et al., 2015, 2014a). The Ottauquechee metasediments experienced metamorphism to about 434 °C, as indicated by RSCM thermometry. This temperature is well above the conventional limit of thermogenic methane. The interaction of this fluid with the BMC promoted serpentinization and additional reduction of the fluid. During this event, the $CO_2$ present in the infiltrating fluid (for reference, a graphite saturated fluid at 400 °C, 10 kbar, and Xo = 0.333 contains a $CH_4/CO_2$ ratio of 1) is expected to be converted into $CH_4$ through a process of $CO_2$ reduction that is, by definition, abiotic. However, its signature would still track a biotic source.

The reduction of carbonates by the serpentinization-related reducing fluids promoted additional formation of methane. This methane must be considered abiotic in origin and, depending on the degree of mixing with the external fluid, may still record its inorganic source. However, in the case of the BMC, the isotopic signature of the reactant carbonates was negative (-7.26 to -1.43 ‰) and was potentially affected by previous interaction with fluids recording an organic carbon source.

Grozeva et al., 2020 report $\delta^{13}C$ isotopic values for abiotic methane in inclusions from two actives serpentinization systems ranging from -16.7 ‰ to -4.4 ‰ in the Von Damm hydrothermal field and ranging from -12.4 ‰ to -2.8 ‰ for the Zambales ophiolite. C1/C2 values range from 163 to 1372 and cluster around 400 for both datasets. The main mechanism proposed for methane formation is the conversion of mantle $CO_2$ to $CH_4$ and the carbon isotopic composition of the $CH_4$ reflects the isotopic composition of mantle $CO_2$ along with variations caused by the carbon isotopic composition in the host rock. Data from Grozeva et al. 2020 are akin to measurement from V18-2 and V18-4 fluid inclusions reflecting the abiotic hydrocarbon production of the BMC. However, the fluid composition of the BMC (rich in C, N, and S) strongly differs from the inclusions analyzed by Grozeva et al. 2020, and the collected data point to a different, metamorphic origin in the Taconic subduction zone.

The distribution of more biotic or abiotic signatures across the BMC depict the complexity of the process of fluid infiltration and fluid-rock interactions that affected the massif. Also, the collected data stress the complexity of methane generation and evolution in metamorphic settings and call for additional analyses on these metamorphic gases. In particular methane clumped isotope analysis has proven to provide additional insight on the discrimination between abiotic and biotic processes (Ono et al., 2021; Shuai et al., 2018; Young et al., 2017).

In conclusion, the results obtained in this work indicate that the origin and chemistry of metamorphic methane can be more complex than previously assumed.

### 5.5.5 Implication on large scale methane production

Fresh ultramafic bodies in subduction can act as a massive converter of $CO_2$ in $CH_4$ and other reduced carbon phases such as graphite. Because these fluids can circulate in the subduction channel, they can have a significant impact on the redox budgets in the subduction zone. Redox barriers can act as sinks of carbon, such as through graphite deposition, effectively halting a percentage of the C transfer in metamorphic fluids.

When considering the serpentinizing mantle wedge, which could similarly act as a powerhouse of $H_2$ and $CH_4$ formation, the path taken from the resultant fluids will impact significantly on the becoming of these compounds. This can hamper the quantification of the methane release from subduction zones, as many redox barriers – including the activity of microorganisms within the biosphere – can be expected within the mantle wedge and above inside the crust.

## 5.6 Appendices

### 5.6.1 Fluid inclusions composition

Fluid inclusions observed across samples in the study zone were investigated using microRaman microscopy. Inclusions were found in olivine, calcite, titanite and plagioclase crystals. Spectra reveals $CH_4$ bands (2912 $cm^{-1}$), as well as $N_2$ (2327 $cm^{-1}$), $NH_3$ (3324 $cm^{-1}$), S-H/$H_2S$ (2575 $cm^{-1}$). $CH_4$ and $N_2$ are particularly dominant across the study zone.

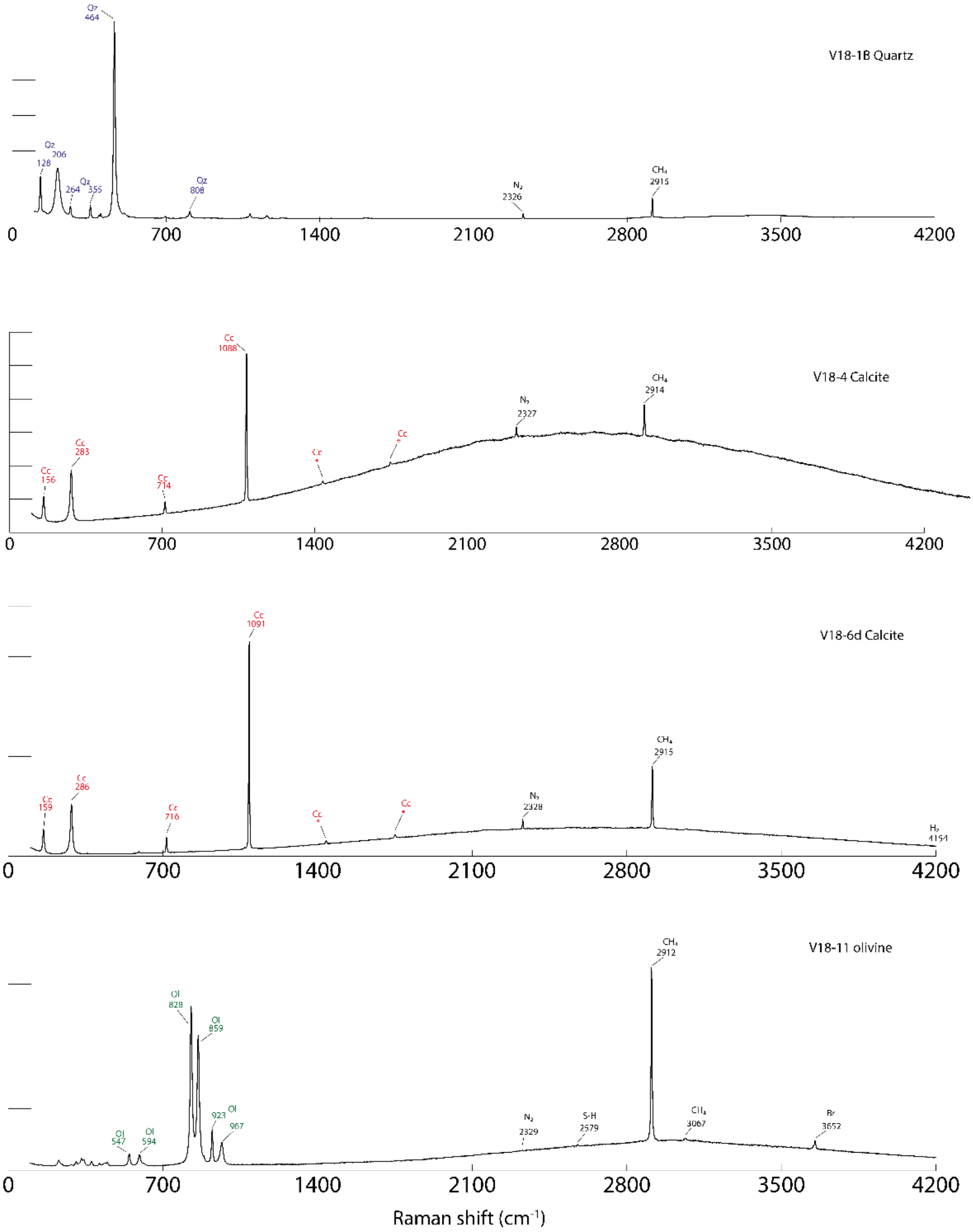

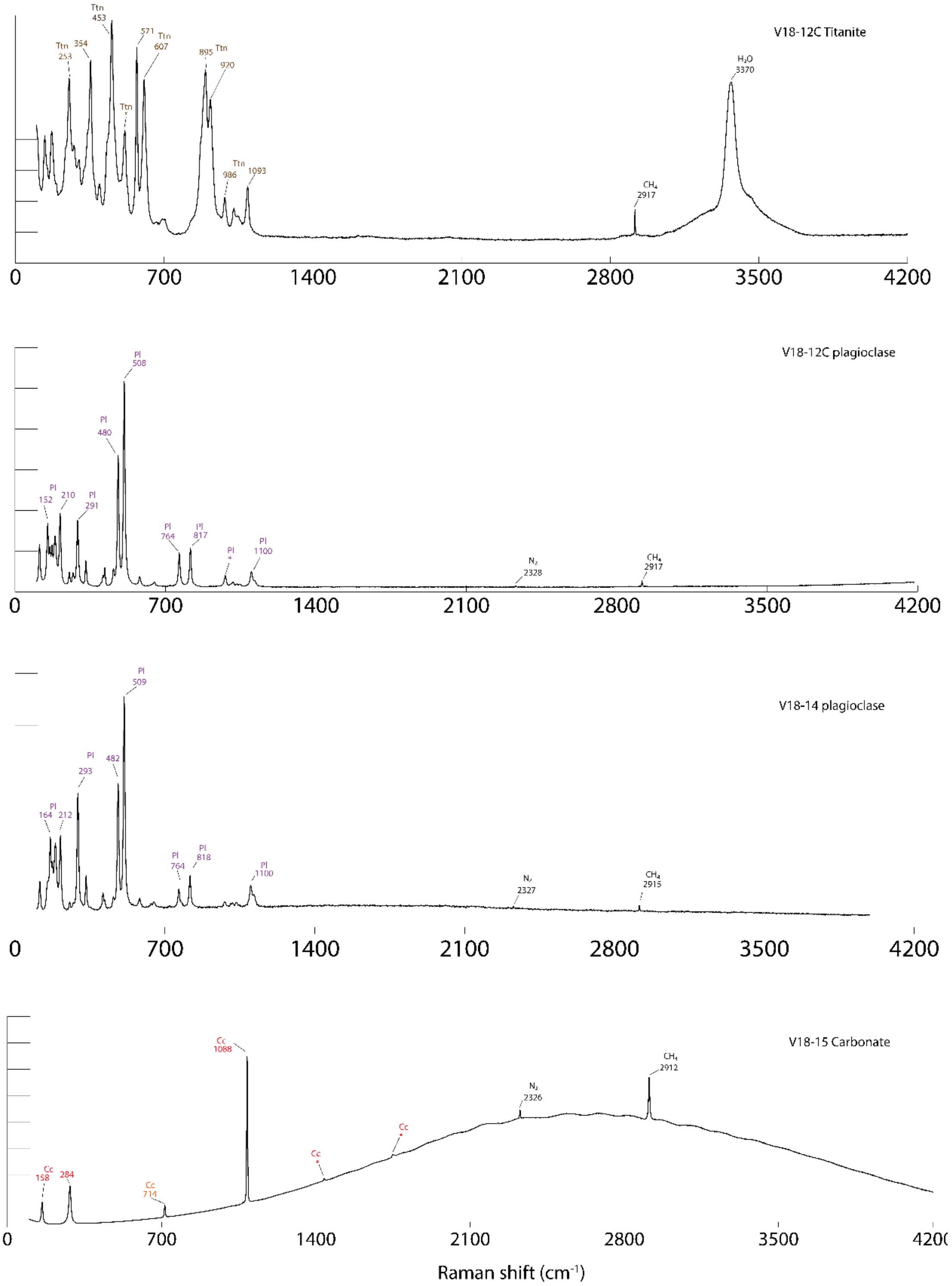

*Supplementary figure 1: Compilation of Raman spectra of fluid inclusion from the study zone.*

### 5.6.2 REE spectra

Rare-earth elements spectra (Chondrite-normalized) of representative samples. Sample V18-1a is enriched in REE and the pattern corresponds to a differentiated crustal material (Balaram, 2019). In the same way ultramafic samples are depleted in REE, typical of upper mantle signatures. Samples from Graphite zone A do not show different a pattern from the rest of the ultramafic body. Samples from the amphibolite body and Graphite zone B show higher REE concentrations relative to the BMC ultramafic rock and pattern typical of gabbroic rocks (Brophy and Pu, 2012), with the Eu anomaly attributed to preferential incorporation in plagioclase. REE spectra suggest that the protolith of graphite zone A and B, corresponded to depleted mantle, and differentiated mantle, respectively.

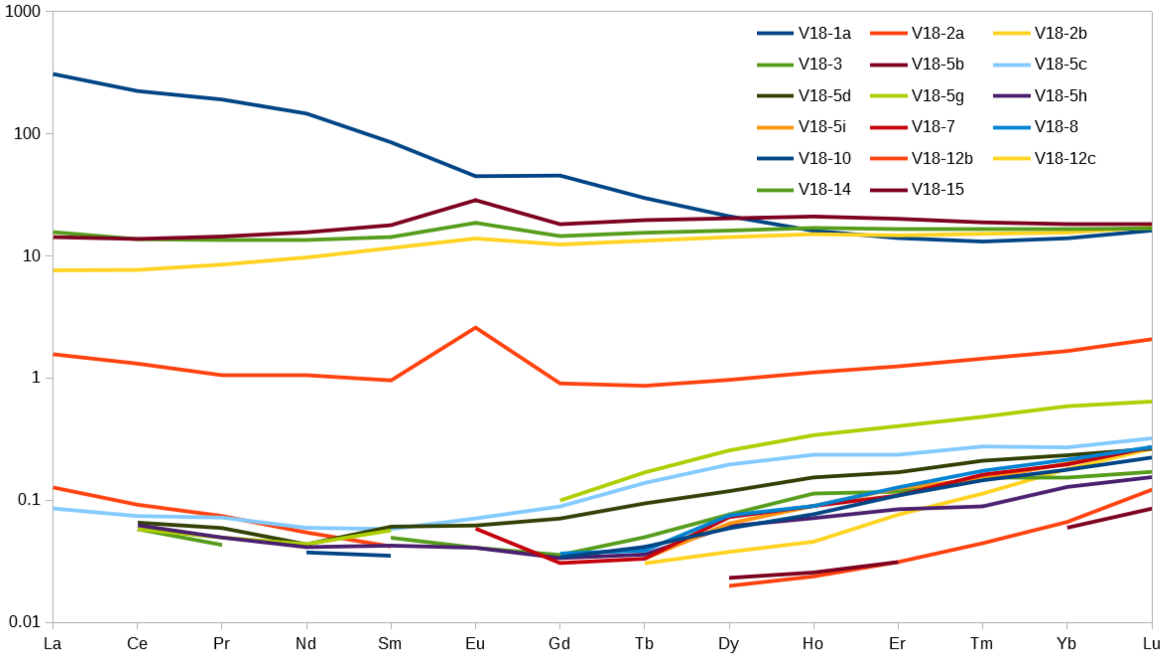

*Supplementary figure 2: REE CHIUR normalized spectra of representative samples from the BMC.*

Major elements:

The MgO vs $Al_2O_3$ ultramafic rocks of the BMC are displayed in supplementary figure 3. The more weakly serpentinized peridotites (18-2a,b) are displaying a relatively high amount of MgO up to 48 wt.% while more fully serpentinized samples have values between 27 and 37 wt.%. This includes serpentinized antigorite-rich samples of the graphite zone A. Tremolite-rich (V18-5c,d) samples from the graphite zone are grouped along lower MgO content 28 wt.% along higher $Al_2O_3$ content over 3 wt.% whereas the rest of the ultramafic samples display values below 2 wt.%.

The $SiO_2$ vs $Fe_2O_3$ contents of ultramafic rocks of the BMC are displayed in supplementary figure 4. The tremolite-rich samples (V18-5c,d) display higher $SiO_2$ content around 48 wt.% while the serpentinized samples range between 37 to 44 wt.%. Iron composition ranges from 6 to 7.5 wt.%. Sample V18-7 displays different compositions owing to the increased presence of carbonate veins as indicated by a CaO content of 15 wt.% along $CO_2$ of 19 wt.%.

Mafic rocks of the BMC show $SiO_2$ content of 34 to 47 wt.%, $Fe_2O_3$ content of 13.2 to 14.5 wt.%, $AL_2O_3$ content of 11.6 to 13.2 wt.% and MgO content of 8 to 12 wt.% for samples not directly affect by the graphite zone B (V18-12c, V18-14, V18-15), and $SiO_2$ content of 50 wt.%, $Fe_2O_3$ content of 7.3 wt.%, $AL_2O_3$ content of 1.8 wt.% and MgO content of 18 wt.% for sample in the graphite zone B (V18-12b).

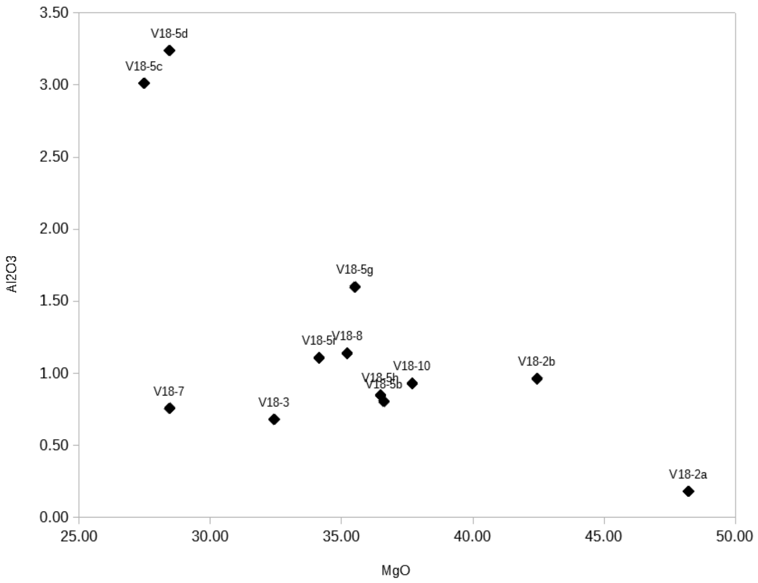

*Supplementary figure 3: $Al_2O_3$ (wt%) vs MgO (wt%) of ultramafic samples of the BMC.*

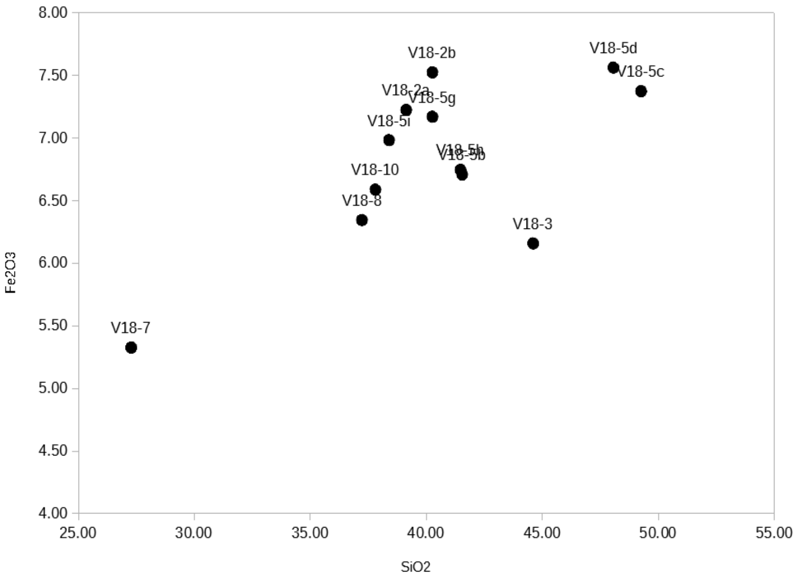

*Supplementary figure 4: $Fe_2O_3$ (wt%) vs $SiO_2$ (wt%) of ultramafic samples of the BMC.*

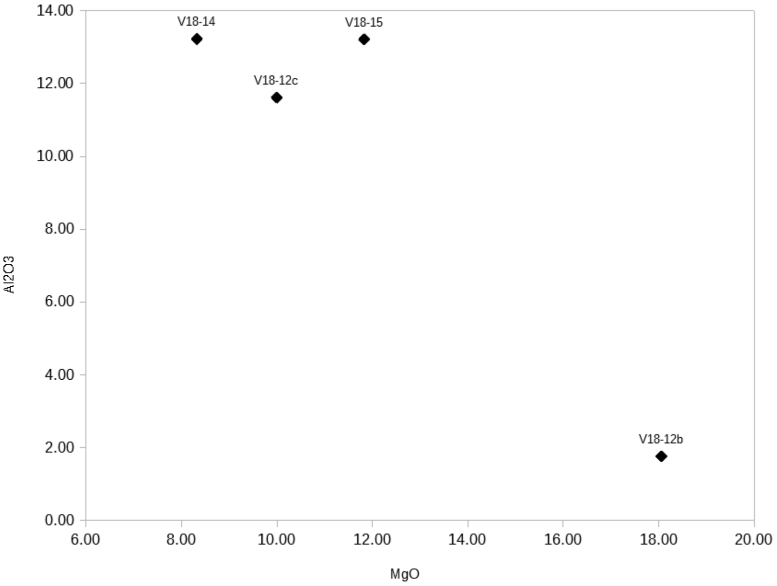

*Supplementary figure 5: $Al_2O_3$ (wt%) vs MgO (wt%) of mafic samples of the BMC.*

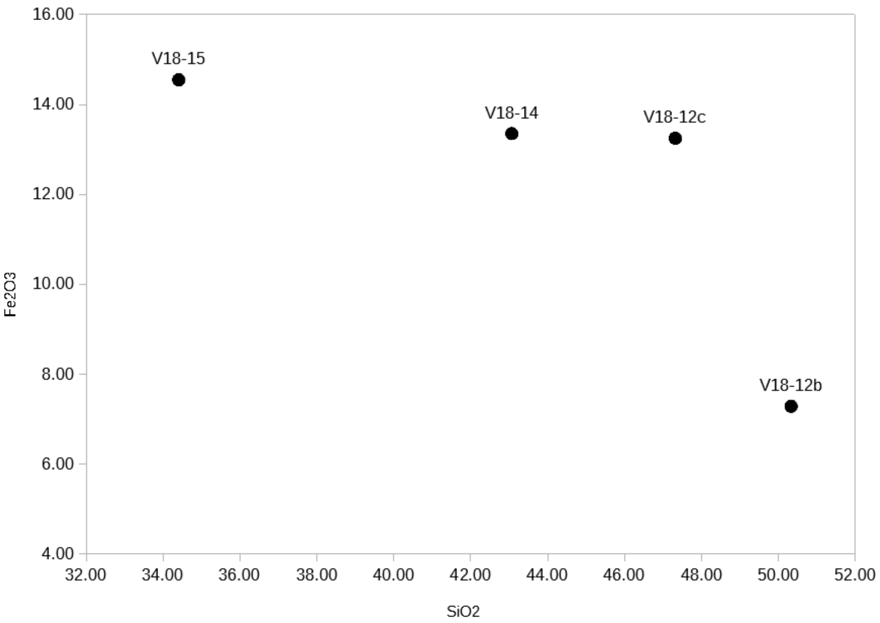

*Supplementary figure 6: $Fe_2O_3$ (wt%) vs $SiO_2$ (wt%) of mafic samples of the BMC.*

### 5.6.3 Details of carbon analyses

Supplementary table 7: solid carbon analyses

| Sample | $\delta^{13}C_{tot}$ | $\delta^{13}C_{tot}$ SD | $\delta^{13}C_{org}$ | $\delta^{13}C_{org}$ SD | C tot (wt%) | Ctot(wt%) SD | C org (wt%) | Corg(wt%) SD |
|---|---|---|---|---|---|---|---|---|
| V18-1a | -24.98 | 0.372 | -25.33 | 0.036 | 0.65 | 0.021 | 0.58 | 0.040 |
| V18-1c | -21.68 | 0.243 | -25.03 | 0.152 | 0.39 | 0.028 | 0.17 | 0.072 |
| V18-1e | -25.16 | 0.053 | -25.03 | 0.150 | 2.07 | 0.135 | 1.99 | 0.104 |
| V18-2a | -12.45 | 0.855 | -27.42 | 0.016 | 0.04 | 0.002 | 0.02 | 0.003 |
| V18-2b | -16.18 | 0.890 | -28.32 | 0.107 | 0.03 | 0.003 | 0.03 | 0.002 |
| V18-3a | -17.02 | 0.714 | -28.07 | 0.149 | 0.05 | 0.004 | 0.03 | 0.003 |
| V18-3b | -15.53 | 0.736 | -28.48 | 0.118 | 0.05 | 0.001 | 0.03 | 0.001 |
| V18-4 | -3.28 | 1.274 | -21.68 | 0.099 | 1.86 | 0.581 | 0.01 | 0.005 |
| V18-5a | -12.79 | 0.609 | -15.49 | 0.677 | 1.84 | 0.325 | 1.39 | 0.388 |
| V18-5b | -14.62 | 0.107 | -15.20 | 0.500 | 1.55 | 0.629 | 1.65 | 0.084 |
| V18-5c | -15.00 | 0.277 | -15.55 | 0.593 | 2.24 | 0.737 | 1.51 | 0.137 |
| V18-5d | -14.58 | 0.139 | -14.59 | 0.895 | 1.41 | 0.063 | 1.08 | 0.154 |
| V18-5e | -17.52 | 0.784 | -17.02 | 0.188 | 1.31 | 0.169 | 1.03 | 0.171 |
| V18-5f | -15.19 | 0.295 | -15.32 | 0.331 | 3.93 | 1.228 | 3.90 | 0.320 |
| V18-5g | -15.69 | 0.137 | -15.57 | 0.707 | 3.86 | 0.164 | 2.76 | 1.082 |
| V18-5h | -15.99 | 0.164 | -16.45 | 0.164 | 1.50 | 0.080 | 1.45 | 0.141 |
| V18-5i | -16.41 | 0.911 | -17.73 | 0.326 | 1.50 | 0.393 | 1.02 | 0.034 |
| V18-6a | -3.99 | 0.111 | -28.64 | 0.181 | 10.84 | 1.111 | 0.05 | 0.031 |
| V18-6d | -4.60 | 0.816 | -29.52 | 0.372 | 9.75 | 1.122 | 0.03 | 0.025 |
| V18-7a | -4.60 | 0.281 | -24.72 | 0.558 | 10.12 | 0.129 | 0.07 | 0.048 |

| | | | | | | | | |
|---|---|---|---|---|---|---|---|---|
| V18-7c | -2.95 | 0.093 | -20.15 | 0.188 | 11.07 | 0.430 | 0.08 | 0.054 |
| V18-8 | -3.42 | 0.721 | -27.70 | 0.414 | 2.51 | 0.109 | 0.02 | 0.002 |
| V18-9 | -5.07 | 0.069 | -27.87 | 0.334 | 0.43 | 0.113 | 0.02 | 0.003 |
| V18-10 | -24.57 | 0.213 | -25.06 | 0.101 | 0.55 | 0.088 | 0.37 | 0.037 |
| V18-11 | -14.57 | 0.381 | -27.66 | 0.110 | 0.03 | 0.000 | 0.02 | 0.001 |
| V18-12a | -12.30 | 0.091 | -15.46 | 0.096 | 5.68 | 0.096 | 3.69 | 0.224 |
| V18-12b | -10.33 | 1.475 | -13.57 | 0.053 | 1.79 | 0.029 | 0.96 | 0.107 |
| V18-12c | -16.67 | 0.615 | -16.88 | 0.152 | 0.22 | 0.026 | 0.21 | 0.024 |
| V18-13 | -13.63 | 0.322 | -14.76 | 0.341 | 1.14 | 0.072 | 0.77 | 0.098 |
| V18-14 | -12.10 | 0.592 | -20.54 | 0.042 | 0.39 | 0.017 | 0.14 | 0.004 |
| V18-15 | -1.40 | 0.604 | -15.40 | 0.449 | 8.69 | 0.373 | 0.43 | 0.052 |

## Supplementary table 8: methane and dihydrogen analyses

| Sample | $\delta^{13}C_{CH4}$ Picarro | $\delta^{13}C_{CH4}$ SD Picarro | $\delta^{13}C_{CH4}$ GC-MS | $\delta^{13}C_{CH4}$ SD GC-MS | $\delta^{2}H_{CH4}$ GC-MS | $\delta^{2}H_{CH4}$ SD GC-MS | $\delta^{2}H_{H2}$ GC-MS | $\delta^{2}H_{H2}$ SD GC-MS |
|---|---|---|---|---|---|---|---|---|
| V18-1 | -46.28 | 0.30 | -46.34 | 0.198 | -226.00 | 2.107 | -812.52 | 27.85 |
| V18-2 | -12.66 | 0.07 | -12.93 | 0.608 | -171.14 | 9.682 | | |
| V18-4 | -15.48 | 0.07 | -17.88 | 0.072 | -177.65 | 3.859 | | |
| V18-6c | -31.25 | 0.41 | -29.00 | 0.657 | | | | |
| V18-11 | -45.23 | 0.14 | -42.49 | 0.335 | -226.72 | 4.326 | | |
| V18-12a | -22.36 | 0.02 | -22.46 | 0.061 | -161.82 | 0.619 | | |
| V18-12c | -18.59 | 0.04 | -20.66 | 0.048 | -140.40 | 2.529 | -680.26 | 17.215 |
| V18-14 | -36.95 | 0.22 | -33.45 | 0.187 | -168.11 | | | |
| V18-15 | -20.19 | 0.09 | -20.18 | 0.302 | -168.87 | 2.418 | | |

# 6 Thermotopes-C, a software for isotopes calculations of C bearing species, and fluid speciation of COH-fluid

Antoine Boutier[1,2]*, Alberto Vitale Brovarone[3,4], Isabelle Martinez[2]

[1]*Dipartimento di Scienze della Terra, Università degli Studi di Torino, Via Valperga Caluso 35, Torino, Italy*

[2]*Institut de Physique du Globe de Paris, Sorbonne Paris Cité, Université Paris Diderot, UMR 7154 CNRS, 1 rue Jussieu, F-75005 Paris, France*

[3]*Dipartimento di Scienze biologiche, geologiche e ambientali, Via Zamboni, 67, Bologna, Italy*

[4]*Institut de Minéralogie, de Physique des Matériaux et de Cosmochimie (IMPMC), Sorbonne Université, Muséum National d'Histoire Naturelle, UMR CNRS 7590, IRD UR206, 75005 Paris, France*

## Abstract

Thermotopes-COH is a python-based software allowing modeling of conventional carbon isotopic exchanges and more advanced thermodynamic and isotopic processes in the C-O-H system and in the 300 - 900 °C and 1 - 50 kbar pressure-temperature range. The software allows user-friendly modeling and graphical visualization of five major functions: (1) Carbon isotope equilibrium between two phases, (2) Carbon isotope fractionation modeling, (3) Multi-component graphite precipitation, (4) C-O-H fluid speciation, and (5)

dissolution/precipitation. The software is available for Windows or MacOS. Data produced by the software can be extracted as .txt file and .svg file. Along with a description of the software functions, this contribution also provides practical examples based on published geological data.

## 6.1 Introduction

The carbon cycle is a central topic of the Earth-system sciences, linking geological and biological processes and shallow to deep energy and environmental quests (Berner, 1999; Dasgupta, 2013; Dasgupta and Hirschmann, 2010; Evans, 2011). In particular, carbon is omnipresent in geologic fluid, either in small amounts in aqueous fluid or dominant in $CO_2$-rich or hydrocarbon-rich fluids (Connolly and Cesare, 1993; Kokh et al., 2017). Isotopic geochemistry has long been used to track sources and processes of geologic systems (Bebout and Fogel, 1992; Duke and Rumble, 1986; Kitchen and Valley, 1995; Luque et al., 2012; Mason et al., 2017b; Ray, 2009; Ray and Ramesh, 2000; Stachel et al., 2017a; Valley, 2018). Although numerical tools allowing computation of simple isotope equilibria exist (Beaudoin and Therrien, 2009, 2004), such computations are often done by the use of spreadsheets or similar tools.

The isotopic evolution of a redox-sensitive element like carbon is strongly related to the thermodynamics of the considered geologic system. The COH thermodynamic system has long been used to assess the evolution of carbon-bearing fluids as a function of pressure (P), temperature (T), and redox state (e.g., $fO_2$; $X_O$; Cesare, 1995; Connolly, 1995; Connolly and Cesare, 1993; Taylor and Liou, 1978; Taylor and Green, 1986; Ulmer and Luth, 1991). It also provides a solid thermodynamic basis to reconstruct the isotope evolution of molecular carbon-bearing fluid species (mainly $CH_4$ and $CO_2$) and graphite/diamond as a function of the considered P-T-redox variables. Although resources to perform simple isotope equilibria are available (e.g., Beaudoin and Therrien, 2009, 2004), and the equations governing the thermodynamics of the COH system and complex isotope are also available (Burnham et al., 1969; Cesare, 1995; Connolly, 1995; Connolly and Cesare, 1993; de Santis et al., 1974; French, 1966; Holloway, 1984; Huizenga, 2005; Luque del Villar et al., 1998; Ohmoto and Kerrick, 1977; Spycher and Reed, 1988), the integration of these tools into a single, user-friendly software is not available to date.

Thermotopes-COH integrates isotope and COH thermodynamic models in order to facilitate the study of carbon isotopes in the COH system. The software features multiple functions through five interactive tabs: (1) Carbon isotope equilibrium between two phases, (2) Carbon isotope fractionation modeling, (3) Multi-component graphite precipitation, (4) C-O-H fluid speciation, and (5) Dissolution/precipitation. This Python-based software runs on Windows and Mac and requires no installation. It is available at https://zenodo.org/record/6550956. This chapter describes the equation used for each function, along with a practical application based on literature data from Ortega et al., (2010) on the Borrowdale graphite deposit. A user manual is available as a complementary description of the software options and capabilities at https://zenodo.org/record/6550956.

## 6.2 Methods

Thermotopes-COH is subdivided into five interactive tabs. The first three tabs (Isotopic equilibrium, Isotopic fractionation, and Multi-component graphite/diamond precipitation) are solely based on isotopic equations. The last two tabs (Speciation of COH fluids and Graphite/diamond dissolution/precipitation) combine carbon isotopic equations and thermodynamic equations of COH fluids. The following methodological description introduces the equations and models used to compile the isotopic and thermodynamic functions and their integrations.

### 6.2.1 Isotopic database

The carbon isotopic database used in Thermotopes-COH is presented in Supplementary Material S1. Isotopic equations can be presented under various form, such as:

$$\Delta = 1000 ln\alpha = A\frac{(10^{3n})}{T^n} + \cdots + D\frac{(10^6)}{T^2} + E\frac{(10^3)}{T} + F \qquad (1)$$

Where Δ is the “big delta”, α is the fractionation factor, (A,…,D,E,F) are experimentally determined constant and T the temperature in K.

However, the isotopic database of Thermotopes-COH uses a simplified version of the general equation to the second power:

$$\Delta = 1000 ln\alpha = A\frac{(10^6)}{T^2} + B\frac{(10^3)}{T} + C \qquad (2)$$

The isotopic database is built upon the following parameters: isotopic couple, A, B and C constants characteristic of a chemical couple, first species, second species, Initial pathway of reaction, Temperature range of confidence, bibliographic reference.

Ex: Calcite-CO2 = (3.73, -9.81, 3.72, 'Calcite', 'CO2', 'Calcite to CO2', (100,700), '100-700°C-Bottinga, Y. (1969)'), (A, B, C, Calcite, CO2, Calcite to CO2, (Tmin, Tmax), Reference),…

### 6.2.2 Thermodynamic database

The thermodynamic calculations in the Thermotopes-COH software follow the COH model by Huizenga (2005). The thermodynamic data are taken from Holland and Powell (1998) and Shi and Saxena (1992). Oxygen fugacity values for the considered buffers (FMQ: Fayalite-Magnetite-Quartz, HM: Hematite-Magnetite, IW: Iron-Wustite, Ni-NiO, EMOD: Enstatite-Magnesite-Olivine-Diamond/Graphite) are calculated according to Ohmoto and Kerrick, (1977)(FMQ); O'Neill and Wall (1987)(FMQ); Ballhaus et al. (1991)(HM, IW, Ni-NiO); Stagno and Frost (2010)(EMOD); Frost (2018)(HM, IW, Ni-NiO); Miozzi and Tumiati (2020)(FMQ). The thermodynamic dataset for diamond/graphite is from Holland and Powell (1998), data from Day, (2012), and the Gibbs equation of state for carbon Fried and Howard, (2000).

### 6.2.3 Isotopic equilibrium

The first tab of Thermotopes-COH, labeled "Isotopic equilibrium", calculates simple isotopic equilibria between two carbon bearing species (Fig. 6.1).

Isotopic equilibrium between two compounds A and B is calculated following the general expression:

$$\delta_A = \delta_B + \Delta_{A-B} \qquad (3)$$

Where $\delta_A$ is the delta value of A in permil (‰), $\delta_B$ is the delta value of B in permil (‰), $\Delta_{A-B}$ is the big delta between A and B calculated after equation (2) (Kendall and McDonnell, 2012; Sharp, 2017).

For example, the user may select the calcite-$CO_2$ equilibrium and choose the calcite to $CO_2$ pathway to calculate the $CO_2$ carbon isotopic composition from a chosen calcite carbon isotopic composition. The user can then select a fractionation factor from a list of references. Once a valid temperature in °C, and a valid isotopic composition in the $\delta^{13}C$ notation are entered, the big delta ($\Delta$), the fractionation factor $\alpha$ and the isotopic compositions of the selected species will automatically be updated and displayed on the interface.

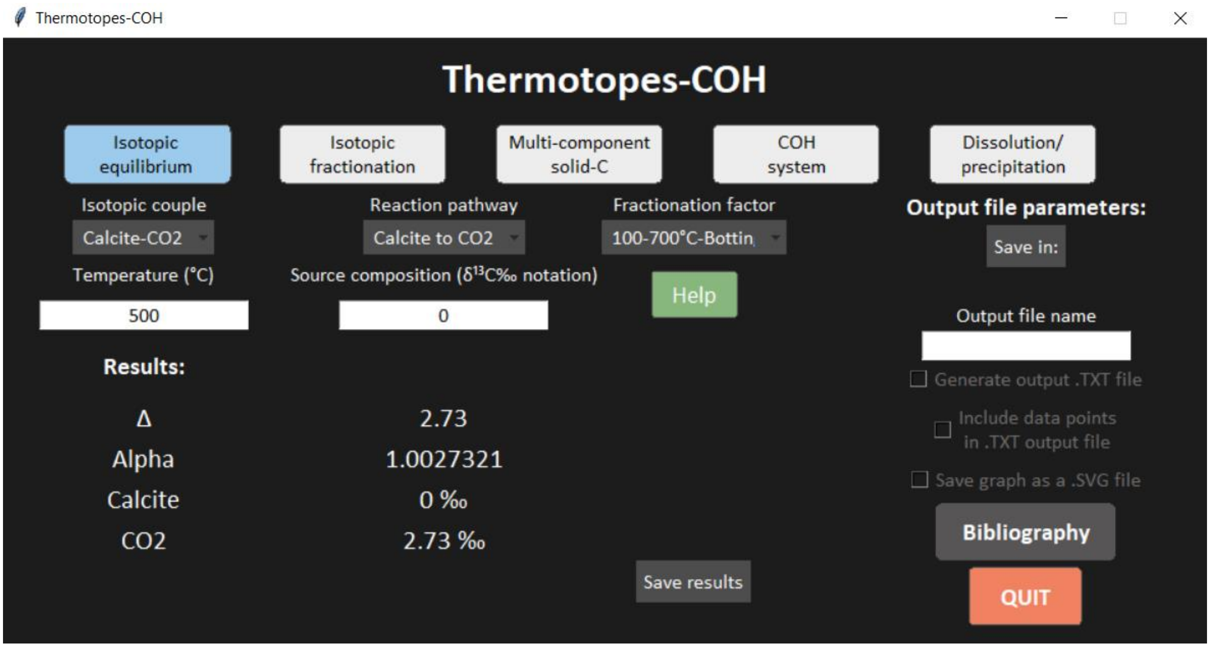

Isotopic couple: Calcite-CO2

Reaction pathway: Calcite to CO2

Fractionation factor: 100-700°C-Bottin

Temperature (°C): 500

Source composition ($\delta^{13}$C‰ notation): 0

**Results:**

| | |
|---|---|
| Δ | 2.73 |
| Alpha | 1.0027321 |
| Calcite | 0 ‰ |
| CO2 | 2.73 ‰ |

*Figure 6.1: Isotopic equilibrium tab of the Thermotopes COH software. Example of results for the isotopic equilibrium between calcite and $CO_2$ at 500°C. With the input of the isotopic composition of calcite, $\Delta$, $\alpha$, and the isotopic value of $CO_2$ and calcite are displayed.*

### 6.2.4 Isotopic Fractionation

The second tab of Thermotopes-COH, labeled “Isotopic fractionation”, calculates batch or Rayleigh fractionation evolutions of a C-bearing species. Isotopic fractionation between species A to B is calculated at equilibrium. In a closed system (or batch) the following equation is used:

$$\delta_{B\,f} = (\delta_{A\,ini} + \Delta_{A-B}) \times (1 - f) + (\delta_{A\,ini} * f) \qquad (4)$$

$$\delta_{A\,f} = \delta_{B\,f} - \Delta_{A-B} \qquad (5)$$

In open system (or Rayleigh), the calculation follows the Rayleigh equation (Rayleigh, 1896):

$$\delta_{A\,f} = ((1000 + \delta_{A\,ini})f^{\alpha_{A-B}-1}) - 1000 \qquad (6)$$

$$\delta_{B\,f} = \alpha_{A-B}(1000 + \delta_{A\,f}) - 1000 \qquad (7)$$

Where $f$ is the remaining fraction of A, $\delta_{A\,ini}$ is the initial delta value at the start of the fractionation, $\delta_{A\,f}$ and $\delta_{B\,f}$ are the delta value at $f$, and $\alpha_{A-B}$ is the fractionation factor calculated after equation (2) (Dansgaard, 1964; Kendall and McDonnell, 2012; Sharp, 2017; Valley, 2018).

For example, the user may select the calcite-$CO_2$ couple and choose the calcite to $CO_2$ pathway to model the fractionation of calcite into $CO_2$ from a chosen calcite isotopic composition. The user can then select a fractionation factor from a list of references. Once a valid temperature in °C and a valid isotopic composition in the $\delta^{13}C$ notation are entered, the calculation can be executed. A graph will be displayed showing the $\delta^{13}C$ evolutions of both the calcite and the produced $CO_2$ as a function of the remaining fraction of the reacting calcite species (Fig 6.2).

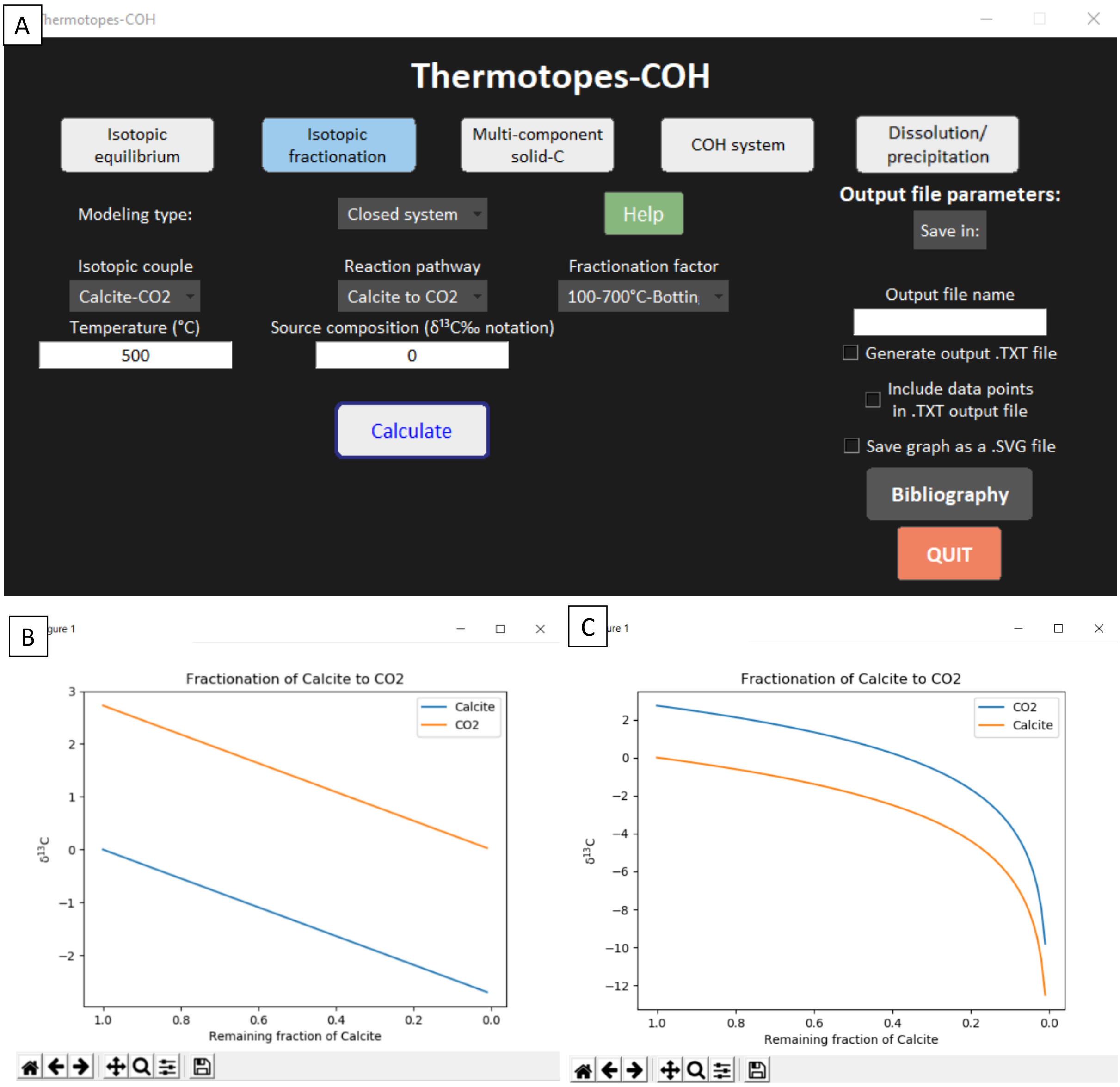

Modeling type: Closed system

Isotopic couple: Calcite-CO2

Reaction pathway: Calcite to CO2

Fractionation factor: 100-700°C-Bottin

Temperature (°C): 500

Source composition ($\delta^{13}C$‰ notation): 0

Output file name:

☐ Generate output .TXT file

☐ Include data points in .TXT output file

☐ Save graph as a .SVG file

*Figure 6.2: Isotopic fractionation tab of the Thermotopes COH software. A: Example of results for the isotopic fractionation between calcite to $CO_2$ at 500°C in closed (B) and open (C) systems.*

### 6.2.5 Multi-component G/D-C-O-H modeling

The third tab of Thermotopes-COH, labeled “Multi-component solid-C'', models the precipitation of either graphite or diamond, from a fluid containing both $CO_2$ and $CH_4$ according to the equation described in Ray (2009) and Ray and Ramesh (2000) (Fig. 6.3). The precipitation of solid carbon from a fluid containing both $CO_2$ and $CH_4$ follows two steps:

initially, $CO_2$ and $CH_4$ contribute equally to the isotopic value of the resulting $C_{solid}$ (0.5 mole each per mole of produced graphite/diamond). Then, when the initially less abundant phase either $CH_4$ or $CO_2$ is consumed, the precipitation evolves as a single component system following a classical Rayleigh model (as available in Tab 2). During the first step, the equation defining the isotopic value of $C_{solid}$ varies if the system is $CH_4$ dominated or $CO_2$ dominated (Ray, 2009; Ray and Ramesh, 2000; Stachel et al., 2017b). When $CH_4$ is more abundant than $CO_2$ the equations are:

$$r = \frac{XCO_2}{XCH_4} \quad (8)$$

$$\mathrm{A} = \frac{1+ \alpha_{CO2-CH4}}{2} \quad (9)$$

$$B = (1-r)\frac{\alpha_{CO2-CH4}-1}{2+2^{r}} \qquad (10)$$

$$\delta^{13}C_{fluid\ f} = 1000\left(\frac{\alpha_{C-CH4}}{A} ln\frac{Af-B}{A-B} - lnf\right) + \delta^{13}C_{fluid\ initial} \qquad (11)$$

$$\delta^{13}C_{C\ solid\ f} = 1000\left(\frac{\alpha_{C-CH4}}{A-\frac{B}{f}} - 1\right) + \delta^{13}C_{fluid\ f}\left(\frac{\alpha_{C-CH4}}{A-\frac{B}{f}}\right) \quad (12)$$

When $CO_2$ is more abundant than $CH_4$:

$$r = \frac{XCH_4}{XCO_2} \quad (13)$$

$$\mathrm{A} = \frac{1+\frac{1}{\alpha_{CO2-CH4}}}{2} \quad (14)$$

$$B = (1-r)\frac{\alpha_{CO2-CH4}}{2+2^{r}} \quad (15)$$

$$\delta^{13}C_{fluid\ f} = 1000\left(\frac{\alpha_{C-CO2}}{A} ln\frac{Af-B}{A-B} - lnf\right) + \delta^{13}C_{fluid\ initial} \qquad (16)$$

$$\delta^{13}C_{C\ solid\ f} = 1000\left(\frac{\alpha_{C-CO2}}{A-\frac{B}{f}} - 1\right) + \delta^{13}C_{fluid\ f}\left(\frac{\alpha_{C-CO2}}{A-\frac{B}{f}}\right) \quad (17)$$

Where $\delta^{13}C_{fluid\ initial}$ is the initial isotopic composition of the fluid, $\delta^{13}C_{fluid\ f}$ the isotopic composition of the fluid at the remaining fraction of fluid $f$, $\delta^{13}C_{C\ solid\ f}$ is the composition of graphite/diamond at the remaining fraction of fluid $f$, $\alpha_{CO2-CH4}$ the fractionation factor between $CO_2$ and $CH_4$, $\alpha_{C-CO2}$ the fractionation factor between solid carbon and $CO_2$ and $\alpha_{C-CH4}$ the fractionation factor between graphite/diamond and $CH_4$.

The multi component tab offers different input options for the $\delta^{13}C$ isotopic composition of the fluid: Total C, Fluid mixing, Known $CH_4$ composition, Known $CO_2$ composition.

-Total C: with this method, the fluid is considered at isotopic equilibrium and the global $\delta^{13}C$ of the fluid is entered. The isotopic compositions of $CO_2$ and $CH_4$ are then calculated based on their respective proportion at the desired temperature.

-Fluid mixing: with this method, two fluids initially at isotopic disequilibrium contain either $CO_2$ or $CH_4$. Once the precipitation starts, the two fluids mix to reach isotopic equilibrium and then ensue the precipitation of solid carbon.

-Known $CH_4$ composition: with this method, the fluid is considered at isotopic equilibrium but only the $\delta^{13}C$ $CH_4$ composition is known by the user. The software then models the associated $\delta^{13}C$ $CO_2$ composition at the desired temperature and derives the precipitation of solid carbon.

-Known $CO_2$ composition: with this method, the fluid is considered at isotopic equilibrium but only the $\delta^{13}C$ $CO_2$ composition is known by the user. The software models the associated $\delta^{13}C$ $CH_4$ composition at the desired temperature and then derives the precipitation of solid carbon.

The user must then select the type of solid phases (graphite/diamond) precipitating, indicate the isotopic composition(s), the temperature (in °C), the $\frac{XCO_2}{XCH_4}$ ratio (this ratio must be ≠1) and select a fractionation factor from a reference list. After executing the calculation, the software will yield a graph showing the evolution of the $\delta^{13}C$ of both the bulk fluid composition and the solid carbon as a function of the remaining fraction of carbon in the fluid (Fig 6.3B). A dashed line will be displayed whenever either $CO_2$ or $CH_4$ is exhausted and the precipitation evolves as a single component system. This option models the isotopic evolution in the event of solid-C precipitation from a COH fluid from a pure mass balance basis, no thermodynamic modeling involved.

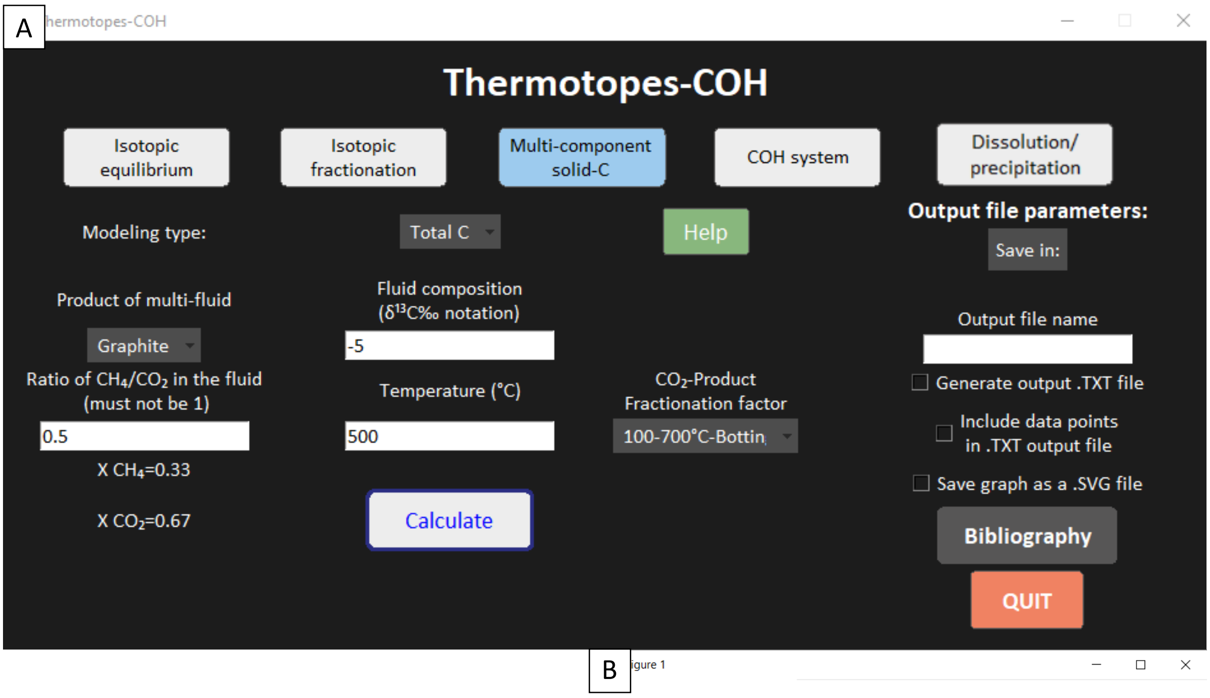

Modeling type: Total C

Product of multi-fluid: Graphite

Fluid composition ($\delta^{13}C$‰ notation): -5

Ratio of $CH_4/CO_2$ in the fluid (must not be 1): 0.5

Temperature (°C): 500

X $CH_4$=0.33

X $CO_2$=0.67

$CO_2$-Product Fractionation factor: 100-700°C-Bottin

☐ Generate output .TXT file

☐ Include data points in .TXT output file

☐ Save graph as a .SVG file

*Figure 6.3: Multi-component C precipitation tab of the Thermotopes-COH software. A: Software interface before any input. B: Example of result of a multi-component precipitation "Total C" of a fluid with an initial $\delta^{13}C$ composition of -5 ‰ and a $CH_4/CO_2$ ratio of 0.8 at 500 °C.*

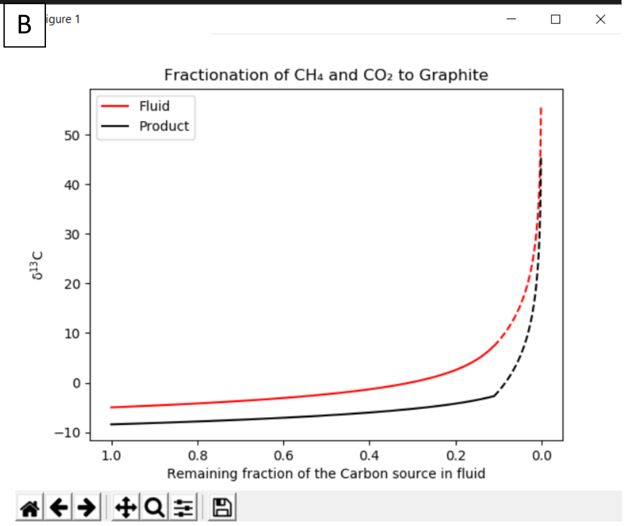

### 6.2.6 COH fluid speciation

The fourth tab of Thermotopes-COH labeled “COH system”, models the speciation of COH fluids, the carbon activity, the $X_O$, and the oxygen and hydrogen fugacities. The modeling follows equations from Huizenga (2005) and references therein. The speciation of the COH fluid is calculated from constant of reaction of the following equilibria:

$$CO + {}^{1}\!/_{2}\, O_2 = CO_2 \qquad (18)$$

$$H_2 + {}^{1}\!/_{2}\, O_2 = H_2O \qquad (19)$$

$$CH_4 + 2\, O_2 = CO_2 + 2\, H_2O \qquad (20)$$

$$C_{solide} + O_2 = CO_2 \qquad (21)$$

From these equilibria, the oxygen fugacity $fO_2$ along with the molar fractions of $XH_2O$, $XCO_2$, $XCH_4$, $XH_2$ and $XCO$, are calculated.

Details of the equation for the constants of reaction and fugacity coefficients can be found in Huizenga (2005) and reference therein.

The $fH_2$ is calculated according to the following equation (Holloway, 1977):

$$fH_2 = \gamma_H \times P \times XH_2 \qquad (22)$$

Where $XH_2$ is the molar fraction of $H_2$, P is the pressure in kbar, and $\gamma_H$ is the fugacity coefficient of hydrogen calculated with equations from Huizenga (2005) based on Gibbs free energy.

The user can select among different options that require either 2 or 3 input parameters, such as:

- known **carbon activity, *f*O₂ buffer**, and **Δlog *f*O₂ from this buffer**.
- Known **carbon activity** and $\frac{XCO_2}{XCO_2+XCH_4}$ **ratio**. An optional *f*O₂ buffer can be indicated for reference.
- Known $\frac{XCO_2}{XCO_2+XCH_4}$ **ratio, *f*O₂ buffer**, and **Δlog *f*O₂ from this buffer**.
- Known **carbon activity** and **$X_O$**. An optional *f*O₂ buffer can be indicated for reference.
- Known $\frac{XCO_2}{XCO_2+XCH_4}$ **ratio** and **$XH_2O$**. An optional *f*O₂ buffer can be indicated for reference.

The carbon activity is the effective concentration of carbon in the fluid, with a carbon activity of 1 indicating that the fluid is saturated in carbon and coexists with solid carbon. Carbon activity over to 1 will produce a carbon oversaturated fluid. Carbon activity lower than one refers to graphite/diamond-undersaturated conditions. Different $fO_2$ buffers are available to the user as previously introduced. The delta (Δ) is Δlog $fO_2$ relative to the selected oxygen fugacity buffer. For example, for a fluid at ΔlogFMQ+1, the Δ will be 1. $XCO_2$, $XCH_4$, and $XH_2O$ correspond to the molar fraction of $CO_2$, $CH_4$ and $H_2O$ in the fluid, respectively. $X_O$ is defined as $XO=\frac{n_O}{n_O+n_H}$ where $n_O$ and $n_H$ are the mole quantities of oxygen and hydrogen in the fluid, respectively.

Once valid temperature (in °C) and pressure (in kbar) values are inserted, and an $fO_2$ buffer selected from the dropdown list, the results will automatically update on the software interface (Fig. 6.4), and include the molar fractions of COH species $XH_2O$, $XCO_2$, $XCH_4$, $XH_2$, $XCO$, the carbon activity of the fluid (aC), $X_O$, the $\frac{XCO_2}{XCO_2+XCH_4}$ ratio, the $\frac{XCO_2}{XCH_4}$ ratio, the $fO_2$, the log$fO_2$, the Δlog $fO_2$ from the selected buffer, the $fH_2$, and finally whether graphite/diamond is stable. Additionally, the results can be visualized on a ternary COH diagram (Fig. 6.4B), displaying the position of the carbon saturation curve and the position of the modeled the COH fluid composition.

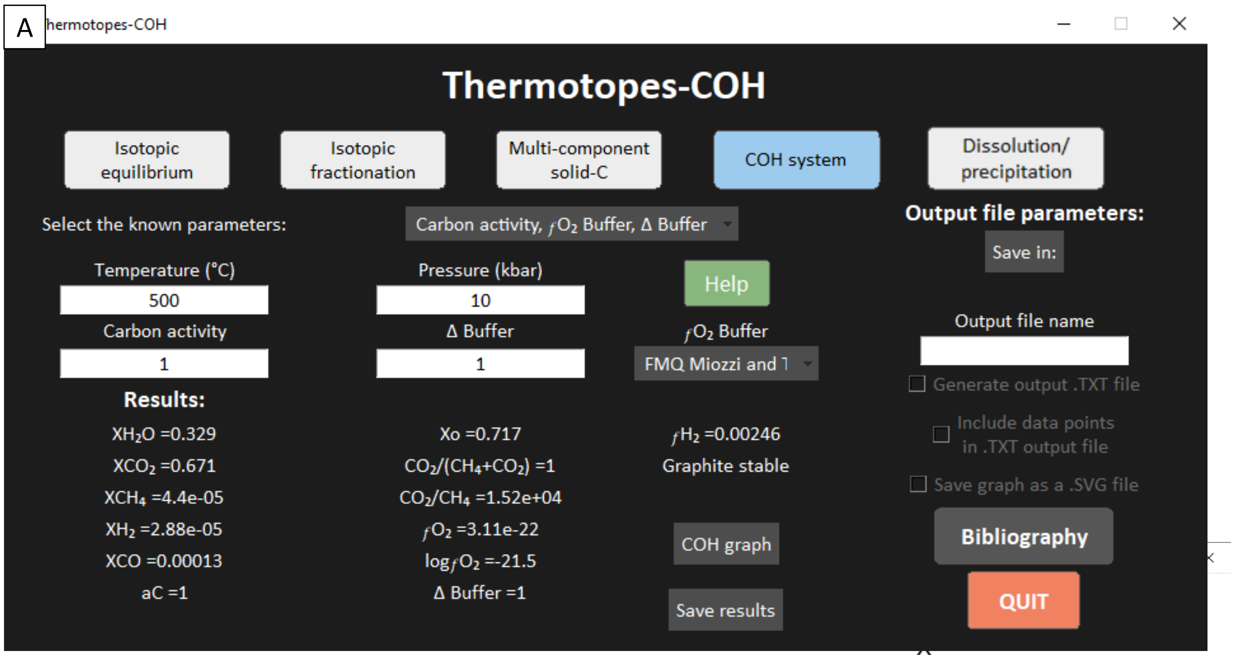

Select the known parameters: Carbon activity, $_fO_2$ Buffer, Δ Buffer

Temperature (°C): 500

Pressure (kbar): 10

Carbon activity: 1

Δ Buffer: 1

$_fO_2$ Buffer: FMQ Miozzi and 1

Output file parameters:

Output file name:

☐ Generate output .TXT file

☐ Include data points in .TXT output file

☐ Save graph as a .SVG file

**Results:**

$XH_2O$ =0.329
$XCO_2$ =0.671
$XCH_4$ =4.4e-05
$XH_2$ =2.88e-05
XCO =0.00013
aC =1

Xo =0.717
$CO_2/(CH_4+CO_2)$ =1
$CO_2/CH_4$ =1.52e+04
$_fO_2$ =3.11e-22
$\log_fO_2$ =-21.5
Δ Buffer =1

$_fH_2$ =0.00246
Graphite stable

*Figure 6.4: COH system tab of the Thermotopes-COH software. A: Example of input of a COH fluid at 500 °C and 10 kbar calculated from the carbon activity and the $fO_2$ defined as FMQ +1. B: Ternary diagram of the calculated COH fluid.*

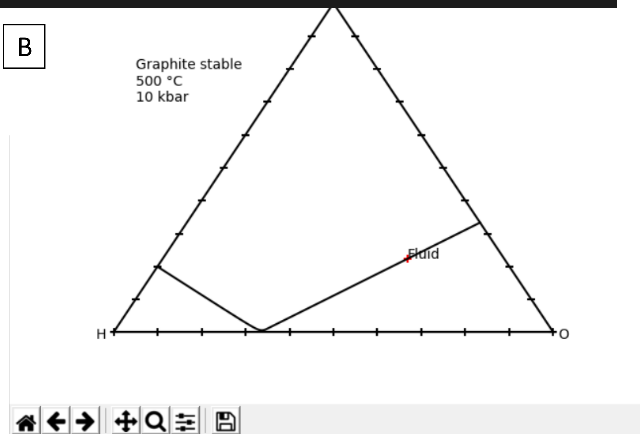

## 6.2.7 Dissolution/precipitation

The fifth tab of Thermotopes-COH, labeled “Dissolution/precipitation” is dedicated to model the precipitation and dissolution of graphite/diamond along different proposed processes and the associated isotopic evolution of the system (Fig 6.5). The processes proposed and leading to the precipitation/dissolution of graphite/diamond are: fluid mixing, fluid mixing buffered, desiccation, desiccation buffered, pressure changes, temperature changes.

A graphite/diamond dissolution/precipitation model has been developed for the purposes of the Thermotopes-COH software. It assumes that the system is at equilibrium. The model tracks the carbon activity of a COH-fluid through various reactions (according to equations presented in the COH system based on Huizenga (2005). In the event that the carbon activity increases above 1, and the fluid becomes supersaturated, the software models carbon precipitation until the carbon activity reaches 1 and is no longer supersaturated along the following reaction:

$$CH_4 + CO_2 = 2\ H_2O + 2\ C_{solid} \qquad (23)$$

The corresponding isotopic composition of the solid and fluid is calculated along the reaction through the previously described reaction (23). If the carbon activity is below 1, graphite/diamond is solubilized along the reverse reaction to reach carbon saturation.

Because graphite/diamond can behave as a chemically reactive but isotopically inert phase, an option is provided to consider graphite/diamond as isotopically reactive (Valley and O'Neil, 1981), Tiumati and al. tbp). When this option is toggled on, the initial and newly formed graphite/diamond in the system is able to freely equilibrate with other C-bearing species in the system and participate in the mass balance. The isotopic system is considered to be closed, with carbon being either in the fluid or as graphite/diamond. The composition of the solid-C is calculated along the following equation:

$$\delta^{13}C_{solid} = \delta^{13}C_{system} - \frac{nCO_2}{nC_{total}}\Delta_{CO2-C} - \frac{nCH_4}{nC_{total}}\Delta_{CH4-C} \qquad (24)$$

with $\delta^{13}C_{solid}$ being the isotopic composition of solid-C, $\delta^{13}C_{system}$ the isotopic composition of the system, *n*$CO_2$ and *n*$CH_4$ the number of moles of $CO_2$ and $CH_4$, respectively, *n*$C_{total}$ the total number of moles of carbon in the system $\Delta_{CO2-C}$ and $\Delta_{CH4-C}$ the isotopic big delta between $CO_2$ and graphite/diamond and $CH_4$ and graphite/diamond respectively.

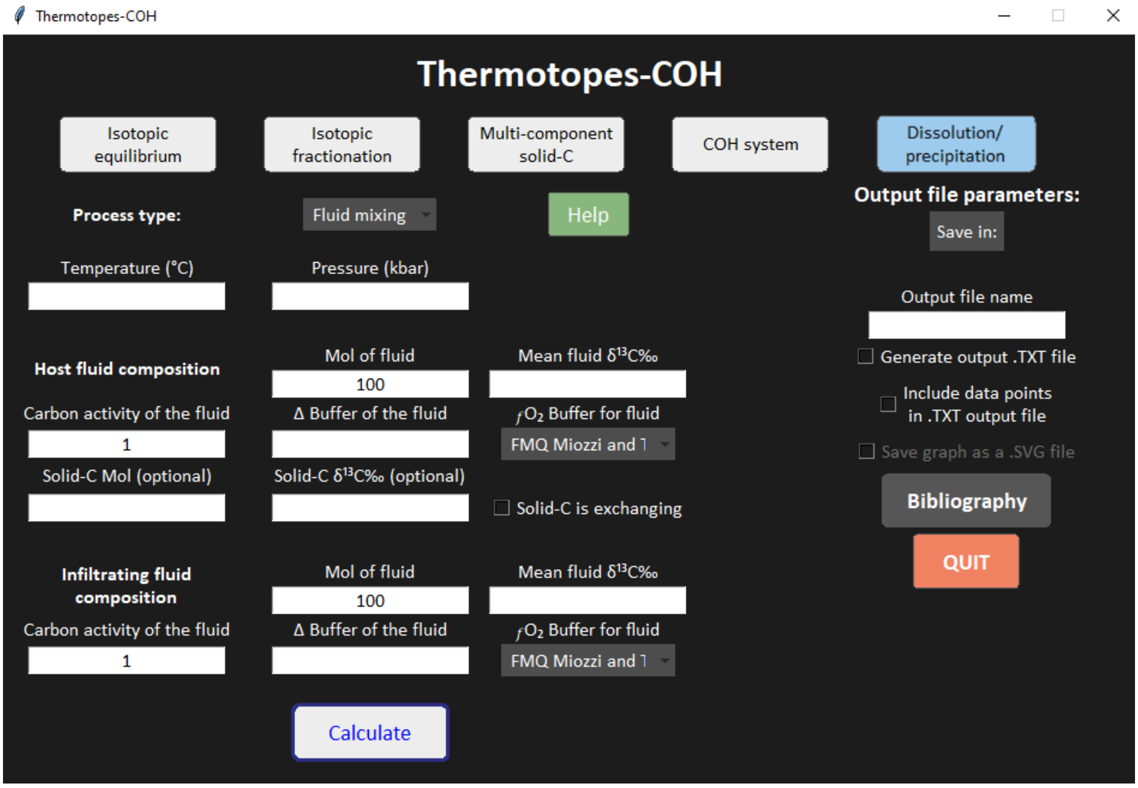

Process type: Fluid mixing

**Host fluid composition**

Mol of fluid: 100

Carbon activity of the fluid: 1

$f$O₂ Buffer for fluid: FMQ Miozzi and T

**Infiltrating fluid composition**

Mol of fluid: 100

Carbon activity of the fluid: 1

$f$O₂ Buffer for fluid: FMQ Miozzi and T

*Figures 6.5: Precipitation/dissolution tab of the Thermotopes-COH software. Interface before any input. More examples on the application of this page are presented in Section 6.4.*

When this option is toggled off, graphite/diamond in the system does not participate in the isotopic mass balance unless a fraction of this solid-C is solubilized. In this case, the isotopic composition of the newly formed graphite/diamond is calculated considering the instantaneous remaining fraction of carbon in the fluid $f$ as follows:

$$f = 1 - \left(\frac{nC_{solid\ new}}{nCH_4 + nCO_2}\right) \qquad (25)$$

The isotopic compositions of the instantaneous graphite/diamond and the total graphite/diamond are then calculated from a combination of equation (4) and an isotopic mass balance. A comparison of the isotopic calculation between the multicomponent system and the Dissolution/precipitation model is presented in Supplementary material 6.1.

Thermotopes-COH can model carbon dissolution/precipitation under 6 different processes, described as follows.

### *Fluid mixing*

The fluid mixing process models the interaction of two different COH-fluids and its potential to dissolve or precipitate graphite/diamond (Fig 6.6A). The software models the titration of the second fluid into the first through an iteration process. The titration step is defined as 0.1% of the second fluid being mixed in the first one. The carbon activity of the fluid is calculated and, if =1, the next titration proceeds to the next step. If the carbon activity is either > 1 or < 1, a sub-iteration starts with either dissolution or precipitation of graphite/diamond until the carbon activity reaches 1. The associated isotopic evolution of fluid species and graphite/diamond bearing species is computed at each step. The titration proceeds until the totality of the second fluid is mixed within the first one.

### *Fluid mixing (buffered)*

This option models the interaction of a fluid with an $fO_2$ buffer, to simulate interaction in a buffered medium (Fig 6.6B). The $fO_2$ is Δlog relative to a list of buffers (e.g., FMQ), fixed for the entirety of the process, and the software models the composition of an external fluid equilibrating with a fixe $fO_2$. If graphite/diamond precipitates, its isotopic composition is also calculated. Geologically, buffering the $fO_2$ is not a trivial assumption and should be selected if it is coherent with the natural or experimental conditions.

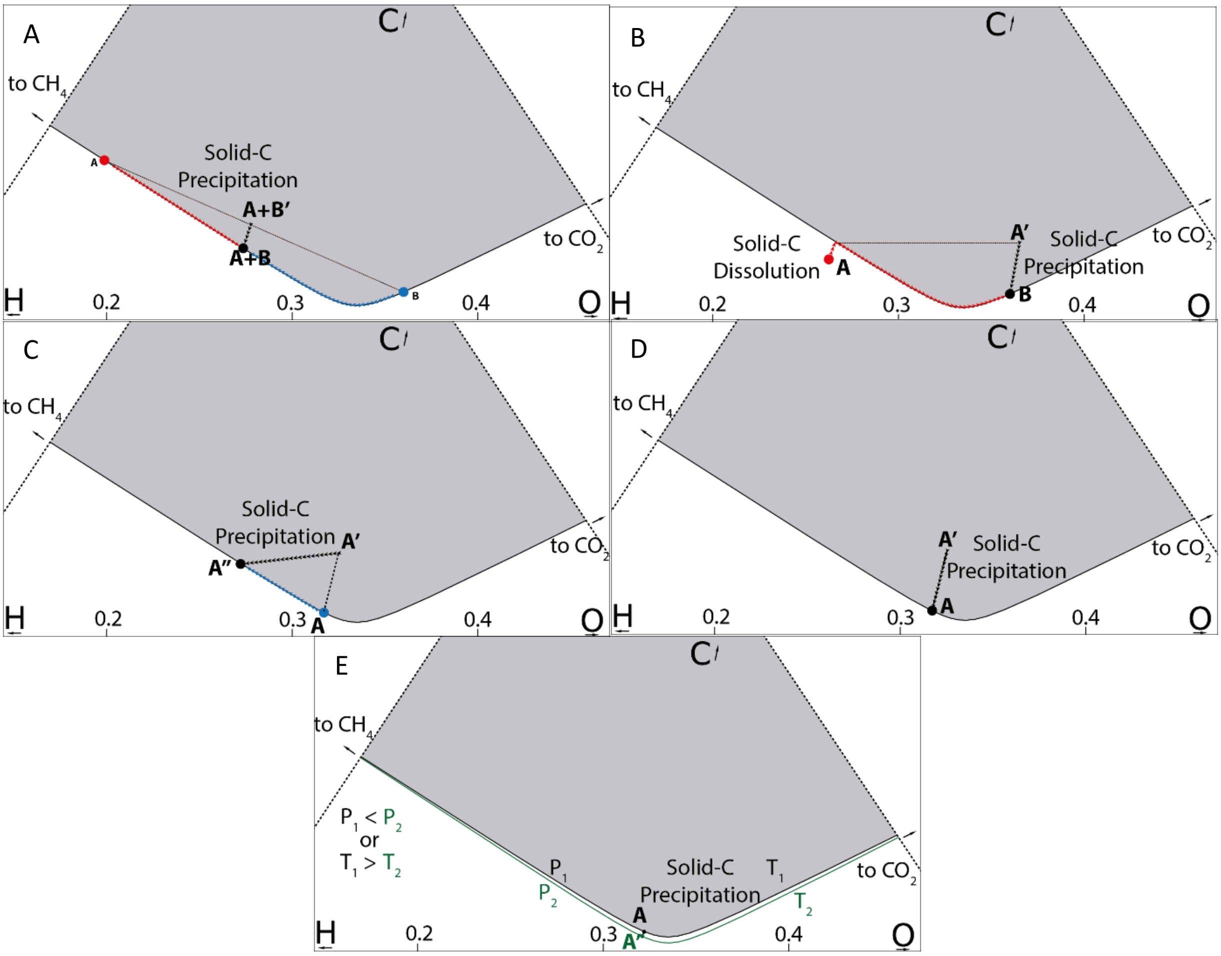

*Figure 6.6: Example of the different processes proposed by the 5th tab of Thermotopes-COH and shown in output COH triangular compositional diagrams. A: Fluid mixing of a reduced fluid A and an oxidized fluid B to produce A+B. A+B′ corresponds to a transient, metastable carbon-oversatured fluid. B: Mixing of a fluid A with a buffer B. Only A is able to change its composition. A′ corresponds to a transient, metastable carbon-oversaturated fluid. The A′-B joint corresponds to a fixed* $fO_2$ *(or* $X_O$*) value. C: Water loss (desiccation) of a fluid A. A′ corresponds to a transient, metastable carbon-oversaturated fluid. A′′ corresponds to the final composition of the fluid. D: Water loss of a fluid A in a buffered system. A′ corresponds to a transient, metastable carbon-oversaturated fluid. E: Isothermal pressure change of a fluid A from* $P_1$ *to* $P_2$ *and associated shift of the position of the carbon saturation curve. A similar behavior in an isobaric temperature change from* $T_1$ *to* $T_2$ *is also shown.*

### *Desiccation*

This interaction models the evolution of a desiccating COH fluid (e.g., through rock hydration reaction, or respeciation of H and O into C-bearing fluid species) and calculates the associated precipitation of graphite/diamond. The desiccation is here defined as the loss of $H_2O$ mole in the fluid. In the Desiccation mode, the oxygen fugacity is free to evolve during the reaction (Fig. 6.6C). During fluid desiccation, the carbon concentration increases and, if carbon saturation is reached, graphite/diamond precipitates. The degree of desiccation must be entered, corresponding to the fraction of the water loss ($XH_2O$). The model is iterative and, at each step, 0.01% of the moles of $H_2O$ ($nH_2O$) is removed, the carbon activity is calculated, and the number of moles of precipitated graphite/diamond and its isotopic value are derived. The process proceeds until the desired water fraction is lost.

*Desiccation buffered*

This option models the evolution of a desiccating COH fluid at buffered $fO_2$ (Fig. 6.6D). The desiccation is here defined as the loss of $H_2O$ mole in the fluid, and because the $fO_2$ is fixed during the interaction, the water fraction in the fluid will remain constant if the fluid reaches carbon saturation. In other words, the actual amount of water decreases rather than the molar fraction. In this instance, any mole loss of $H_2O$ is accompanied by the loss of an equivalent amount of other species in the fluid in order to maintain a constant $XH_2O$. The amount of desiccation must be entered, because redox conditions are buffered, the $XH_2O$ remains constant during desiccation. If graphite/diamond precipitates, its isotopic composition is also calculated. Geologically speaking, buffering the $fO_2$ is not a trivial assumption and this option should be selected only if the specific assumptions are relevant. This option is probably more functional to experimental rather than natural conditions.

*Pressure change*

The pressure change option models the evolution of an equilibrium COH fluid undergoing isothermal pressure changes (Fig. 6.6E). The model is iterative. At each pressure step (every

0.1 kbar), the thermodynamic parameters of the COH system are calculated. If graphite/diamond is dissolved/precipitated, its isotopic composition is calculated.

*Temperature change*

The pressure change option models the evolution of an equilibrium COH fluid undergoing isobaric thermal changes (Fig. 6.6E). The model is iterative. At each temperature (every 1 °C), the thermodynamic parameters of the COH system are recalculated. If In the event of graphite/diamond is dissolved/precipitated, its isotopic composition is calculated.

For each option, the temperature (in °C), the pressure (in kbar), and fluid parameters must be entered. A number of moles of fluid, its mean $\delta^{13}C$ isotopic composition, a carbon activity and the $fO_2$ (Δlog relative to a selected buffer) also need to be defined by the user.

The “Calculate” button launches the calculation after checking the validity of input parameters. Two graphs will be displayed for each calculation. The first is a ternary COH compositional diagram showing the position of the initial fluid(s) and the final one, along with the amount of graphite/diamond precipitated and its isotopic composition. The second graph includes 4 diagrams showing the evolution of various parameters along with the interaction such as the amount of dissolved/precipitated graphite/diamond, the $fO_2$, the $XH_2O$ and the $\frac{XCO_2}{XCO_2+XCH_4}$, and the isotopic compositions of the fluid and graphite/diamond. In the case of buffered computation, only the isotopic compositions are shown on the second graph, as the $fO_2$ is fixed throughout the computation.

## 6.3 Limitations

-Maximum temperature and pressure:

The Thermotopes-COH software is defined on a pressure-temperature range corresponding to crustal and upper mantle geological conditions spawning from the initial constraints of the equation the software is based on and may react poorly in eclogitic or granulitic conditions. Thermodynamic equations from Huizenga, (2005) are defined on the 300-1000 °C and 1 >kbar range. “Extreme” couple of temperatures and pressure can lead to unexpected results or errors.

-Critical Fluids and melts

This model does not take account change of behavior of fluid as critical fluid or melts at higher P-T conditions with the model and equation working in the same fashion regardless of the pressure-temperature.

-Pure $CO_2$ fluid

At higher temperature (≈< 850 °C) the composition of COH fluids tends towards pure $CO_2$ and $CH_4$ becomes completely absent. Conversely, should the user input overwhelmingly reduced conditions featuring only pure $CH_4$ fluid, the COH system will be left to the CH system. Because of the way the software is built, mathematical errors arise from ratios leading to division by zero. In this event, the software will inform that the modeling cannot be pursued due to fluid being pure $CO_2$ or $CH_4$.

-Graphite/diamond precipitation

Graphite/diamond precipitation is based on the equation (23) (see Section 6.2.7) as the sole precipitation reaction. More reactions could be considered, as the model strays from reality when only $CO_2$ or $CH_4$ remains present in the fluid.

## 6.4 Application to a natural case study

Thermotopes-COH can be used to test conceptual models inspired by natural data, such as the volcanic-hosted graphite deposit at Borrowdale in Cumbria, UK. This site has been the subject of numerous studies (Barrenechea et al., 2009; Lindgren and Parnell, 2006; Luque del Villar et al., 1998; Luque et al., 2009; Strens, 1965; Weis et al., 1981), dataset of which will be used herein to illustrate a Thermotopes-COH application with respect to graphite deposition (Tab 5).

### 6.4.1 Borrowdale graphite deposit context (from Ortega et al., (2010))

The Borrowdale graphite deposit consists of andesitic and dioritic intrusions affected by a metasomatic reaction with external fluids (Lindgren and Parnell, 2006; Luque et al., 2009). These fluid/rock interactions lead to graphite, chlorite, and quartz deposition. Graphite is present in different forms, including nodular masses within pipe-like bodies, along fault planes in the volcanic rocks, and as replacements (dissemination) within the igneous host rocks.

The work by Ortega et al., (2010) provided data on both the isotopic composition of the carbon in the system and geologically significant data such as the PT conditions of the interaction and fluid compositions during the event of graphite deposit. Carbon isotopic data allowed constraining both the mechanism of graphite precipitation and the inferred carbon source.

Quartz-hosted, vapor-rich fluid inclusions in the Borrowdale were interpreted to correspond to the initial fluid infiltrating the host rock and leading to the graphite mineralization (Barrenechea et al., 2009; Weis et al., 1981). The P-T conditions of early graphite precipitation were estimated at about 500 °C and 2 kbar by fluid inclusion microthermometry, and the $fO_2$ constrained at ~FMQ (Luque et al., 2009). The bulk composition of vapor fluid inclusions shows a water molar fraction of the inclusions clustering at 0.64 (Ortega et al., 2010). The inclusions show a consistent $\frac{XCO_2}{XCO_2+XCH_4}$ ratio of 0.69. Based on the estimated compositions and P-T formation conditions of the fluid inclusions, Luque et al. (2009) suggested that the fluid was carbon-saturated at the time of trapping. Carbon supersaturation conditions were also suggested by the morphology of the Borrowdale graphite (Barrenechea et al., 2009). The $\delta^{13}C$ of the Borrowdale graphite ranges from -28.3 ‰ to -23.4 ‰ and clusters at about -26.5 ‰ (supplementary material 6.2). The source of carbon at the origin of the mineralization is inferred to be the Skiddaw metapelite, with measured total organic carbon $\delta^{13}C$ clustering around -27 ‰ (Supplementary material 6.2). It is proposed that the carbonic fluid was composed of pure $CO_2$ generated at high temperature (1100 °C) during the intrusion of the magmatic body. Considering the graphite-$CO_2$ fractionation at this temperature, the $\delta^{13}C$ of the fluid was calculated at -23 ‰ (Ortega et al., 2010). Ortega et al. (2010) proposed two successive processes at the origin of the graphite mineralization, both happening at constant $fO_2$. Firstly, a partial desiccation of the fluid, resulting in the formation of chlorite in the infiltrated rock at 500 °C. This event was followed by the cooling of the resulting fluid to 400 °C (Ortega et al., 2010)

### 6.4.2 Application of Thermotopes-COH to the Borrowdale graphite deposit

Based on the existing data on the Borrowdale graphite reported above, we present a practical application of Thermotopes-COH aimed at reproducing the geological interpretation by Ortega et al., (2010) and to highlight additional features thanks to the software options.

### 6.4.3 Initial fluid composition

Following Ortega et al., (2010), the initial composition of the infiltrated fluid was set at *X*H2O = 0.64 and $\frac{XCO_2}{XCO_2+XCH_4}$ = 0.69. Based on these input parameters, Thermotopes-COH predicts a carbon activity of 2.55, corresponding to supersaturated conditions as estimated (Fig 6.7). The software predicts that the *f*$O_2$ of such fluid corresponds to Δlog FMQ -0.674 (FMQ defined by Miozzi and Tiumati 2020), equivalent to Δlog FMQ -0.191 (FMQ defined by Ohmoto and Kerrick 1977). This value refines the previous estimate by Ortega et al., (2010), which assumed Δlog FMQ 0 (by Ohmoto and Kerrick, 1977).

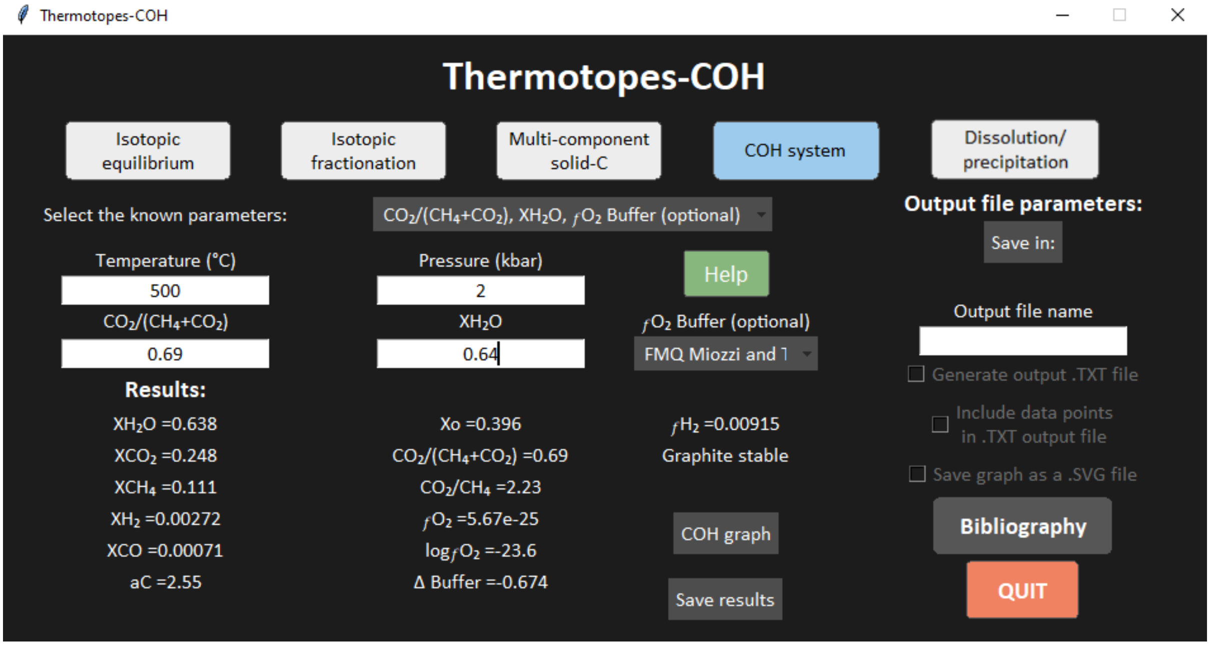

Select the known parameters: $CO_2/(CH_4+CO_2)$, $XH_2O$, *f*$O_2$ Buffer (optional)

Temperature (°C): 500

Pressure (kbar): 2

$CO_2/(CH_4+CO_2)$: 0.69

$XH_2O$: 0.64

*f*$O_2$ Buffer (optional): FMQ Miozzi and T

**Results:**

$XH_2O$ =0.638
$XCO_2$ =0.248
$XCH_4$ =0.111
$XH_2$ =0.00272
XCO =0.00071
aC =2.55

Xo =0.396
$CO_2/(CH_4+CO_2)$ =0.69
$CO_2/CH_4$ =2.23
*f*$O_2$ =5.67e-25
log*f*$O_2$ =-23.6
Δ Buffer =-0.674

*f*$H_2$ =0.00915
Graphite stable

*Figure 6.7: Input parameters for the initial infiltrating fluid proposed by* Ortega et al. (2010) *for the Borrowdale graphite deposit, calculated from $CO_2/(CO_2+CH_4)$ ratio and $XH_2O$.*

### 6.4.4 Cooling

Following Ortega et al., (2010), the cooling event of the Borrowdale graphite formation was modeled by using the "Temperature change" in Thermotopes-COH (Fig. 6.8A). Cooling of 100 mol of fluid from 500 °C to 400°C was modeled. The $fO_2$ previously calculated of FMQ -0.674

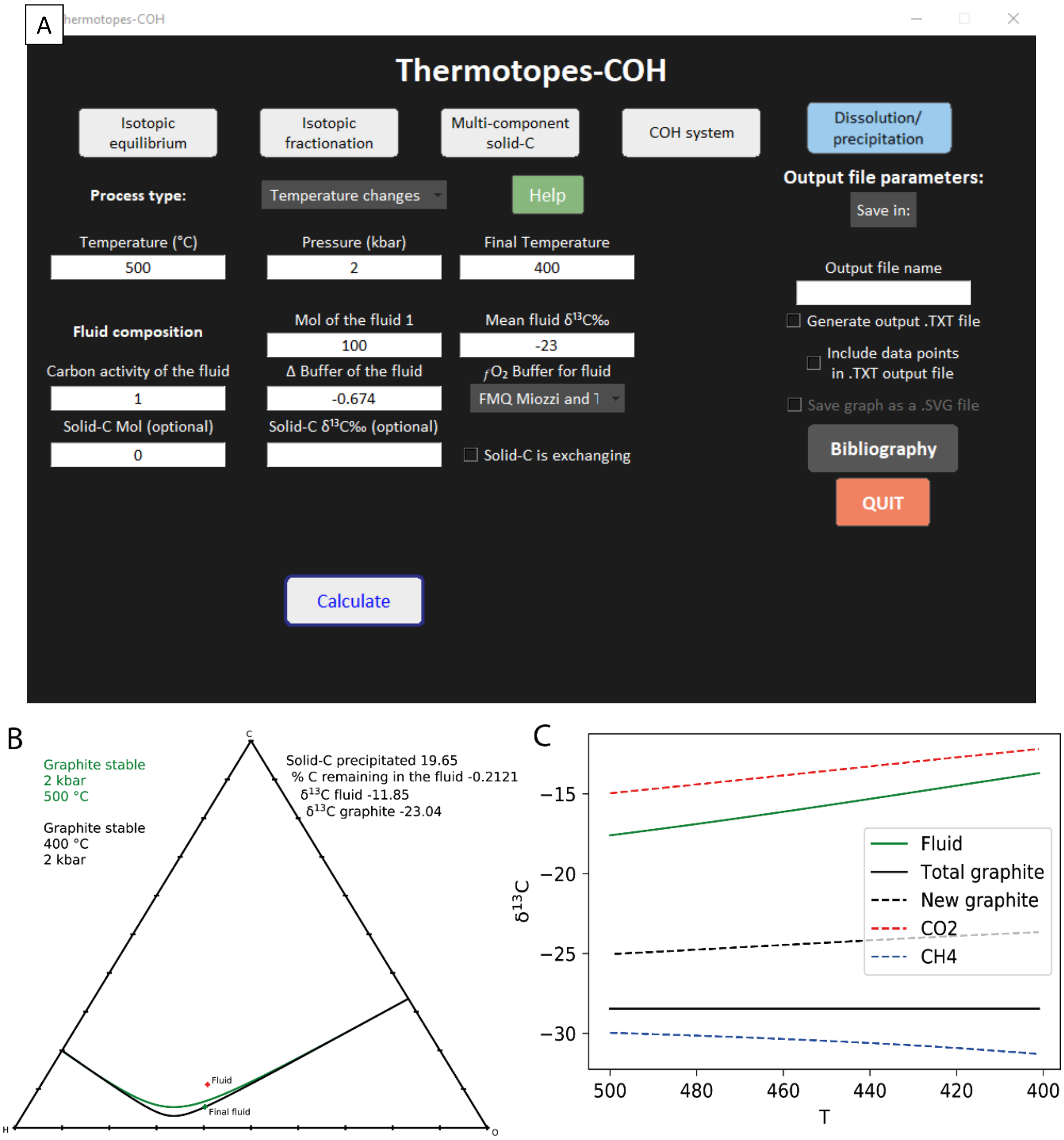

Process type: Temperature changes

Temperature (°C): 500

Pressure (kbar): 2

Final Temperature: 400

Fluid composition

Mol of the fluid 1: 100

Mean fluid δ13C‰: -23

Carbon activity of the fluid: 1

Δ Buffer of the fluid: -0.674

ƒO₂ Buffer for fluid: FMQ Miozzi and T

Solid-C Mol (optional): 0

Solid-C δ13C‰ (optional):

☐ Solid-C is exchanging

Output file parameters:

Output file name:

☐ Generate output .TXT file

☐ Include data points in .TXT output file

☐ Save graph as a .SVG file

Solid-C precipitated 19.65
% C remaining in the fluid -0.2121
δ13C fluid -11.85
δ13C graphite -23.04

*Figure 6.8: Calculation of the cooling of the fluid at 500°C and 2 kbar and constant $fO_2$ to 400 °C using fluid composition calculated in Fig 6.7 (A). The results of the model show a supersaturated fluid leading to the precipitation of graphite. The results of the model fluid leading to the precipitation of graphite (B) with a composition increasingly lighter as the fluid keeps cooling (C).*

was used along with an initial fluid isotopic composition of -23 ‰ from Ortega et al. (2010). The initial fluid appears on Figure 6.8B, showing a carbon supersaturated fluid (initial carbon activity at 2.55 as previously estimated). It is predicted that the cooling precipitates 19.65 mol of graphite per 100 moles of fluid, with a graphite $\delta^{13}C$ composition of -28 ‰ with newly formed graphite being progressively lighter. However, because a significant part of the graphite precipitation results from the carbon oversaturated nature of the fluid, the newly formed graphite as the temperature decreases weakly affects the global isotopic composition (Fig. 6.8C). The range of predicted value from Thermotopes-COH falls within the measured value of Ortega et al., (2010) and is presented in Supplementary material 6.2.

### 6.4.5 Desiccation

Along with the cooling, graphite deposition at the Borrowdale deposit was associated with fluid-rock interactions leading to the hydration of the rocks and fluid desiccation. However, the amount of fluid water loss during desiccation was not constrained by Ortega et al., (2010). The "Desiccation” option in Thermotopes-COH was used considering a wide range of degrees of desiccation (up to 100%). An amount of infiltrating fluid of 100 mol was considered with an original $fO_2$ of FMQ -0.674 and a carbon activity of 1, as the fluid oversaturation was already resolved by the cooling model (Fig. 6.9A).

Results of the desiccation model are presented in Figure 6.9 and shows the progressive evolution of the isotopic composition as the desiccation progresses. The model predicts up to 11.68 moles of graphite precipitating for complete (100%) desiccation. The graphite $\delta^{13}C$ composition becomes progressively lighter, from -28 ‰ to 25% at complete desiccation of the fluid (Fig. 6.9C). The modeled graphite isotopic compositions are in line with the measured values of the Borrowdale graphite (-28.4/ -24 ‰, Ortega et al., 2010, Supplementary material

6.2). The model predicts a linear formation of graphite in respect to the intensity of the desiccation. Consequently, 50% of desiccation would yield half the amount of mole of graphite and isotopic compositions of -26.5 ‰, as indicated in Figure 6.9C for 50% desiccation.

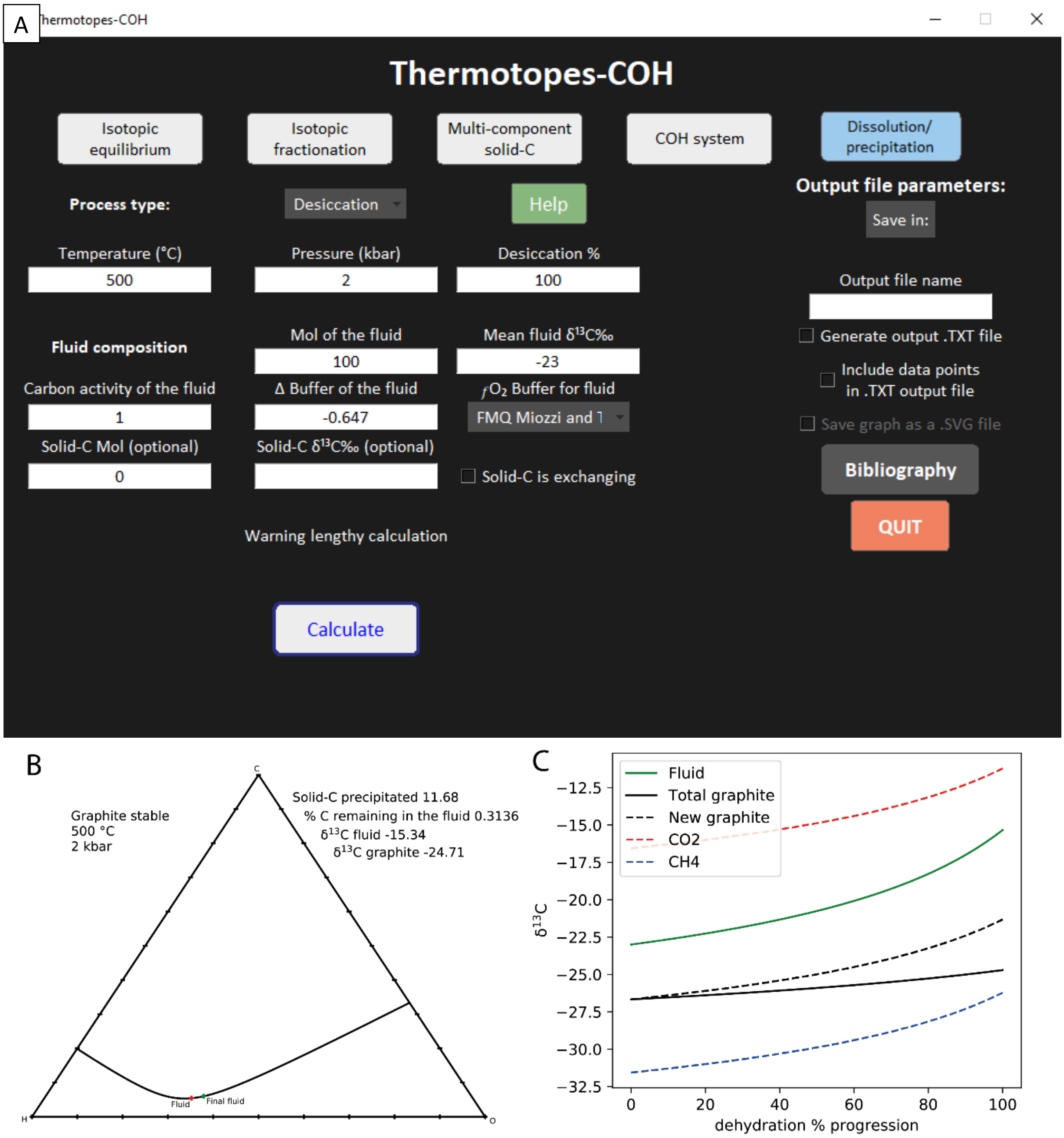

**Process type:** Desiccation

Temperature (°C): 500

Pressure (kbar): 2

Desiccation %: 100

**Fluid composition**

Mol of the fluid: 100

Mean fluid $\delta^{13}C$‰: -23

Carbon activity of the fluid: 1

Δ Buffer of the fluid: -0.647

$fO_2$ Buffer for fluid: FMQ Miozzi and 1

Solid-C Mol (optional): 0

Solid-C $\delta^{13}C$‰ (optional):

☐ Solid-C is exchanging

Warning lengthy calculation

**Output file parameters:**

Output file name

☐ Generate output .TXT file

☐ Include data points in .TXT output file

☐ Save graph as a .SVG file

Graphite stable
500 °C
2 kbar

Solid-C precipitated 11.68
% C remaining in the fluid 0.3136
$\delta^{13}C$ fluid -15.34
$\delta^{13}C$ graphite -24.71

*Figure 6.9: A: Calculation of the fluid water-loss at 500°C and 2 kbar. The carbon activity was set at 1 as the previous interaction presented in Fig 6.8 resolved the initial supersaturation (A). The results of the model show a fluid leading to the precipitation of graphite with changing $fO_2$ as the water fraction diminishes (B) with a graphite isotopic composition increasingly lighter as the fluid keeps losing its water fraction (C).*

Overall, Thermotopes-COH could reproduce the interpretation by Ortega et al. (2010) and allowed to expand on the potential redox changes of the system as well as to estimate the amount of graphite precipitated for a given amount of fluid. However, Ortega et al., (2010) argued that the final part of the Borrowdale graphite mineralization is driven by the preferential consumption of $CO_2$, leading to $CH_4$-dominant final fluid compositions. Modeling such precipitation is currently out of the scope of Thermotopes-COH and leads to some degrees of inaccuracy of the model.

Acknowledgment

Isotopic parameters come mainly from a compilation of isotopic fractionation equations from “IsoFrace” Jordi Delgado Martin. This work is part of a project that has received funding from the European Research Council (ERC) under the European Union’s Horizon 2020 research and innovation program (Grant agreement No. 864045; project acronym DeepSeep). A MIUR Rita Levi Montalcini grant and a Richard Launsbery grant to AVB are also acknowledged.

## 6.5 Appendices

Supplementary material 6.1:

The multicomponent model featured in tab 3 allows to monitor the isotopic evolution of a fluid containing both $CO_2$ and $CH_4$ in the case of precipitation of graphite/diamond. However, it does not consider the mechanism, nor the thermodynamic settings linked to the precipitation. The Dissolution/precipitation model presented in tab 5 aims to couple thermodynamic and isotopic evolutions. Here is presented comparison of results provided by both methods from the modeling of desiccation of a fluid at $CH_4/CO_2=0.9$ at 800°C and 4 GPa (in the diamond stability field) from a fluid with an initial $\delta^{13}C$ composition of 0 ‰. Supplementary Figure 6.1. shows the results for each model, which are in excellent agreement. However, these methods can only be compared by desiccation process as this is the only process supported by the multicomponent model.

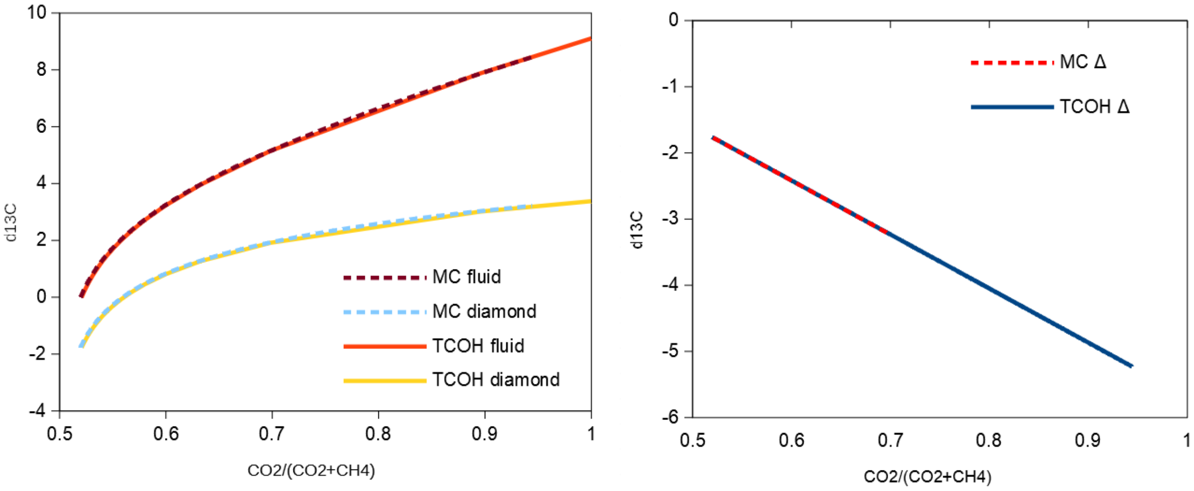

Supplementary figure 6.1: Comparison of the diamond and fluid in the Thermotopes-COH (TCOH) tab 5 Dissolution/precipitation and from the multicomponent system (MC). A: Evolution of the $\delta^{13}C$ of diamond and fluid for each system as function of the $CO_2/(CO_2+CH_4)$ ratio. B: evolution of the Δ diamond-fluid for each system as function of the $CO_2/(CO_2+CH_4)$ ratio.

Supplementary Table 6.2: Isotopic data of the Borrowdale graphite and inferred source of carbon from Ortega et al. (2010).

| **Graphite deposit** | | **Carbon Source** | | |
|---|---|---|---|---|
| Sample name | $\delta^{13}$C(PDB) | Sample | $\delta^{13}$C(PDB) | |
| P0-05 Grand Pipe | -26.9 | SK-1-1 (<53 lm) | -28.14 | -28.34 |
| P0-06 Grand Pipe | -25.8 | SK-1-2 (<53 lm) | -27.78 | -27.85 |
| G201 Gill’s level | -25 | SK-1-3 (<25 lm) | -24.35 | -24.38 |
| G2-02 Gill’s level | -26.2 | SK-2-1 (<53 lm) | -29.86 | -30.07 |
| G2-03 Gill’s level | -26.2 | SK-2-2 (<53 lm) | -30.12 | -30.09 |
| G2-04 Gill’s level | -26.1 | SK-2-3 (<25 lm) | -28.14 | -28.05 |
| G2-05 Gill’s level | -26.4 | SK-3-1 (<53 lm) | -27.27 | -27.38 |
| G2-06 Gill’s level | -26.5 | SK-3-2 (<53 lm) | -27.41 | -27.35 |
| G2-07 Gill’s level | -23.4 | SK-3-3 (<25 lm) | -23.57 | -23.41 |
| G2-08 Gill’s level | -27.4 | | | |
| G2-09 Gill’s level | -27.4 | | | |
| G2-10 Gill’s level | -26.5 | | | |
| G2-11 Gill’s level | -27.1 | | | |
| G2-12 Gill’s level | -26.6 | | | |
| G2-13 Gill’s level | -26.6 | | | |
| G4 Gill’s level | -27.1 | | | |
| G6 Gill’s level | -26.3 | | | |
| GB3 Gilbert’s level | -28.3 | | | |
| GB9 Gilbert’s level | -28.3 | | | |
| P2-1 Grand Pipe | -26.3 | | | |
| F1-1 Farey’s level | -26.4 | | | |
| F1-2 Farey’s level | -26.3 | | | |

# Part III – Conclusions and perspectives

## 7 Conclusions

This thesis provides new insights into the mechanisms and controlling factors of abiotic methane formation and the mobility of carbon in subduction based on natural examples from a metamorphic ultramafic body. Through a combination of field, petrological, and geochemical data with thermodynamic modeling, the present work sheds new light on: (i) the patterns of serpentinization of ultramafic bodies in subduction zone; (ii) the associated genesis of o abiotic methane; (iii) the mechanism of migration and recycling of carbon-rich fluids in subduction settings from the natural laboratory of the Belvidere Mountain Complex (BMC), northern Vermont, USA. Additionally, this thesis allowed developing new numerical tools to model the thermodynamic and isotopic evolution of COH fluids.

Although the BMC underwent a complex tectonic evolution potentially characterized by multiple stages of hydration from the (sub)seafloor to subduction and exhumation, the collected data point to a major event of high-pressure serpentinization that took place in the Appalachian subduction zone at 400 °C and 1 GPa. Furthermore, metamorphic olivine in the BMC serpentinized peridotite is interpreted as the product of rock hydration rather than dehydration, linked to the high-pressure serpentinization event. Our data support the hypothesis that the methane observed in olivine-hosted secondary fluid inclusions is genetically linked to serpentinization in the antigorite stability field, which is consistent with the high-pressure portion of either the prograde or retrograde P-T path experienced by the BMC. This suggests an abiotic origin for this methane, even though a biotic origin for the C source is indicated by the collected isotopic data. The C- and N-rich composition of fluid inclusions suggests a metasediment-derived origin for the serpentinizing fluid. The high-pressure serpentinization and related abiotic methane generation place the Belvidere mountain complex as a suitable proxy for the study of mantle wedge serpentinization.

Further, petrological, Raman, and isotopic data provided additional insights on the fate of carbon at the Belvidere Mountain Complex, Appalachian belt, Northern Vermont. The exceptional graphite deposit observed across the study site highlights the carbon mobility in the subduction zone and the complex mechanism of fluid interaction with evolving redox conditions. The carbon, strontium, and boron isotopes indicate fluid infiltrations evolving from metasedimentary rocks in subduction as the initial fluid influx responsible for the high-pressure serpentinization and first metasomatic event. Isotopic investigation of methane in fluid inclusions highlights a complex evolution involving both metasediment-derived, high-temperature thermogenic (biotic) and serpentinization-related (abiotic) $CH_4$-forming processes. Collected data and numerical results point toward graphite precipitation as the results of the mixing of $CH_4$ released by the HP serpentinization of the BMC with more oxidized infiltrating fluid (possibly the same fluid driving the serpentinization). This study outlines that ultramafic bodies in subduction can retain their potential to be abiotic producers of methane during relatively shallow subduction conditions (before antigorite destabilization). However, the redox state of surrounding formations seems to play an important role as it could severely impede fluid mobility of carbon. In this scope, the mantle wedge interacting with the slab as a source of water and carbon could host similar reactions, with implications for the redox state of subduction, carbon cycling in subduction and for the interpretation of biotic vs. abiotic signatures on earth and potentially beyond. A recent study highlights such a phenomenon with the high oxidation potential of the metasedimentary cover of the slab demonstrating capability to convert a high amount of fluid (Ague et al., 2022).

The hypotheses and conclusions presented above required a complex integration of thermodynamic and isotopic calculations. This need motivated the computation of Thermotopes-COH, a Python-based software that allows modeling and visualizing the thermodynamic properties and isotopic composition of COH fluids and graphite/diamond in equilibrium with them. This software is available at https://zenodo.org/record/6550956 with a Windows and Mac version. It can plot data on many different binary diagrams which may be saved under various formats and the data can be extracted as a .txt file.

## 7.1 Perspectives

The results of the present Ph.D thesis are a step forward for the understanding of the formation of abiotic methane in planetary interior, the related high-pressure fluid-rock interactions in ultramafic rocks, and their implications of the global carbon cycle.

As a whole, this Ph.D thesis highlights the complexity of carbon mobility in subduction especially in the presence of complex fluid-rock interactions such as serpentinization. Pluri-disciplinary approaches are key to investigate the succession of events often observed in subduction related samples. Especially when investigating abiotic methanogenesis, this work outlines the need to differentiate abiotic/biotic processes and carbon originating from an abiotic/source, where all these concepts can find themselves mixed in subduction zones settings. Because of this, hydrocarbons produced by abiotic processes may display isotopic compositions classically attributed to thermogenic or other biological processes if the carbon mobilized is from biotic origin.

This work contributes to the understanding of the redox state of carbon in subduction zones, where ultramafic rocks in the subducted slab and in the overlying mantle wedge can provide significant release of reduced compound. Further investigations on fluid phases from subduction zones would help unravel the complexity of the redox state, with the coupling of new analysis methods, such as using $CH_4$-clumped isotopes processes (Ono et al., 2021; Shuai et al., 2018; Young et al., 2017).

By providing easy accessing isotopic and thermodynamic tools, the Thermotopes-COH software may allow an increasing number of studies to include such tools and better discuss and track carbon at depth. The modeling of carbon mobility provides application outside of subduction settings and may see uses in diamond formation or “meteorite study”. The coupling of thermodynamic modeling and isotope modeling allows better investigation of numerous geological processes. Pursuing the combination of both fluids and rocks phases on a more complex system than the COH system would allow even more in-depth modeling of complex study zones and interconnected geological processes.

# Part IV – References

## 8 References

Abers, G.A., van Keken, P.E., Kneller, E.A., Ferris, A., Stachnik, J.C., 2006. The thermal structure of subduction zones constrained by seismic imaging: Implications for slab dehydration and wedge flow. Earth Planet. Sci. Lett. 241, 387–397.

Adams, M.W., 1992. Novel iron—sulfur centers in metalloenzymes and redox proteins from extremely thermophilic bacteria. Adv. Inorg. Chem. 38, 341–396.

Agrinier, P., Cannat, M., 1997. Oxygen-isotope constraints on serpentinization processes in ultramafic rocks from the Mid-Atlantic Ridge (23 N). Notes 47, 95–1.

Ague, J.J., 2017. Element mobility during regional metamorphism in crustal and subduction zone environments with a focus on the rare earth elements (REE). Am. Mineral. 102, 1796–1821.

Ague, J.J., Nicolescu, S., 2014. Carbon dioxide released from subduction zones by fluid-mediated reactions. Nat. Geosci. 7, 355.

Ague, J.J., Tassara, S., Holycross, M.E., Li, J.-L., Cottrell, E., Schwarzenbach, E.M., Fassoulas, C., John, T., 2022. Slab-derived devolatilization fluids oxidized by subducted metasedimentary rocks. Nat. Geosci. 1–7.

Alt, J.C., Garrido, C.J., Shanks III, W.C., Turchyn, A., Padrón-Navarta, J.A., Sánchez-Vizcaíno, V.L., Pugnaire, M.T.G., Marchesi, C., 2012. Recycling of water, carbon, and sulfur during subduction of serpentinites: A stable isotope study of Cerro del Almirez, Spain. Earth Planet. Sci. Lett. 327, 50–60.

Alt, J.C., Schwarzenbach, E.M., Früh-Green, G.L., Shanks III, W.C., Bernasconi, S.M., Garrido, C.J., Crispini, L., Gaggero, L., Padrón-Navarta, J.A., Marchesi, C., 2013. The role of serpentinites in cycling of carbon and sulfur: Seafloor serpentinization and subduction metamorphism. Lithos 178, 40–54.

Alt, J.C., Shanks III, W.C., Bach, W., Paulick, H., Garrido, C.J., Beaudoin, G., 2007. Hydrothermal alteration and microbial sulfate reduction in peridotite and gabbro exposed by detachment faulting at the Mid-Atlantic Ridge, 15° 20′ N (ODP Leg 209): A sulfur and oxygen isotope study. Geochem. Geophys. Geosystems 8.

Alt, J.C., Teagle, D.A., 1999. The uptake of carbon during alteration of ocean crust. Geochim. Cosmochim. Acta 63, 1527–1535.

Andréani, M., Mével, C., Boullier, A.-M., Escartin, J., 2007. Dynamic control on serpentine crystallization in veins: Constraints on hydration processes in oceanic peridotites. Geochem. Geophys. Geosystems 8.

Andreani, M., Munoz, M., Marcaillou, C., Delacour, A., 2013. µXANES study of iron redox state in serpentine during oceanic serpentinization. Lithos 178, 70–83.

Arai, S., Ishimaru, S., Mizukami, T., 2012. Methane and propane micro-inclusions in olivine in titanoclinohumite-bearing dunites from the Sanbagawa high-P metamorphic belt, Japan: Hydrocarbon activity in a subduction zone and Ti mobility. Earth Planet. Sci. Lett. 353, 1–11.

Auzende, A.-L., Daniel, I., Reynard, B., Lemaire, C., Guyot, F., 2004. High-pressure behaviour of serpentine minerals: a Raman spectroscopic study. Phys. Chem. Miner. 31, 269–277.

Bach, W., Garrido, C.J., Paulick, H., Harvey, J., Rosner, M., 2004. Seawater-peridotite interactions: First insights from ODP Leg 209, MAR 15 N. Geochem. Geophys. Geosystems 5.

Bach, W., Rosner, M., Jöns, N., Rausch, S., Robinson, L.F., Paulick, H., Erzinger, J., 2011. Carbonate veins trace seawater circulation during exhumation and uplift of mantle rock: Results from ODP Leg 209. Earth Planet. Sci. Lett. 311, 242–252.

Balaram, V., 2019. Rare earth elements: A review of applications, occurrence, exploration, analysis, recycling, and environmental impact. Geosci. Front. 10, 1285–1303.

Ballhaus, C., Berry, R.F., Green, D.H., 1991. High pressure experimental calibration of the olivine-orthopyroxene-spinel oxygen geobarometer: implications for the oxidation state of the upper mantle. Contrib. Mineral. Petrol. 107, 27–40.

Barrenechea, J.F., Luque, F.J., Millward, D., Ortega, L., Beyssac, O., Rodas, M., 2009. Graphite morphologies from the Borrowdale deposit (NW England, UK): Raman and SIMS data. Contrib. Mineral. Petrol. 158, 37–51.

Barry, P.H., de Moor, J.M., Giovannelli, D., Schrenk, M., Hummer, D.R., Lopez, T., Pratt, C.A., Segura, Y.A., Battaglia, A., Beaudry, P., 2019. Forearc carbon sink reduces long-term volatile recycling into the mantle. Nature 568, 487–492.

Beaudoin, G., Therrien, P., 2009. The updated web stable isotope fractionation calculator. Handb. Stable Isot. Anal. Tech. 2, 1120–1122.

Beaudoin, G., Therrien, P., 2004. The web stable isotope fractionation calculator. Handb. Stable Isot. Anal. Tech. 1, 1045–1047.

Beaudry, P., Stefánsson, A., Fiebig, J., Rhim, J.H., Ono, S., 2021. High temperature generation and equilibration of methane in terrestrial geothermal systems: evidence from clumped isotopologues. Geochim. Cosmochim. Acta 309, 209–234.

Bebout, G.E., 1991. Field-based evidence for devolatilization in subduction zones: implications for arc magmatism. Science 251, 413–416.

Bebout, G.E., Barton, M.D., 1993. Metasomatism during subduction: products and possible paths in the Catalina Schist, California. Chem. Geol. 108, 61–92.

Bebout, G.E., Fogel, M.L., 1992. Nitrogen-isotope compositions of metasedimentary rocks in the Catalina Schist, California: implications for metamorphic devolatilization history. Geochim. Cosmochim. Acta 56, 2839–2849.

Bebout, G.E., Penniston-Dorland, S.C., 2016. Fluid and mass transfer at subduction interfaces—The field metamorphic record. Lithos 240–243, 228–258. https://doi.org/10.1016/j.lithos.2015.10.007

Beeskow, B., Treloar, P.J., Rankin, A.H., Vennemann, T.W., Spangenberg, J., 2006. A reassessment of models for hydrocarbon generation in the Khibiny nepheline syenite complex, Kola Peninsula, Russia. Lithos 91, 1–18.

Beinert, H., Holm, R.H., Münck, E., 1997. Iron-sulfur clusters: nature's modular, multipurpose structures. Science 277, 653–659.

Berkesi, M., Hidas, K., Guzmics, T., Dubessy, J., Bodnar, R.J., Szabó, C., Vajna, B., Tsunogae, T., 2009. Detection of small amounts of H2O in CO2-rich fluid inclusions using Raman spectroscopy. J. Raman Spectrosc. Int. J. Orig. Work Asp. Raman Spectrosc. High. Order Process. Also Brillouin Rayleigh Scatt. 40, 1461–1463.

Berman, R.G., 1988. Internally-consistent thermodynamic data for minerals in the system Na2O-K2O-CaO-MgO-FeO-Fe2O3-Al2O3-SiO2-TiO2-H2O-CO2. J. Petrol. 29, 445–522.

Berndt, M.E., Allen, D.E., Seyfried Jr, W.E., 1996. Reduction of CO2 during serpentinization of olivine at 300 C and 500 bar. Geology 24, 351–354.

Berner, R.A., 1999. A new look at the long-term carbon cycle. Gsa Today 9, 1–6.

Berner, R.A., Kothavala, Z., 2001. GEOCARB III: a revised model of atmospheric CO2 over Phanerozoic time. Am. J. Sci. 301, 182–204.

Blakely, R.J., Brocher, T.M., Wells, R.E., 2005. Subduction-zone magnetic anomalies and implications for hydrated forearc mantle. Geology 33, 445–448.

Bostock, M.G., Hyndman, R.D., Rondenay, S., Peacock, S.M., 2002. An inverted continental Moho and serpentinization of the forearc mantle. Nature 417, 536.

Bottinga, Y., 1969. Calculated fractionation factors for carbon and hydrogen isotope exchange in the system calcite-carbon dioxide-graphite-methane-hydrogen-water vapor. Geochim. Cosmochim. Acta 33, 49–64.

Boutier, A., Brovarone, A.V., Martinez, I., Sissmann, O., Mana, S., 2021. High-pressure serpentinization and abiotic methane formation in metaperidotite from the Appalachian subduction, northern Vermont. Lithos 106190.

Bradley, A.S., Summons, R.E., 2010. Multiple origins of methane at the Lost City Hydrothermal Field. Earth Planet. Sci. Lett. 297, 34–41.

Breitenbach, S.F., Bernasconi, S.M., 2011. Carbon and oxygen isotope analysis of small carbonate samples (20 to 100 Âµg) with a GasBench II preparation device. Rapid Commun. Mass Spectrom. 25, 1910–1914.

Bromiley, G.D., Pawley, A.R., 2003. The stability of antigorite in the systems MgO-SiO2-H2O (MSH) and MgO-Al2O3-SiO2-H2O (MASH): The effects of Al3+ substitution on high-pressure stability. Am. Mineral. 88, 99–108.

Brooks, J.D., Smith, J.W., 1969. The diagenesis of plant lipids during the formation of coal, petroleum and natural gas—II. Coalification and the formation of oil and gas in the Gippsland Basin. Geochim. Cosmochim. Acta 33, 1183–1194.

Brooks, J.D., Smith, J.W., 1967. The diagenesis of plant lipids during the formation of coal, petroleum and natural gas—I. Changes in the n-paraffin hydrocarbons. Geochim. Cosmochim. Acta 31, 2389–2397.

Brophy, J.G., Pu, X., 2012. Rare earth element–SiO2 systematics of mid-ocean ridge plagiogranites and host gabbros from the Fournier oceanic fragment, New Brunswick, Canada: a field evaluation of some model predictions. Contrib. Mineral. Petrol. 164, 191–204.

Burnham, C.W., Holloway, J.R., Davis, N.F., 1969. Thermodynamic Properties of Water to 1, 0000 C and 10,000 Bars. Geological Society of America.

Burton, M.R., Sawyer, G.M., Granieri, D., 2013. Deep carbon emissions from volcanoes. Rev. Mineral. Geochem. 75, 323–354.

Cannaò, E., Scambelluri, M., Agostini, S., Tonarini, S., Godard, M., 2016. Linking serpentinite geochemistry with tectonic evolution at the subduction plate-interface: The Voltri Massif case study (Ligurian Western Alps, Italy). Geochim. Cosmochim. Acta 190, 115–133.

Cannat, M., Fontaine, F., Escartin, J., 2010. Serpentinization and associated hydrogen and methane fluxes at slow spreading ridges. Divers. Hydrothermal Syst. Slow Spreading Ocean Ridges 188, 241–264.

Carbotte, S.M., Scheirer, D.S., 2004. Variability of ocean crustal structure created along the global mid-ocean ridge. Hydrogeol. Ocean. Lithosphere 59–107.

Carlsen, K.S., Gale, M.H., Thompson, W.B., Kierstead, M., 2015. Belvidere Mountain Asbestos Quarries, Lowell/Eden, Vermont. Rocks Miner. 90, 510–551.

Carter, L.B., Dasgupta, R., 2016. Effect of melt composition on crustal carbonate assimilation: Implications for the transition from calcite consumption to skarnification and associated CO 2 degassing. Geochem. Geophys. Geosystems 17, 3893–3916.

Castonguay, S., Kim, J., Thompson, P.J., Gale, M.H., Joyce, N., Laird, J., Doolan, B.L., 2012. Timing of tectonometamorphism across the Green Mountain anticlinorium, northern Vermont Appalachians: 40Ar/39Ar data and correlations with southern Quebec. GSA Bull. 124, 352–367. https://doi.org/10.1130/B30487.1

Caumon, M.-C., Tarantola, A., Wang, W., 2019. Raman spectra of gas mixtures in fluid inclusions: Effect of quartz birefringence on composition measurement. J. Raman Spectrosc.

Cesare, B., 1995. Graphite precipitation in C—O—H fluid inclusions: closed system compositional and density changes, and thermobarometric implications. Contrib. Mineral. Petrol. 122, 25–33.

Chew, D.M., van Staal, C.R., 2014. The ocean–continent transition zones along the Appalachian–Caledonian Margin of Laurentia: Examples of large-scale hyperextension during the opening of the Iapetus Ocean. Geosci. Can. 41, 165–185.

Chidester, A.H., Albee, A.L., Cady, W.M., 1978. Petrology, structure, and genesis of the asbestos-bearing ultramafic rocks of the Belvidere Mountain area in Vermont. US Govt. Print. Off.,.

Christensen, N.I., 1966. Elasticity of ultrabasic rocks. J. Geophys. Res. 71, 5921–5931.

Ciais, P., Sabine, C., Bala, G., Bopp, L., Brovkin, V., Canadell, J., Chhabra, A., DeFries, R., Galloway, J., Heimann, M., 2014. Carbon and other biogeochemical cycles, in: Climate Change 2013: The Physical Science Basis. Contribution of Working Group I to the Fifth Assessment Report of the Intergovernmental Panel on Climate Change. Cambridge University Press, pp. 465–570.

Clift, P.D., 2017. A revised budget for Cenozoic sedimentary carbon subduction. Rev. Geophys. 55, 97–125.

Collins, N.C., Bebout, G.E., Angiboust, S., Agard, P., Scambelluri, M., Crispini, L., John, T., 2015. Subduction zone metamorphic pathway for deep carbon cycling: II. Evidence from HP/UHP metabasaltic rocks and ophicarbonates. Chem. Geol. 412, 132–150.

Colman, D.R., Poudel, S., Stamps, B.W., Boyd, E.S., Spear, J.R., 2017. The deep, hot biosphere: Twenty-five years of retrospection. Proc. Natl. Acad. Sci. 114, 6895–6903.

Connerney, J.E.P., Acuna, M.H., Wasilewski, P.J., Ness, N.F., Reme, H., Mazelle, C., Vignes, D., Lin, R.P., Mitchell, D.L., Cloutier, P.A., 1999. Magnetic lineations in the ancient crust of Mars. Science 284, 794–798.

Connolly, J.A.D., 1995. Phase diagram methods for graphitic rocks and application to the system C-O- H- FeO- TiO 2- SiO 2. Contrib. Mineral. Petrol. 119, 94–116.

Connolly, J.A.D., Cesare, B., 1993. C-O-H-S fluid composition and oxygen fugacity in graphitic metapelites. J. Metamorph. Geol. 11, 379–388.

Cook-Kollars, J., Bebout, G.E., Collins, N.C., Angiboust, S., Agard, P., 2014. Subduction zone metamorphic pathway for deep carbon cycling: I. Evidence from HP/UHP metasedimentary rocks, Italian Alps. Chem. Geol. 386, 31–48.

Craig, H., Lupton, J.E., 1976. Primordial neon, helium, and hydrogen in oceanic basalts. Earth Planet. Sci. Lett. 31, 369–385.

Croswell, K., 1996. The alchemy of the heavens.

Curtis, A.C., Wheat, C.G., Fryer, P., Moyer, C.L., 2013. Mariana forearc serpentinite mud volcanoes harbor novel communities of extremophilic archaea. Geomicrobiol. J. 30, 430–441.

Dandar, O., Okamoto, A., Uno, M., Oyanagi, R., Nagaya, T., Burenjargal, U., Miyamoto, T., Tsuchiya, N., 2019. Formation of secondary olivine after orthopyroxene during hydration of mantle wedge: evidence from the Khantaishir Ophiolite, western Mongolia. Contrib. Mineral. Petrol. 174, 86.

Dansgaard, W., 1964. Stable isotopes in precipitation. Tellus 16, 436–468.

Dasgupta, R., 2013. Ingassing, Storage, and Outgassing of Terrestrial Carbon through Geologic Time. Rev. Mineral. Geochem. 75, 183–229. https://doi.org/10.2138/rmg.2013.75.7

Dasgupta, R., Hirschmann, M.M., 2010. The deep carbon cycle and melting in Earth’s interior. Earth Planet. Sci. Lett. 298, 1–13. https://doi.org/10.1016/j.epsl.2010.06.039

Dasgupta, R., Hirschmann, M.M., Withers, A.C., 2004. Deep global cycling of carbon constrained by the solidus of anhydrous, carbonated eclogite under upper mantle conditions. Earth Planet. Sci. Lett. 227, 73–85.

Day, H.W., 2012. A revised diamond-graphite transition curve. Am. Mineral. 97, 52–62.

de Santis, R., Breedveld, G.J.F., Prausnitz, J.M., 1974. Thermodynamic properties of aqueous gas mixtures at advanced pressures. Ind. Eng. Chem. Process Des. Dev. 13, 374–377.

Debret, B., Bolfan-Casanova, N., Padrón-Navarta, J.A., Martin-Hernandez, F., Andreani, M., Garrido, C.J., Sanchez-Vizcaino, V.L., Gómez-Pugnaire, M.T., Munoz, M., Trcera, N., 2015. Redox state of iron during high-pressure serpentinite dehydration. Contrib. Mineral. Petrol. 169, 36.

Debret, B., Nicollet, C., Andreani, M., Schwartz, S., Godard, M., 2013. Three steps of serpentinization in an eclogitized oceanic serpentinization front (Lanzo Massif–Western Alps). J. Metamorph. Geol. 31, 165–186.

Debret, B., Sverjensky, D.A., 2017. Highly oxidising fluids generated during serpentinite breakdown in subduction zones. Sci. Rep. 7, 1–6.

Deines, P., 1992. Mantle carbon: concentration, mode of occurrence, and isotopic composition, in: Early Organic Evolution. Springer, pp. 133–146.

Deschamps, F., Godard, M., Guillot, S., Hattori, K., 2013. Geochemistry of subduction zone serpentinites: A review. Lithos 178, 96–127.

Deschamps, F., Guillot, S., Godard, M., Andreani, M., Hattori, K., 2011. Serpentinites act as sponges for fluid-mobile elements in abyssal and subduction zone environments. Terra Nova 23, 171–178.

Deschamps, F., Guillot, S., Godard, M., Chauvel, C., Andreani, M., Hattori, K., 2010. In situ characterization of serpentinites from forearc mantle wedges: timing of serpentinization and behavior of fluid-mobile elements in subduction zones. Chem. Geol. 269, 262–277.

Doolan, B.L., Gale, M.H., Gale, P.N., Hoar, R.S., St-Julien, P., 1982. Geology of the Quebec re-entrant: possible constraints from early rifts and the Vermont-Quebec serpentine belt. Major Struct. Zones Faults North. Appalach. Ed. P St-Julien J Béland Geol. Assoc. Can. Spec. Pap. 24, 87–115.

Douglas, P.M., Stolper, D.A., Eiler, J.M., Sessions, A.L., Lawson, M., Shuai, Y., Bishop, A., Podlaha, O.G., Ferreira, A.A., Neto, E.V.S., 2017. Methane clumped isotopes: Progress and potential for a new isotopic tracer. Org. Geochem. 113, 262–282.

Duke, E.F., Rumble, D., 1986. Textural and isotopic variations in graphite from plutonic rocks, south-central New Hampshire. Contrib. Mineral. Petrol. 93, 409–419.

Duncan, M.S., Dasgupta, R., 2017. Rise of Earth’s atmospheric oxygen controlled by efficient subduction of organic carbon. Nat. Geosci. 10, 387–392.

Dvir, O., Kessel, R., 2017. The effect of CO2 on the water-saturated solidus of K-poor peridotite between 4 and 6 GPa. Geochim. Cosmochim. Acta 206, 184–200.

Ehrenfreund, P., Charnley, S.B., 2000. Organic molecules in the interstellar medium, comets, and meteorites: a voyage from dark clouds to the early Earth. Annu. Rev. Astron. Astrophys. 38, 427–483.

Etiope, G., Schoell, M., 2014. Abiotic gas: atypical, but not rare. Elements 10, 291–296.

Etiope, G., Schoell, M., Hosgörmez, H., 2011. Abiotic methane flux from the Chimaera seep and Tekirova ophiolites (Turkey): understanding gas exhalation from low temperature serpentinization and implications for Mars. Earth Planet. Sci. Lett. 310, 96–104.

Etiope, G., Sherwood Lollar, B., 2013. Abiotic methane on Earth. Rev. Geophys. 51, 276–299.

Evans, B.W., 2010. Lizardite versus antigorite serpentinite: Magnetite, hydrogen, and life (?). Geology 38, 879–882.

Evans, B.W., 2008. Control of the products of serpentinization by the Fe2+ Mg- 1 exchange potential of olivine and orthopyroxene. J. Petrol. 49, 1873–1887.

Evans, B.W., 2004. The serpentinite multisystem revisited: chrysotile is metastable. Int. Geol. Rev. 46, 479–506.

Evans, K., 2011. Metamorphic carbon fluxes: how much and how fast? Geology 39, 95–96.

Evans, K.A., 2012. The redox budget of subduction zones. Earth-Sci. Rev. 113, 11–32. https://doi.org/10.1016/j.earscirev.2012.03.003

Evans, K.A., Bickle, M.J., Skelton, A.D.L., Hall, M., Chapman, H., 2002. Reductive deposition of graphite at lithological margins in East Central Vermont: a Sr, C and O isotope study. J. Metamorph. Geol. 20, 781–798.

Evans, K.A., Frost, B.R., 2021. Deserpentinization in Subduction Zones as a Source of Oxidation in Arcs: A Reality Check. J. Petrol.

Evans, K.A., Reddy, S.M., Tomkins, A.G., Crossley, R.J., Frost, B.R., 2017. Effects of geodynamic setting on the redox state of fluids released by subducted mantle lithosphere. Lithos 278–281, 26–42. https://doi.org/10.1016/j.lithos.2016.12.023

Evans, K.A., Tomkins, A.G., Cliff, J., Fiorentini, M.L., 2014. Insights into subduction zone sulfur recycling from isotopic analysis of eclogite-hosted sulfides. Chem. Geol. 365, 1–19.

Faccenda, M., 2014. Water in the slab: A trilogy. Tectonophysics 614, 1–30.

Facq, S., Daniel, I., Montagnac, G., Cardon, H., Sverjensky, D.A., 2014. In situ Raman study and thermodynamic model of aqueous carbonate speciation in equilibrium with aragonite under subduction zone conditions. Geochim. Cosmochim. Acta 132, 375–390.

Ferry, J.M., 2007. The role of volatile transport by diffusion and dispersion in driving biotite-forming reactions during regional metamorphism of the Gile Mountain Formation, Vermont. Am. Mineral. 92, 1288–1302.

Fischer, F., Tropsch, H., 1926. The synthesis of petroleum at atmospheric pressures from gasification products of coal. Brennst.-Chem. 7, 97–104.

Förster, B., Braga, R., Aulbach, S., Pò, D.L., Bargossi, G.M.G.M., Mair, V., 2017. A petrographic study of carbonate phases in the Ulten Zone ultramafic rocks: insights into carbonation in the mantle wedge and exhumation-related decarbonation. Ofioliti 42, 105–127.

Forster, P., Ramaswamy, V., Artaxo, P., Berntsen, T., Betts, R., Fahey, D.W., Haywood, J., Lean, J., Lowe, D.C., Myhre, G., 2007. Changes in atmospheric constituents and in radiative forcing. Chapter 2, in: Climate Change 2007. The Physical Science Basis.

Foster, G.L., 2008. Seawater pH, pCO2 and [CO2- 3] variations in the Caribbean Sea over the last 130 kyr: A boron isotope and B/Ca study of planktic foraminifera. Earth Planet. Sci. Lett. 271, 254–266.

Foustoukos, D.I., Seyfried Jr, W.E., 2004. Hydrocarbons in hydrothermal vent fluids: the role of chromium-bearing catalysts. Science 304, 1002–1005.

French, B.M., 1966. Some geological implications of equilibrium between graphite and a C-H-O gas phase at high temperatures and pressures. Rev. Geophys. 4, 223–253.

Frezzotti, M.L., Selverstone, J., Sharp, Z.D., Compagnoni, R., 2011. Carbonate dissolution during subduction revealed by diamond-bearing rocks from the Alps. Nat. Geosci. 4, 703–706.

Frezzotti, M.L., Tecce, F., Casagli, A., 2012. Raman spectroscopy for fluid inclusion analysis. J. Geochem. Explor. 112, 1–20.

Fried, L.E., Howard, W.M., 2000. Explicit Gibbs free energy equation of state applied to the carbon phase diagram. Phys. Rev. B 61, 8734.

Frost, B.R., 2018. Introduction to oxygen fugacity and its petrologic importance, in: Oxide Minerals. De Gruyter, pp. 1–10.

Frost, B.R., 1985. On the stability of sulfides, oxides, and native metals in serpentinite. J. Petrol. 26, 31–63.

Frost, B.R., Beard, J.S., 2007. On silica activity and serpentinization. J. Petrol. 48, 1351–1368.

Früh-Green, G.L., Connolly, J.A., Plas, A., Kelley, D.S., Grobéty, B., 2004. Serpentinization of oceanic peridotites: implications for geochemical cycles and biological activity. Subseafloor Biosphere -Ocean Ridges 144, 119–136.

Früh-Green, G.L., Plas, A., Lécuyer, C., 1996. 14. Petrologic and stable isotope constraints on hydrothermal alteration and serpentinization of the EPR shallow mantle at Hess Deep (site 895), in: Proceedings of the Ocean Drilling Program, Scientific Results. pp. 255–291.

Fryer, P., Wheat, C.G., Mottl, M.J., 1999. Mariana blueschist mud volcanism: Implications for conditions within the subduction zone. Geology 27, 103–106.

Fullerton, K.M., Schrenk, M., Yücel, M., Manini, E., Fattorini, D., di Carlo, M., Regoli, F., Nakagawa, M., Smedile, F., Vetriani, C., 2019. Plate tectonics drive deep biosphere microbial community composition. Prepr. Httpseartharxiv Orggyr7n.

Fumagalli, P., Klemme, S., 2015. Phase transitions and mineralogy of the upper mantle.

Gale, M.H., 2007. Bedrock Geologic Map of the Hazens Notch and Portions of the Eden and Lowell Quadrangles, Vermont. Vt. Geol. Surv., Vermont geological open file report VG07-2, plate 1.

Gale, M.H., 1986. Geologic map of the Belvidere Mountain area, Eden and Lowell, Vermont (USGS Numbered Series No. 1560), IMAP.

Gale, M.H., 1980. Geology of the Belvidere Mountain Complex, Eden and Lowell, Vermont. US Geological Survey,.

Galvez, M.E., Beyssac, O., Martinez, I., Benzerara, K., Chaduteau, C., Malvoisin, B., Malavieille, J., 2013. Graphite formation by carbonate reduction during subduction. Nat. Geosci. 6, 473.

Giardini, A.A., Salotti, C.A., 1969. Kinetics and relations in the calcite-hydrogen reaction and relations in the dolomite-hy-drogen and siderite-hydrogen systems. Am. Mineral. J. Earth Planet. Mater. 54, 1151–1172.

Gilat, A.L., 2012. Degassing of primordial hydrogen and helium as the major energy source for internal terrestrial processes. Geosci. Front. 3, 911–921.

Giuntoli, F., Vitale Brovarone, A., Menegon, L., 2020. Feedback between high-pressure genesis of abiotic methane and strain localization in subducted carbonate rocks. Sci. Rep. 10, 1–15.

Gold, T., 1979. Terrestrial sources of carbon and earthquake outgassing. J. Pet. Geol. 1, 3–19.

Gonzalez, J.P., Baldwin, S.L., Thomas, J.B., Nachlas, W.O., Fitzgerald, P.G., 2020. Evidence for ultrahigh-pressure metamorphism discovered in the Appalachian orogen. Geology 48, 947–951.

Gorczyk, W., Guillot, S., Gerya, T.V., Hattori, K., 2007. Asthenospheric upwelling, oceanic slab retreat, and exhumation of UHP mantle rocks: Insights from Greater Antilles. Geophys. Res. Lett. 34.

Gorman, P.J., Kerrick, D.M., Connolly, J. a. D., 2006. Modeling open system metamorphic decarbonation of subducting slabs. Geochem. Geophys. Geosystems 7. https://doi.org/10.1029/2005GC001125

Green, D.H., Falloon, T.J., Taylor, W.R., 1987. Mantle-derived magmas-roles of variable source peridotite and variable CHO fluid compositions.

Grozeva, N.G., Klein, F., Seewald, J.S., Sylva, S.P., 2020. Chemical and isotopic analyses of hydrocarbon-bearing fluid inclusions in olivine-rich rocks. Philos. Trans. R. Soc. A 378, 20180431.

Guillot, S., Hattori, K., Agard, P., Schwartz, S., Vidal, O., 2009. Exhumation processes in oceanic and continental subduction contexts: a review. Subduction Zone Geodyn. 175–205.

Guillot, S., Hattori, K.H., de Sigoyer, J., 2000. Mantle wedge serpentinization and exhumation of eclogites: insights from eastern Ladakh, northwest Himalaya. Geology 28, 199–202.

Guillot, S., Schwartz, S., Reynard, B., Agard, P., Prigent, C., 2015. Tectonic significance of serpentinites. Tectonophysics 646, 1–19.

Hacker, B.R., 2008. H2O subduction beyond arcs. Geochem. Geophys. Geosystems 9.

Halama, R., Bebout, G.E., John, T., Scambelluri, M., 2014. Nitrogen recycling in subducted mantle rocks and implications for the global nitrogen cycle. Int. J. Earth Sci. 103, 2081–2099.

Hayes, J.M., Waldbauer, J.R., 2006. The carbon cycle and associated redox processes through time. Philos. Trans. R. Soc. Lond. B Biol. Sci. 361, 931–950. https://doi.org/10.1098/rstb.2006.1840

Hermann, J., Müntener, O., Scambelluri, M., 2000. The importance of serpentinite mylonites for subduction and exhumation of oceanic crust. Tectonophysics 327, 225–238.

Hibbard, J.P., Van Staal, C.R., Rankin, D.W., Williams, H., 2006. Lithotectonic map of the Appalachian orogen, Canada–United States of America. Geol. Surv. Can. Map A 2096, 2.

Hilton, D.R., McMurtry, G.M., Kreulen, R., 1997. Evidence for extensive degassing of the Hawaiian mantle plume from helium-carbon relationships at Kilauea volcano. Geophys. Res. Lett. 24, 3065–3068.

Hirschmann, M.M., 2018. Comparative deep Earth volatile cycles: The case for C recycling from exosphere/mantle fractionation of major (H2O, C, N) volatiles and from H2O/Ce, CO2/Ba, and CO2/Nb exosphere ratios. Earth Planet. Sci. Lett. 502, 262–273.

Hofmann, A.W., 1997. Mantle geochemistry: the message from oceanic volcanism. Nature 385, 219–229.

Holland, T.J.B., Powell, R., 1998. An internally consistent thermodynamic data set for phases of petrological interest. J. Metamorph. Geol. 16, 309–343.

Holloway, J.R., 1984. Graphite-CH4-H2O-CO2 equilibria at low-grade metamorphic conditions. Geology 12, 455–458.

Holloway, J.R., 1977. Fugacity and activity of molecular species in supercritical fluids, in: Thermodynamics in Geology. Springer, pp. 161–181.

Holm, N.G., Charlou, J.L., 2001. Initial indications of abiotic formation of hydrocarbons in the Rainbow ultramafic hydrothermal system, Mid-Atlantic Ridge. Earth Planet. Sci. Lett. 191, 1–8.

Holm, N.G., Oze, C., Mousis, O., Waite, J.H., Guilbert-Lepoutre, A., 2015. Serpentinization and the Formation of H2 and CH4 on Celestial Bodies (Planets, Moons, Comets). Astrobiology 15, 587. https://doi.org/10.1089/ast.2014.1188

Honsberger, I.W., 2015. Metamorphism, deformation, geochemistry, and tectonics of exhumed ultramafic and mafic rocks in the central and north-central Vermont Appalachians.

Honsberger, I.W., Laird, J., Thompson, P.J., 2017. A tectonized ultramafic-mafic-pelitic package in Stockbridge, Vermont: Metamorphism resulting from subduction and exhumation. Am. J. Sci. 317, 1019–1047.

Horita, J., Berndt, M.E., 1999. Abiogenic methane formation and isotopic fractionation under hydrothermal conditions. Science 285, 1055–1057.

Huang, F., Daniel, I., Cardon, H., Montagnac, G., Sverjensky, D.A., 2017. Immiscible hydrocarbon fluids in the deep carbon cycle. Nat. Commun. 8, 1–8.

Huang, F., Sverjensky, D.A., 2019. Extended Deep Earth Water Model for predicting major element mantle metasomatism. Geochim. Cosmochim. Acta 254, 192–230.

Huizenga, J.M., 2005. COH, an Excel spreadsheet for composition calculations in the COH fluid system. Comput. Geosci. 31, 797–800.

Hyndman, R.D., Peacock, S.M., 2003. Serpentinization of the forearc mantle. Earth Planet. Sci. Lett. 212, 417–432.

Iyer, K., Austrheim, H., John, T., Jamtveit, B., 2008. Serpentinization of the oceanic lithosphere and some geochemical consequences: constraints from the Leka Ophiolite Complex, Norway. Chem. Geol. 249, 66–90.

Javoy, M., Pineau, F., Delorme, H., 1986. Carbon and nitrogen isotopes in the mantle. Chem. Geol. 57, 41–62.

Johnston, F.K., Turchyn, A.V., Edmonds, M., 2011. Decarbonation efficiency in subduction zones: Implications for warm Cretaceous climates. Earth Planet. Sci. Lett. 303, 143–152.

Kamiya, S., Kobayashi, Y., 2000. Seismological evidence for the existence of serpentinized wedge mantle. Geophys. Res. Lett. 27, 819–822.

Karabinos, P., Samson, S.D., Hepburn, J.C., Stoll, H.M., 1998. Taconian orogeny in the New England Appalachians: Collision between Laurentia and the Shelburne Falls arc. Geology 26, 215–218. https://doi.org/10.1130/0091-7613(1998)026<0215:TOITNE>2.3.CO;2

Kasting, J.F., 2005. Methane and climate during the Precambrian era. Precambrian Res. 137, 119–129.

Kelemen, P.B., Manning, C.E., 2015. Reevaluating carbon fluxes in subduction zones, what goes down, mostly comes up. Proc. Natl. Acad. Sci. 112, E3997–E4006. https://doi.org/10.1073/pnas.1507889112

Kelley, D.S., Karson, J.A., Früh-Green, G.L., Yoerger, D.R., Shank, T.M., Butterfield, D.A., Hayes, J.M., Schrenk, M.O., Olson, E.J., Proskurowski, G., Jakuba, M., Bradley, A., Larson, B., Ludwig, K., Glickson, D., Buckman, K., Bradley, A.S., Brazelton, W.J., Roe, K., Elend, M.J., Delacour, A., Bernasconi, S.M., Lilley, M.D., Baross, J.A., Summons, R.E., Sylva, S.P., 2005. A Serpentinite-Hosted Ecosystem: The Lost City Hydrothermal Field. Science 307, 1428–1434. https://doi.org/10.1126/science.1102556

Kempf, E.D., Hermann, J., 2018. Hydrogen incorporation and retention in metamorphic olivine during subduction: Implications for the deep water cycle. Geology 46, 571–574.

Kendall, C., McDonnell, J.J., 2012. Isotope tracers in catchment hydrology. Elsevier Science Publishers: Amsterdam.

Kerper, D., van Baalen, M.R., Dunn, S., 2008. Anomalous graphite at the Belvidere Mountain serpentinite, Vermont, in: GSA Northeastern Regional Meeting, Buffalo, New York. pp. 35–12.

Kerrick, D.M., Connolly, J. a. D., 1998. Subduction of ophicarbonates and recycling of CO2 and H2O. Geology 26, 375–378. https://doi.org/10.1130/0091-7613(1998)026<0375:SOOARO>2.3.CO;2

Kerrick, D.M., Connolly, J.A.D., 2001a. Metamorphic devolatilization of subducted marine sediments and the transport of volatiles into the Earth's mantle. Nature 411, 293–296.

Kerrick, D.M., Connolly, J.A.D., 2001b. Metamorphic devolatilization of subducted oceanic metabasalts: implications for seismicity, arc magmatism and volatile recycling. Earth Planet. Sci. Lett. 189, 19–29. https://doi.org/10.1016/S0012-821X(01)00347-8

Khalil, M.A.K., Butenhoff, C.L., Rasmussen, R.A., 2007. Atmospheric methane: trends and cycles of sources and sinks. Environ. Sci. Technol. 41, 2131–2137.

Khalil, M.A.K., Rasmussen, R.A., 1983. Sources, sinks, and seasonal cycles of atmospheric methane. J. Geophys. Res. Oceans 88, 5131–5144.

Kitchen, N.E., Valley, J.W., 1995. Carbon isotope thermometry in marbles of the Adirondack Mountains, New York. J. Metamorph. Geol. 13, 577–594.

Klein, F., Bach, W., 2009. Fe–Ni–Co–O–S phase relations in peridotite–seawater interactions. J. Petrol. 50, 37–59.

Klein, F., Bach, W., Humphris, S.E., Kahl, W.-A., Jöns, N., Moskowitz, B., Berquó, T.S., 2014. Magnetite in seafloor serpentinite—Some like it hot. Geology 42, 135–138.

Klein, F., Bach, W., McCollom, T.M., 2013. Compositional controls on hydrogen generation during serpentinization of ultramafic rocks. Lithos 178, 55–69.

Klein, F., Grozeva, N.G., Seewald, J.S., 2019. Abiotic methane synthesis and serpentinization in olivine-hosted fluid inclusions. Proc. Natl. Acad. Sci. 116, 17666–17672.

Klein, F., Le Roux, V., 2020. Quantifying the volume increase and chemical exchange during serpentinization. Geology 48, 552–556.

Kokh, M.A., Akinfiev, N.N., Pokrovski, G.S., Salvi, S., Guillaume, D., 2017. The role of carbon dioxide in the transport and fractionation of metals by geological fluids. Geochim. Cosmochim. Acta 197, 433–466.

Kompanichenko, V.N., 2017. Astrobiology: Approaches to the Origin of Life on Earth and Beyond, in: Thermodynamic Inversion. Springer, pp. 1–14.

Konn, C., Charlou, J.-L., Donval, J.-P., Holm, N.G., Dehairs, F., Bouillon, S., 2009. Hydrocarbons and oxidized organic compounds in hydrothermal fluids from Rainbow and Lost City ultramafic-hosted vents. Chem. Geol. 258, 299–314.

Kwok, S., 2009. Organic matter in space: from star dust to the Solar System. Astrophys. Space Sci. 319, 5–21.

Labotka, T.C., Albee, A.L., 1979. Serpentinization of the Belvidere Mountain ultramafic body, Vermont; mass balance and reaction at the metasomatic front. Can. Mineral. 17, 831–845.

Laird, J., Bothner, W.A., Thompson, P.J., Thompson, T., Gale, M., Kim, J., 2001. Geochemistry, petrology, and structure of the Tillotson Peak and Belvidere Mountain mafic complexes, northern Vermont, in: Geological Society of America Abstracts with Programs. p. A59.

Laird, J., Lanphere, M.A., Albee, A.L., 1984. Distribution of Ordovician and Devonian metamorphism in mafic and pelitic schists from northern Vermont. Am. J. Sci. 284, 376–413.

Laird, J., Trzcienski, W.E., Bothner, W.A., Cheney, J.T., Hepburn, J.C., 1993. High-pressure, Taconian, and subsequent polymetamorphism of southern Quebec and northern Vermont. Contrib. Dep. Univ. Mass. 67, 1–32.

Lamadrid, H.M., Rimstidt, J.D., Schwarzenbach, E.M., Klein, F., Ulrich, S., Dolocan, A., Bodnar, R.J., 2017. Effect of water activity on rates of serpentinization of olivine. Nat. Commun. 8, 1–9.

Li, L., Cartigny, P., Ader, M., 2009. Kinetic nitrogen isotope fractionation associated with thermal decomposition of NH3: Experimental results and potential applications to trace the origin of N2 in natural gas and hydrothermal systems. Geochim. Cosmochim. Acta 73, 6282–6297.

Ligi, M., Bonatti, E., Rasul, N., 2015. Seafloor spreading initiation: geophysical and geochemical constraints from the Thetis and Nereus Deeps, central Red Sea, in: The Red Sea. Springer, pp. 79–98.

Lindgren, P., Parnell, J., 2006. Petrographic criteria for fluid mobility of graphitic carbon in terrestrial and extraterrestrial samples. J. Geochem. Explor. 91, 126–129.

Luisi, P.L., 2016. The emergence of life: from chemical origins to synthetic biology. Cambridge University Press.

Lundin, E.R., Doré, A.G., 2011. Hyperextension, serpentinization, and weakening: A new paradigm for rifted margin compressional deformation. Geology 39, 347–350.

Lünsdorf, N.K., Dunkl, I., Schmidt, B.C., Rantitsch, G., von Eynatten, H., 2014. Towards a higher comparability of geothermometric data obtained by Raman spectroscopy of carbonaceous material. Part I: Evaluation of biasing factors. Geostand. Geoanalytical Res. 38, 73–94.

Luque del Villar, F.J., Pasteris, J.D., Wopenka, B., Rodas, M., Fernández Barrenechea, J.M., 1998. Natural fluid-deposited graphite: mineralogical characteristics and mechanisms of formation. Am. J. Sci. 298, 471–498.

Luque, F.J., Crespo-Feo, E., Barrenechea, J.F., Ortega, L., 2012. Carbon isotopes of graphite: Implications on fluid history. Geosci. Front. 3, 197–207.

Luque, F.J., Ortega, L., Barrenechea, J.F., Millward, D., Beyssac, O., Huizenga, J.M., 2009. Deposition of highly crystalline graphite from moderate-temperature fluids. Geology 37, 275–278.

Maffione, M., Morris, A., Anderson, M.W., 2013. Recognizing detachment-mode seafloor spreading in the deep geological past. Sci. Rep. 3, 2336.

Majumdar, A.S., Hövelmann, J., Vollmer, C., Berndt, J., Mondal, S.K., Putnis, A., 2016. Formation of Mg-rich olivine pseudomorphs in serpentinized dunite from the Mesoarchean Nuasahi Massif, Eastern India: Insights into the evolution of fluid composition at the mineral–fluid interface. J. Petrol. 57, 3–26.

Malaspina, N., Tumiati, S., 2012. The role of COH and oxygen fugacity in subduction-zone garnet peridotites. Eur. J. Mineral. 24, 607–618.

Malvoisin, B., 2015. Mass transfer in the oceanic lithosphere: serpentinization is not isochemical. Earth Planet. Sci. Lett. 430, 75–85.

Malvoisin, B., Zhang, C., Müntener, O., Baumgartner, L.P., Kelemen, P.B., Party, O.D.P.S., 2020. Measurement of volume change and mass transfer during serpentinization: insights from the oman drilling project. J. Geophys. Res. Solid Earth 125, e2019JB018877.

Mangenot, X., Gasparrini, M., Rouchon, V., Bonifacie, M., 2018. Basin-scale thermal and fluid flow histories revealed by carbonate clumped isotopes (Δ47)–Middle Jurassic carbonates of the Paris Basin depocentre. Sedimentology 65, 123–150.

Manning, C.E., 2014. A piece of the deep carbon puzzle. Nat. Geosci. 7, 333–334.

Manning, C.E., Shock, E.L., Sverjensky, D.A., 2013. The chemistry of carbon in aqueous fluids at crustal and upper-mantle conditions: experimental and theoretical constraints. Rev. Mineral. Geochem. 75, 109–148.

Martin, C., Flores, K.E., Vitale-Brovarone, A., Angiboust, S., Harlow, G.E., 2020. Deep mantle serpentinization in subduction zones: Insight from in situ B isotopes in slab and mantle wedge serpentinites. Chem. Geol. 545, 119637.

Martin, W., Baross, J., Kelley, D., Russell, M.J., 2008. Hydrothermal vents and the origin of life. Nat. Rev. Microbiol. 6, 805–814.

Martini, A.M., Walter, L.M., McIntosh, J.C., 2008. Identification of microbial and thermogenic gas components from Upper Devonian black shale cores, Illinois and Michigan basins. Aapg Bull. 92, 327–339.

Marty, B., Alexander, C.M.O., Raymond, S.N., 2013. Primordial origins of Earth's carbon. Rev. Mineral. Geochem. 75, 149–181.

Mason, E., Edmonds, M., Turchyn, A.V., 2017a. Remobilization of crustal carbon may dominate volcanic arc emissions. Science 357, 290–294.

Mason, E., Edmonds, M., Turchyn, A.V., 2017b. Remobilization of crustal carbon may dominate volcanic arc emissions. Science 357, 290–294.

Masters, C., 1979. The Fischer-Tropsch Reaction, in: Advances in Organometallic Chemistry. Elsevier, pp. 61–103.

Maurice, J., Bolfan-Casanova, N., Padrón-Navarta, J.A., Manthilake, G., Hammouda, T., Hénot, J.M., Andrault, D., 2018. The stability of hydrous phases beyond antigorite breakdown for a magnetite-bearing natural serpentinite between 6.5 and 11 GPa. Contrib. Mineral. Petrol. 173, 1–22.

McCollom, T.M., 2016. Abiotic methane formation during experimental serpentinization of olivine. Proc. Natl. Acad. Sci. 113, 13965–13970.

McCollom, T.M., 2013. Laboratory simulations of abiotic hydrocarbon formation in Earth's deep subsurface. Rev. Mineral. Geochem. 75, 467–494.

McCollom, T.M., Bach, W., 2009. Thermodynamic constraints on hydrogen generation during serpentinization of ultramafic rocks. Geochim. Cosmochim. Acta 73, 856–875.

McCollom, T.M., Seewald, J.S., 2007. Abiotic synthesis of organic compounds in deep-sea hydrothermal environments. Chem. Rev. 107, 382–401.

McCollom, T.M., Seewald, J.S., 2006. Carbon isotope composition of organic compounds produced by abiotic synthesis under hydrothermal conditions. Earth Planet. Sci. Lett. 243, 74–84.

McCollom, T.M., Seewald, J.S., 2001. A reassessment of the potential for reduction of dissolved CO2 to hydrocarbons during serpentinization of olivine. Geochim. Cosmochim. Acta 65, 3769–3778.

McDermott, J.M., Seewald, J.S., German, C.R., Sylva, S.P., 2015. Pathways for abiotic organic synthesis at submarine hydrothermal fields. Proc. Natl. Acad. Sci. 112, 7668–7672.

Ménez, B., Pisapia, C., Andreani, M., Jamme, F., Vanbellingen, Q.P., Brunelle, A., Richard, L., Dumas, P., Réfrégiers, M., 2018. Abiotic synthesis of amino acids in the recesses of the oceanic lithosphere. Nature 564, 59–63. https://doi.org/10.1038/s41586-018-0684-z

Menzel, M.D., Garrido, C.J., López Sánchez-Vizcaíno, V., Marchesi, C., Hidas, K., Escayola, M.P., Delgado Huertas, A., 2018. Carbonation of mantle peridotite by CO2-rich fluids: the formation of listvenites in the Advocate ophiolite complex (Newfoundland, Canada). Lithos, ABYSS 323, 238–261. https://doi.org/10.1016/j.lithos.2018.06.001

Merkulova, M.V., Muñoz, M., Brunet, F., Vidal, O., Hattori, K., Vantelon, D., Trcera, N., Huthwelker, T., 2017. Experimental insight into redox transfer by iron-and sulfur-bearing serpentinite dehydration in subduction zones. Earth Planet. Sci. Lett. 479, 133–143.

Mével, C., 2003. Serpentinization of abyssal peridotites at mid-ocean ridges. Comptes Rendus Geosci. 335, 825–852.

Miozzi, F., Tumiati, S., 2020. Aqueous concentration of CO2 in carbon-saturated fluids as a highly sensitive oxybarometer. Geochem Persp Let 16, 30–34.

Molina, J.F., Poli, S., 2000. Carbonate stability and fluid composition in subducted oceanic crust: an experimental study on H2O–CO2-bearing basalts. Earth Planet. Sci. Lett. 176, 295–310. https://doi.org/10.1016/S0012-821X(00)00021-2

Moody, J.B., 1976. Serpentinization: a review. Lithos 9, 125–138.

Nakamura, K., Morishita, T., Bach, W., Klein, F., Hara, K., Okino, K., Takai, K., Kumagai, H., 2009. Serpentinized troctolites exposed near the Kairei Hydrothermal Field, Central Indian Ridge: Insights into the origin of the Kairei hydrothermal fluid supporting a unique microbial ecosystem. Earth Planet. Sci. Lett. 280, 128–136.

Nisbet, E.G., Sleep, N.H., 2001. The habitat and nature of early life. Nature 409, 1083.

Nozaka, T., 2018. Compositional variation of olivine related to high–temperature serpentinization of peridotites: Evidence from the Oeyama ophiolite. J. Mineral. Petrol. Sci. 180420.

Nozaka, T., 2003. Compositional heterogeneity of olivine in thermally metamorphosed serpentinite from Southwest Japan. Am. Mineral. 88, 1377–1384.

O'Brien, P.J., 2001. Subduction followed by collision: Alpine and Himalayan examples. Phys. Earth Planet. Inter. 127, 277–291.

Ohara, Y., Reagan, M.K., Fujikura, K., Watanabe, H., Michibayashi, K., Ishii, T., Stern, R.J., Pujana, I., Martinez, F., Girard, G., 2012. A serpentinite-hosted ecosystem in the Southern Mariana Forearc. Proc. Natl. Acad. Sci. 109, 2831–2835.

Ohmoto, H., Kerrick, D.M., 1977. Devolatilization equilibria in graphitic systems. Am. J. Sci. 277, 1013–1044.

O'Neill, H.S.C., Wall, V.J., 1987. The Olivine—Orthopyroxene—Spinel oxygen geobarometer, the nickel precipitation curve, and the oxygen fugacity of the Earth's Upper Mantle. J. Petrol. 28, 1169–1191.

Ono, S., Rhim, J.H., Gruen, D.S., Taubner, H., Kölling, M., Wegener, G., 2021. Clumped isotopologue fractionation by microbial cultures performing the anaerobic oxidation of methane. Geochim. Cosmochim. Acta 293, 70–85.

Orcutt, B.N., Daniel, I., Dasgupta, R., 2019. Deep Carbon: Past to Present. Cambridge University Press.

Ortega, L., Millward, D., Luque, F.J., Barrenechea, J.F., Beyssac, O., Huizenga, J.-M., Rodas, M., Clarke, S.M., 2010. The graphite deposit at Borrowdale (UK): a catastrophic mineralizing event associated with Ordovician magmatism. Geochim. Cosmochim. Acta 74, 2429–2449.

Oufi, O., Cannat, M., Horen, H., 2002. Magnetic properties of variably serpentinized abyssal peridotites. J. Geophys. Res. Solid Earth 107, EPM-3.

Padrón-Navarta, J.A., Hermann, J., Garrido, C.J., López Sánchez-Vizcaíno, V., Gómez-Pugnaire, M.T., 2010a. An experimental investigation of antigorite dehydration in natural silica-enriched serpentinite. Contrib. Mineral. Petrol. 159, 25–42.

Padrón-Navarta, J.A., Lopez Sanchez-Vizcaino, V., Garrido, C.J., Gómez-Pugnaire, M.T., 2011. Metamorphic record of high-pressure dehydration of antigorite serpentinite to chlorite harzburgite in a subduction setting (Cerro del Almirez, Nevado–Filábride Complex, Southern Spain). J. Petrol. 52, 2047–2078.

Padrón-Navarta, J.A., Sánchez-Vizcaíno, V.L., Hermann, J., Connolly, J.A., Garrido, C.J., Gómez-Pugnaire, M.T., Marchesi, C., 2013. Tschermak's substitution in antigorite and consequences for phase relations and water liberation in high-grade serpentinites. Lithos 178, 186–196.

Padrón-Navarta, J.A., Tommasi, A., Garrido, C.J., Sánchez-Vizcaíno, V.L., Gomez-Pugnaire, M.T., Jabaloy, A., Vauchez, A., 2010b. Fluid transfer into the wedge controlled by high-pressure hydrofracturing in the cold top-slab mantle. Earth Planet. Sci. Lett. 297, 271–286.

Peltola, E., 1968. On some geochemical features in the black schists of the Outokumpu area, Finland. Bull Geol Soc Finl. 40, 39–50.

Peng, W., Zhang, L., Tumiati, S., Brovarone, A.V., Hu, H., Cai, Y., Shen, T., 2021. Abiotic methane generation through reduction of serpentinite-hosted dolomite: implications for carbon mobility in subduction zones. Geochim. Cosmochim. Acta 311, 119–140.

Penniston-Dorland, S.C., Ferry, J.M., 2006. Development of spatial variations in reaction progress during regional metamorphism of micaceous carbonate rocks, northern New England. Am. J. Sci. 306, 475–524.

Petersilie, I.A., Ikorski, S.V., Smirnova, L.I., Romanikhin, A.M., Proskuryakova, E.B., 1961. Application of gas logging to the investigation of natural gases and bitumens in the Khibina intrusive massif. Geochem. Int. 10, 945–962.

Phillips, R.J., Hansen, V.L., 1998. Geological evolution of Venus: Rises, plains, plumes, and plateaus. Science 279, 1492–1497.

Philpotts, J.A., Schnetzler, C.C., 1968. Europium anomalies and the genesis of basalt. Chem. Geol. 3, 5–13.

Piccoli, F., Brovarone, A.V., Beyssac, O., Martinez, I., Ague, J.J., Chaduteau, C., 2016. Carbonation by fluid–rock interactions at high-pressure conditions: implications for carbon cycling in subduction zones. Earth Planet. Sci. Lett. 445, 146–159.

Piccoli, F., Hermann, J., Pettke, T., Connolly, J.A.D., Kempf, E.D., Duarte, J.V., 2019. Subducting serpentinites release reduced, not oxidized, aqueous fluids. Sci. Rep. 9, 1–7.

Piccoli, F., Vitale Brovarone, A., Ague, J.J., 2018. Field and petrological study of metasomatism and high-pressure carbonation from lawsonite eclogite-facies terrains, Alpine Corsica. Lithos 304–307, 16–37. https://doi.org/10.1016/j.lithos.2018.01.026

Pinto, V.H.G., Manatschal, G., Karpoff, A.M., Ulrich, M., Viana, A.R., 2017. Seawater storage and element transfer associated with mantle serpentinization in magma-poor rifted margins: A quantitative approach. Earth Planet. Sci. Lett. 459, 227–237.

Plank, T., Langmuir, C.H., 1998. The chemical composition of subducting sediment and its consequences for the crust and mantle. Chem. Geol. 145, 325–394.

Plank, T., Manning, C.E., 2019. Subducting carbon. Nature 574, 343–352.

Plümper, O., John, T., Podladchikov, Y.Y., Vrijmoed, J.C., Scambelluri, M., 2017a. Fluid escape from subduction zones controlled by channel-forming reactive porosity. Nat. Geosci. 10, 150–156. https://doi.org/10.1038/ngeo2865

Plümper, O., King, H.E., Geisler, T., Liu, Y., Pabst, S., Savov, I.P., Rost, D., Zack, T., 2017b. Subduction zone forearc serpentinites as incubators for deep microbial life. Proc. Natl. Acad. Sci. 114, 4324–4329.

Plümper, O., King, H.E., Vollmer, C., Ramasse, Q., Jung, H., Austrheim, H., 2012a. The legacy of crystal-plastic deformation in olivine: high-diffusivity pathways during serpentinization. Contrib. Mineral. Petrol. 163, 701–724.

Plümper, O., Piazolo, S., Austrheim, H., 2012b. Olivine pseudomorphs after serpentinized orthopyroxene record transient oceanic lithospheric mantle dehydration (Leka Ophiolite Complex, Norway). J. Petrol. 53, 1943–1968.

Poli, S., 2015. Carbon mobilized at shallow depths in subduction zones by carbonatitic liquids. Nat. Geosci. 8, 633–636. https://doi.org/10.1038/ngeo2464

Power, I.M., Wilson, S.A., Dipple, G.M., 2013. Serpentinite carbonation for CO2 sequestration. Elements 9, 115–121.

Proskurowski, G., Lilley, M.D., Seewald, J.S., Früh-Green, G.L., Olson, E.J., Lupton, J.E., Sylva, S.P., Kelley, D.S., 2008. Abiogenic hydrocarbon production at Lost City hydrothermal field. Science 319, 604–607.

Ranero, C.R., Phipps Morgan, J., McIntosh, K., Reichert, C., 2003. Bending-related faulting and mantle serpentinization at the Middle America trench. Nature 425, 367–373.

Rasmussen, R.A., Khalil, M.A.K., 1981. Atmospheric methane (CH4): Trends and seasonal cycles. J. Geophys. Res. Oceans 86, 9826–9832.

Rasmussen, S., Chen, L., Nilsson, M., Abe, S., 2003. Bridging nonliving and living matter. Artif. Life 9, 269–316.

Ray, J.S., 2009. Carbon isotopic variations in fluid-deposited graphite: evidence for multicomponent Rayleigh isotopic fractionation. Int. Geol. Rev. 51, 45–57.

Ray, J.S., Ramesh, R., 2000. Rayleigh fractionation of stable isotopes from a multicomponent source. Geochim. Cosmochim. Acta 64, 299–306.

Rayleigh, Lord, 1896. L. Theoretical considerations respecting the separation of gases by diffusion and similar processes. Lond. Edinb. Dublin Philos. Mag. J. Sci. 42, 493–498.

Reay, D., Smith, P., van Amstel, A., 2010. Methane and climate change. Earthscan.

Reveillaud, J., Reddington, E., McDermott, J., Algar, C., Meyer, J.L., Sylva, S., Seewald, J., German, C.R., Huber, J.A., 2016. Subseafloor microbial communities in hydrogen-rich vent fluids from hydrothermal systems along the M id-C ayman R ise. Environ. Microbiol. 18, 1970–1987.

Rieder, R., Economou, T., Wanke, H., Turkevich, A., Crisp, J., Bruckner, J., Dreibus, G., McSween Jr, H.Y., 1997. The chemical composition of Martian soil and rocks returned by the mobile alpha proton X-ray spectrometer: Preliminary results from the X-ray mode. Science 278, 1771–1774.

Rouméjon, S., Andreani, M., Früh-Green, G.L., 2019. Antigorite crystallization during oceanic retrograde serpentinization of abyssal peridotites. Contrib. Mineral. Petrol. 174, 60.

Rumble, D., Duke, E.F., Hoering, T.L., 1986. Hydrothermal graphite in New Hampshire: Evidence of carbon mobility during regional metamorphism. Geology 14, 452–455.

Rumble, D., Hoering, T.C., 1986. Carbon isotope geochemistry of graphite vein deposits from New Hampshire, USA. Geochim. Cosmochim. Acta 50, 1239–1247.

Rüpke, L.H., Hasenclever, J., 2017. Global rates of mantle serpentinization and H2 production at oceanic transform faults in 3-D geodynamic models. Geophys. Res. Lett. 44, 6726–6734.

Rüpke, L.H., Morgan, J.P., Hort, M., Connolly, J.A., 2004. Serpentine and the subduction zone water cycle. Earth Planet. Sci. Lett. 223, 17–34.

Russell, M.J., Nitschke, W., 2017. Methane: fuel or exhaust at the emergence of life? Astrobiology 17, 1053–1066.

Saad, A.H., 1969. Magnetic properties of ultramafic rocks from Red Mountain, California. Geophysics 34, 974–987.

Saccocia, P.J., Seewald, J.S., Shanks III, W.C., 2009. Oxygen and hydrogen isotope fractionation in serpentine–water and talc–water systems from 250 to 450 C, 50 MPa. Geochim. Cosmochim. Acta 73, 6789–6804.

Sapienza, G.T., Scambelluri, M., Braga, R., 2009. Dolomite-bearing orogenic garnet peridotites witness fluid-mediated carbon recycling in a mantle wedge (Ulten Zone, Eastern Alps, Italy). Contrib. Mineral. Petrol. 158, 401–420.

Scambelluri, M., Bebout, G.E., Belmonte, D., Gilio, M., Campomenosi, N., Collins, N., Crispini, L., 2016. Carbonation of subduction-zone serpentinite (high-pressure ophicarbonate; Ligurian Western Alps) and implications for the deep carbon cycling. Earth Planet. Sci. Lett. 441, 155–166. https://doi.org/10.1016/j.epsl.2016.02.034

Scambelluri, M., Cannaò, E., Gilio, M., 2019. The water and fluid-mobile element cycles during serpentinite subduction. A review. Eur. J. Mineral. 31, 405–428.

Scambelluri, M., Müntener, O., Hermann, J., Piccardo, G.B., Trommsdorff, V., 1995. Subduction of water into the mantle: history of an Alpine peridotite. Geology 23, 459–462.

Scambelluri, M., Strating, E.H., Piccardo, G.B., Vissers, R.L.M., Rampone, E., 1991. Alpine olivine-and titanian clinohumite-bearing assemblages in the Erro-Tobbio peridotite (Voltri Massif, NW Italy). J. Metamorph. Geol. 9, 79–91.

Scambelluri, M., Tonarini, S., 2012. Boron isotope evidence for shallow fluid transfer across subduction zones by serpentinized mantle. Geology 40, 907–910.

Schlaphorst, D., Kendall, J.-M., Collier, J.S., Verdon, J.P., Blundy, J., Baptie, B., Latchman, J.L., Massin, F., Bouin, M.-P., 2016. Water, oceanic fracture zones and the lubrication of subducting plate boundaries—insights from seismicity. Geophys. J. Int. 204, 1405–1420.

Schmidt, M., Poli, S., 2014. 4.19. Devolatilization during subduction. The Crust, Treatise on Geochemistry.

Schneider, M.E., Eggler, D.H., 1986. Fluids in equilibrium with peridotite minerals: implications for mantle metasomatism. Geochim. Cosmochim. Acta 50, 711–724.

Schrenk, M.O., Brazelton, W.J., Lang, S.Q., 2013. Serpentinization, carbon, and deep life. Rev. Mineral. Geochem. 75, 575–606.

Schroeder, T., Bach, W., Jöns, N., Jöns, S., Monien, P., Klügel, A., 2015. Fluid circulation and carbonate vein precipitation in the footwall of an oceanic core complex, O cean D rilling P rogram S ite 175, M id-A tlantic R idge. Geochem. Geophys. Geosystems 16, 3716–3732.

Schulte, M., Blake, D., Hoehler, T., McCOLLOM, T., 2006. Serpentinization and its implications for life on the early Earth and Mars. Astrobiology 6, 364–376.

Schwartz, S., Guillot, S., Reynard, B., Lafay, R., Debret, B., Nicollet, C., Lanari, P., Auzende, A.L., 2013. Pressure–temperature estimates of the lizardite/antigorite transition in high pressure serpentinites. Lithos 178, 197–210.

Schwarzenbach, E.M., Früh-Green, G.L., Bernasconi, S.M., Alt, J.C., Plas, A., 2013. Serpentinization and carbon sequestration: A study of two ancient peridotite-hosted hydrothermal systems. Chem. Geol. 351, 115–133.

Sephton, M.A., Hazen, R.M., 2013. On the origins of deep hydrocarbons. Rev. Mineral. Geochem. 75, 449–465.

Seyfried Jr, W.E., Foustoukos, D.I., Fu, Q., 2007. Redox evolution and mass transfer during serpentinization: An experimental and theoretical study at 200 C, 500 bar with implications for ultramafic-hosted hydrothermal systems at Mid-Ocean Ridges. Geochim. Cosmochim. Acta 71, 3872–3886.

Sharp, Z., 2017. Principles of Stable Isotope Geochemistry, 2nd Edition. Pearson Prentice Hall. https://doi.org/10.25844/h9q1-0p82

Shen, T., Hermann, J., Zhang, L., Lü, Z., Padrón-Navarta, J.A., Xia, B., Bader, T., 2015. UHP metamorphism documented in Ti-chondrodite-and Ti-clinohumite-bearing serpentinized ultramafic rocks from Chinese southwestern Tianshan. J. Petrol. 56, 1425–1458.

Shi, P., Saxena, S.K., 1992. Thermodynamic modeling of the CHOS fluid system. Am. Mineral. 77, 1038–1049.

Shilobreeva, S., Martinez, I., Busigny, V., Agrinier, P., Laverne, C., 2011. Insights into C and H storage in the altered oceanic crust: Results from ODP/IODP Hole 1256D. Geochim. Cosmochim. Acta 75, 2237–2255.

Shuai, Y., Etiope, G., Zhang, S., Douglas, P.M., Huang, L., Eiler, J.M., 2018. Methane clumped isotopes in the Songliao Basin (China): New insights into abiotic vs. biotic hydrocarbon formation. Earth Planet. Sci. Lett. 482, 213–221.

Sleep, N.H., Bird, D.K., 2007. Niches of the pre-photosynthetic biosphere and geologic preservation of Earth's earliest ecology. Geobiology 5, 101–117.

Sleep, N.H., Meibom, A., Fridriksson, T., Coleman, R.G., Bird, D.K., 2004. H2-rich fluids from serpentinization: geochemical and biotic implications. Proc. Natl. Acad. Sci. 101, 12818–12823.

Spandler, C., Hermann, J., Arculus, R., Mavrogenes, J., 2003. Redistribution of trace elements during prograde metamorphism from lawsonite blueschist to eclogite facies; implications for deep subduction-zone processes. Contrib. Mineral. Petrol. 146, 205–222.

Spandler, C., Hermann, J., Faure, K., Mavrogenes, J.A., Arculus, R.J., 2008. The importance of talc and chlorite "hybrid" rocks for volatile recycling through subduction zones; evidence from the high-pressure subduction mélange of New Caledonia. Contrib. Mineral. Petrol. 155, 181–198.

Spandler, C., Pirard, C., 2013. Element recycling from subducting slabs to arc crust: A review. Lithos 170, 208–223.

Spycher, N.F., Reed, M.H., 1988. Fugacity coefficients of H2, CO2, CH4, H2O and of H2O- CO2-CH4 mixtures: A virial equation treatment for moderate pressures and temperatures applicable to calculations of hydrothermal boiling. Geochim. Cosmochim. Acta 52, 739–749. https://doi.org/10.1016/0016-7037(88)90334-1

Stachel, T., Chacko, T., Luth, R.W., 2017a. Carbon isotope fractionation during diamond growth in depleted peridotite: Counterintuitive insights from modelling water-maximum CHO fluids as multi-component systems. Earth Planet. Sci. Lett. 473, 44–51.

Stachel, T., Chacko, T., Luth, R.W., 2017b. Carbon isotope fractionation during diamond growth in depleted peridotite: Counterintuitive insights from modelling water-maximum CHO fluids as multi-component systems. Earth Planet. Sci. Lett. 473, 44–51.

Stagno, V., 2019. Carbon, carbides, carbonates and carbonatitic melts in the Earth's interior. J. Geol. Soc. 176, 375–387.

Stagno, V., Frost, D.J., 2010. Carbon speciation in the asthenosphere: Experimental measurements of the redox conditions at which carbonate-bearing melts coexist with graphite or diamond in peridotite assemblages. Earth Planet. Sci. Lett. 300, 72–84.

Stanley, R.S., Roy, D.L., Hatch, N.L., Knapp, D.A., 1984. Evidence for tectonic emplacement of ultramafic and associated rocks in the pre-Silurian eugeoclinal belt of western New England; vestiges of an ancient accretionary wedge. Am. J. Sci. 284, 559–595. https://doi.org/10.2475/ajs.284.4-5.559

Stern, R.J., 2002. Subduction zones. Rev. Geophys. 40, 3–1.

Stewart, E.M., Ague, J.J., Ferry, J.M., Schiffries, C.M., Tao, R.-B., Isson, T.T., Planavsky, N.J., 2019. Carbonation and decarbonation reactions: Implications for planetary habitability. Am. Mineral. J. Earth Planet. Mater. 104, 1369–1380.

Stolper, D.A., Lawson, M., Davis, C.L., Ferreira, A.A., Neto, E.S., Ellis, G.S., Lewan, M.D., Martini, A.M., Tang, Y., Schoell, M., 2014a. Formation temperatures of thermogenic and biogenic methane. Science 344, 1500–1503.

Stolper, D.A., Martini, A.M., Clog, M., Douglas, P.M., Shusta, S.S., Valentine, D.L., Sessions, A.L., Eiler, J.M., 2015. Distinguishing and understanding thermogenic and biogenic sources of methane using multiply substituted isotopologues. Geochim. Cosmochim. Acta 161, 219–247.

Stolper, D.A., Sessions, A.L., Ferreira, A.A., Neto, E.S., Schimmelmann, A., Shusta, S.S., Valentine, D.L., Eiler, J.M., 2014b. Combined 13C–D and D–D clumping in methane: Methods and preliminary results. Geochim. Cosmochim. Acta 126, 169–191.

Strens, R.G.J., 1965. The graphite deposit of Seathwaite in Borrowdale, Cumberland. Geol. Mag. 102, 393–406.

Sugisaki, R., Mimura, K., 1994. Mantle hydrocarbons: abiotic or biotic? Geochim. Cosmochim. Acta 58, 2527–2542.

Sverjensky, D.A., Harrison, B., Azzolini, D., 2014a. Water in the deep Earth: the dielectric constant and the solubilities of quartz and corundum to 60 kb and 1200 C. Geochim. Cosmochim. Acta 129, 125–145.

Sverjensky, D.A., Stagno, V., Huang, F., 2014b. Important role for organic carbon in subduction-zone fluids in the deep carbon cycle. Nat. Geosci. 7, 909.

Syracuse, E.M., van Keken, P.E., Abers, G.A., 2010. The global range of subduction zone thermal models. Phys. Earth Planet. Inter. 183, 73–90.

Szostak, J.W., Bartel, D.P., Luisi, P.L., 2001. Synthesizing life. Nature 409, 387–390.

Takai, K., Nakamura, K., Suzuki, K., INAGAKI, F., NEALSON, K.H., KUMAGAI, H., 2006. Ultramafics-Hydrothermalism-Hydrogenesis-HyperSLiME (UltraH3) linkage: a key insight into early microbial ecosystem in the Archean deep-sea hydrothermal systems. Paleontol. Res. 10, 269–282.

Tao, R., Zhang, L., Tian, M., Zhu, J., Liu, X., Liu, J., Höfer, H.E., Stagno, V., Fei, Y., 2018. Formation of abiotic hydrocarbon from reduction of carbonate in subduction zones: Constraints from petrological observation and experimental simulation. Geochim. Cosmochim. Acta 239, 390–408.

Taylor, B.E., Liou, J.G., 1978. The low-temperature stability of andradite in COH fluids. Am. Mineral. 63, 378–393.

Taylor, W.R., Green, D.H., 1986. The role of reduced COH fluids in mantle partial melting, in: International Kimberlite Conference: Extended Abstracts. pp. 211–213.

Tonarini, S., Pennisi, M., Leeman, W.P., 1997. Precise boron isotopic analysis of complex silicate (rock) samples using alkali carbonate fusion and ion-exchange separation. Chem. Geol. 142, 129–137.

Touret, J.L.R., 2001. Fluids in metamorphic rocks. Lithos 55, 1–25.

Trommsdorff, V., Evans, B.W., 1974. Alpine metamorphism of peridotitic rocks.

Trommsdorff, V., Evans, B.W., 1972. Progressive metamorphism of antigorite schist in the Bergell tonalite aureole (Italy). Am. J. Sci. 272, 423–437.

Trommsdorff, V., Sánchez-Vizcaíno, V.L., Gomez-Pugnaire, M.T., Müntener, O., 1998. High pressure breakdown of antigorite to spinifex-textured olivine and orthopyroxene, SE Spain. Contrib. Mineral. Petrol. 132, 139–148.

Truche, L., McCollom, T.M., Martinez, I., 2020. Hydrogen and abiotic hydrocarbons: molecules that change the world. Elem. Int. Mag. Mineral. Geochem. Petrol. 16, 13–18.

Tumiati, S., Fumagalli, P., Tiraboschi, C., Poli, S., 2013. An experimental study on COH-bearing peridotite up to 3· 2 GPa and implications for crust–mantle recycling. J. Petrol. 54, 453–479.

Tumiati, S., Tiraboschi, C., Sverjensky, D.A., Pettke, T., Recchia, S., Ulmer, P., Miozzi, F., Poli, S., 2017. Silicate dissolution boosts the CO2 concentrations in subduction fluids. Nat. Commun. 8, 1–11.

Ueno, Y., Yamada, K., Yoshida, N., Maruyama, S., Isozaki, Y., 2006. Evidence from fluid inclusions for microbial methanogenesis in the early Archaean era. Nature 440, 516.

Ulmer, P., Luth, R.W., 1991. The graphite-COH fluid equilibrium in P, T, $$ f_ ${$O_2$}$ $$ space. Contrib. Mineral. Petrol. 106, 265–272.

Ulmer, P., Trommsdorff, V., 1995. Serpentine stability to mantle depths and subduction-related magmatism. Science 268, 858–861.

Valley, J.W., 2018. Stable isotope geochemistry of metamorphic rocks. Stable Isot. High Temp. Geol. Process. 445–490.

Valley, J.W., O'Neil, J.R., 1981. 13C12C exchange between calcite and graphite: a possible thermometer in Grenville marbles. Geochim. Cosmochim. Acta 45, 411–419.

Van Baalen, M.R., Mossman, B.T., Gunter, M.E., Francis, C.A., 2009. Environmental Geology of Belvidere Mt.

Van Keken, P.E., Vrijmoed, J.C., Wilson, C.R., Spiegelman, M., Hacker, B.R., 2011. Metamorphic devolatilization in subduction zones: thermal, dynamic and thermodynamic modeling, in: AGU Fall Meeting Abstracts. pp. U51D-07.

Vitale Brovarone, A., Martinez, I., Elmaleh, A., Compagnoni, R., Chaduteau, C., Ferraris, C., Esteve, I., 2017. Massive production of abiotic methane during subduction evidenced in metamorphosed ophicarbonates from the Italian Alps. Nat. Commun. 8, 14134.

Vitale Brovarone, A., Sverjensky, D.A., Piccoli, F., Ressico, F., Giovannelli, D., Daniel, I., 2020. Subduction hides high-pressure sources of energy that may feed the deep subsurface biosphere. Nat. Commun. 11, 1–11.

Viti, C., Mellini, M., Rumori, C., 2005. Exsolution and hydration of pyroxenes from partially serpentinized harzburgites. Mineral. Mag. 69, 491–507.

Wada, I., Wang, K., 2009. Common depth of slab-mantle decoupling: Reconciling diversity and uniformity of subduction zones. Geochem. Geophys. Geosystems 10.

Wada, I., Wang, K., He, J., Hyndman, R.D., 2008. Weakening of the subduction interface and its effects on surface heat flow, slab dehydration, and mantle wedge serpentinization. J. Geophys. Res. Solid Earth 113.

Wassmann, S., Stoeckhert, B., 2013. Rheology of the plate interface—Dissolution precipitation creep in high pressure metamorphic rocks. Tectonophysics 608, 1–29.

Weis, P.L., Friedman, I., Gleason, J.P., 1981. The origin of epigenetic graphite: evidence from isotopes. Geochim. Cosmochim. Acta 45, 2325–2332.

Welte, D.H., Tissot, P.B., 1984. Petroleum formation and occurrence. Springer.

Wenner, D.B., Taylor, H.P., 1974. D/H and O18/O16 studies of serpentinization of ultramaflc rocks. Geochim. Cosmochim. Acta 38, 1255–1286.

Wenner, D.B., Taylor, H.P., 1971. Temperatures of serpentinization of ultramafic rocks based on O 18/O 16 fractionation between coexisting serpentine and magnetite. Contrib. Mineral. Petrol. 32, 165–185.

Wicks, F.J., Whittaker, E.J.W., 1977. Serpentine textures and serpentinization. Can. Mineral. 15, 459–488.

Wolery, Tj., Jarek, R.L., 2003. Software user's manual: EQ3/6, version 8.0. Softw. Doc. 8–0.

Woodland, A.B., Bulatov, V.K., Brey, G.P., Girnis, A.V., Höfer, H.E., Gerdes, A., 2018. Subduction factory in an ampoule: Experiments on sediment–peridotite interaction under temperature gradient conditions. Geochim. Cosmochim. Acta 223, 319–349.

Yamaoka, K., Ishikawa, T., Matsubaya, O., Ishiyama, D., Nagaishi, K., Hiroyasu, Y., Chiba, H., Kawahata, H., 2012. Boron and oxygen isotope systematics for a complete section of oceanic crustal rocks in the Oman ophiolite. Geochim. Cosmochim. Acta 84, 543–559.

Young, E.D., Kohl, I.E., Lollar, B.S., Etiope, G., Rumble, D., Li, S., Haghnegahdar, M.A., Schauble, E.A., McCain, K.A., Foustoukos, D.I., 2017. The relative abundances of resolved l2 CH 2 D 2 and 13 CH 3 D and mechanisms controlling isotopic bond ordering in abiotic and biotic methane gases. Geochim. Cosmochim. Acta 203, 235–264.

Zahnle, K., Arndt, N., Cockell, C., Halliday, A., Nisbet, E., Selsis, F., Sleep, N.H., 2007. Emergence of a habitable planet. Space Sci. Rev. 129, 35–78.

Zhang, S., Ague, J.J., Vitale Brovarone, A., 2018. Degassing of organic carbon during regional metamorphism of pelites, Wepawaug Schist, Connecticut, USA. Chem. Geol. 490, 30–44. https://doi.org/10.1016/j.chemgeo.2018.05.003

Zheng, Y.-F., 1999. Oxygen isotope fractionation in carbonate and sulfate minerals. Geochem. J. 33, 109–126.

Zheng, Y.-F., 1993. Calculation of oxygen isotope fractionation in hydroxyl-bearing silicates. Earth Planet. Sci. Lett. 120, 247–263.